Cranfield University

Omeed Karimi

The Production and Characterisation of Inorganic Combinatorial Libraries

PhD Thesis

2010

Cranfiled University

Cranfield Health

Ph.D. Thesis

2010

Omeed Karimi

The Production and Characterisation of Inorganic Combinatorial Libraries

Supervisor – Professor Keith Rogers

October 2010

Abstract

With the increasing demand for research into new materials, techniques which are able to produce and characterise a large number of samples rapidly are becoming indispensable. Thin film technology has the potential to improve the amount of information contained on deposited samples by creating compositionally graded libraries. Conventionally, raster scan methods are used to interrogate such libraries.

The production of combinatorial samples by methods not previously employed in this role has been carried out. Both solution based electrochemical deposition and electrostatic spray vaporisation production methods have been successfully modified to produce thin film continuous compositional spread (CCS) samples. Additional samples have been produced by off-axis direct current magnetron sputtering, a method already established in the combinatorial field.

Presented here is a different approach to provide high-throughput data collection and analysis of combinatorial libraries using an X-ray diffraction (XRD) probe. An extended X-ray beam was used to illuminate the polycrystalline libraries and a large area detector used to collect the data. A new partitioning algorithm has been employed to analyze the collected data and extract the crystallographic information from the illuminated area. The results of the technique have been compared with the raster scans showing that the algorithm provides reliable data equivalent to multiple point data collections with significantly increased data acquisition speed.

With the new chemical libraries and other simplified samples the partitioning method has been shown to be appropriate for the analysis of both distinct composition high density chemical libraries and also CCS samples. To achieve the validation of the new method the new libraries have been illumination with the extended beam X-ray source. The resultant superimposed diffraction patterns are partitioned with the novel software and compared with conventional XRD.

The resolution of the partitioning method has been shown to be in the 1 mm range when applied to CCS libraries and 1.5 mm for high density chemical libraries. For randomly orientated polycrystalline samples the d-spacing change between the partitioned data and the corresponding raster scanned data is not statistically significant. This corresponds to d-spacing determination with a precession of < 0.01 Å when used with the Bruker D8 diffractometer and our geometry.

Contribution to knowledge

During this investigation two methods of thin solid film sample production have been adapted to produce continuous compositional spread chemical libraries. These methods have not previously been used to produce chemical libraries in this way and as such the project has added to potential combinatorial production methods available to future researchers.

Sequential electrochemical layering of variable thickness metallic layers has been achieved for a number of elemental combinations. This was achieved using a novel variable time electroplating method that negates the complex and inflexible charge density distribution methods used by other researchers. The continuous compositional spread samples produced by this method have been used as precursor materials for the production of higher order combinatorial systems.

Electrostatic spray deposition methods have been used to produce simultaneously deposited combinatorial systems, a first for this production method. This research has shown that the positive characteristics of electrostatic spraying, its cost effectiveness and flexibility, can be brought to combinatorial production.

The robustness of the method in terms of precursor solution choice has enabled the deposition of both metallic and the non-metallic components. This has allowed the production of inter-metallic combinatorial systems in a single step.

Additionally a novel method that allows the collection of X-ray diffraction data simultaneously from a large area of polycrystalline combinatorial libraries is presented. The process employs extended X-ray illumination of a portion of these libraries followed by a unique partitioning process. Thus, for the first time, it is possible to reliably extract the diffraction patterns from multiple polycrystalline samples collected in a single area intensity map. This new method has been shown to give diffraction results that are equivalent to the more conventional but significantly slower multiple point source collections. Using this method, the material identification and lattice parameter information for a number of closely packed materials can be simultaneously established.

This procedure has been shown to give significant improvements in data collection time which is acknowledged to be a limiting factor in the employment of XRD in the analysis of

high density libraries. Hence an improvement over standard diffraction techniques has been achieved.

Using simulated diffraction data the theoretical constraints caused by the chosen partitioning method has been explored. The theoretical basis for employing this system is illustrated. The effect of sample morphology such as non random crystalline orientation on the new method is presented.

The process has been validated and optimised using simple phantom samples fabricated from standard diffraction materials. The partition method has been successfully employed in the determination of both distinct compositional area libraries and constant compositional spread samples fabricated as part of the investigation. In both cases practical resolution limits of the partitioned data have been collected and presented. These results compare favourably with conventionally collected diffraction data, justifying adoption of the process.

The work has so far produced two research paper publications in mainstream peer reviewed journals.

Acknowledgments

I would like to thank Professor Keith Rogers, Dr David Lane and Dr Scilla Roncallo for their help and guidance; Mr Kyle Hutchings for the use of the multisource electrostatic spray kit of his design; Professor Laurence Peters and Mr Jonathan Scragg from the University of Bath for their help and the use of equipment.

I would also like to express my gratitude to Dr Guillaume Zoppi at Northumbria University for the post deposition selinisation of samples; Dr John Mathew Gregory of Cornell University for the production of some sputtered libraries and finally, Mr Mike Sellwood for his technical support.

Contents

List of figures

Chapter 2

.

Chapter 3

Chapter 4

Chapter 5

Chapter 6

List of tables

Chapter 3

Chapter 4

Chapter 5

Chapter 6

Glossary

A = Lattice parameter

A = Atomic mass

Å = Angstrom

c = Lattice parameter

C = Moseley's constant

C_1 = Electrolytic constant

C_2 = Electrolytic constant

CCD = Charge couple device

CCS = Continuous compositional spread samples

CIGS = $Cu(In, Ga)Se_2$

CIS = $CuInSe_2$

CZTS = Cu_2ZnSnS_4

d = Atomic plane spacing

D = Density

D = The sample to detector distance

D = Perpendicular source to sample distance

D1= Perpendicular source to sample distance

D2 = Modified particle fight distance

DCA = Distinct compositional area samples

DC = Direct current

EDS = Energy Dispersive X-ray Spectroscopy

E_c = Critical ionisation voltage

EQE = External quantum efficiency

ESD = Electrostatic Spray Deposition

ESAVD = Electrostatic spray assisted vapour deposition

F = Faradays constant (96500)

FWHM = Full width half maximum

GADDS = General analysis diffraction detector system

k = intensity

k = the kinetic factor

hkl = Miller index reflection

(hkl) = Miller index plane

HTP = High throughput

i = Total cell current

I = Current density

k = Intensity

$K = E_1 / E_0$ = Kinematic factor

L = Cell distance

M_1 = Mass of incident particle

M_2 = Mass of target material

N_A = Avogadro's number

NBS 640c = silicon powder XRD standard

NIST = National institute of standards and technology

Q = Amount deposited

QSAR = Quantitative structural-activity relationship

PO = Preferred orientation

PV = Photovoltaic

R = Sample to detector distance

R = Deposition rate

r_1 = The x axis displacement error

R^2 = Coefficient of determination

RAM = Relative atomic mass

RBS = Rutherford Backscattering spectrometry

RF = Radio frequency

RGB = Red green blue

RMM = relative molecular mass

S = Sample displacement relative to the instrument centre

SRM 1976 = Al_2O_3 XRD standard

t = Time

TCO = Transparent conducting oxide

Tec 15 = Pilkington group SnO_2 coated soda lime silicate glass

v = Frequency

V = Volt

XRD = X-ray diffraction

WDS = Wavelength dispersive X-ray spectroscopy

y = Grid position / Position on substrate

Z = Atomic number

ZAP = Atomic number effects (Z), absorption effect (A) and fluorescence (F)

α = Metallic alloy phase

β = Metallic alloy phase

γ = Metallic alloy phase

η = Material valence

ε = Metallic alloy phase

ρ = Density

λ = Wavelength

ρ = Thickness atoms per cm^2

Ω = Ohm

σ = Moseley's constant

θ = angle from incident beam

θ_{std} = The expected diffraction angle

χ_1 and χ_2 = Azimuthal limits

Chapter 1

1. Project Aims and introduction

One of the main aims of this investigation is to produce a range of binary and ternary constant compositional spread (CCS) chemical libraries of varying complexity and with a range of characteristics. The libraries will be produced by a range of methods as each method is expected to have associated advantages and disadvantages:

- Direct current magnetron sputtering - This is an established method for combinatorial production, with a significant literature base to draw on. A high level of confidence in this method means that a large number of good quality libraries can be produced. Both binary and higher order samples can be produced without significant alteration to the accepted method. The use of the binary compositional gradients can be expanded by post deposition treatment to produce ternary, sudo-ternary, and other higher order systems. By these means after the initial trials it should be possible to concentrate on systems not previously investigated by combinatorial means.

- Solution based electrochemical deposition - This is highly developed method in the production of uniform thin films. There are only a few examples of combinatorial production being linked to this method. Combinatorial production by this technique currently uses a method that is flawed, it being complex and limited to only low throwing power solutions. It is hoped that other potentially superior methods can be developed. The first of the two main aims required to make this deposition method viable for combinatorial production is to make production simpler. This therefore protects the advantages of resource efficiency that should be associated with combinatorial production. The second is to improve the versatility of the combinatorial method, ideally by using a method where all the materials and deposition condition normally available to the electro chemical researcher can be transferred to a combinatorial approach.

- Electrostatic spray deposition - This method is relatively lightly explored even for the production of conventional samples. Exploration of the technique is desirable

however due to the methods simplicity, versatility and robustness. These characteristics make it resource efficient and as such would compliment combinatorial production. The flexibility of this procedure means that a range of samples both simultaneously and sequentially fabricated can be studied.

By combining the three production techniques outlined above it is hoped that both the continued use of established combinatorial methods and the custom modifications of existing techniques, which have not yet been used in combinatorial synthesis, will be researched. This process means that the relatively low risk incremental expansion of existing knowledge and more radical blue sky ideas can be coupled. All three methods will merit investigation as they have the potential as practical production methods for binary, ternary or higher order chemical libraries or the precursors for pseudo-ternary and larger elemental systems.

The production of a range of samples is arranged by production technique in the method section. Discussion of the libraries created in the investigation will also be arranged by production technique so that the advantages and disadvantages experienced when the new methods are applied to different elemental systems can be fully appreciated. In the results section the data will be grouped primarily in terms of the analytical process used for characterisation. This arrangement with aid the second major aim of the investigation the development and validation of the extended beam XRD method by allowing conventional XRD and partitioned data to be readily compared.

The libraries will be characterised for elemental composition, structural and physical properties such as film thickness by several different approaches. To this end the techniques should include:

- X-ray powder diffraction to give the phase of the material at a particular position on the libraries. The use of an area detector for the XRD is desired as this will allow direct measurement of crystal orientation and grain size for every sample position.

- Energy dispersive X-ray spectroscopy will be used to give a quantitative measure of the elemental composition of the samples at all of the positions on the virtual grid.

- Rutherford backscattering spectroscopy will be used to confirm the elemental composition of the samples. It will also be used to measure the thickness of the

individual layers in sequentially deposited compositional spreads. In the case of co-deposited spreads and thermal diffused samples the method will be used to confirm the homogeneity of the sample within the characterisation volume and within the elimination volume of the EDS system.

By interrogating portions of the compositional spreads with these methods it is hoped that isothermal sections of the corresponding phase diagram can be deduced.

These libraries along with simple phantom samples and theoretical models will be used in the development of a new approach to X-ray diffraction data collection. Validation of the new extended beam XRD method will require:

- Production of simulated data matrices comparable with the output of an area detector under various conditions. Using these simulations the effect of changing detector resolution, illumination properties, and sample characteristics on the theoretical limit of the method can be determined. In this section the best possible partitioning algorithm, from a theoretical point of view, can be chosen. This choice can be the starting point for the optimisation of the partitioning process to true combinatorial libraries.
- The production and illumination of phantom samples to investigate the method under easily understood circumstances. With this process the investigation into how the new method compliments material combinations and sample characteristic can be moved from theoretical to real samples.
- The use of phantom samples to optimise the data collection geometry to make the most of the new technique. Improving signal to noise ratio and resolution in terms of both position on the sample and d-spacing calculation is best done using these simple one and two component systems, before the validation process is expanded.
- The use of the extended beam to characterise the high density chemical libraries made earlier in the investigation. This will not only give a measure of the processes effectiveness on these samples but also due to the libraries variety an indication of general trends of effectiveness. Through this a board understanding of the methods advantages and disadvantages will be gained.

The study of the extended beam collection method and its subsequent partitioning will allow the process to be compared to conventional diffraction in areas such as d-spacing and spatial

resolution, sensitivity and signal to noise ratio. To this end the extended beam diffraction data will be presented to the reader in one section, for clarity the types of library and then the production method of the CCS samples will be listed as subsections of this chapter. A judgment as to the usefulness and limitations of the new method to the characterisation of different materials, film properties, film production methods and data collection circumstances will then be made. Any anomalous results that could constitute a limitation of the method will be explained on an individual sample basis. Results showing a response more beneficial than would be expected can likewise be drawn to the reader's attention.

The use of the new technique with alternative X-ray sources such as synchrotron radiation will be considered, and prelimery findings are presented. The development of the partitioning method specifically optimised for synchrotron data collection is however outside the scope of this investigation.

A range of experimental geometries will be studied and modifications to these arrangements as to fully optimise the conditions to accommodate the new method will be proposed. This information is important for the planning of further research where a more extensive modification of the data collection equipment may be desired.

The use of a combination of both production and analysis of new materials with potential for the photovoltaic industry will be illustrated in an additional section. In particular how the information gained from the new extended beam XRD screening method will be used in aiding the production on conventional samples will be brought to the reader's attention.

Chapter 2

2. Background

2.1 Combinatorial Chemistry

Combinatorial chemistry is generally regarded as any chemical process where large numbers of materials are synthesised simultaneously. The processes evolved from organic synthesis reactions where the same reaction was carried out with different precursor reactants to produce products that are different but structurally similar. While the expansion of combinatorial methods to many other fields now means that the requirement for structural analogues may not apply, working around a family of base compositions is still common [1]. The most important principle to be retained from the original inception is using a small number of deposition steps each one designed to add to the library by a multiple of the original samples [2]. In this respect combinatorial methods differ from the multitude of other high throughput processes that rely on rapid sequential production of chemical libraries [3].

Regardless of the exact experimental design or even the purpose of the study combinatorial methods aim to reduce time, expense, materials and energy required for new product design. This material design stage includes not only the production of materials but also their characterisation, as such many of the steps towards advanced materials can be aided by the employment of combinatorial principles. [4]

2.1.1 Combinatorial Production

A combinatorial chemical approach in inorganic material science, specifically the production of thin film samples, has been utilised since the 1950s. J. J Hanak started co-sputtering metallic thin films to produce high density libraries during the early 1970s [5]. Despite the significant advantages that were immediately apparent for the combinatorial techniques, these methods were slow to develop in inorganic fields. This was partially due to legitimate technical issues, such as the unavailability of suitable computers and related IT equipment as well as lack of appropriate high resolution characterisation tools which reduced the desirability of high throughput techniques (HTP) [6]. However, a significant reason for the

relatively unsuccessful start to these high throughput techniques was due to an attitude among many researchers who believed that as these techniques produced discoveries through chance the approaches were less desirable than if the same discoveries had been made using rational material design [7].

Researchers in other areas were much quicker to utilise high throughput chemical methods. The best example of this was the pharmaceutical industry whose members had no prejudice against benefiting from chance discoveries [8]. This type of discovery has been common in the industry since its inception where pharmaceutical materials have long been developed from natural materials. Another reason for the quick and successful uptake of HTP techniques by the pharmaceutical industry was the way in which it could be adopted in a step-by-step fashion. An example of this is the way that compounds could be tested for biological activity in a combinatorial manner even though their production was conventional. When this situation led to a bottleneck giving a shortage of compounds to be tested, it was a small step to producing organic compounds by combinatorial methods. The most common of these techniques is the "split and pool" method that allows the production of very large numbers of similar compounds to be manufactured and tested for biological activity in a short period of time [9]. These compounds are still conventionally produced in the sense that the final products are isolated in their own reaction vessel and the chemical libraries consist of these reaction vessels stored in a conventional way. In most cases, computer controlled robotics are needed to manipulate very large numbers of reaction vessels and complete the fabrication simultaneously [8].

Even in the pharmaceutical and biochemical fields where combinatorial methods have been of undeniable successes there has always been a pressure to use sample production methods that use large amounts of quantitative structural-activity relationship (QSAR) knowledge. While QSAR is acknowledged to be an extremely powerful tool in the long term it fair to say that at least some of the preference for this method over random screening is cultural and not science based.

It is rarely the case that discovery methods are used in isolation and the large amount of data produced by pharmaceutical companies using these high throughput techniques allowed them to start to link the structure of the molecule to its biological activity. In this field at least combinatorial production and screening with input from QSAR calculations have opened the possibility of more rational drug design. Here computer modelling is used to determine a

narrowed choice of theoretically advantageous materials, combinatorial production then being used to produce a range of compounds that fulfil these characteristics. It was this move away from the unpopular serendipitous approach towards more logic-based methodologies that helped popularise combinatorial chemistry in other fields.

As with pharmaceutical research many other fields have too many structures of potential benefit to use purely random means to detect the desired activity. It is normal for combinatorial screening to be informed by an ongoing process where structural data is analysed at its most basic level. Advances in data mining to search and utilise this data as well as more powerful computer simulations are being developed [10]. Attempts to calculate the band gap of theoretical semiconductor junctions from first principles, for example, will in turn encourage the acquisition of more real world data on which to base the work.

Despite a slow start the advantages of combinatorial production of materials is now firmly established in many fields. Beginning in the mid-1990s the number of inorganic production methods adapted for combinatorial work and the types of samples to be screened are now growing very strongly [11].

The development of catalysts is one area where HTP methods are now at the forefront of research [12] [13]. Successful research into high temperature superconductors further popularised the combinatorial field [6].

Out of all the fields that have recently adopted combinatorial methods research into catalyst development has been the most successful. The intense effort in this area is due to the combination of the subject's scientific and economic importance as well as the large number of variables that are known to affect catalytic activity. The ability to test many catalytic effects quickly and thus avoid a bottle neck in the workflow is advantageous. [11] Many of the successes in this area are by the high throughput production of conventional samples, however for many classes of solid state catalysts the thin film production method is suitable.

Cost advantages were clearly an early draw to the combinatorial method with the high cost and the time consuming nature of producing samples for screening being problematic. It is the issues of cost in particular that has meant only approximately 5% of possible metallic ternaries and less than 1% of quaternary phase diagrams have been fully investigated [14]. Assuming 50 stable and practical elements to choose from there are in the rejoin of 10^{10} decanary combinations. [15]

During advanced material development such as for the photovoltaic (PV) industry very small compositional changes can have a marked effect on chemical properties. Dopent level changes in the <0.1% range can substantially effect for example the semi conduction and photo activity. For this reason bulk production of compounds for screening for these properties can potentially totally miss desired properties, even if the composition gaps used in these productions are very small.

Problems with producing unique bulk materials on an individual basis are not confined to the loss of potentially significant characteristics. The combinatorial approach to material synthesis has benefits other than its increased speed and efficiency over conventional methods. One such advantage is as the samples are produced at the same time the technique eliminates subtle but potentially significant experiment-to-experiment differences increasing the consistency of the experimental conditions used [16].

An accurate picture of the structural-activity relationship can best be gained by sample production and analytical techniques where sample composition is continually changing or where a larger number of slightly different materials can be examined. It is generally acknowledged that any experimental situation where these ranges of material are produced in parallel is a combinatorial process. For most researchers it is solely the production of the samples that gives the combinatorial status regardless of the method of analysis.

The use of very simple phenomenon can produce the desired continuous compositional spread (CCS), for example utilising the phenomenon of thermal dissociation of atoms within metallic structures. If two metallic elements in bulk form are brought very close together and a suitable heat and pressure regime is applied then atomic dissociation will occur and a small region of alloy will be formed at the junction [17]. Three or more metallic elements can be brought together at similar junctions to produce ternary or higher alloys [14]. Within this diffusion layer alloys of different composition are present so moving analytical probes across this region can give insight into the structure of the materials. However the diffusion area is very small. Therefore to gain significant information from this arrangement the spatial resolution of any probes used must be exceptionally good. This issue constitutes a major short fall in the bulk diffusion method. While being limited the diffusion junction method is important as the physical principles most notably the principle of thermal interdiffusion is replicated in many combinatorial methods [18].

When dealing with thin films complete dissociation of the elements can be achieved through the film giving a uniform composition in this dimension. The arrangement of the materials would generally be set up in such a way that the compositional change occurs across the film rather than through it. Therefore alloys of specific composition will be much further spatially separated than in examples using dissociation at the junction of two bulk materials. The flexibility in spatial resolution makes thin film techniques potently excellent for compositional spreads. This is a major reason why many researchers have concentrated on high density chemical libraries. It is these thin solid film chemical libraries that will be the focus in the following sections.

2.1.2 Chemical Libraries

Inorganic high density chemical libraries can be imagined as simply many thin film samples contained on the one substrate. These thin film libraries are particularly useful for characterisation by non-destructive analytical techniques but are less effective when destructive methods have been chosen. Both elemental and structural determinations are usually required for each material in the library and also further physical and chemical characteristics need to be assigned. For many destructive methods a shortage of material for analysis can prevent a full set of measurements being collected. This is exaggerated significantly where combinatorial production confines the area of interest in the other dimensions. Even when the characterisation is confined to non-destructive methods the lack of material means that the choice of analysis is more limited than for general thin film research. Sensitivity issues can also make thin films less desirable for non-destructive analytical methods, however in the case of PV research the final product is a thin film so in most cases suitable methods are already routinely used.

Two main types of thin film chemical libraries are common. One type is samples with distinct compositional areas (DCA), where the composition does not change within the cell. The composition then changes abruptly to another material, which can be potentially unrelated to its neighbours. The other type is continuous compositional spread (CCS) libraries where the composition changes gradually through the film and the individual samples are produced by the superimposition of a virtual grid. The choice of grid size and therefore the number of compositions tested is determined primarily by time constraints. The size of the sample and

therefore the precision of the composition determination is generally limited by resolution of the analytical probes.

Each kind of chemical library has advantages and disadvantages. While the subtle differences in the libraries design will only become apparent when considered in relation to the specific application, some general points can be acknowledged.

Distinct composition matrices are very flexible and can be used on many materials with ease. If the production method allows it the samples adjacent on the substrate do not have to be chemically related. If the production of one sample is unsuccessful the rest of the substrate can still be tested. However with this method materials of interest are more likely to be missed and for this reason large scale screening of systems where little prior information is available can be unwise. The use of this targeted production to confirm other studies or to produce materials highlighted by theoretical studies in preferred.

CCS samples have theoretically an unlimited resolution, with the number of samples on a given substrate being limited by probe specification. All thermodynamically stable phases created during the library production should be present even if they only exist in a small compositional range and therefore for a small physical distance on the graded sample. Due to this, when suitable analytical probes are chosen, missing of short lived phases in these samples is much less likely. Full utilisation of this library design with many of the conventional analytical methods is difficult not least due to the data collection time. The collection time is a concern due to the real or perceived issues with diminishing returns on invested machine time. It is this lack of analytical data collection time that allows phases confined to a limited area on the substrate to be completely missed.

Another negative side to the CCS sample design is additional inaccuracies can be produced as the gradient continues within the illumination area of the analytical probes. For this reason choice of characterisation tools is more limited. With this in mind, the choice of size of the virtual grid is more difficult because as the spots on the grid increase the assumed homogeneity inside that illumination area becomes less acceptable. Also as the spot size on the grid is reduced data collection time becomes higher.

In binary or ternary systems it is possible that all, or at least large parts of the phase diagram can be represented by CCS systems [19]. With higher order systems the distribution of the materials on the substrate will not allow for all combinations. It would therefore be prudent to

design the distribution so that it was optimised to a specific part of a high order phase diagram. One way to simplify these multi elemental studies is to produce substrates with gradation in some of the elements. A four component system could best be examined by producing a number of pseudo quaternary systems. These would be ternary systems where the fourth components concentration only changed between the substrates.

With CCS samples the choice of the material can be more limited than for other types on high density chemical library. This is because, if certain compositions do not deposit as expected they can produce problems for the whole film rather than only affecting the sample where the problem occurred. An example of this is where some compositions produce adhesion issues, (it is well established that different composition will have different levels of adhesion [20]). In the case of CCS libraries, an overly stressed phase could de-adhere, this process propagating through the library causing the entire substrate to become detached.

Up until now the examples have concentrated on stoichiometry, with the substrates constituting horizontal lines on a phase diagram. It is not just the composition that can be changed using combinatorial principles, other deposition variables can be altered in the same systematic way. As we know that phase formation can vary with both stoichiometry and temperature it may be desirable to combine these two factors into one production method, as in figure 2.1. A heat source and heat sink can be positioned so that a large and controllable temperature gradient can be held across a substrate. This method can be used in conjunction with a conventionally produced single composition samples to achieve a vertical line on a phase diagram. For maximum efficiency the two can be combined in order to look at a larger portion of the system. [21]

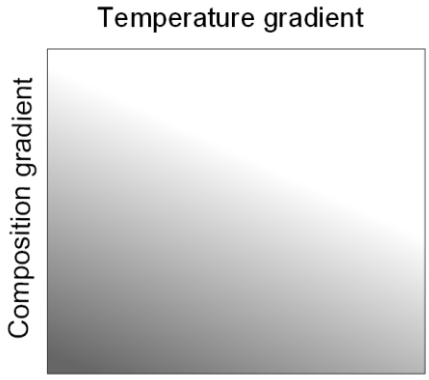

Figure 2.1. A representation of how a two dimensional CCS thin film library would look on a square substrate.

An additional complication to the simultaneous depositions is seen when effects that are deposition rate or total thickness controlled are encountered. These effects are not related to composition and can be seen even in elemental depositions. An example of deposition rate dependence to the film morphology is where the substrate has a dominant crystal structure, deposited materials can be more or less likely to acquire this orientation with different deposition rates. This epitaxial growth is for the most part deposition rate dependent with slower rates encouraging the phenomenon in the majority of cases. The development of crystal orientation occurs by a number of mechanisms. In ZnO films for example, very thin films are generally randomly orientated but as the thickness increases the material is more likely to move to its preferred state with the (002) plane lying parallel to the substrate. [22]

While a number of the combinatorial processes use incident angle as a means of altering deposition rate the effect of these angular changes alone need to be considered. Using the example of Ti-Pd-Au films investigated by Garrido et al [23], this study shows that with a glancing incident angle the growth of dendrites increases and the film porosity increases. These two factors were found to be responsible for reducing the adhesion by increasing the hydration of the films. These additional systematic effects add to the complexity of linking the composition of a material to its properties and are consequently undesired in most combinatorial fabrications.

2.1.3 Solar Cell Applications

Photovoltaic cells can be regarded as any material that can turn photons of light into a flow of electricity. They therefore represent the basic energy transfer medium in solar energy systems. Many semiconductor materials have a photovoltaic effect where electrons are energetically promoted in the presence of light. This leaves the conducting electrons and the opposite holes of positive charge free in the material. If junctions between the n-type and p-type semiconductor can be fashioned so that the electric fields present let the electrons and holes be separated by the device, they can then be allowed to recombine only by flowing through the electrical circuit and so doing useful work [24]. To be useful industrially materials where the photovoltaic effect is achieved with photons of wavelengths seen in sunlight are required.

A number of different materials and device structures have been produced and a significant number are commercially available. Most of the current commercially available PV devices are silicon based with the crystalline form taking the biggest market share due to an efficiency of over 15 % and proven robustness. This system is not however regarded as a global scale solution as the processing costs of the Si wafers are too high to compete with other electricity supply methods [25]. While the cost of producing silicon wafers is becoming more competitive in relation to conventional electricity production other solutions to solar are being sort [26].

An alternative solution is to produce cells that, due to the materials chosen, the quantities required and the manufacturing method used, will have an economic advantage over conventional electricity production methods. Also the elements used in these new cells should ideally be common so that the devices can be produced in much larger quantities. Sacrificing total efficiency for an improved energy per cost ratio is regarded as the way forward, improving both energy as well as cost payback time which potentially allows a larger area to be covered with solar cells.

Dye-sensitised TiO_2 based cells utilising Ru containing organo-metallic compounds [27] or mercury based systems [28] are becoming successful on a research and development scale. While the long term prospects for these bulk junction devices are substantial, not least because of the flexibility for separating light absorption and charge carrier transport into two separate structures [29], concerns over the degradation time of many of these systems have not yet been resolved.

For their medium and possibly long term potential inorganic two component cells, specifically thin film n-p junction structures deposited on a rigid substrate or often a transparent superstrate are still preferred. A number of binary, ternary and quaternary materials with the desired properties have already been found [30]. It is assumed that other high order materials with desirable characteristics are waiting to be discovered, many of these could be studied by combinatorial methods.

FeS_2, a potential absorber, has been deposited by electro deposition with the ratio of sulphur being increased by post annealing in a sulphur atmosphere [31]. Cu_3BiS_3 has also been used as a solar absorber [32] and this can be deposited by both electroplating and sputtering [33] in conjunction with post deposition sulphurisation. These and similar materials could therefore be deposited combinatorially. Higher order materials such as Cu_2ZnSnS_4 [34] and

$Cu(InGa)(SeS)_2$ [35] have also been investigated. There is reason to believe that many other ternary plus materials will have similar characteristics and rapid screening of potential compounds is therefore desirable.

2.2 Summary of Sample Production Methods

Combinatorially produced thin film libraries that are used in structural determination give major advantages over conventional methods. Fortunately most of the methods used for producing uniform thin films can be adapted to make spatially separated libraries or continuous compositional spread (CCS) samples [36]. Discussed here are some of the deposition methods and the ways that they have been adapted.

For maximum usefulness, the density of the distinct cells or virtual cells in CCS samples should be variable and therefore, thin film deposition methods that produce these flexible sample densities are preferred. Other technical issues such as energy and material efficiencies are also considered.

2.2.1 Distinct compositional area (DCA) samples

One of the most popular ways of producing DCA samples is a technique where one area of the substrate is exposed with the rest being masked. Multiple sources of different elements are used to co deposit a predetermined composition at this point. The mask is then move and the next sample is made at a slightly different position on the substrate. This procedure is high throughput and material is saved but it is not truly combinatorial.

An alternative method is to have multiple masks and multiple sources when the masks are moved in sequences to expose a number of sample positions at the same time. Each area will be exposed to the sources at different times building up layers that when diffused will produce a unique composition for every position. This is truly combinatorial as a number samples are made with the same deposition, as shown in figure 2.2, fixed physical masking of the sample and moving the mask between different deposition processes will produce areas of distinct layer composition [37].

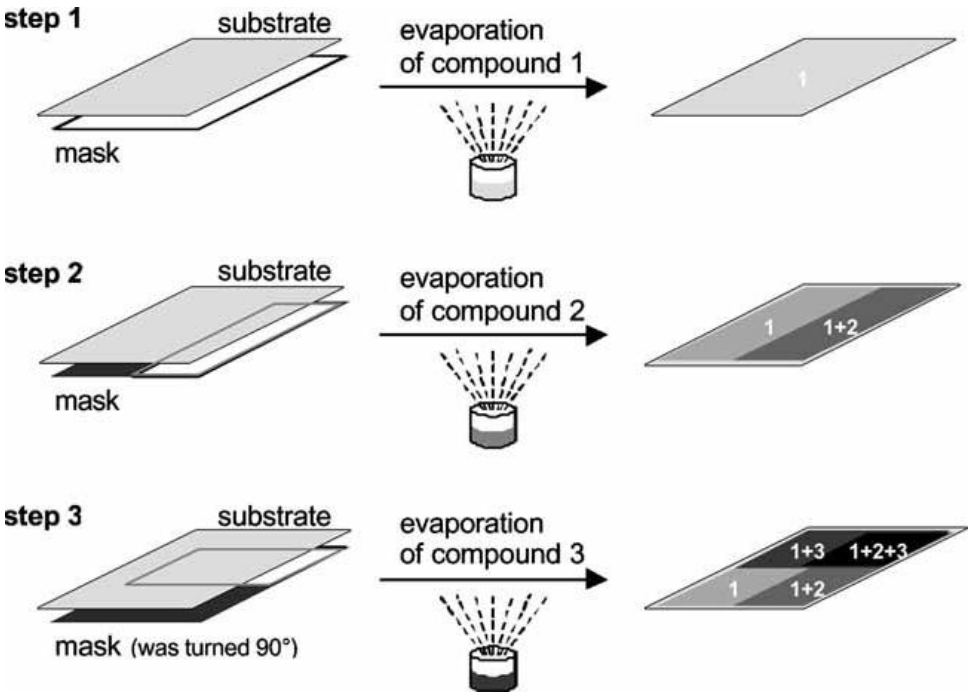

Figure 2.2. An example of a spatially separated library produced using the movable mask system. Sputtering and thermal evaporation systems are often treated in this way [16].

2.2.2 Continuous compositional spread (CCS) samples

These types of samples can be made similarly to the distinct samples with masking and building up of the different layers. However, in this case, moving masks are used to create a gradient of thickness of a particular layer in relation to the other thin film components. When these components are diffused together and alloyed or reacted with each other to form stable compounds compositional spreads will result. Figure 2.3 shows how the mask can be moved slowly during the deposition of a material to manufacture CCS samples.

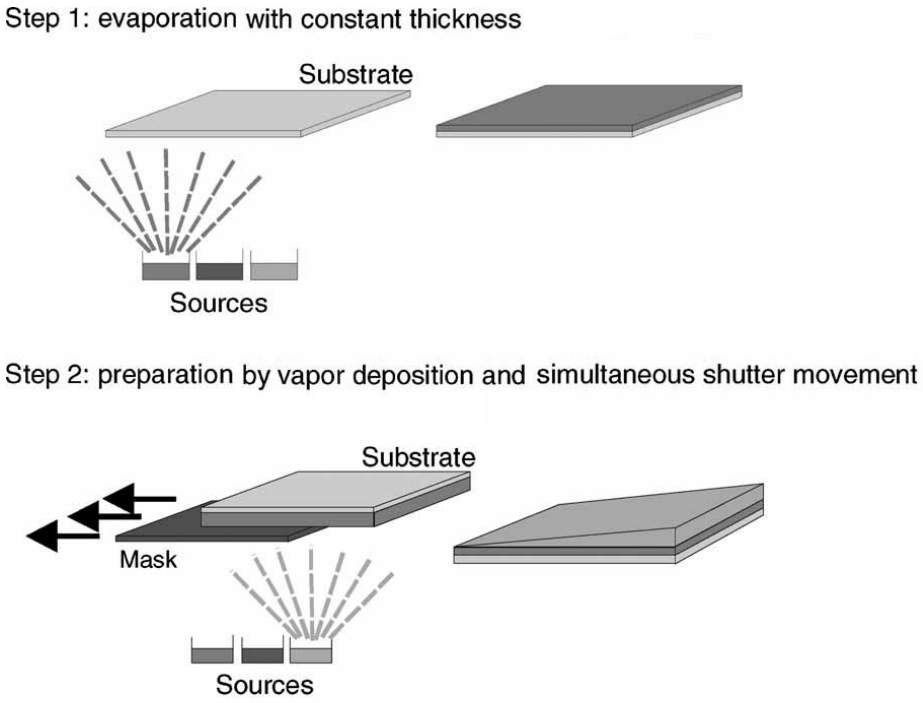

Figure 2.3. This shows an example of how a continuous compositional spread (CCS) sample could be produced [16]. The material in step one is deposited conventionally, in step two the mask in this case is moved during the deposition. This gives rise to the gradient of thickness in the second material.

Many deposition processes allow significant variation to be achieved using geometry alone. During sputter deposition source to substrate, geometry will affect film thickness as the particle paths are altered by scattering from the ionisation gas inside the chamber. [38] The geometric effect shown in figure 2.4 will also change other properties as the angle of contact with the substrate and distance travelled by the particles change the energy of the system.

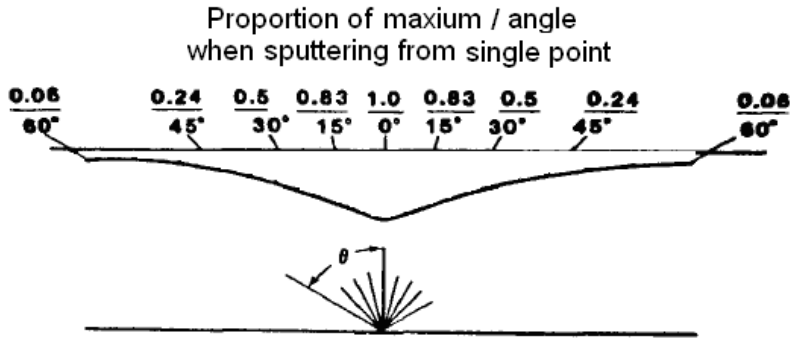

Figure 2.4. A diagram of the geometric effect on the deposition rate of physically produced thin film. This is a simplified system as few sources are truly a single point.

Methods that utilise geometric disparities between the source of the material and the substrate are common in the production of CCS samples generally and are the main method with physical deposition. Source angle in relation to the substrate as well as distance to the substrate are important.

In a simple example where the probability of a particle being liberated at any angle is equal to the distribution of particles reaching the substrate, i.e. there is no in-flight scattering of the particles. The deposition rate can be calculated by trigonometry;

$$R = \frac{D}{Tan\ \theta}$$

Where R = deposition rate, D = perpendicular source to sample distance and θ is the angle of the liberated particle. This holds true when using an ultra high vacuum system. In other systems scattering of the carrier gas further reduces the yield at less oblique angles as the likelihood of scattering is directly proportional to the particles flight path length.

$$D2 = \frac{D1}{Cos\ \theta}$$

Where θ is the angle of the liberated particle, D1 is the perpendicular source to sample distance and D2 is the new fight distance.

In techniques where the particle liberation method introduces a strong directional bias the scattering from secondary collisions between moving deposition material and gas particles in the chamber is the most important mechanism affecting film thickness. In the case of liquid deposition methods diffusion limited characteristics of the solution have a similar effect as they are also linked to path length.

Both of the two main sample types outlined above can be manufactured by adapting either geometric or masking methods to a range of deposition techniques. The various production methods which have been employed to utilise combinatorial methods have been grouped by deposition methods and detailed in section 2.2.1.

2.2.3 Sputtering

Sputtering is one of the most common methods of producing thin film samples. It is preferred over a number of different methods due to the ease in which a large number of elements and compounds can be deposited. Sputtering lends its self to combinatorial methods as the composition of a sputtered film can be easily controlled in relation to its spatial position with both masking and geometric off axis sputtering available.

Both radio frequency (RF) and direct current (DC) magnetron sputtering are equally suitable as similar results can be achieved by each method. Both techniques can use a low pressure inert atmosphere often argon which is ionised and used to bombard the target material to produce the sputtered vapour [39] [40]. As with conventional sputtering, reactive sputtering with, for example, an oxygen atmosphere is possible when producing graded films [41].

Using standard geometry but with masks very close to the sample gives the distinct compositional areas that are favoured by some researchers, Black et al [42] has produced 256 total distinct samples on one substrate using 15 depositions with masking. Due to the production of multiple layers, samples produced by this method need a longer diffusion time. The thin layers (< 100 Å) employed by these researches limit the annealing time to 4 hours.

Similar masking was used in photovoltaic research when investigating CuBiS, CuSbS and PbSbS compounds as potential light absorbers [43]. The individual nature of the samples in these libraries was beneficial as each sample in the library was made into a full cell by fitting front and back contacts. Each sample could then be tested for photo activate simultaneously and in situ.

Other systems use off-axis sputtering that is generally simpler and quicker to deposit. With this arrangement, the materials can be co-sputtered so the annealing time for diffusion can be shorter. Started first by Hanack [5] for general metallurgy combinatorial production has moved into a range of specific areas. Renewable energy applications such as transparent conducting oxides In-Zn-O have been researched by Perkins et al [44], here three to five libraries were used to cover a full compositional range with binary (sudo-ternary) lines. Ginley [45] has been depositing up to quaternary material systems on to 2” x 2” substrates by both DC and ions assisted sputtering, which also aided in the development of TCO materials.

Libraries with more gentle gradients are used to study subtle effects Van Hest [46] has used a modest gradient to investigate the effect of molybdenum doping of In_2O_3. In this case the dopent concentration did not exceed 12 % atomic.

The off-axis sputtering system produces setup difficulties not present in either conventional sputtering or in library production using masking because some of the variables cannot be optimised with the usual freedoms. In conventional DC magnetron sputtering the deposition rate is determined by the ion-current density and secondarily by the ion energy (related to the applied voltage) [47]. At a particular fixed position on the substrate the deposition rate is influenced by the gas pressure and the electrical power applied to the system. Changing the power output and the argon pressure will change the rate of sputtering and therefore the film thickness. This change would also cause different film properties [48]. Changing these variables will have other repercussions for example increased power output can increase the crystallinity of the deposited material, this is usually because under these conditions the sputtered particles that hit the substrate with more potential energy and this will promote atomic rearrangement [49] [50]. Deposition is also effected by other factors such as the shape of the target material [13]. In most cases thickness will be changed by altering the time taken for deposition so the other variables once optimised are left unchanged. Other methods of ion beam sputtering have an advantage in this respect as the flux and the energy of the deposited particles are controlled independently [51].

Other variables such as substrate temperature can also be changed affecting the film structure [52] but, as multiple materials are present on the substrate, this effect is more difficult to predict. The normal method of tailoring the production conditions to the target material is not possible.

Permanent adhesion to the substrate is more difficult to produce in combinatorial libraries as the methods to improve adhesion cannot be optimised for a single compound. In all cases, a factor in the adhesion of the thin film is the amount of internal stress present in the film. This is important as virtually all vacuum deposited films have some level of internal stress [53]. Excessive internal stress present in the thin films is not limited to vacuum deposited films, many other methods such as chemical vapour deposition and physical vapour deposition produce films with internal stress. This is therefore a general concern during combinatorial fabrication. These stresses are often reduced by heat treatment or ion bombardment [54] the same techniques can be applied to chemical libraries but the different compositions mean

conditions cannot be optimised. Also the different compositions present in the libraries mean that an applied binding layer may not be as effective in some areas of the substrate [55].

The nature of combinatorial sputtering makes changes in energy applied to different parts of the substrate unavoidable when using geometry based methods. Scattering off the gas in the chamber is one of the most marked producers of thickness gradients but it also affects individual particle energy. Scattering effects the potential energy contained in the particle when it reaches the substrate, by transfer of momentum to the fill gas. Changes in energy by this mechanism may cause a marked and unexpected change in film characteristics through the library.

Ideally, attempts to make chemical libraries would not involve changing energy densities optimised for conventional film deposition in order to maintain the required crystal structure and to produce appropriate physical properties such as good adhesion [56]. The change in energy caused by the variety of path lengths and the associated momentum transfer makes this more complicated.

In some masking methods where the mask is set away from the sample to avoid a distinct edge in the composition profile there is no clear path from source to substrate in the masked region. The scattering events with the argon in the chamber are the sole mechanism for film growth inside the masked area. In these cases relative differences in particle momentum are higher and can be problematic. This is another example of how it is easier to optimise the energy for conventional uniform films than for masked sputtering.

Regardless of these drawbacks sputtering has been used by a number of researchers to produce CCS samples with positioning optimised to give either a large or small change in composition. The flexibility of co-sputtering from two or more different targets at different positions to give samples with the required range in composition outweighs the problems [57] [58] [59].

Combining both methods is also possible by using masking to emphasise the geometric effect. Inversely, geometric principles can be used to add subtle changes to dopent levels simultaneously to a large number of different compositions produced by the total mask layering method.

Sputtering is one of the combinatorial methods that can also be used to produce libraries of the same elemental composition but fabricated under different conditions. An example of this

is applying a temperature gradient to the substrate during sample production as used by Meredith [60]. Similarly differing annealing regimes can be produced on a single substrate by simultaneous methods.

2.2.4 Electrochemical Deposition

Electrochemical Deposition or electroplating as it is referred to industrially is very widely used for coatings of bulk materials. In many of these cases the coating consists of a < 5 µm film, so the employment in other thin film applications was a logical step. Simultaneous deposition of multiple materials can be used to form the alloys required in high-tech industries. Alloys including light absorber films or there metallic precursors are routinely deposited for several applications [61]. Bi-Sb-Te containing p-type semiconductors have been deposited by Tittes [62]. These were deposited simultaneously from an electrolytic solution containing all the required elements. In this case and in fact in the majority of cases the process is used to produce conventional samples. If a variety of materials are required the solutions will be changed between depositions to produce different samples for testing.

Solar cell absorber materials such as bismuth telluride [63] have been deposited by electroplating. This alloy was simultaneously deposited from a single solution onto molybdenum conducting substrates with the stoichiometry being controlled by the composition of the electrolytic solution.

Depositing the materials simultaneously is convenient but difficult as the compositional requirements of the electrolytic bath makes optimisation of its other required properties more difficult. For this reason most of the fabrication methods are achieved by the layering of the different materials. Complex materials such as Cu_2ZnSnS_4 have been produced by the sequential deposition of Cu, Sn and Zn. The layers are then exposed to an excess of elemental sulphur at high temperature to produce the required film [64]. This system is an interesting route for combinatorial trials as other intermetalic compositions may also be useful and should be screened. The low toxicity of all the materials in this compound and their abundance increases the desirability of their use.

Combinatorial synthesis of tungsten-molybdenum oxides library using a multiwall parallel reactor block that can vary composition of the solution and the deposition voltage in the

individual chambers has been used to produce a 63 sample array of distinct composition and production condition samples [65]. When utilised for ZnO photocatalyts [66] the nature of the substrate means that these individual samples can be tested for activity in situ. While this system is combinatorial in some respects the different materials are produced in isolation and are all distinct in composition. For this reason, some of the most desirable aspects of combinatorial synthesis, notably its ability to produce compositional or conditional spreads is lost.

It is preferred that a single bath and a single substrate are used to fully exploit the combinatorial potential of the method. To achieve this, the characteristics of the method must be understood and exploited. If the bath has enough stirring the mass transport kinetics are not a limiting factor so the amount of deposition on the substrate is given by Faraday's law;

$$Q = \frac{A\ I\ t}{\eta\ \rho\ F}$$

Where Q = the amount of material deposited, A = the atomic mass of the material, ŋ is the valency of the material, ρ is the density, I is the current density, t = time and F (96500) is Faraday's constant. [67] The current density being proportional to the distance between the anode and the cathode;

$$\text{Current density} = i(C_1 - C_2 \log L)$$

Where i is the total cell current, L is the cell distance and C_1 and C_2 are constants depending on the nature of the electrolytic solution.

From this it is clear that the rate of deposition, and through this, morphology is affected by the current density at any point between the electrodes. This in turn is affected by the Ohmic effect of the solution [68], and the current path lengths, for a given solution, this is therefore geometry related. The use of a hull cell with geometry giving large differences in the distance between electrodes is used to investigate these properties [69]. Originally these hull cell tests were used to find solutions that limited the effect of distance i.e. to find solutions with good throwing power.

The usefulness of using exaggerated current densities compared to other factors such as mass transport and diffusion layer characteristics, to quickly investigate different morphologies is now well established. Similar hull cells, as illustrated in figure 2.5, can be used to deposit

layers of different thicknesses with elements being combined to fabricate different alloys. Successful implementation of this method includes the production of Sn-Zn spread alloys libraries for screening by multiple analytical methods [69].

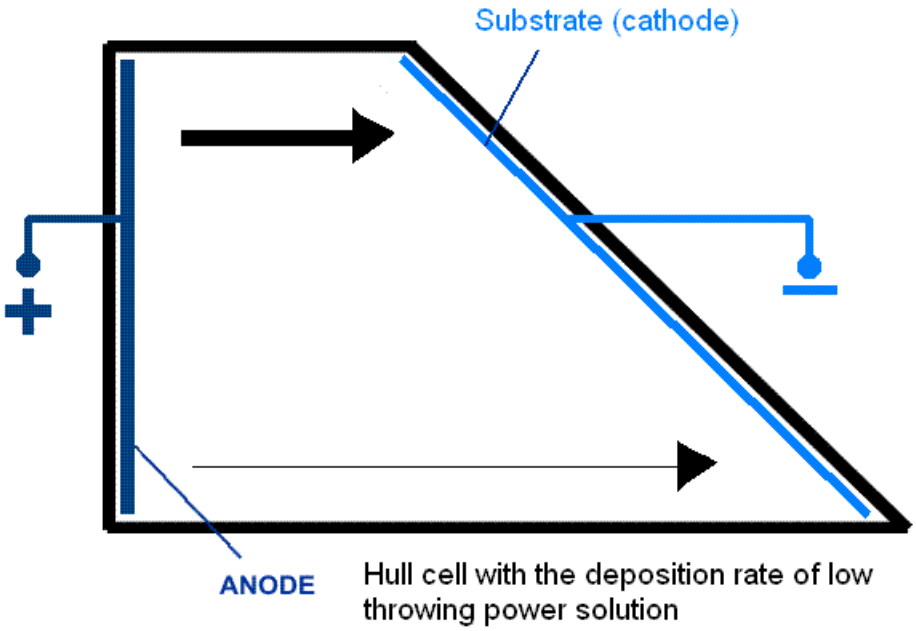

Figure 2.5. An example of a hull cell where the distance between the counter and working electrodes can be varied. Current density is inversely proportional to the inter electrode distance. [68]

A similar geometric effect can be utilised in co-deposited fabrications. A successful example of this is the deposition of $Cu_{1-x}Sn_x$ alloys using one poor throwing power solution. In this case the applied potential is pulsed with tin being deposited during the on pulse, its thickness being varied with position as the current density changes [70]. In the off period the copper is deposited by ion exchange, the rate being determined by diffusion and is therefore constant throughout the sample. This will give proportionally higher concentrations of copper where the tin film is thinner [71].

While the above examples show successes, limitations of the classic hull cell are that in many situations the mass transport effects are large compared with the usually minor current density effect. Meaning that, in most cases, the variations across the substrate are small. Also the variable rate of gas production at the cathode in these cells limits their usefulness in electroplating [68].

SSC samples have been produced by several novel methods Jayaraman et al [72] have added ions to a gel and let them diffuse. The diffused material was then electrochemically

transferred to a stable substrate to produce a permanent library. The concentration gradient caused by the diffusion step was evident in the final sample.

SSC samples can also be produced by changing the amount of time that the plating is carried out. One simple response to this need is to vary the coverage of the substrate by the electrolytic solution during the deposition. This has not until now been investigated in any depth.

Usually, the deposition rate in electrodeposition is fast. This can be advantageous, however if the mechanics of smoothly and accurately changing the position of the electrolytic solution are cumbersome and slow longer deposition times are preferred. Samples produced by varying layer thickness will, therefore, have layers that are thicker than would be normally used in conventional methods. This can have a detrimental effect on adhesion but a positive effect of the choice of characterisation probe. As with conventional methods the film thickness is often determined by the sensitivity of analytical methods employed. When the samples deposited in elemental layers are thicker the reaction and diffusion time to produce the required alloys is often longer and so potential for unwanted reactions with the substrate are increased. Black et al [42] shows the formation of MoS_2 under Cu_2ZnSnS_4 film as sulphur is added to the Cu_2ZnSn precursor.

2.2.5 Electro-static Spray deposition (ESD)

Electrostatic production of thin films, in both the micro and nano range is becoming increasingly popular due to the low cost and easy setup. The simplicity of the equipment allows easy adaptation to a range of different research requirements [73]. The method can also be scaled up to large continuous processes for industrial applications. These positive attributes have gathered interest for solar cell applications [74].

All setups regardless of the production scale rely on precursor solutions or colloidal suspensions that can be injected out of a capillary or peso injector with a flow rate typically 1 ml h^{-1} [75], or 2 ml h^{-1} [76]. Although flow rates of 20-40 ml h^{-1} are preferred for depositions of some materials [73]. With solutions of most concentrations this slow flow rate requires that multiple deposition sources are often employed for fast depositions over large areas [77].

Electro spray deposition utilises electrical forces for liquid atomisation [78]. These static shear forces are created when the needle is held at a high potential. Unlike mechanical atomisers electrosprayed droplets can have a very large size range from 10 nm to 100 µm. The efficiency of spray onto a substrate is higher than for mechanical methods, mostly as the smaller particles that would not have the momentum to reach the substrate will be electrostaticaly attracted [79]. Moreover no carrier gas is required so without this factor to consider it is easier to adjust film morphology. The downside to the solely electrostatic mechanism is that no additional shaping streams are added to mould the profile of the cone. [79]

For solutions with a certain surface tension, conductivity and viscosity the particle size can be controlled by electrostatic effects, therefore this droplet size range can be fully utilised by using flow rate and applied voltage [80]. Solutions with lower surface tensions are by and large more flexible as voltage effects are easier to tune in these cases. The precursor solutions can be aqueous but are more efficient when containing ethanol or another solvent with a lower surface tension.

The voltage effect also produces the changes in particle motion and consequently distribution of the materials on the substrate. The charged particles can be focused or deflected in a way that is not possible with mechanically produced uncharged particle sprays.

Flight path time is the largest single factor affecting the size of the particles arriving at the substrate. The splitting of the particles and evaporation of the solvent will proceed for the whole time of flight. The flight time is most easily changed by altering the distance from the substrate. Higher flow rates give larger droplets for the same distance travelled.

The shape of the needle will effect electrostatic interactions with the solution and will thus effect both the direction and the characteristics of the cone [81]. Different capillary shapes and sizes will interact with the physical properties of the solution to give differing spray modes. These interaction results can be very complex even if random coronal discharge events are not considered. Field enhanced dripping modes produce droplets that have a larger diameter than the capillary and are intermittent. Cone jets have a meniscus that are smaller than the capillary and usually give rise to more varied size and direction for droplets. Higher applied voltages cause the jet to split into multiple jets, the effect of these multiple sources has the main consequence of reducing the average size of the droplets for a given flow rate [82].

Substrate temperature affects the evaporation rate of droplets, if the material is still in solution when it gets to the substrate then the film will be more uniform. However precursor solutions may require pyrolysis or other heat induced chemical reactions to achieve the desired structure so temperature regimes have to be balanced [83].

Precursor solution selection needs careful optimisation not only for the ability to deposit the correct material and to give the desired physical properties but also for its trace elemental content. Non-volatile modifiers are often necessary but are undesirable as they can act as subtle unwanted dopents. An example of this is the addition of HCl as a pH modifier. Even in very small concentrations the residue chlorine will be evident in the film [84].

Electrostatic depositions of compositional gradients can be produced with the deposition of the separate elements being either sequential or parallel. Co-deposition has the advantage that the materials are already diffused on a microscale. They will, therefore, quickly intermix on a nonoscale and reactions or alloying will proceed more readily.

Studies into material with small compositional variation have been carried out using electrostatic spray deposition techniques [85]. While many can be thought of as high throughput as they use the speed and simplicity (once optimised) of the ESD method to produce large numbers of samples the samples are predominantly conventional [86].

One of the ways that electrospray deposition can be adapted to high throughput screening has been investigated by Fujimoto [87]. In this case, multiple syringe plumps are used as reservoirs for different precursor solutions. When in operation they inject through a manifold and out the same syringe. The rate of flow in each syringe is changed over time resulting in different solutions being sprayed. As the deposition continues the needle can be moved over the surface of the substrate or a masking can be used to isolate a range of physically or chemically distinct areas.

Alternatively, multiple needles can be used to deposit different solutions. As the formation of droplets varies in frequency or size at different angles a geometry equivalent to off-axis sputtering can be produced.

Tests of different materials co-spraying are rare, however investigations into the same materials with different nozzles normally with the aim of increasing coverage rates (without altering the flow rate at any individual capillary) give useful insights. Regele et al [88] show

that with multiple capillaries more applied voltage is required to produce the cone jet due to electrical screening. This effect is only significant if the intercapillary gap is less than 10 mm.

More deposition occurs at the edge of the cone than in the middle due to mutual repletion of the droplets [83]. At the edges there is a stable reduction of thickness with distance from the focus point.

2.2.6 Diffusion and alloying

Thermal treatment to promote the alloying of sequentially deposited elemental thin films to homogenise the depth profile is highly dependent on elemental composition, treatment temperature as well as film thickness. Alloying of elemental clusters mixed on a nano scale as in the case of some co-sputtered materials is often achieved by annealing. Some examples, such as Cu-Sn, diffuse and alloy easily even at low temperature. Films of a total thickness of 500 nm alloy to form both Cu_3Sn and Cu_6Sn_5 in 36 hours at as low as 60 °C [89]. This affinity to form the alloyed form is beneficial but can also be problematic as it continues readily even at room temperature and is accompanied by grain size increases and also the spontaneous formation of tin whiskers in strained films. Where the diffusion follows an interstitial mechanism the rate is high and strongly temperature related, substitutional solids generally have lower diffusion rates [90]. Tamura el al [91] produce alloyed films from 2 µm Sn on a Cu foil in < 24 hours at 200 °C, the thickness of the foil allows the formation of multiple phases changing with depth.

Panjan et al [92] shows that the temperature required to get detectable diffusion in materials after 5 hours is 300°C for Al/Cr and 400°C for Cr/Fe. Materials such as molybdenum are resistant to alloying with most metals at < 550°C and are therefore suitable to be an inert presence in the libraries that require a conducting substrate. However MoS_2 has been produced directly from metallic Mo annealed in a sulphur rich atmosphere at 550°C, [93] so similar effects require consideration.

Solid state formation of Cu_3BiS_3 by the addition of S to Cu_3Bi [32] or the addition of Bi to CuS [94] at different temperature regimes and elemental compositions allow the formation of least 12 other phases of these materials, a number of which could be produced and studied by combinatorial methods.

Other leading photoactive materials have been produced by deposition and post annealing. Cu-Se has been electrodeposited with an indium layer added by sputtering. The composite was then heat treated to from $CuInSe_2$, at 400 °C. A homogeneously diffused layer 2 µm thick can be produced in 30 minutes. [95] Sputtered Cu-In precursors can be reacted with Se to form the same $CuInSe_2$ phase, this shows that the alloy formation is independent of deposition method [96]. Although blocking layers mean that the diffusion is governed by the layering order is some cases.

2.2.7 Use of phase diagrams

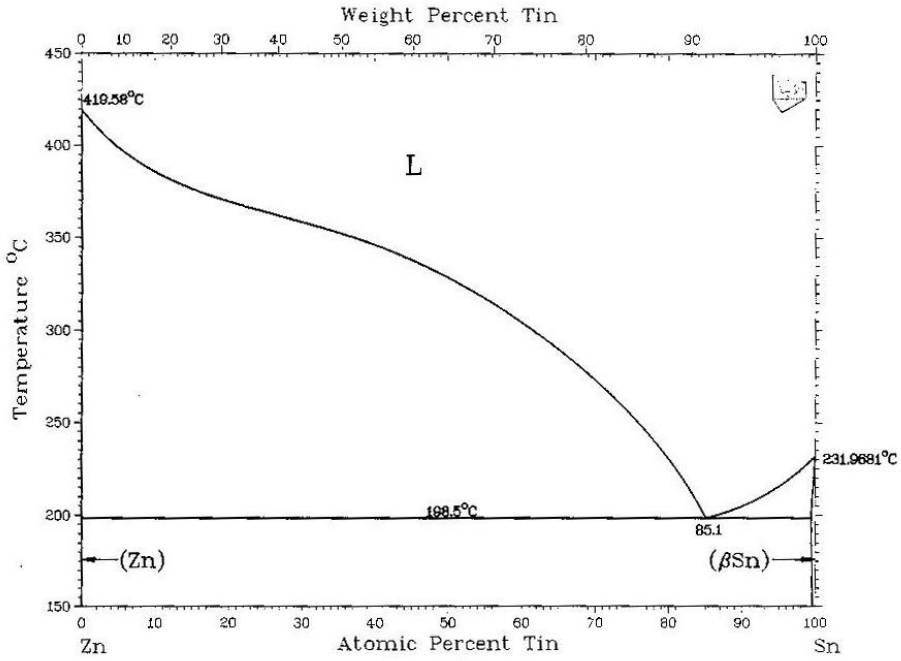

Figure 2.6. Phase diagram of the binary zinc-tin system, this is an example of elements with very low mutual solubility [138].

The low mutual affinity of the elemental zinc and tin, shown in figure 2.6, means that no alloys are observed in the temperature range of interest in this investigation, this give size to a simple binary phase diagram over a large temperature and compositional range. The diffusion of the material around each other is important as the rate of production of a desired ternary alloy with the addition of another element will be determined by the macro scale positioning of the potential reactants.

For the copper-bismuth system a similar propensity to remain in the elemental forms giving rise to a similar lack of identifiable phases, the determination of the atomic percentage of

these mixtures can be determined by XRD by calculation of the relative intensities of the elemental diffraction patterns.

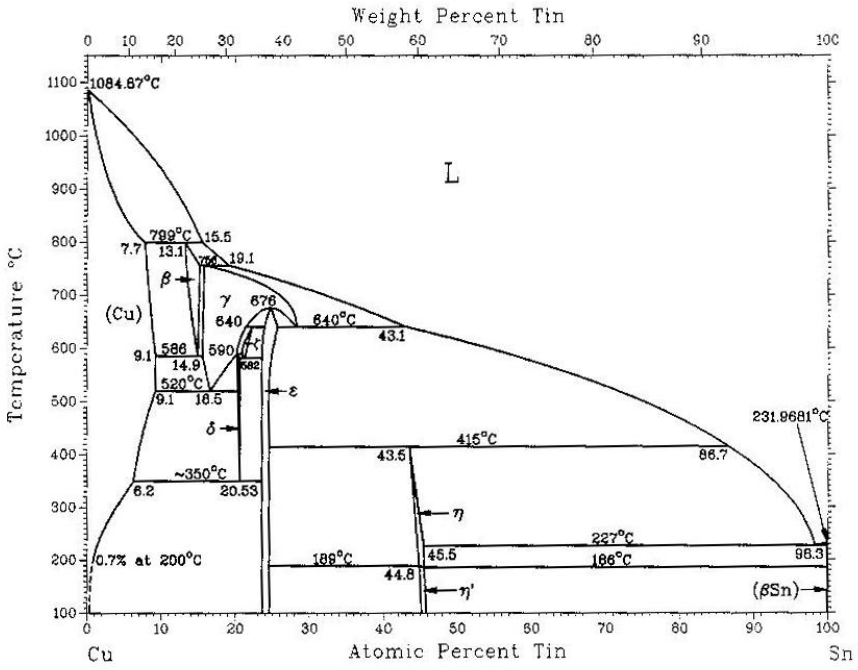

Figure 2.7. Copper-tin binary phase diagram. This system is a complex multiphase system with significant temperature as well as composition dependency [138].

The copper-tin phase diagram, shown in figure 2.7, is characteristic of the results seen for systems that have a high affinity to form alloys. The effect of temperature as well as elemental composition on the phase formation is clear. In many cases the ratios of the elements are the same but different phases with different unit cells are produced. XRD is one of the most useful methods of determining the space group of a particular unit cell, this information being linked to the physical or electro optical properties determined by other characterisation methods. Study of the phases produced at higher temperatures is carries out either at the temperatures quoted or by locking in the phases by rapid cooling of the sample material. The fixing of phases by quenching may be temporary as in many systems the energy available at room temperature may still allow significant atomic rearrangement.

The examples of phase diagrams presented here are isobaric the data being collected at normal atmospheric pressure. Some phase formation is known to be affected by pressure [97] so this and other factors need consideration. The production of higher order systems by the direct reaction of the precursor with a gas phase reactant may be carried out at a reduced

pressure. The sulphurisation of samples using an elemental source is an example of a production technique that requires low pressure due to the low vapour pressure of this element. The presentation of higher order phase diagrams is more difficult due to the difficulty in representing multiple axis, in these cases representing an isothermal section of the system is usually the most pragmatic approach.

2.3 Library Characterisation

2.3.1 X-Ray Diffraction

X-ray diffraction (XRD), both powder diffraction and diffraction of epitaxial films is discussed here, with regard to possible simultaneous data collection.

XRD is a highly favoured characterisation method as it is a non-destructive structural determination method for crystalline samples. The angle of diffraction is linked to the interplaner distances of the diffracting planes, this information is used to characterise the unit cell in terms of size (lattice parameters) and arrangement (phase group).

Diffraction experiments rely on the detection of coherent radiation emitted from the sample, that is, with the same wavelength as the X-rays originally used to illuminate the sample. The method requires an X-ray source of fixed known wave length so a highly monochromatic source is employed. To achieve an intense and monochromatic source from a standard sealed X-ray tube wavelengths produced by electron rearrangement in the exited atoms of the anode as it is bombarded with electrons are chosen. At these energy levels the X-rays are already more intense than other parts of the spectra. This is because the mechanisms at work during electron shell rearrangement favour the production of photons of set energies as shown in figure 2.8. When selecting an elemental anode the use of Moseley's law to calculate the wavelength of the characteristic X-rays from the atomic size of the element is useful.

$$\sqrt{v} = C(Z - \sigma)$$

Where v is the frequency, Z is the atomic number and C and σ are constants.

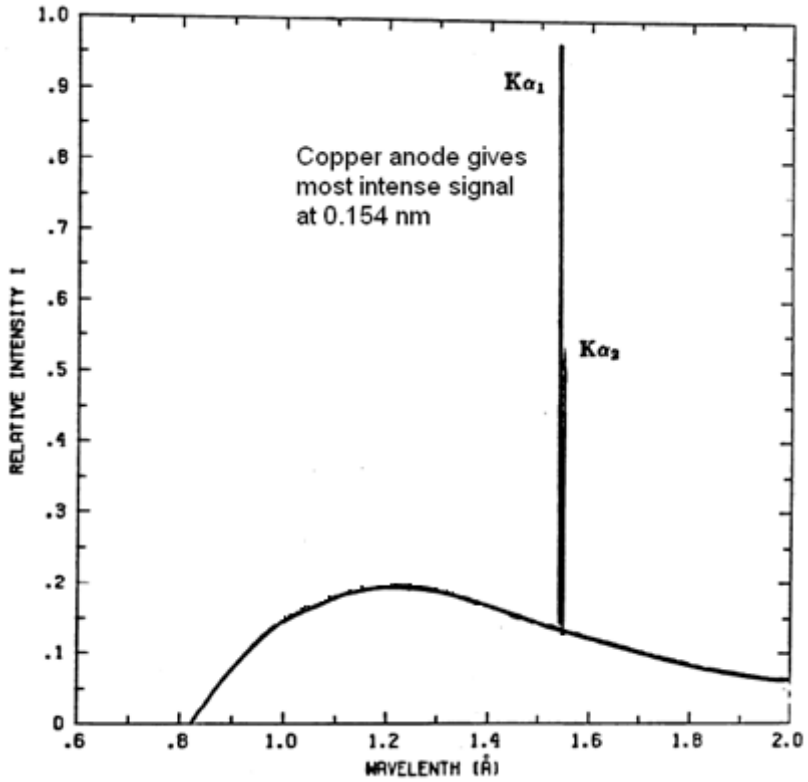

Figure 2.8. Typical intensity profile of a copper anode, showing the prominent Kα_1 and Kα_2 responses, a nickel filter may be used to block the Kα_2. Adapted from [98].

When a monochromatic beam of X-ray phonons of sufficient energy and low enough to avoid photoelectric effects is used to illuminate a material substantial secondary X-rays are produced. Due to the requirement to know the exact wavelength of the detected radiation it is the X-rays that are produced by Thompson scattering, that is by elastic means, which are of interest to diffractionists.

The constructive interferences when this monochromatic source is scattered from the electrons of atoms in different planes of the crystal produces the characteristic angle versus intensity profile. The position of intensity maxima produced by this mechanism is illustrated in figure 2.9. It is these maxima that are recorded during diffraction experiments.

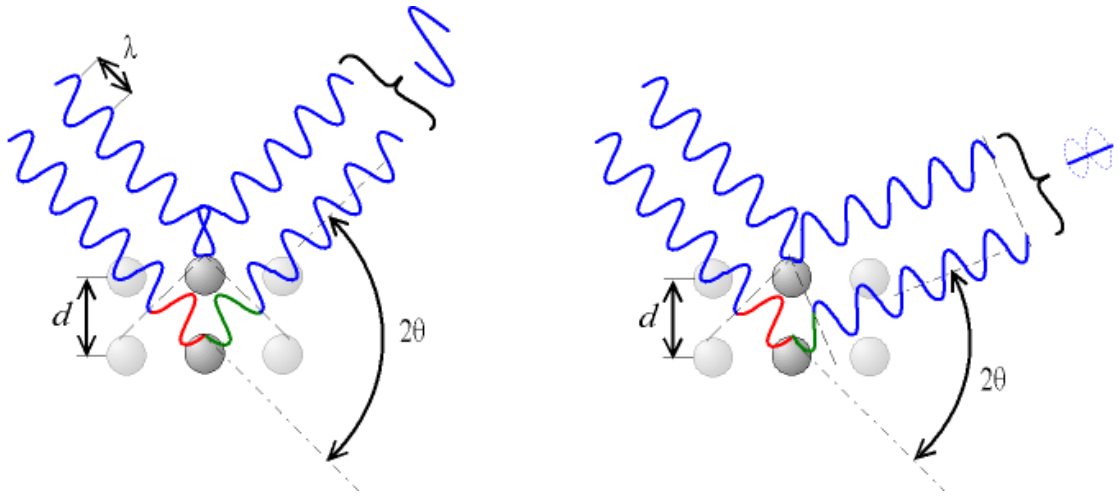

Figure 2.9. Illustrating angles that meet the Bragg condition and an example were the Bragg angle is not achieved. [98]

Using Bragg's law to link diffraction angle to the interplaner distance (d-spacing) will, when a number of planes are considered together, give the required structural information for phase identification. The example shows only the first two planes in a crystalline structure, however significant diffraction peaks require the constructive interferances from multiple atomic planes. At an appropriate angle X-rays penetrating more deeply into the material travel multiple integers of their wavelength before interacting with the atoms hence the constructive additions to signals from higher planes will continue. From this we note that Bragg's equation, linking wavelength (λ), d-spacing and the angle from the incident beam 2θ is essential to calculating plane spacings.

$$\lambda = 2d \sin \theta$$

In the case of powder diffraction the random orientations of the individual grains mean that the diffracting planes are able to constructively scatter in all directions that comprise a certain angle to the incident beam. This gives rise to the Debye cones, a characteristic result of polycrystalline sample illumination.

The Bragg equation also informs the choice of wavelength for the X-ray illumination. Photons monochromated at lower wavelength will produce smaller diffracted angles for the same lattice parameters, changing the resolution and d-spacing range achieved by the same experimental setup [99]. Copper Kα radiation is a common choice as its photons monochromated at 0.154 nm separated the common 1-3 Å interplaner distance over ≈ 15 - 50°.

XRD is useful for phase determination when using the angular intensities from a number of planes. Matching the collected diffraction patterns to diffraction patterns already on record or fitting to theoretical patterns for materials with planes of specific miller indices can lead to accurate structural determination. Relative intensities of the peaks coming from different planes in the material are also useful in the matching of data.

Full uniform Debye cones and therefore the rings collected on an area detector or X-ray plate are possible but most materials will deviate from this ideal to at least some extent. These deviations may be unwanted as incomplete Debye rings can lead to difficulties with material identification.

The fact that XRD results are affected by the preferred orientation (PO) of a sample can be extremely useful as crystal orientation has a large effect on many physical properties [100]. Many advanced material applications rely on the control of preferred orientation in some or all of their components structures. Van Heernen et al [101] have used XRD determination to study the orientation of ZnO thin films during differing temperature and concentration conditions of spray pyrolysis deposition. They have from this devised deposition constraints that preserve the (002) orientation parallel to the substrate which is desirable to make the most of the semiconductor properties. Purica et al [102] have shown that the desired high transparency and conductivity ZnO films produced by chemical vapour deposition maintain the same (002) orientation. Preferred orientation studies using diffraction as the main analytical tool have also linked the record efficiency CIGS solar cell with the ability of its manufactures to orientate the Cu(In, Ga)Se_2 in respect to the (220) and (204) planes [103]. Ideally any new diffraction related method would retain the ability to determine PO.

X-ray diffraction experiments are useful in the determination of crystal grain size of the materials being tested and also internal strain in the sample. Size broadening is a substantial problem in thin films as the sharp peaks envisaged by Bragg's law will be distorted. The reason for this is where the samples are thick a very small deviation from the Bragg angle will give an opposite out of phase signal to cancel the unwanted edges of the peaks. However with a 1.001 per plane shift in the travel distance the opposite peak trough will not occur until the 501^{st} plane. If the sample is too thin or the grains too small to contain these planes the cancelling effect will not occur and the peak will take on a characteristically wide profile [106]. Using this principle the effect of thermal annealing of CdS films has been studied with grain growth described [104]. The deposition of ZnS films for PV applications links grain

size film thickness and dopent concentration [105]. All are crucial for the production of effective solar cells and other advanced electro optical systems. With this in mind it is easy to appreciate how diffraction methods that retain this function are highly desirable.

Phase matching as we have seen makes XRD an important method for general sample identifications. Additionally XRD can be used for identifying the gradual lattice parameter shifts that are characteristic of materials with small compositional differences, vital when considering chemical libraries. The change in composition will express itself in d-spacing shifts as described by Vegard's law [106]. That is if one atom is sufficiently similar in bonding properties to its substitute the structure will remain the same but the unit cell volume will change. Vegard's law thus states that volume of the unit cell in these substitutional solid solutions is linearly proportional to the fraction of sites substitutions [106].

These lattice parameter changes are important when examining the structural effect of dopents know to allow semiconductor properties. The absorption band gap of the $Ga_{1-x}In_xAs$ ternary system can be tuned by the variation of x. As this will produce a Vergards shift, XRD lactic parameter information can be used to determine not only precise composition but through calibration the absorption band gap of the respective material. [107] In a similar way Damonte et al [108] have linked XRD lattice parameter and grain size determination of Al doped ZnO to desired optical properties. In all of these cases, the range of samples have been made conventionally in a sequential manner with all the time and resource burden that this inevitably entails. Each investigation however could be duplicated combinatorially. A combinatorial approach in the production of these samples would likely lead to a bottle neck in the crucial XRD determination so it is reasonable to assume that at least some similar studies would be moved to a combinatorial procedure if the large data collection time required for XRD did not exist.

Important comparisons of XRD data to physical and chemical properties can be made even if not all of the information that can be possibly derived from X-ray diffraction is present. Abrupt change of Miller indices indicating a phase change in the system is often linked to an abrupt change in a specific physical or chemical characteristic [109]. Considering this, it is easy to imagine a situation where a compositional range had been produced, but due to the small range of stociometeries that sustain the phase of interest only a portion of the substrate is deemed worthy of investigation. This constituted a potential inefficiency in the combinatorial method as the raster scanning of all of the substrate would be required to

ensure that the data collection or the areas of interest have been carried out. A quicker diffraction approach that could scan for basic information and use this to position a particular phase on the substrate would be useful.

While not generally regarded as a trace method XRD will detect major components even in thin films. Data collection time is related to material density, atomic size and to the sampled volume of the materials. Data collection time has long been a limiting factor for XRD characterisation and sampled volume restrictions brought about when analysing thin films can exaggerate this problem. Changing the standard Bragg-Brentano geometry to a fixed incident angle with a low incident will increase the interaction volume of thin film samples. When this low incident angle method is employed on systems designed to be used with an area detector the highly parallel low divergence beam will reduce negative effects of this method such as the flat sample error [106].

The development of area detectors that are able to collect a substantial angular range at the same time with a fixed incident angle source have eased the problem of data collection time especially when only moderate data quality is required. Nevertheless when considering a CCS library that can have hundreds or more virtual samples [110] conventional pencil beam illumination of each sample sequentially is still a lengthy process and may not represent the most efficient use of these expensive area X-ray detection systems.

Modest quality data still allows for peak position calculations, giving the dimensions of the unit cell. For cubic, tetragonal and hexagonal systems the plane spacings are given by [99]

cubic

$$\frac{1}{d^2} = \frac{h^2 + k^2 + l^2}{a^2}$$

tetragonal

$$\frac{1}{d^2} = \frac{h^2 + k^2}{a^2} + \frac{l^2}{c^2}$$

and hexagonal

$$\frac{1}{d^2} = \frac{4}{3}\left(\frac{h^2 + hk + k^2}{a^2}\right) + \frac{l^2}{C^2}$$

Previous work by Ohtani et al [111] links spatial mapping with structural determination for epitaxially grown thin film libraries. This arrangement allows suitable monocrystalline films to be positioned on a substrate so that they can be illuminated simultaneously by a single radiation source. The nature of these films means that they will not produce the Debye cones expected for a polycrystalline material but instead the intensity maxima of each component in the library will lie on a separate line. When detected with an area system the patterns will be spatially separated without need for specific partitioning.

The geometric differences in the collecting of highly preferred films mean that the method proposed by Ohtani would not work for powder diffraction but the principle of collecting multiple patterns simultaneously is valid. In the case of powder diffraction the collection of multiple patterns simultaneously from different samples will occur on the same parts of the detector. This incorporation of the different patterns into one intensity profile is much more problematic. The overlaying of the patterns onto the detector does not necessarily mean a loss of information. The reason for this is that the Debye cones from different samples will interact with the detector to form overlapping arcs, which are still characteristic of the starting material.

While the shape of these arcs can still be perceived all of the information contained in all the diffraction patterns is still theoretically available. If partitioning of the arcs so that the radius and the centre point can be accurately determined all that is required to use the diffraction profiles is available. Firstly the radius of each arc will be used to obtain 2θ angle and through this the relevant structural information as usual. Secondly the centre point of a series of arcs will give the position of the Debye cone origin on the substrate. Through this, structural information can be linked to any of the samples illuminated by the X-ray source, for CCS samples the diffraction information will be linked to a position on the virtual grid.

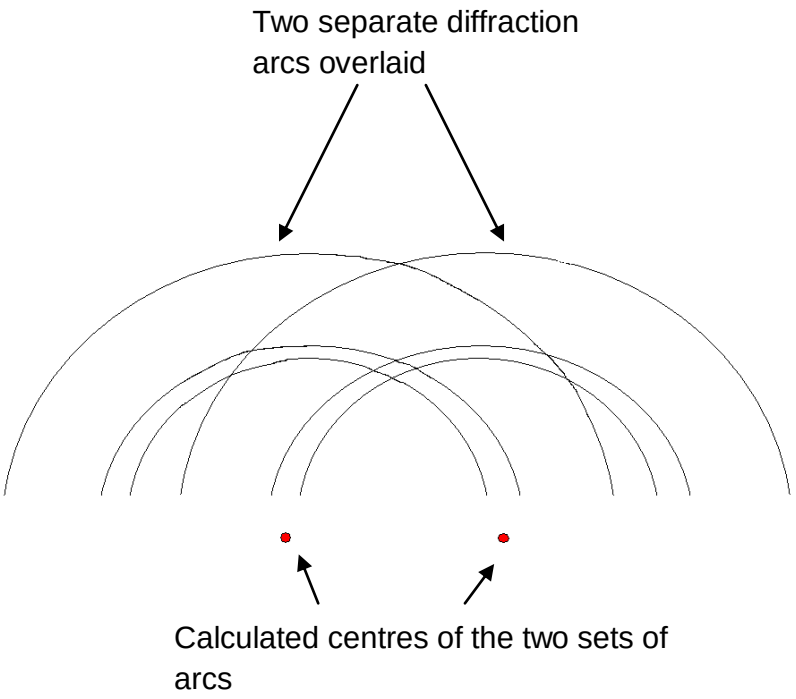

Figure 2.10. An indication of how two separate sets of diffraction arcs can be collected on a single area detector.

As can be seen in figure 2.10 with a simplified example the intensity distribution of the pattern comes from one of two positions, it is precisely this information that is required. A number of methods can potentially be used in order to obtain the consistent parts of the X-ray intensity map. These included deconvolution and wavelet synthesis which, although successful elsewhere, were undermined by the poor signal to noise ratio that is characteristic of these scattering distributions. An empirical approach that transforms the intensity scattering distribution data directly into a normalised intensity map (In(d,y)) on a d-spacing vs. locus (y) grid is possible. It is from such maps that phase and lattice parameters at any point along the library can be determined.

The transformation process is achieved through the superimposition of virtual arcs each with its centre at a different pixel position on the collected intensity matrix. The intensity of the matrix masked by a virtual arc centred in every position is calculated using.

$$\int_{\chi_1}^{\chi_2} I_{2\theta,y}(\chi)d\chi$$

Where the intensity I is a sum of the intensities at all of the values of 2θ & y that are within the azimuthal limits χ_1 and χ_2 and for a given radius of the diffraction arc that will fulfil the equation of a circle.

$$(x-a)^2 + (y-b)^2 = r^2$$

Where x and y are the positions of the centre point with x being fixed by instrument geometry, y being the sample producing the diffraction, while a and b are the components of the coordinates of the arc. From this the radius of the arc r is calculated and as the sample to detector distance is known any value of r can be converted into a d-spacing.

The angular range of this active area is dependent on the scattering angle for our system, so the normalisation of the intensity requires χ_2 - χ_1. Where χ_1 and χ_2 are the limits of the summation and are related to the active area on the detector.

$$In(2\theta, y) = \int_{\chi_1}^{\chi_2} I_{2\theta,y}(\chi) d\chi \Big/ \chi_2 - \chi_1$$

Adoption of Bragg's law will give the convention 2θ to d-spacing calculation, this allows the adoption of.

$$In(d, y) = \int_{\chi_1}^{\chi_2} I_{d,y}(\chi) d\chi \Big/ \chi_2 - \chi_1$$

As the data collection from multiple sample positions is then a simultaneous process and the partitioning described can be carried out separately, an increase in characterisation speed should be easy to achieve. This is particularly important recently as combinatorial processes are expanded and the production of samples becomes faster the emphasis of potential efficiency improvements have shifted to characterisation time.

The potential improvement in collection rate is easy to appreciate as the photon flux at every point on the extended beam is equal to that of a normal pencil beam. Data collection time that can come from the extended beam illumination could be theoretically as high as the proportion of the usual spot size to this new beam. Comparing the new 25 mm beam with a conventional 500 µm spot a 50 times faster data collection could theoretically be achieved.

Data collecting speed is not the only potential advantage, the other benefit is the continuous nature of the illumination, this is particularly useful if the characterisation is to be used with CCS samples.

2.3.2 Synchrotron X-Ray Diffraction

Unlike normal laboratory based systems that use the X-ray released when electrons impact an anode, synchrotrons produce the radiation with a constantly moving stream of confined electrons. While the principle of energy transfer from electron momentum to photon energy is similar synchrotrons employ different mechanisms to produce the X-ray radiation. Anode systems generally use the X-ray photons that are produced by electron shell rearrangement after electron bombardment as these characteristic wavelengths are naturally more intense leading to efficient monochromation. Bremsstrahlung principles are a minor mechanism in anode based systems producing the polychromatic background but are the sole mechanism for synchrotron X-ray production. As the electron stream is magnetically accelerated the X-rays created are intense enough for a high level of monochromation to be feasible at a wide range of wavelengths. Also as the X-rays produced by the Bremsstrahlung mechanism form a continuous energy profile the choice of wave lengths that can be monochromated is less limited. However the lack of availability of suitable crystals for use as pre-sample monochromators means that the polychromatic nature of the Synchrotron emission are not fully exploited.

The total number of photons available for sample illumination is also much higher than for X-ray tube based systems. This alone constitutes a major advantage of the synchrotron sources. The small amount of beam divergence that is seen when using a synchrotron source is also preferred for a range of applications. [112] The photons are most highly collimated in the vertical axis [113] so it would be most practical to make any beam extension horizontally, that is in the same plane as the electron circulation.

Design of the charge couple device (CCD) area detectors used at synchrotron facilities do not vary significantly to those that are employed in laboratory based bench top systems, however the other advantages of synchrotron use justify the employment of a state of the art detector. The larger size of these detectors and the higher pixel density allowing the detectors to be moved closer to the sample combine to allow the largest possible solid angle of X-ray scatter

to be detected. This larger detection surface enables effects such as texture, granularity and preferred orientation to be more completely observed directly. [113]

Synchrotron diffraction is used widely in PV research as the high quality data produced is advantageous notably for the calculation of lattice parameters and from this the composition of for instance CdS-CdTe hetrojunction cells [114]. The intensity of the X-ray beam allows micro size illumination area on samples while maintaining a high flux of photons. Cui et al [115] have used this characteristic effectively to investigate high density sputtered libraries of Ni-Ti-Cu alloys for shape memory properties. Chu et al [116] have used the high flux properties for the characterisation of combinatorial libraries produced by molecular beam epitaxy.

2.3.3 Energy Dispersive X-ray Spectroscopy

Energy Dispersive X-ray Spectroscopy (EDS) is a process where quantitative determination of the elemental composition of an unknown sample can be achieved. The sample of interest is bombarded by a beam of electrons that are produced by a variety of sources. A common production method is the thermionic source where an abundance of electrons given off by a hot tungsten or LaB_6 filament. These electrons are accelerated towards the target material by the application of a potential difference between the source and sample. If higher fluxes of electrons are required a field emission gun can be used, this method liberates electrons from a very compact pin source by the application of a very strong magnetic field ($>10^9$ V/m) [120]. While the designs for different instruments vary significantly all systems have accelerating anodes and confining cathodes. These cathodes control the focus of the electron beam in the same way as in imaging electron microscopes. The other important characteristic of the gun is to regulate the energy of the electron stream.

Each element has a number of characteristic emission peaks in the X-ray energy spectrum. By resolving the emitted X-rays for energy and matching the spectrum to a known pattern, qualitative elemental determination is achieved. The reason for the characteristic energy peaks is the X-ray production mechanism, in the case of the elemental peaks the X-rays are produced by the rearrangement of the electrons in the atomic shells after ionisation by the primary electron beam. These specific rearrangements give elemental energy signatures that rise well above the continuous Bremsstrahlung induced background.

As the energy of an X-ray photon is proportional to its frequency, linked by the Planck relation, both wavelength dispersive techniques and direct photon energy measurements are possible. This direct measurement is carried out in standard detectors by measuring the number of electron hole pairs produced by each photon interaction. The number of electrons and therefore the current detected is linked to the photon energy.

Another common method is the separations of X-rays by wavelength (WDS). This is achieved by changing the wavelength of the X-rays into angular distribution. Separation of photons with similar energies is achievable with this method giving a high confidence for elemental determination. Concerns over the slow data collection time detract from the popularity of this method. As the detector in an EDS system can be placed very near the surface of the sample the electron incident to detected photon ratio is more favourable. In addition to improvements in collection time this reduces the potential damage of the sample caused by a high electron fulx. This is an important consideration when dealing with samples that are both very thin and libraries designed to be characterised with a number of fully non-destructive techniques.

Technical constraints in the engineering of the energy dispersive detectors mean that photons with very low electron volt energies will not be apparent. These low X-ray energies are characteristic of the emission of small atoms and this limits the sensitivity of the EDS system when low atomic number (Z) elements are present. With modern systems all elements above beryllium should be detected if they present are in sufficient quantities [117], although most systems can only detect >10 value elements with any significant quantitative accuracy. EDS can be used for elemental analysis of all the materials of interest in this investigation as aluminium with atomic number of 13 is the lightest element deposited.

Identification of the components in a sample requires a separation of the signals emitting from the different elements, in some cases the characteristic energies of two different shells in two elements are so close in energy that they cannot be resolved. The problem affects EDS to a greater extent than WDS due to technical constraints. The real peak widths are extremely narrow but the electron-hole pair production mechanism means that detected peaks are always broadened substantially (up to a FWHM of 150 eV) for EDS detectors [117]. Masking of the signal from one element by those from other elements in some of the complex systems is possible, this has a detrimental effect on quantitative and even qualitative measurements. Usually this problem is modest as elements can be made to emit at several energies when

exposed to an energetic electron beam. The energy of the bean and other characteristics may have to be constrained by other considerations. When the thickness and electron attenuation of the film are both low the requirement to confine the area of interaction to the homogeneous sample layer and not illuminate the substrate limits the choice of accelerating voltage. Ideally, when analysing thin films, the accelerating voltage should be only slightly larger than the critical ionisation voltage (E_c) for the X-ray energies of interest, as opposed to the 2-2.5 times the E_c used in bulk samples. As the average X-ray production depth is smaller in thin films the reabsorption of X-rays emitted by low Z materials by other high Z materials in the matrix are minimised. In this way one of the major causes of quantitative error the under estimation of low Z materials is minimised.

Sulphur and molybdenum being examples where the Kα of S and the Lα line of Mo are both at 2.3 keV and are difficult to resolve [112], these can still be resolved using energy dispersive detection if the energy of the incoming beam is energetic enough to cause other electron shell transitions [118].

Quantitative calculations use the rate of photon flux to calculate the relative concentrations of all the elements present. The signal strength from the elements is effected by a number of factors in addition to concentrations. ZAP software that compensates for the changes in photon count variations caused by atomic number effects (Z) absorption effect (A) and fluorescence (F) is used on all modern systems. Accurate composition calculations require standards of similar composition and density to the materials of interest, no trivial requirement when dealing with compositional spreads. With appropriate standards quantitative analysis is reported to be better than 2 % relative for major componerts. More conservatively a figure of 4-5 % relative compositional accuracy is expected when using standardless methods [119].

As with the methods using standards the standardless analysis uses the intensity (k) ratio but with the concentration values assigned from these ratios being calculated from first principles. Alternatively in the fitted standards method the intensities are derived from a large suite of standards measured by the manufacturer. The method not only eliminates the requirement for standards with compositions close to those of the material being measured but also allows a simplified experimental setup, reducing the requirement for quantitative control of some of the data collection conditions. Only beam energy, X-ray take off angle

and spectrometer efficiency is required so there is no need for, as an example, the measurement of the exact electron dose. [119]

When calculating the compositions of minor elements (<5 % of the total) or when looking at samples with rough surfaces confidence in the results should be further reduced [117]. All composition calculations assume materials are homogeneous throughout the fluorescing volume, this cannot be simply assumed for very thin samples. [120]

High collection rates will lead to the likelihood of two photons arriving at the detector within the count time of the system. This peak pileup can lead to sum peaks, artefacts in the high energy part of the spectrum, which should be disregarded. The methods employed for the characterisation of thin films usually reduced the photon flux reaching the detector and can reduce this problem.

The positive characteristics of EDS analysis for many applications outweigh the negative aspects so it should be no surprise that EDS has been successfully employed for numerous thin film samples including for high throughput and photovoltaic applications. Specifically material systems have often been characterised with EDS used in conjunction with XRD examples of this are $CuInS_2$ [121] and for ZnTe [122] amongst many.

The linking EDS with XRD is common due to the contrasting information that the methods collect, making elemental compositional information from EDS studies a good addition to many structure based investigations. For combinatorial libraries, electron beam excitation is useful due to its flexibility, making the size of the illumination area the same as the other characterisation tools to be employed while retaining sensitivity is advantageous. This is especially true when measuring CCS samples that rely on a virtual sample grid, direct comparison can only be made in these cases if the part of the substrate characterised is exactly the same.

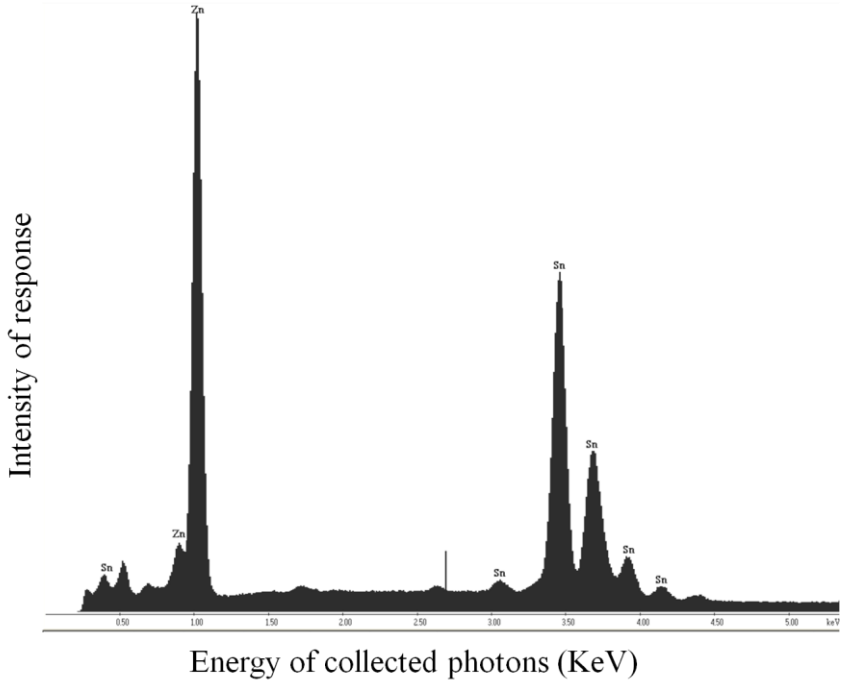

Figure 2.11. An example of EDS data collection from Genesis collection software.

X-ray photon energy is measured and assigned to an energy channel these are intergrated over a set range to determine the signal from a specific electron rearrangement. Using these ratios and ZAP correction the proportions of the individual elements can be determined. With this system the limiting factor in both the qualitative and quantitative determination of the elements is the energy resolution of the detector, this is hard to avoid as the photon to electron conversion ratio has a random component. The electron-hole recombination and energy loss due to electron promotion to a non conducting energy level are not fully predictable.

2.3.4 Rutherford Backscattering spectrometry

Rutherford Backscattering spectrometry (RBS) has grown from a minor technique in the nuclear physics sector to a major solid state non-destructive method, with the ability to determine for example shallow doped layers in semiconductors. [123] It should be noted that the non-destructive characteristics do not hold true in a few notable cases such as the semiconductor GaAs which is rendered insulating after proton bombardment.[123] The method has quantitative accuracy better than 3 % for a range of elemental masses, with simultaneous depth profiling of samples. This can be useful in studying surface effects and for a range of thin film work.

RBS uses a collimated beam for H^+ or He^+ particles with energies in the MeV range traditionally from an electrostatic van der Graaff generator. Coulombic repulsion between the positive ion stream and the nucleus of the test material produces the backscattered particles. The scattering cross section is independent of chemical bonding. The kinematic factor $K = E_1 / E_0$ shows that the reduction in energy of the backscattered particle depends on the mass of the incident particle M_1 the mass of the target material M_2 and θ is the angle between the incident beam and the backscattering. Thus the kinematic factor (K) can be calculated from;

$$K = \frac{E_{scattered}}{E_{incident}} = \left[\frac{\left(1 - \left(\frac{M_1 \sin\theta}{M_2}\right)^2\right)^{\frac{1}{2}} + \frac{M_1 \cos\theta}{M_2}}{1 + \frac{M_1}{M_2}} \right]^2 \quad [114]$$

This calculation assumes that the back scattering occurs at the surface, an additional energy reduction will take place during any transition through the material.

A semiconductor nuclear particle detector that is capable of detecting the relative energies of the backscattered particles is required for mass and therefore elemental determination. While mass alone affects the backscattered energies for a particular angle and incident beam, the choice of some backscattering angles are still beneficial. The particle collection angle can be tuned so that a small difference in mass give detectible changes in energy. [124] Mass resolution can also be increased by using a heavier beam or increasing the beam energy but this will also increase the likelihood of producing unwanted nuclear reactions.

The mechanism of wholly elastic scattering only holds true for the first layer of atoms, particles that eventually scatter from atoms deeper in the material will first lose energy inelastically as they penetrates the material, with more energy being lost as the scattered particles pass back out of the material. This mechanism produces an energy scale for any given material and this can be converted into a depth scale. It is through this that a RBS spectrum can give both elemental identifications and their depth distribution. [123]

A rule of thumb is that the scattering cross section intensity is approximately the square of the element's Z value. This large disparity in signal strength means it may not be possible to detect light elements in the presence of heavy ones. If the materials can be detected, correction for the differences in the intensities is possible. This compensation renders RBS insensitive to sample matrix so the method does not generally require standards.

Profiling is routinely achieved on samples of 2 µm but penetration of up to 20 µm is possible with hydrogen bombardment of a light material. During RBS analysis the amount of material is measured as atoms cm^{-1} so layer thickness calculations require knowledge of material density, (for some materials a density has to be estimated) [117]. Data collection time of 10 minutes gives required scattering spectrum for intermediate and high Z elements envisaged in this study.

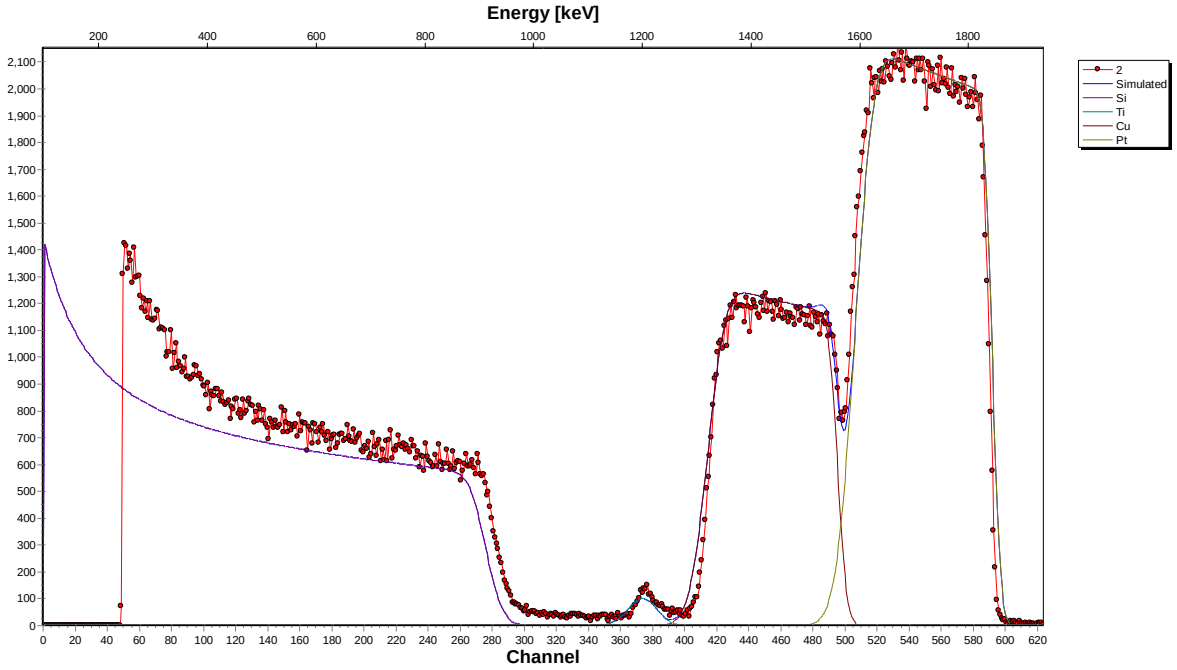

Figure 2.12 Example of the data collection during RBS analysis. Real data points are shown in red while the other colours represent the simulated matches.

In this example, figure 2.12, the measured energies of the backscattered He^{+} ions are recorded along with a simulation of the potential match represented by the solid line. Here a slightly imperfect match is illustrated so that both components can be observed.

2.3.5 Electro Optical Properties

Due to the photovoltaic effect photons of light interacting with semiconductor materials will give an electrical response. Photovoltamitery can be used to observe this effect while External quantum efficiency (EQE) measurements can quantify the conversion efficiency. EQE measures the ratio of electron flux in an external circuit created around the material of interest when it is illuminated and compares this to its dark state. From this the electrical

effect of the original incident photon flux is calculated. The standard setup for these measurements is a light source of standard luminance, usually a xenon lamp for UV/visible work, a monochromator and chopper. The chopper interrupts the light at intervals allowing the photocurrent to be distinguished from background. Thermal effects can often be determined if the measurement of photocurrent changes as a function of chopping rate. [125]

In cases where a complete device is not available the light absorber can be tested in an electrolytic solution that mimics the charge carrying function of the device. The solutions chosen as a charge carrier when testing p-type materials for photoactivity properties must be easily reduced. Electrolyte such as Eu^{3+} solution is often chosen. When testing n-type material properties a Na_2SO_3 solution can be used.

Chapter 3

3. Experimental

3.1 Sample Production

In order to fully investigate the novel X-ray diffraction method a variety of test samples are required, these samples have been produced in two types.

The simple phantom samples are discussed in section 3.5.1, while the combinatorial manufactured thin film samples are explained in sections 3.2.1, 3.2.2 and 3.2.3.

Three production methods have been used to produce samples with different characteristics but in all cases the samples are CCS type libraries deposited on conventional thick rigid substrates. These samples are, therefore, suitable for reflection geometry XRD and other complimentary non-destructive methods.

3.2.1 Chemical library formation by sputtering

Two different sputtering systems have been employed during this investigation, these two arrangements and the related procedures are both outlined.

In the first case, fused quartz (amorphous silica) substrates are have been used for this type of library production method. 75 mm x 25 mm slides have been chosen as this size and shape is both compatible with the production equipment and analytical methods employed. Additionally, the dimensions are appropriate for the containment of the 1-D binary metallic libraries produced here.

Cleaning of the substrates was carried out immediately before use to minimise contamination. First they were ultrasonicated in Decon 90 for 10 minutes then the substrates were rinsed thoroughly in deionised water to remove any surfactant residue. The substrates were dried fully before being added to the high vacuum system to keep plumping time to a minimum.

Sputter coated samples were produced using a Bulzers ultra high vacuum coating system. The fused quartz slides (75 mm x 25 mm) were placed side by side along the axis linking the two sources to be used; this position will produce two identical replicates for later treatment. The chamber was pumped to high vacuum $\approx 1 \times 10^{-5}$ mbar before being back-filled by argon to 3×10^{-2} mbar. This pressure was held accurately by continuous pumping, this process will also further deoxygenate the chamber.

The sputtering sources were positioned to present a flat surface at 45° to the centre of the substrate. These are designed to focus on the same point if the substrate is 100 mm below the centre of the source. In this case the substrate is positioned so that it is only 50 mm below the centre of the source. This produced a focus error that produces the required gradient in the individual elements film thickness. To accentuate this process further custom made masks with triangular gaps that widened towards the bottom were added to both of the sources. This allowed the samples with the desired compositional gradient to be produced.

The composition gradient was optimised in advance by measuring the effect of different sample to substrate angles. This was achieved by masking samples along the gradient during deposition so when this mask was removed an edge suitable for Alpha step measurement was present. During this optimisation only one source was used during each deposition, therefore a gradient of thickness was produced. These thicknesses were used to calculate the compositional gradient of the libraries produced when multiple sources are co-deposited with a particular geometry.

Both the copper and aluminium sputter sources were initiated together with the power set to 350 watts direct current on each of the 45 mm circular targets. This gives an average power density of 22 Wcm^{-2}. The sputtering process was carried out for 5 minutes with a shutter covering the substrates. No deposition took place at this time but the surface of the target was eroded so that the cleanest possible source was available for sample production. Once the shutter was drawn back the co-deposition of both materials progressed for 1 hour. Earlier depositions of single materials and measurement by Alpha step have shown that a maximum thickness (at the respective focus points) of 2.5 microns of copper or 2.2 microns of aluminium per hour can be deposited using this arrangement.

The substrate was not intentionally heated either before or during the deposition but radiated heat from the magnetron sources will raise the temperature of the substrate to ≈100°C during the fabrication process. The substrates were allowed to cool slowly under low pressure argon

before air was allowed back into the chamber. This is important as any disparity in the cooling rate of the film and substrate can lead to a greater chance of the film de-adhering.

Heat treatment of this sample was carried out in a tube furnace under a reducing atmosphere of flowing atmospheric pressure forming gas (90% N_2 10% H_2) so that the film was protected from oxidation. The furnace was heated to 400°C ± 10°C over the whole sample. The temperature was held for 1 hour and then left to cool naturally, this took approximately 2 hours to cool to 100°C.

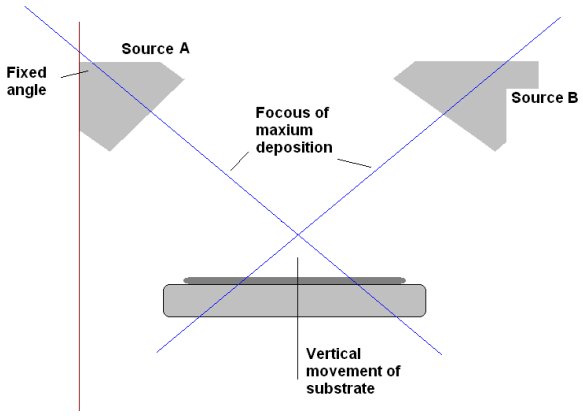

Figure 3.1. A diagram showing the deliberate misalignment of the magnetrons in the sputtering system.

All of the samples produced by our collaborators at Cornell University used their Angstrom sciences Onyx-2 magnetron sputtering system with a four gun arrangement. Targets A, B and C are arranged around a 76 mm substrate each at 120° intervals with the source D being directly in the middle. A, B and C have a 15° tilt while D is parallel to the substrate into which the library is to be deposited. All of the libraries were deposited on circular 3" pure Silicon substrates [126].

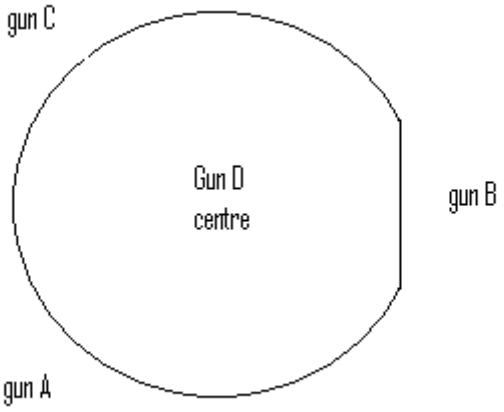

Figure 3.2. Aerial view of the magnetron sources in the Onyx-2 sputtering system.

The name of each sample is chosen so that the elements used and the position of the sources used in their fabrication is immediately apparent. Sample names show the sources used in alphabetical order, with the X representing magnetrons unused in the production of that sample. For example a sample with Cu deposited from gun B and Pt deposited from gun D would be called XCuXPt.

The process was started by the cleaning of the substrate by surface erosion. An ion gun in the chamber meant that the substrates could be cleaned immediately before use. This method will erode both general contamination and also any SiO_2 from the surface of the wafer.

Firstly, a thin layer of 7 nm of titanium (or 12 nm of tantalum) was deposited. This acts as both a binding layer and also aids the quenching of heat through the sample allowing all parts of the library to be deposited under the same thermal conditions. The heating is predominantly radiative and the metallic layer, even of as little as 7 nm, improves the absorbing properties of the Si significantly. This layer was deposited from source D as this gives the most uniform film thickness.

From this point a co-deposition process is employed so all of the elements required for the library are sputtered in parallel and the compositional spreads are premixed through the thickness of the film. All depositions were carried out at 5 mTorr ($6.6x10^{-3}$ mbar) argon. An Inficon crystal deposition monitor that allows the measurement of growth rate at any point on the wafer permits the film thickness to be accurately controlled. To avoid strain that could break film adhesion films with a maximum thickness of 200 nm were fabricated.

Regardless of changes to the precise specification of the sputtering system geometry the stationary off-axis method is maintained. In all of the following examples the different sources are aligned so that the maximum rate of film growth from each source is not focused on the same position on the substrate. The exact rate and deposition profiles are unique to the elements being deposited, the shape of the etching footprint and the power density experienced by the target. As in the other example, the gradient of film thickness of the different elements will manifest itself in a gradient of elemental composition in the final co-sputtered libraries.

Sample name	Under layer	Deposition temperature °C
XXXPt	7 nm Ti	60
XCuXPt	7 nm Ti	200
XPtPbX	12 nm Ta	250
NiXTiX	12 nm Ta	550
ZrXTiX	12 nm Ta	350
RuPtXX	7 nm Ti	400
BiCuSbX	7 nm Ti	100
RuPtPbX	12 nm Ta	250
RhPtSnX	7 nm Ti	250

Table 3.1 Samples produced, their geometry, binding material and the depositing substrate temperature.

3.2.2 Electrochemical Deposition

The underlying substrate for all of the electrochemical deposition was standard soda lime silicate glass covered with a conducting metallic layer. 75 mm x 25 mm glass was used for the one dimensional systems while 50 mm x 50 mm substrates were used in the case of two dimensional systems. Cleaning of the substrates before use to was done by ultrasonication in Decon 90 for 10 minutes, then the substrates were rinsed thoroughly in deionised water to remove any surfactant residue, the samples were dried in air before going into the vacuum chamber.

For the electrochemical process a conducting substrate is required. This was produced by direct current magnetron sputtering with the same Bulzers ultra high vacuum coating system as was used for the combinatorial deposition. The geometry of the system was changed so that a conventional even film was produced. In this case the substrate is placed 100 mm from the magnetron and parallel to the source.

Where molybdenum was required as the conducting substrate the layer is produced in $3x10^{-2}$ mbar argon with a 300 W power input to a single source. 45 minutes produces the required 1000 nm layer.

Where a tin substrate was required a chromium binding layer of 10 nm was sputtered between the tin and the glass. Multiple sources in the chamber mean the chromium can be deposited, the sample then being turned parallel to the second source from which 200 nm of tin is immediately deposited. This limits possible contamination caused by having to open the chamber between depositions. The deposition of the tin took around 30 minutes with an applied power of 100 W (an average of 6.3 Wcm^{-2}); the lower power level chosen for tin sputtering was required to protect the surface of the low melting point tin target from excessive heat.

While the compositions of the electrolytic baths vary depending on the materials being produced they all conform to the same basic design. The working electrode (i.e. the substrate to be plated) and the platinum counter electrode face each other in the bath with a working distance of 50 mm. These are both connected to a potentiostat, so that the required applied voltage can be maintained through the whole process. The reference electrode is present so that the total amount of current passed through the cell during the deposition can be recorded, from this the thickness of the film can be calculated.

After consideration of the mass transport issues [127], all electro depositions were carried out at room temperature without need for stirring. Initial experiments have shown that hydrogen gas formation is minimal under the conditions required for these experiments.

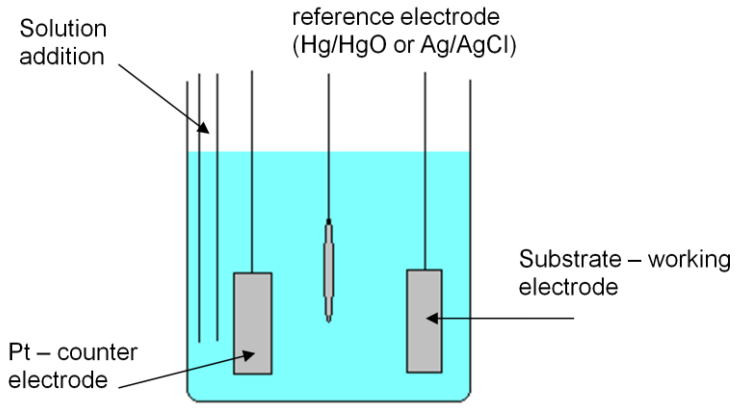

Figure 3.3. A schematic view of the electrolytic cell

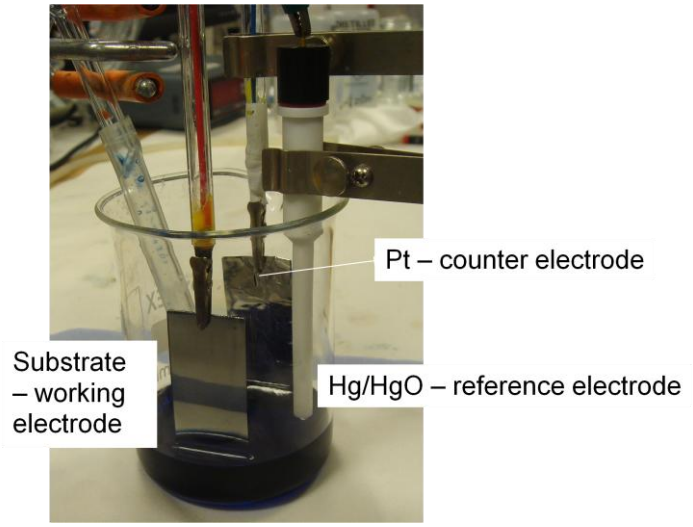

Figure 3.4. The actual combinatorial cell in practice. This is at the start of the deposition of copper and so the electrolitic solution level is low.

As is common with electroplating the different metallic layers are deposited in sequence using a different chemical bath for each layer. The metal that is deposited first has been chosen with regard to the adhesion properties of the metals in any particular library and their position in the electromotive series. The metals that have the highest position on the electromotive series are plated first then the other layers are added. This reduced the tendency for the solution used in the second deposition to oxidise the film back into the solution.

For the production of the high density libraries the compositional gradient has been created by changing the relative thickness of the layers of the sample with respect to the position on the substrate. This film thickness is produced by varying the amount of time that different parts of the substrate are in the solution. To this end the level of the solution is gradually raised throughout the plating so that the plating time varies from about one minute to half an hour depending on the position. The ends of the sample are masked during the deposition step in such a way to leave some of the underlying conducting substrate exposed at each end of the substrate. A portion of the elemental components of the libraries are also masked between depositions so that these simple elemental regions would remain in addition to the compositional spreads.

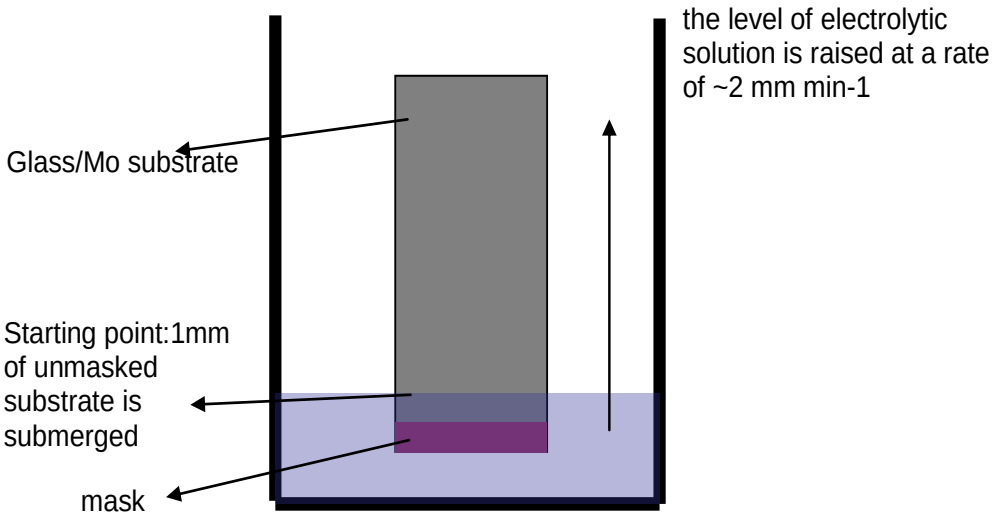

Figure 3.5. Illustration of the Substrate during deposition process. The electrical connections are at the top and so are always clear of the solution.

For the second deposition step the sample was thoroughly washed in water then placed in a new solution with a staring level 1 mm from the mask. Importantly the sample was inverted so that the thickest parts of the two films were at different ends of the substrate.

Heat treatment was required for all samples as the separate layers need to be dissociated into one structure and for the alloy phase to be formed. All of the samples that have been fabricated by electroplating were fully characterised (see sections 3.3 and 3.4) in their as-deposited state before being heat treated. The characterisation was then carried out again.

Solbitol use as complexing agent by Barbosa [128] has been shown to increase plating efficiency but will not be incorporated into the film under any of the conditions used. This allowed it to be used as a complexing agent in these depositions, for the solutions where it would aid film production.

3.2.3 Binary libraries

Cu-Sn librery production was carried out on a sputtered molybdenum substrate. Copper was first deposited by electroplating. The composition of the solution used for this deposition was NaOH 3M, Sorbitol ($C_6H_8OH_6$) 0.2M and $CuCl_2$ 0.1M in aqueous solution [129]. The applied potential during this deposition was -1.1V. The solution used for the deposition of the tin layer was $Sn(CH_3SO_3)_2$ 0.1M, CH_3SO_3H (methylsulfonic acid) 1M and Empigen BB detergent ($C_{16}H_{33}CINNaO_2$) added at 1ml/l. The applied potential was -0.45 V. The thermal

processing for this library was carried out at 250° C held for 3 hour with an additional hour of cooling time. The heat treatment was carried out under flowing forming gas [64]. The temperature was kept low as the samples produced in this case were found to be more prone to de-adhering with rapid high temperature annealing. This is thought to be caused by the different expansion rates of the components.

Cu-Zn deposition was also carried out on a sputtered molybdenum substrate. The copper is deposited first when the composition of the solution was NaOH 3 M, Sorbitol 0.2 M and $CuCl_2$ 0.1 M. The applied potential during this deposition was -1.1 V. The time taken for the solution to cover the whole deposition area was 30 minutes. For the zinc layer the solution consisted of $ZnCl_2$ 0.05 M and KCl 1 M, which was buffered to pH 3, the applied potential was -1.22 V. Heat treatment of this library was carried out at 450°C, being held at temperature for 3 hours plus the cooling time of around 5 hours to fall to room temperature.

The Cu-Sn and Cu-Zn libraries have been chosen for research as the deposition of Cu-Zn-Sn films are becoming important as a precursor materials for improved solar cell absorber layers. It has already been established that Cu_2ZnSnS_4 can be used as a replacement for $CuInS_2$ with potentially large cost advantages. [130] These simple binary samples would be the first stages in a combinatorial study to optimise the deposition requirements for this material as well as the potential screening of other potentially useful phases in this quaternary system. Investigating, for example, how final stociometery and sulpherisation efficiency is affected by precursor composition is important in these systems [131]. Research into how the final quaternary structure is affected by layering order can be achieved combinatorially.

For the Cu-Bi system a molybdenum substrate is again used. The copper is deposited first, the composition of the solution was NaOH 3 M, Sorbitol 0.2 M and $CuCl_2$ 0.1 M. The applied potential during this deposition was -1.1 V. The solution for bismuth deposition is NaOH 2M, sorbitol 0.2M, $Bi(NO_3)_3$ at -0.83 V. Heat treatment of this sample was carried out for 5 hours at 200°C and for 25 hours at 200°C so that the effect of time on the dissociation could be examined. The solutions used for this deposition have been adapted from Jiang et al [132] and Sandnes et al [133].

Three other replicates of the copper-bismuth library were produced using the same experimental conditions. These samples were used for sulphurisation and selenisation reactions with the aim of producing a range of semi conducting CuBiS and CuBiSe compounds.

The sulphurisation was carried out by the thermal evaporation of 0.3 g (a one hundred times excess considering the mass of the film available for reaction) of elemental sulphur positioned 20 mm away from the substrate. The sample is inverted to face away from the sulphur source so that only the fully vaporised sulphur can reach the CuBi film and react with it. The treatment is carried out by heating the sulphur and the surface of the sample to 250°C at the maximum rate of the thermal processor, then from 250 - 450°C at 5°Cm^{-1} the sample is held at 450°C for 30 minutes before being allowed to cool naturally. The whole process is carried out under pure N_2 at atmospheric pressure.

Two libraries were selenised under two heating regimes one with a maximum of 250°C and the other with a maximum of 450°C. Both samples were prepared by the thermal evaporation of metallic selenium on to the surface of the film. The sample was then heated to the reaction temperature and held for 30 minutes in a 20 mbar 90% N_2 10% H_2 atmosphere. Additional selenium was present in the reaction chamber ensuring an excess of the element.

The Cu-Pb system employed a molybdenum substrate, a copper solution consisting of NaOH 3 M, Sorbitol 0.2 M, $CuCl_2$ 0.1 M. For the deposition of lead the solution used was NaOH 2 M, sorbitol 0.2 M and $Pb(NO_3)_3$ 0.1 M. The applied potential was -1.3 V. Heat treatment carried out at 200°C for three hours plus the cooling time.

In forming the Cu-Pb library the same substrate and copper solution as for the Cu-Pb system was used. For the deposition of antimony deposition the solution used was NaOH 2 M, sorbitol 0.2 M and $SbCl_3$ 0.1 M. The heat treatment was at 450°C for 3 hours plus the cooling time.

It was decided that having samples without the Mo background was desirable, for this reason SnZn and SnSb have been produced without this layer. Tin is a good conducting substrate and by using it as the initial sputtered layer then allowing it to be incorporated into the library unnecessary complexity can be avoided.

Another reason for electroplating the Sn-Zn library on a tin substrate is that the tin will not deposit well onto the molybdenum. The solution used was $Sn(CH_3SO_3)_2$ 0.1M, CH_3SO_3H (methylsulfonic acid) 1M and Empigen BB detergent ($C_{16}H_{33}CINNaO_2$) added at 1ml/l, a potential of -0.45 V was employed. For the zinc layer the solution consisted of $ZnCl_2$ 0.05 M and KCl 1 M, this was buffered to pH 3. The applied potential was -1.22 V. Heat treatment was at 200°C for 3 hours plus cooling time.

For the Sn-Sb the solution used was $Sn(CH_3SO_3)_2$ 0.1M, CH_3SO_3H (methylsulfonic acid) 1M and Empigen BB detergent ($C_{16}H_{33}ClNNaO_2$) added at 1ml/l. Again a potential of -0.45 V was preferred. For the antimony NaOH 2 M, sorbitol 0.2 M and $SbCl_3$ 0.1 M was used. The heat treatment was completed at 200° C with a 3 hour hold at maximum and then cooling time.

3.2.4 Ternary libraries

This process was expanded to produce a 2-D three material system consisting of zinc over tin over copper on a 50 mm x 50 mm molybdenum covered glass substrate. The process was started as with the 1-D system with a layer of copper deposited followed by a 180° turn of the sample allowing the tin to be deposited with its thickness gradient in the opposite direction. After rinsing the library is placed fully in the copper bath so a thin even layer of copper (1 minute of applied voltage) can be electroplated to the whole substrate. This step was added as the zinc was found to plate better on copper than on tin. The substrate was then turned 90° to the gradients of the other two materials. When the zinc is plated with its gradient of thickness in this direction the result is a two dimensional spread. Heat treatment has been achieved at 450° C for three hours then the cooling time [64].

3.2.5 Electrostatic Spray Deposition (ESD)

This section describes potential methods for producing combinatorial libraries by the electrostatic spraying of organometallic precursor solutions, with the aim that this method could be used as a cheap and fast alternative to the high vacuum direct current sputtering method described in sections 1.2.1 and 3.2.1.

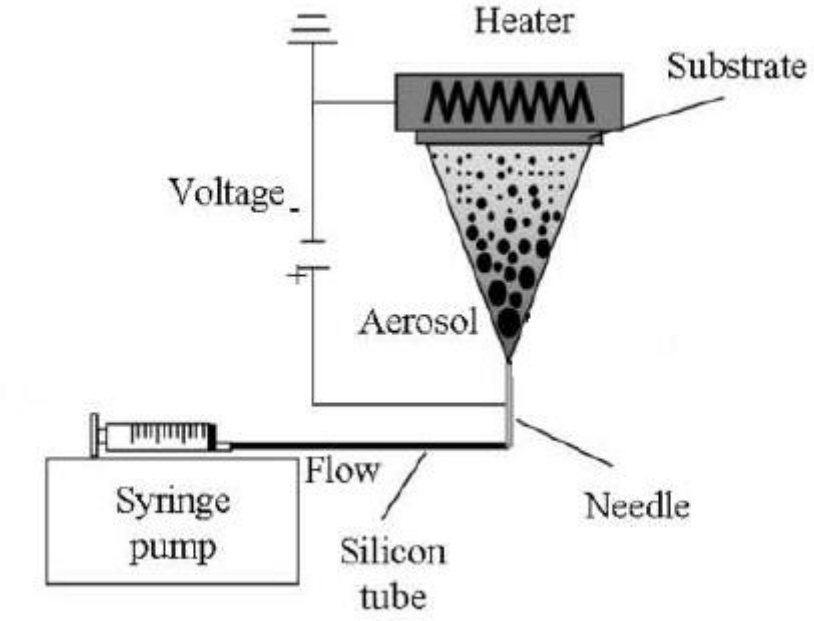

Figure 3.6. Schematic of the electrostatic spray system. This design is the same as the system employed by Roncallo et al [134].

The system employed has the general arrangement shown in figure 3.6 except for the addition of a second needle in some experiments to allow the co-deposition of different materials focussed on different parts of the substrate. The alternative is to use sequential depositions where the relative positions of the source and substrate are changed between depositions. Additionally, to accommodate the second deposition source changes in geometry are required. These changes also allow the production of films with larger than usual variation in thickness of the deposited film for each of the individual deposited precursors. The results of these changes can be seen in figure 3.7. As with the sputtering and the electrochemical deposition it is the ratio of the thickness of these layers that is the major factor in producing the final compositional gradients.

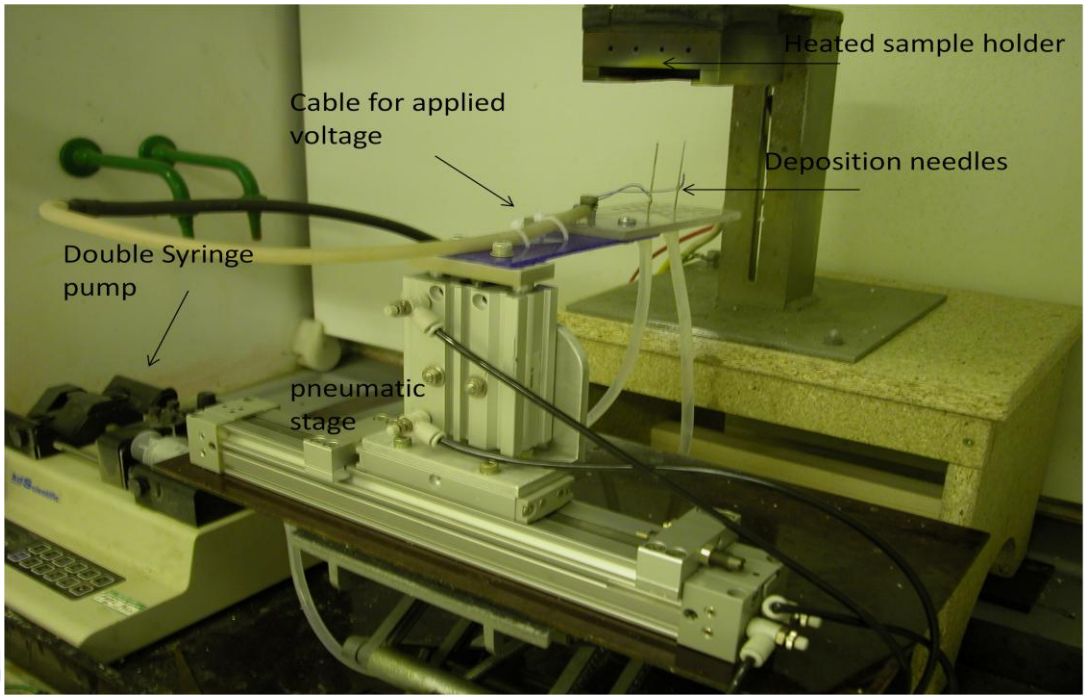

Figure 3.7. The electrostatic spray equipment as actually employed for library production. This equipment was modified for combinatorial depositions by Kyle Hutchings.

In all cases the potential applied to the needles in order to nebulise the solutions was 20 kV. The needles were stationary and positioned perpendicular to the surface of the substrate. The pump rate from the syringes was 5 ml/hour unless otherwise stated.

The formulation of the precursor solutions have been optimised to allow the quick deposition of films of a consistant quality. Unless otherwise stated the formulation of the solutions are as follows.

Solution name	Composition
Thiourea	$CS(NH_2)_2$ 0.1 mol dissolved in solution 90% ethanol 10% water (by volume).
Copper chloride	$CuCl_2$ 0.05 mol dissolved in solution 90% ethanol 10% water (by volume).
Copper acetate	$Cu(CO_2CH_3)_2.H_2O$ 0.02 mol dissolved in solution 90% ethanol 10% water (by volume).
Chromium acetate	$Cr_3(CO_2CH_3)_7(OH)_2$ 0.007 mol dissolved in solution 90% ethanol 10% water (by volume).
Tin acetate	$Sn(CO_2CH_3)_2$ 0.02 mol dissolved in solution 90% ethanol 10% water (by volume). Plus one drop of concentrated HCl per 50ml. [84]
Zinc acetate	$Zn(CO_2CH_3)_2.2H_2O$ 0.02 mol dissolved in solution 90% ethanol 10% water (by volume). Plus one drop of concentrated HCl per 50 ml to dissolve any zinc hydroxide formed [82].
Nickel acetate	Ni(CO2CH3)2.4H2O 0.0202 mol dissolved in solution 90% ethanol 10% water (by volume).

Table 3.2. Composition of electrostatic spray precurser solutions.

Here is demonstrated the production of samples for determining how film thickness effect characterisation. The deposition rate was calculated by using RBS measurements; this was related to the quality of data that was achieved in the X-ray diffraction investigation.

These samples were deposited on plain glass with one flat needle 60 mm away from the substrate and the deposition temperature was set at 200°C. The sample was then heated at 450°C for two hours under flowing forming gas atmosphere.

Sample code	Volume of solution used in deposition
Zinc thickness test1	1 ml Zn $(CO_2CH_3)_2.2H_2O$ 0.02mol
Zinc thickness test2	2 ml Zn $(CO_2CH_3)_2.2H_2O$ 0.02mol
Zinc thickness test5	5 ml Zn $(CO_2CH_3)_2.2H_2O$ 0.02mol
Zinc thickness test10	10 ml Zn $(CO_2CH_3)_2.2H_2O$ 0.02mol
Zinc thickness test20	20 ml Zn $(CO_2CH_3)_2.2H_2O$ 0.02mol

Table 3.3. Sample ID and its related precursor composition.

A range of samples have been produced to determine the effect of the geometry on the two needle systems. The samples used were copper and zinc continuous compositional spread libraries deposited on transparent conducting oxide (TCO) (Pilkington Tec 15 tin oxide) coated glass. 10 ml of each solution was sprayed at a rate of 5 ml per hour.

Sample	Geometry	Deposition	Needle	Substrate temperature
ES-CuZn-A	Needles 40 mm from substrate and 20 mm apart.	Co-deposition	ground needles	500 ºC
ES-CuZn-B	Needles 40 mm from substrate Needles 20 mm apart.	Sequential deposition Zn first Cu over the top.	ground needles.	500 ºC
ES-CuZn-C	Needles 60 mm from substrate Needles 30 mm apart.	Co-deposited.	Pointed (non-ground) needles.	500 ºC
ES-CuZn-D	Needles 40 mm from substrate Needles 20 mm apart.	Co-deposited.	Pointed (non-ground) needles.	500 ºC
ES-CuZn-E	Needles 60 mm from substrate Needles 20 mm apart.	Co-deposited.	Pointed (non-ground) needles.	500 ºC

Table 3.4. Sample identification and its related deposition conditions. These experiments were required for geometry optimisation.

Production of the combinatorial libraries on TCO (Tec 15)

The fabrication of these samples is carried out with the two needles 6 cm away from the substrate and 2 cm away from each other. The deposition used 20 ml of each of the materials at 5 ml per hour. Needles that had been ground flat were used in all case. When the lower deposition temperatures were used the samples were heated under forming gas to remove any unwanted organic material that had not already been thermally decomposed.

Sample name	Deposition solutions	Substrate temperature	Heat treatment temperature
ZnS	Zinc acetate, Thiourea	500°C	No treatment
NiZn 25609	Nickel acetate and zinc acetate co-deposited	200°C	500°C
ZnCu 2569	copper acetate and zinc acetate co-deposited	200°C	500°C
NiCu 24609	copper acetate and Nickel acetate co-deposited	200°C	450°C

Table 3.5. Sample identification and its related deposition conditions for library production.

For the production of the combinatorial libraries on plain soda lime silicate glass, the deposition conditions were the same as above except for the substitution of substrate. SnCr was carried out with the pointed needle arrangement where the ground faces of the needles were facing away from each other.

Sample name	Deposition solutions and conditions	Substrate temperature	Heat treatment temperature
SnZn 161009	Tin acetate and Zinc acetate co-deposition	200°C	450°
SnCr 251009	Tin acetate and Chromium acetate Thin layer of tin acetate (2 ml of solution) laid down first then co-deposition	200°C	450°
CrNi 1769	Tin acetate and Chromium acetate Thin layer of tin acetate (2 ml solution) laid down then co-deposited	200°C	450°
SnCu 191009	Tin acetate and copper acetate used a thin layer of tin acetate (2 ml of solution) laid down first and then co-deposited.	200°C	450°
ZnNi 21009	Tin acetate and Nickel acetate co-deposited	200°C	450°
CuNi 25908	Copper acetate and Nickel acetate co-deposited	200°C	450°
ZnCu 256	Copper acetate and zinc acetate co-deposited	200°C	400°

Table 3.6. Sample ID and its related deposition conditions for library production on non-coated glass.

3.2.6 Production of Conventional Single Phase samples

The justification of the choice of the material and the fabrication methods for these samples is explained fully in section 4.3.1.

Production of these samples was carried out by conventional electrochemical deposition where the substrate is coated evenly with the relevant precursor layers before the gas phase sulphurisation step.

A sample with code Cu30Bi was an attempt to make Cu_3BiS_3. The characterisation of the combinatorially produced library confirmed the presence of this phase and analysis of its position on the substrate allows calculation of the deposition times of the precursor layers. The substrate use for this experiment was the 860 nm molybdenum on glass produced at Northumbria University. The copper was deposited from the NaOH 3 M, Sorbitol ($C_6H_8OH_6$) 0.2 M and $CuCl_2$ 0.1 M in aqueous solution. The plating was stopped when the digital current integrator showed that 60 counts (1.2 coulombs) of current had passed. After rinsing the sample the bismuth was deposited from a NaOH 2 M, sorbitol 0.2 M and $Bi(NO_3)_3$ 0.1 M aqueous solution with an applied potential of -0.83 V. Three times fewer Bi atoms are required form this deposition so 30 counts (0.6 coulombs) was allowed to flow before the experiment plating was halted. 0.6 C was used instead of 0.4 C due to the differences in valancy, a +3 charge on Bi and a +2 charge for the copper ions.

In a second conventional deposition a sample with code Cu60Bi was produced. This was an attempt to make $Cu_{2.94}Bi_{4.8}S_9$ as this has been linked with semiconducting and possible solar absorber properties. For this material the same solutions and applied potential is used but the number of counts for which the deposition took place was 30 counts (0.6 C) for the copper and 72 counts (1.44 C) for the bismuth.

In both cases the sulphurisation was carried out directly on the as deposited samples using the same method that was described when sulphurising the copper bismuth compositional spreads. It is the analysis of the compositional spreads that confirms that the sulpherisation conditions would produce the desired phases where the precursor stociometery allows it.

3.3 Elemental Analysis

For the characterisation of the high density chemical libraries three analytical methods were chosen, all have a system where a portion of the sample is illuminated for characterisation. In each case, the size and position of the illuminated area needed to be the same so that for any position on the library several analytical systems could be combined. The results could then be compared to each other and with the extended beam X-ray diffraction data collection method discussed later.

Spot size has been chosen at 500 µm along the gradient of the library. This was achieved by the use of a final collimator of 0.5 mm for the RBS ion beam giving a circular footprint of illumination of the desired dimension. When data was being collected with the EDS 'full scan' mode was used. Changing the magnification when operating in this mode allows the size of the scanned area to be tuned at will. The slight difference with this method is that the spot size is rectangular. However the length of the compositional gradient that is illuminated is still 500 µm.

A 0.5 mm spot size has been found to be large enough to produce good data collection with all the chosen analytical methods but is still small enough to allow densely packed analytical points, making the most of the continuous compositional spread samples.

For both the 75 mm x 25 mm and the 50 mm x 50 mm libraries the rectangular shape of the substrates makes the process of choosing sampling positions simple. One marked corner is used as the origin and a virtual grid is superimposed over the substrate. For the one-dimensional systems only a single track of scanning points is required so a central strip covering the whole gradient is analysed. The data collection has been done at 1 or 2 mm spacing as stated. For the two-dimensional library a virtual grid of 2 mm steps was used to cover the whole substrate, again one marked corner acted as the origin.

The libraries deposited on silicon were made on circular 3" wafers. In contrast to the conventional Euclidean grids these samples were collected using a polar coordinates system. The straight lines of data points were collected at regular intervals along various radii, the starting point of these lines was set at 45° intervals. The flat portion characteristic of these wafers allows the substrates to be fixed into a sample holder in a unique position. Pre-marked crosses scribed onto the custom made sample holder gave a fixed starting position for each of

the desired angles. In all cases the first point for the data collection was 5 mm from the scribed cross towards the centre of the sample, the collection was carried out at 2 mm intervals until the opposite edge of the sample was reached.

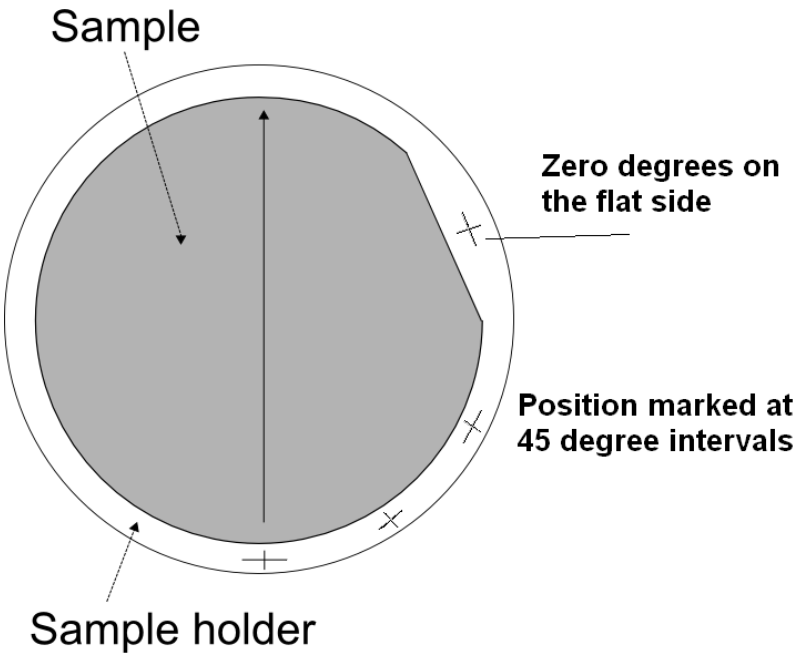

Figure 3.8. Sample holder to allow highly accurate repetition of characterisation points. This example is for the radial measurements.

Sample name	Angle(s) collected for each method		
	EDS	RBS	XRD
XCuXPt	0	0	0
XPtPbX	45	Non	45
NiXTiX	90	90	90
ZrXTiX	90	90	90
RuPtXX	0,45,90,135	0,135	135
BiCuSbX	0,45,90,135	90	0,45,90,135
RuPtPbX	0,45,90,135	Non	0,45,90,135
RhPtSnX	0,45,90,135	Non	0,45,90,135

Table 3.7. The positions at which the radial interrogation were carried out.

Extended beam X-ray diffraction collection has always been taken in a way so it will match a number of consecutive points from the conventional raster scanned XRD. The beam length of approximately 25 mm means that a maximum of three data collections were required to cover the whole area of interest.

3.3.1 Energy Dispersive X-Ray Spectroscopy

All of the EDS measurements were carried out on a Jeol 84A scanning electron microscope using Genesis EDAX data collection and processing software. For consistency the data collection conditions are kept the same for all the samples where possible. In some cases the chemical composition of the samples or other physical properties means that this is not prudent. In these cases, the collection conditions are optimised on a library by library basis. In all cases, the collection conditions are kept the same for every point on a particular substrate. This, to a certain extent, compromises the collection at individual points on the library but this is still thought to be the best solution.

Generally the large number of collection points in these combinatorial samples means that only one collection is carried out on a particular position. However in some cases 5 sets of data have been collected so that the precision of the compositional analysis can be shown.

Point-to-point continuity was measured on the electrochemically deposited samples with points 20 and 40 mm from the sample origin being repeated 5 times each for later statistical studies.

In all cases, an area scan was employed. A magnification of 515 times was set as this produced an area of illumination of 500 µm x 500 µm, this size is similar to the characterisation area of the other techniques. Data collection time of 300 seconds (except for CuZn and CuBi which was 100 seconds) real time is used per collection point. The I probe was 1600 nA, filament target was 2.66 A and beam current was 400 µA.

Sample type	Applied voltage and other variations
Electrochemically deposited samples	15 kV
Except for CuSnZn	10 kV
Sputtered CuAl	15 kV
Electrostatically sprayed	15 kV
Sputtered samples (except for RuPtXX, XXCuPt and RuPtPbX)	8 kV
Sputtered RuPtXX, XXCuPt and RuPtPbX	10 kV

Table 3.8. The applied voltage which has been chosen for each library.

3.3.2 Rutherford Backscattering Spectrometry

The Rutherford Backscattering Spectrometry was carried out with particle energies of 2000 KeV produced by a single ended Van de Graaff generator. Ion beam collimation of 0.5 mm at the final slit was used in all cases. For all the samples the incident beam geometry was perpendicular to the target with the backscattering detector held at 165°. The detector is a 672 (143A) 50 pips with energy selective multichannel analyser (Easy MCA). During each data collecting session high purity Pt, Au and Al standards have been used for energy level and intensity calibration. These included a thin film Au 5 % - Al 95 % alloy sample produced by thermal evaporation this was made to be similar to the sputtered thin films and was 220 nm ± 20 nm thick when measured by alpha step physical profiling. The model creation and fitting to the collected RBS energy distribution was carried out using SIM NRA software.

3.4 Structural Analysis

3.4.1 X-Ray Diffraction

Point by point raster scanned analysis of all libraries was carried out using a Bruker D8 X-ray diffractometer with a general analysis diffraction detector system (GADDS) detector. In all cases copper Kα radiation (wavelength 1.54 nm) has been used. A 500 µm collimator was used to collect the data. The centre of the detector was at 38° unless otherwise stated. Data collection time was 120 seconds per frame. The applied voltage was 40 kV and the current 40 mA. For the extended beam method, a 25 mm x 0.5 mm slit collimator was used to collect the data. In this case, the data collection time was 300 seconds per frame.

Conventional single composition samples of Cu_3BiS_3 and $Cu_{2.94}Bi_{4.8}S_9$ were analysed by PANalytical X'pert PRO multi-purpose diffractometer using copper Kα radiation with an applied voltage of 40 kV and a current 40 mA. A PIXcel detector was used to collect data over a 2θ angular range of 10° - 80°.

3.5 Extended Beam X-ray Diffraction

3.5.1 Application Phantom Samples

For the full exploration of the new technique and the testing of the partitioning software experiment, some basic phantom samples were required. A custom made sample holder with several small cells 5 mm^2 has been produced from glass. This amorphous container can be filled with powdered diffraction standard (silicon NBS 640c) so that different combinations of the cells can be filled at different times. This was used to illustrate and test features of the partitioning algorithm as it is applied to different material combinations in different positions along the illuminated area.

A glass step wedge where the height of each step was 0.34 mm and where each step could be loaded with silicon powder has been produced. The area of each step was ~2 mm x 3 mm. This provided an extended sample where each component step was displaced by a fixed amount from the centre of the diffractometer. This deliberate displacement error resulted in diffraction maxima shifts as

$$\Delta 2\theta = -2S\cos\theta / D$$

Where $\Delta 2\theta$ is the variation of scattering angle, D is the sample to detector distance, and S is the sample displacement relative to the instrument centre. Thus this phantom represented a first approximation to a material with continuous changes in lattice parameter along the illuminated area.

Similar experiments have been carried out using homogeneous metallic copper thin films deposited upon glass slides by sputter coating. This was fabricated under 3 $x10^{-2}$ mbar argon with a 300 watt power input to a single magnetron source. A deposition time of 30 minutes produces a ≈1000 nm layer; this was thick enough to be effectively opaque to the X-rays used here. This film was mounted within the diffractometer initially with its surface parallel to the incident beams long axis (conventional setting). Subsequent data collections were undertaken with the sample rotated such that each end of the sample was displaced by the same amount (but one end with a positive displacement and the other a negative displacement) from the instrument centre. The midpoint of the library sample remained on

the diffractometers focal point. Due to the deliberate displacement error, the diffraction data would appear to be derived from a continuously graded composition along the illuminated area. This gave diffraction maxima with positional shifts analogous to the changes in lattice parameters expected of samples with a changing compositional gradient and obeying Vegard's law [179].

3.5.2 Data collection geometry optimisation

Early indications suggest that the large X-ray photon flux from the extended beam produced a larger amount of inelastic (Compton) scatter. Optimisation of the data collection to create the best signal to noise ratio is therefore desirable. Approaches including the production and use of a purpose built knife-edge have been investigated. The setup of this knife-edge differed from some other systems as its mounting was achieved separate from the sample stage allowing for full manipulation of the high density libraries after the source, knife-edge and detector positions have been optimised. For the optimisation the knife-edge was moved up and down in 1 mm steps, and as shown here it was moved from side to side towards and away from the X-ray beam.

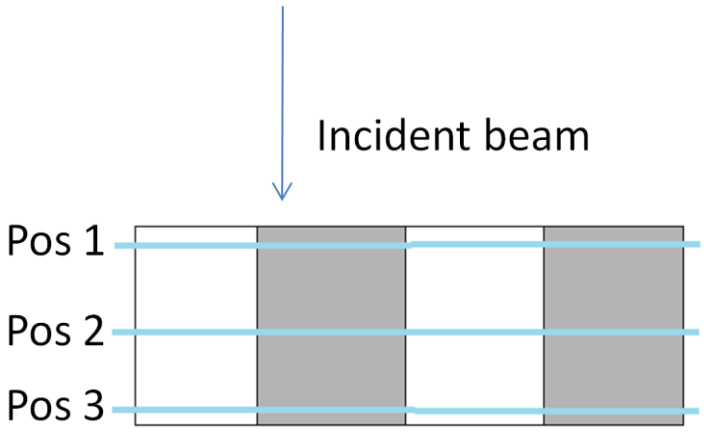

Figure 3.9. Examples of some knife edge positions. The grey represents Si powder in 5 mm^2 cells the rest is a non-diffracting substrate. The three positions vary by 1 mm steps.

3.5.3 Procedure to establish resolution limits

In this experiment two diffraction standards were illuminated simultaneously so that the ability of the extended beam and the partitioning to detect the minor component can be measured. Two plates of Al_2O_3 (srm1976) were held at a range of distances apart with the

gap being filled with silicon powder (NBS 640c). In all cases the Si made up a small proportion of the length of the beam (from 1.9 mm - 0.8 mm). The ability of the method to identify this material and give its correct position can therefore be quantified.

3.5.4 Application High Density Chemical Libraries

The basic arrangement during these collections is for samples to be positioned so that the extended X-ray beam illuminates a large compositional gradient. A position is chosen so that the extended beam overlays the virtual grid used in the conventional method. It, therefore, produces diffraction from a number of raster points at the same time. With this link between the two different collection methods results from the partitioning algorithm and the conventional results can be directly compared.

3.5.5 Knife edge geometry and application

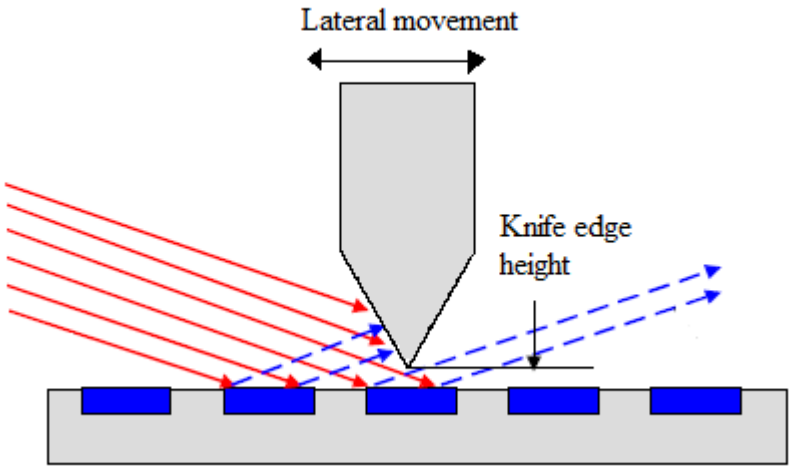

Figure 3.10. Illustration of typical knife edge geometry, both the height and the lateral position require movement independent of the sample.

The knife edge arrangement envisaged and shown in figure 3.10 has two main functions. Firstly to reduce random air scatter as the only free path from the incident side it the legitimate route for diffraction. Secondly to further define the incident beam, this additional collimation is particularly important when the extended bean X-ray source is used in conjunction with two dimensional combinatorial libraries.

3.6 Electro Optical Properties

Materials were tested with the LED light source 100 mm from the working electrode (sample). The reference electrode used was Ag/AgCl, and the counter electrode was Pt. When testing for p-type properties a 0.2 mol Eu^{3+} solution was used. When testing for n-type properties a 1 mol Na_2SO_3 solution was used. The beam was chopped at 14 Hz during the measurements.

Chapter 4

4 Results

In the following section, the results for the high density chemical libraries are displayed, concentrating on the three main conventional methods used in the investigation. The elemental compositional data has been compiled from EDS and RBS data collection, while the RBS is also used to determine the thickness of the samples. This is complimented by the phase identification from the X-ray diffraction. Once this information has been established the partition results from the extended beam data collection have been judged in its full context. Elemental composition information has been obtained by two different methods; the results from both methods have only been presented for two example libraries so that confidence in the consistency of the two approaches can be established.

4.1 Elemental Analysis

4.2 Energy Dispersive X-Ray Spectroscopy

Due to the nature of the chemical libraries and multiple samples that they contain the number of data collection points is already high. For this reason it was deemed that multiple repeats of the data collection could not be taken for each sample position. The consistency of the EDS system data collection was confirmed by multiple collections at the same points in the virtual grid. The process was generally carried out by the collection of five replicants for two points in each library. In this example, table 4.1, positions 11 and 14 of the CuBi system have been repeated. These results are typical of the consistencies achieved.

Repeats	13.04	33.03
	12.42	31.8
	12.42	31.81
	12.76	32.49
	12.7	32.37
Standard Deviation	0.26	0.52
Average	12.7	32.3

Table 4.1. Shown are the bismuth atomic percentages at the two positions with the average and standard deviation for the separate data collection results.

As most virtual samples only have one data collection a measure of the confidence in this single result has to be produced from the limited number of multiple collections. To achieve this, standard deviations were calculated for the cases where multiple collections were available. From this a percentage error equivalent to one standard deviation from the mean was calculated. The percentage errors for the points in the libraries where multiple collections had been made were averaged and this was used as the percentage error for the single data collection situations.

The statistical tests described later in the section assume a normal distribution. In the cases where the 5 data collection points are present, the Shapiro-Wilk test for normality was carried out [135]. With only 5 samples in the data set, this test should only be regarded as an indication of normality. Encouragingly none of the data sets where the Shapiro-Wilk tests was performed required the assumption of a normal distribution to be rejected.

4.2.1 Electrochemically deposited libraries

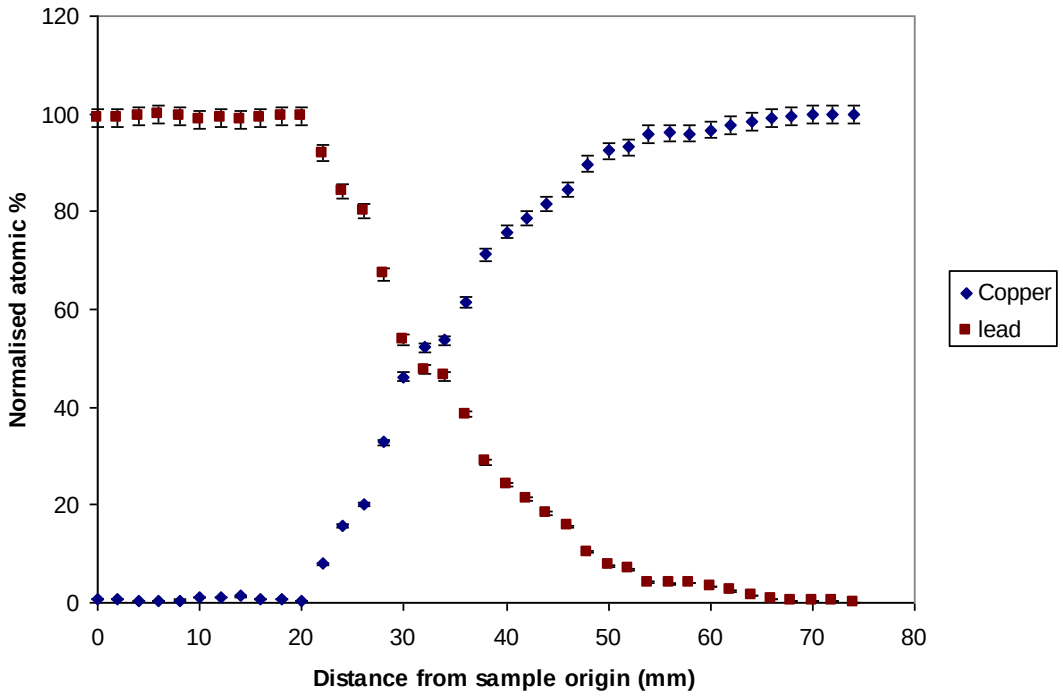

Figure 4.1. Electrochemically deposited Cu-Pb library. This is a heat-treated sample and is homogeneous with respect to depth. The error bars represent the equivalent to one standard deviation.

As with all of the electrodeposited libraries the edges of the samples were masked, the mask was moved between the two deposition steps so that purely elemental areas are fabricated to border the library. It can be seen in figure 4.1 that the graded area is confined to the central section with the area of interest covering approximately 40 mm.

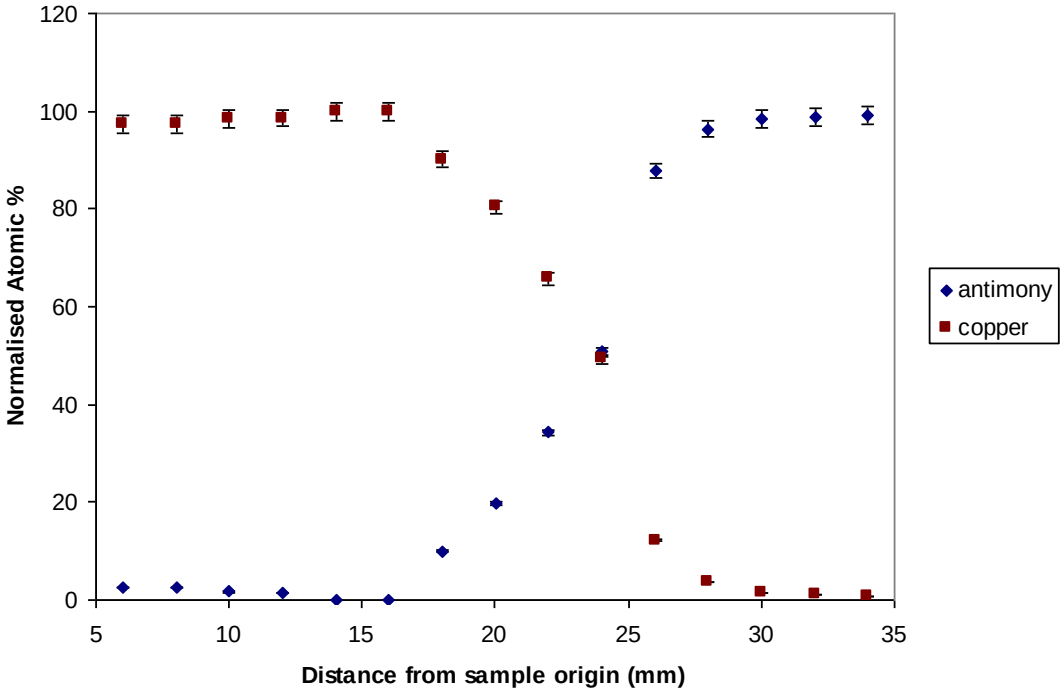

Figure 4.2. Electrochemically deposited Cu-Sb library. This is a heat-treated sample and is homogeneous with respect to depth. The error bars represent the equivalent to one standard deviation.

In the antimony-copper system seen in figure 4.2 the area of compositional range is confined to a smaller area than in the copper lead system, with 95 % of the compositional range being confined to 15 mm of the substrate. It is important to have produced samples where the compositional gradient is both very compact and others where it is less steep to determine when the extended X-ray probe can be most effectively exploited.

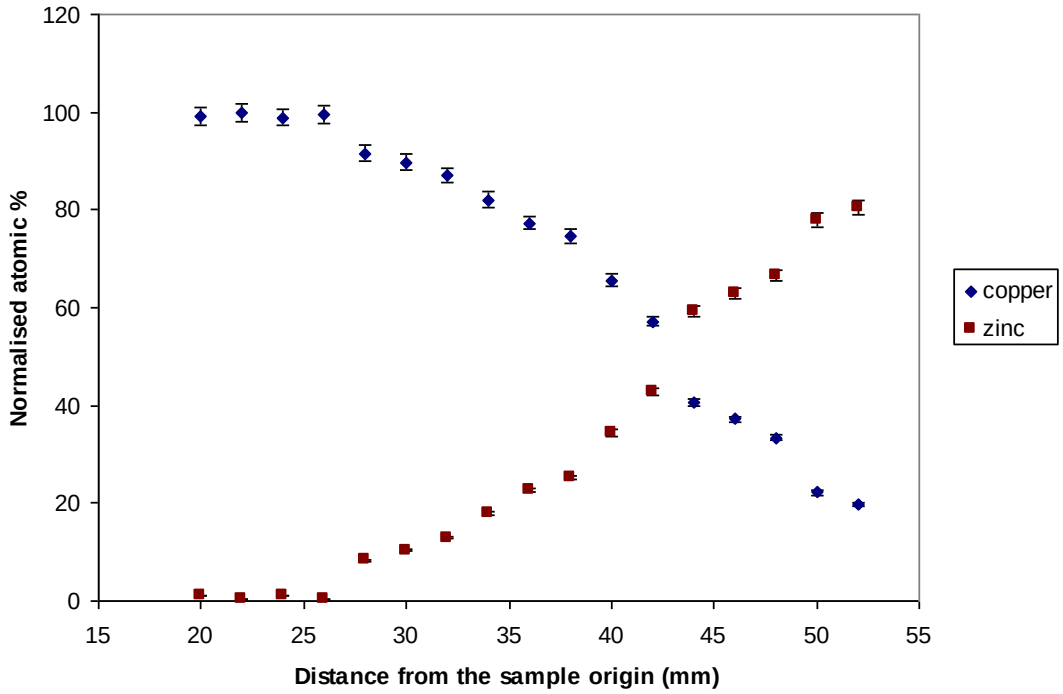

Figure 4.3. A portion of the electrochemically deposited Cu-Zi library. This is a heat-treated sample and is homogeneous with respect to depth. The error bars represent the equivalent to one standard deviation.

Copper-zinc has been made with a similar gradient to the copper-lead but with a more linear arrangement. The other significant difference between these samples is the similarity of the atomic masses and densities of the copper and zinc. This means that the copper-zinc library shown in figure 4.3 is also evenly graded in weight percentage. This was not the case in the copper lead system.

In all of the three cases in figures 4.1, 4.2, 4.3., the samples were deposited on a molybdenum layer. This did not diffuse significantly into the other materials and therefore was not detected by the EDS probe as the conditions of analysis were chosen to confine the data collection to the upper homogeneous portion of the film. The choice of substrate gives these samples different properties to the subsequent ones to be discussed in figures 4.4 and 4.5, which are produced with a substrate that will become part of the system of interest. The reason for the employment of two approaches giving samples with and without substrate signals are discussed when the XRD characterisation is presented.

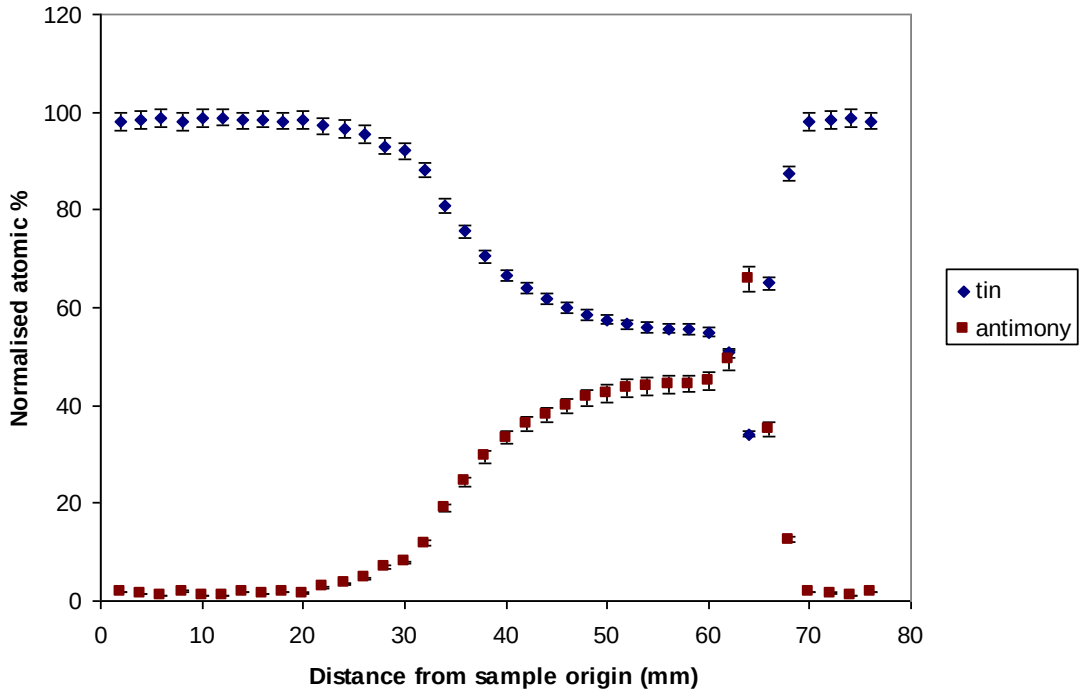

Figure 4.4. The electrochemically deposited Cu-Sb library. This is a heat treated sample and is homogeneous with respect to depth. The error bars represent the equivalent to one standard deviation.

The tin-antimony system, the EDS results of which are shown in figure 4.4, has been produced with a more gradual gradient with the tin concentration falling from 100 to 60 % in 30 mm of the substrate. This will aid the characterisation as the resolution requirements for the analysis of the libraries are less rigorous. In other respects, this gentle gradient detracts from the combinatorial method as less of the binary phase diagram can be represented in a given area or with a certain number of data collection points.

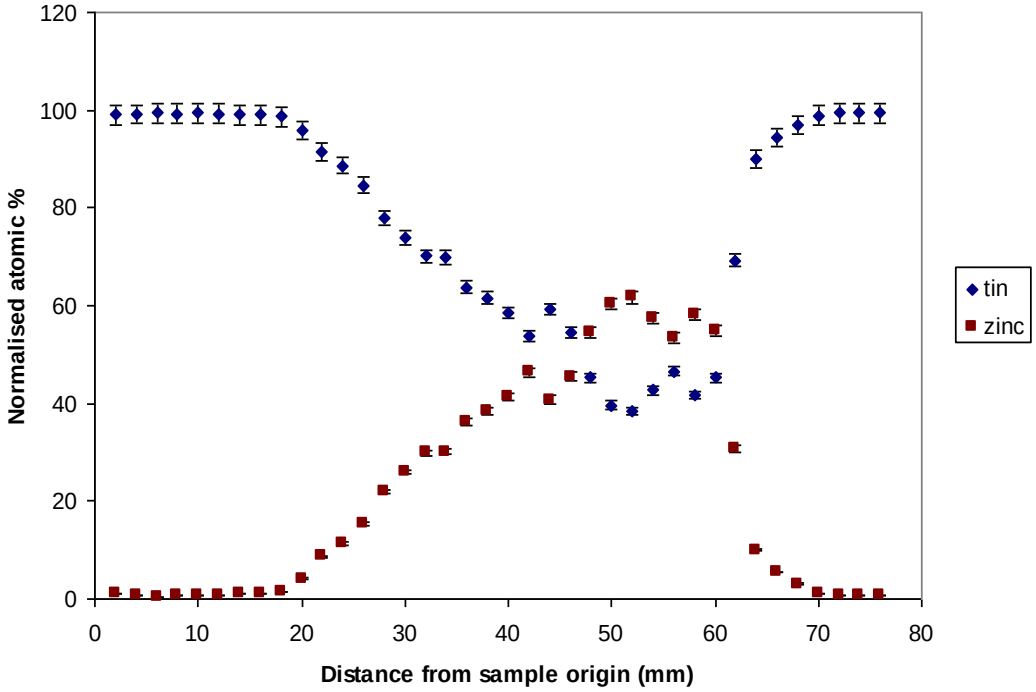

Figure 4.5. Electrochemically deposited Sn-Zn library. This is a heat treated sample and is homogeneous with respect to depth. The error bars represent the equivalent to one standard deviation.

The tin-zinc system illustrated in figure 4.5 gives a smooth linear gradient as the zinc concentration rises from 0 to 60 %. After this point the concentration of zinc fails to rise further despite the proportionally longer time that the zinc was deposited. This cannot be explained by standard deposition as the tin and zinc have been found to coat successfully together in a range of compositions by both co-deposition [136] and sequential layering. Structural effect such as tin whisker formation where the layer is sufficiently thick [137] can affect the surface available for subsequent depositions and therefore change the perceived ratios by these morphology effects. In this way, it is proposed that the zinc deposited comparatively poorly on the smoother layers of thin tin compared with the rough whiskered layer seen when the sample is thicker.

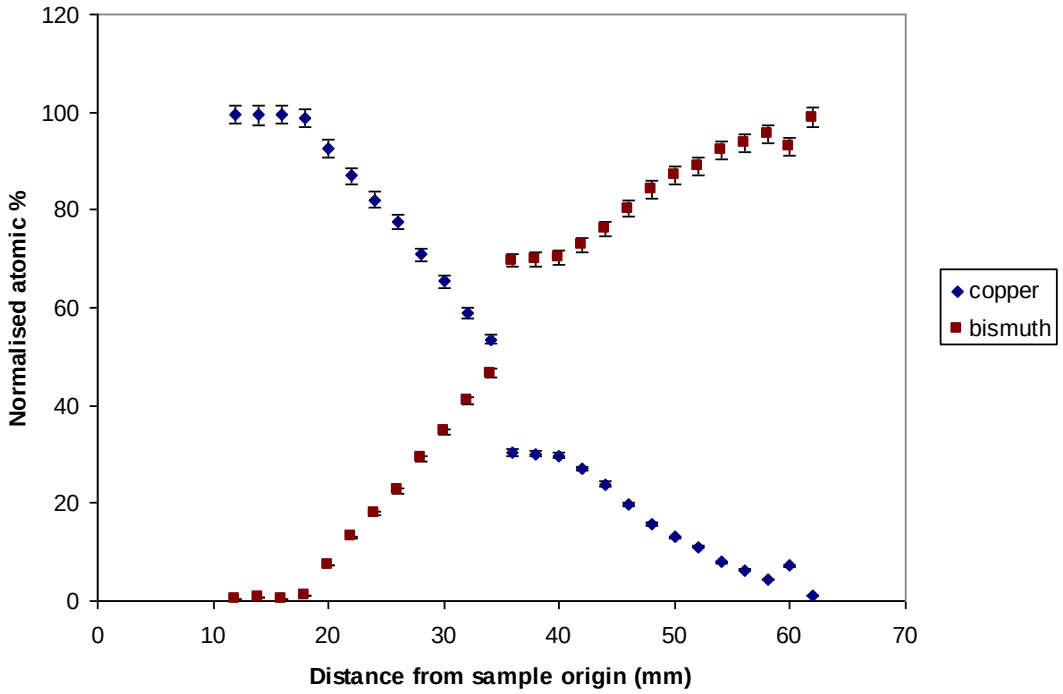

Figure 4.6. Electrochemically deposited Cu-Bi library. This is a heat treated sample and is homogeneous with respect to depth. The error bars represent the equivalent to one standard deviation.

The copper-bismuth library shown in figure 4.6 is the only electrodeposited binary arrangement where there was a significant discontinuity in the atomic ratio. Between 34 and 36 mm from the sample origin a 22% increase in bismuth concentration and the corresponding fall in copper concentration have been observed. As it is a precursor for CuBiS and CuBiSe production, this system has been fabricated multiple times by both electroplating and sputtering the discontinuity is seen in samples from both methods.

4.2.2 Electrostatic spray deposition libraries

The parameter optimisation for the electrostatically sprayed samples is more complex than that of the sputtering. The consequences of some of the parameter changes have been indicated using the production of copper and zinc continuous compositional spread libraries. The difference between co-deposition and sequential deposition is covered and the result of needle shape is also listed. These were carried out in addition to the exact positioning of the needles relative to each other and the substrate being recorded. The consequences of the geometry require optimisation as this is expected to be comparable to the source position effects seen in magnetron sputtering.

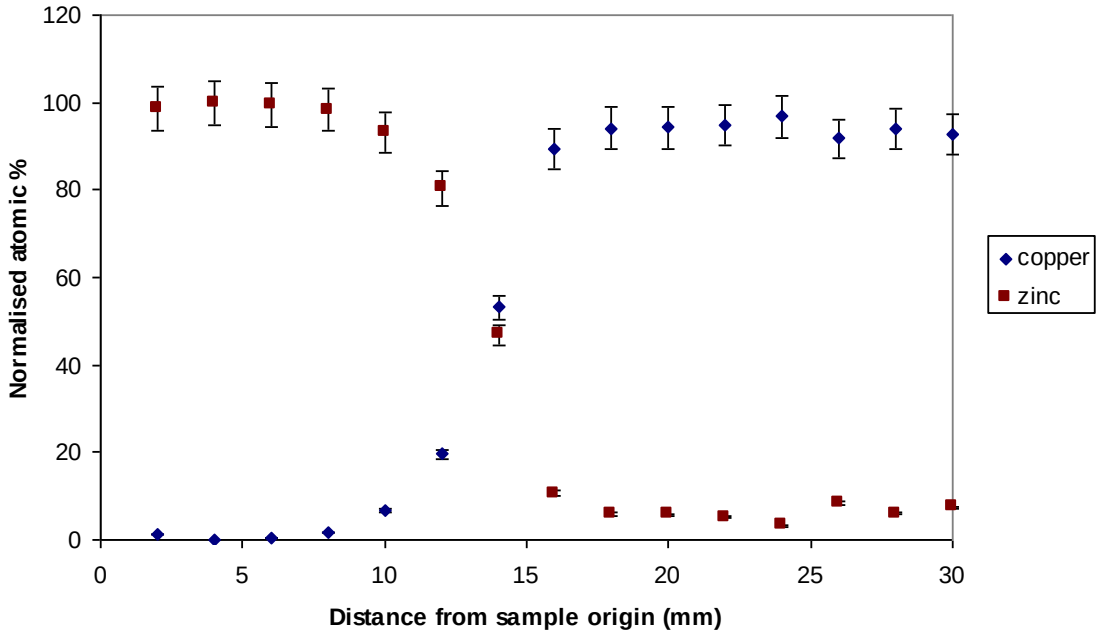

Figure 4.7. Copper and zinc concentration versus position on the sample for deposition conditions ES-CuZn-A. The error bars represent the equivalent to one standard deviation.

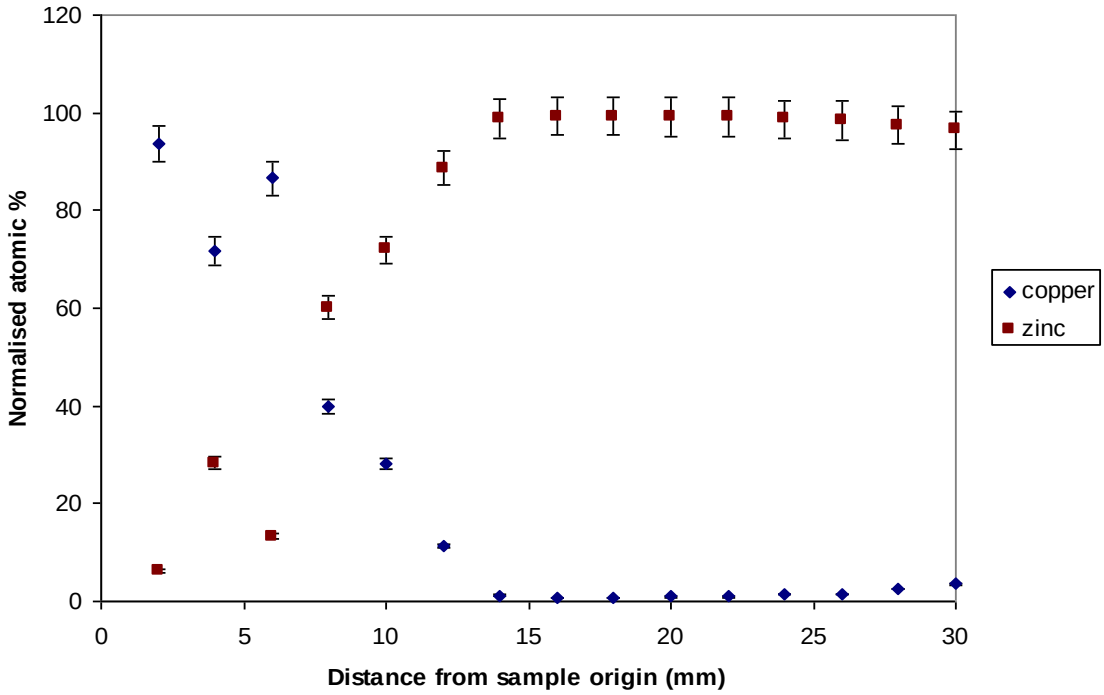

Figure 4.8. Copper and zinc atomic percentages with position for the ES-CuZn-B deposition conditions. The error bars represent the equivalent to one standard deviation.

The EDS results displayed in figures 4.7 and 4.8 are from samples deposited with the same geometry and the same solutions. The difference between them is caused by the changes from sequential to simultaneous depositions. The sequential depositions give the profile that was expected from the individual depositions but the simultaneous depositions give a lower concentration of copper. The area of copper coverage is also smaller and less even, in terms of consistency of layer thickness. While this could have been down to interaction between the cones of charged particles, other results point instead to substrate adhesion with the copper depositing better in the presence of zinc.

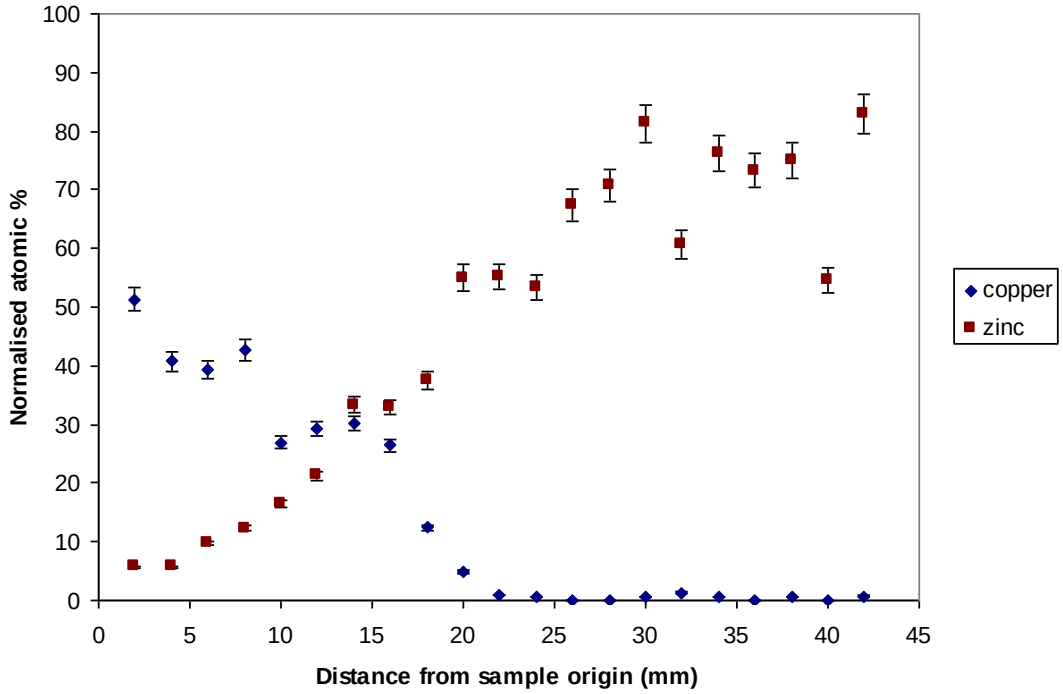

Figure 4.9. Copper and zinc atomic percentage with position for the ES-CuZn-C deposition conditions. The error bars represent the equivalent to one standard deviation.

Another parameter to be considered is the effect of needle shape. This is indicated by figure 4.9, the shape is known to influence the rate of deposition at different points. Ksapabutr et al [81] discussed the types of cone that could be expected and their resulting deposition profile, the results broadly agree with these conclusions as far as the whole profile goes. The ground needles give a toroid shaped profile hence giving a double peak while the sharp needle gives a more Gaussian distribution. This effect is observed only on the large scale. In the ≈ 20-50 mm range that is of interest here these large scale effects are not apparent. The pointed needles experimental setup is problematic as if the alignment of the needles is incorrect by even a small amount the effect can be seen in the samples and for this reason ground needles may be preferred.

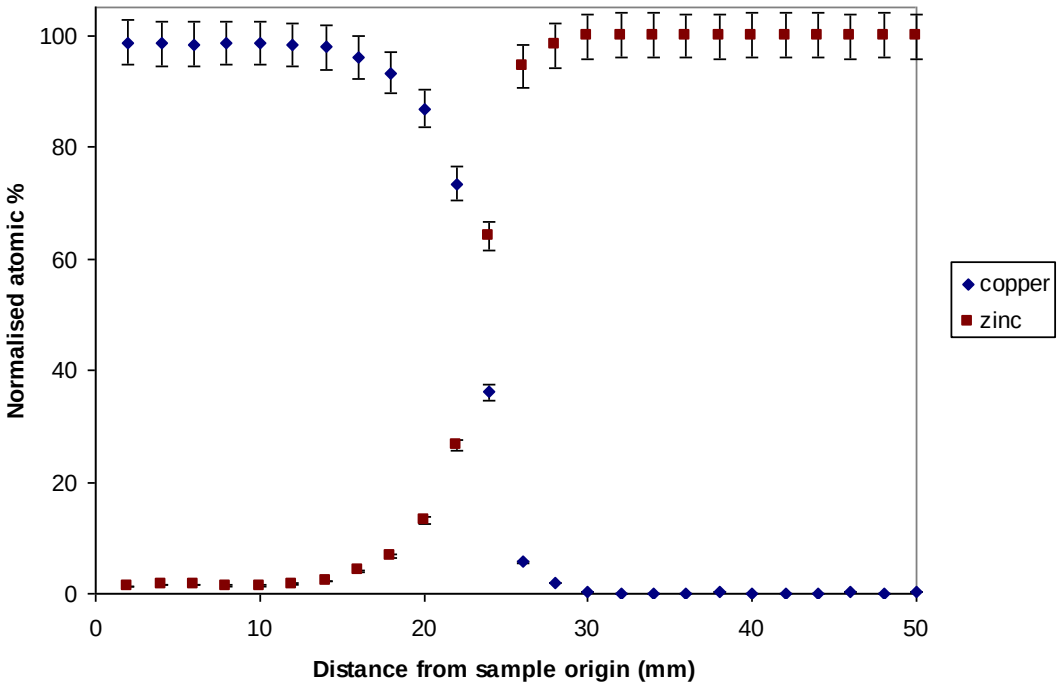

Figure 4.10. Copper and zinc atomic percentages with position for the deposition conditions ES-CuZn-D. The error bars represents the equivalent to one standard deviation.

The one difference that is apparent is the way in that the pointed needles generally give a more rapid transition between one material and another. This can be seen when comparing figures 4.8 and 4.10. This is due to the more markedly directional spray cone that forms under this setup. It is difficult to judge whether this rapid transition from one material to another is positive without knowing the end use of the samples. Generally a slower compositional change with distance would be preferred as more small changes can be identified. In the case of the extended beam illumination a simpler faster change could be beneficial so a compromise is desirable.

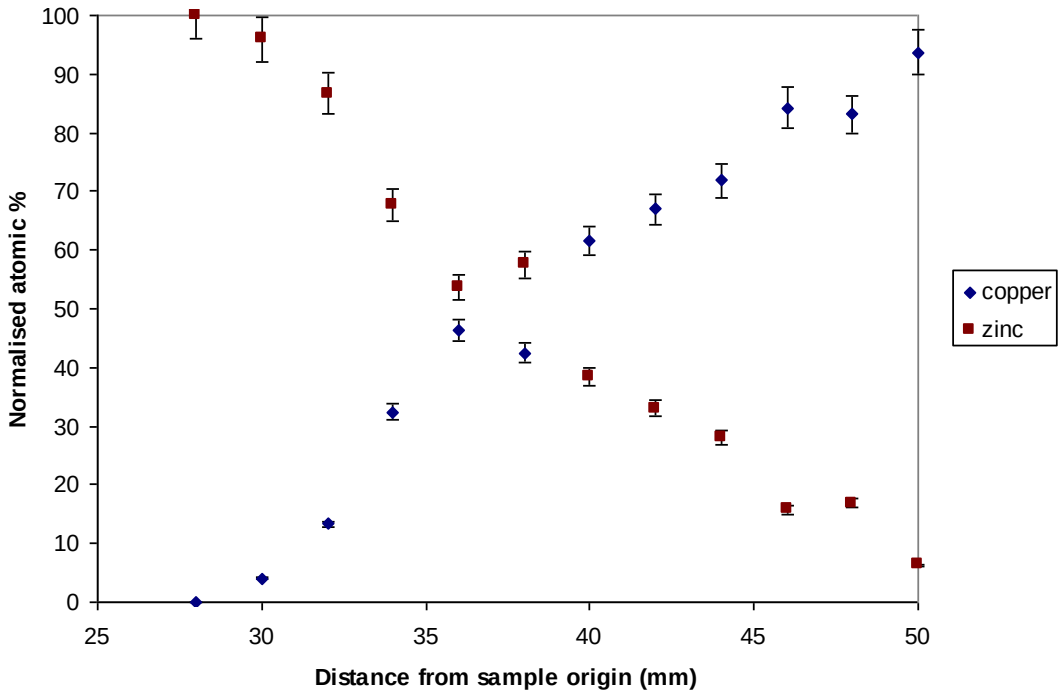

Figure 4.11. Copper and zinc atomic percentage with position for the deposition conditions ES-CuZn-E. The error bars represents the equivalent to one standard deviation.

Here in figures 4.10 and 4.11 it has been shown that if the distance between the source and the sample is increased the gradient of the changing composition is reduced. This can be explained partially by geometric effects as the spread increases with increasing source to substrate distance. In the case of the 40 mm the distance of change between 95 and 5 percent takes ≈ 20 mm while in the case of the 60 mm source to substrate distance this takes only slightly more ≈ 25 mm.

$$\tan^{-1}\frac{20}{40} = 26.6° \quad \text{and} \quad \tan^{-1}\frac{25}{60} = 22.3°$$

The equations show that the angle expected to deposit 5 % of the maximum is not consistent. The difference between the expected and the observed could be explained by the greater electrostatic interactions between the two cones in situations where the flight paths are longer.

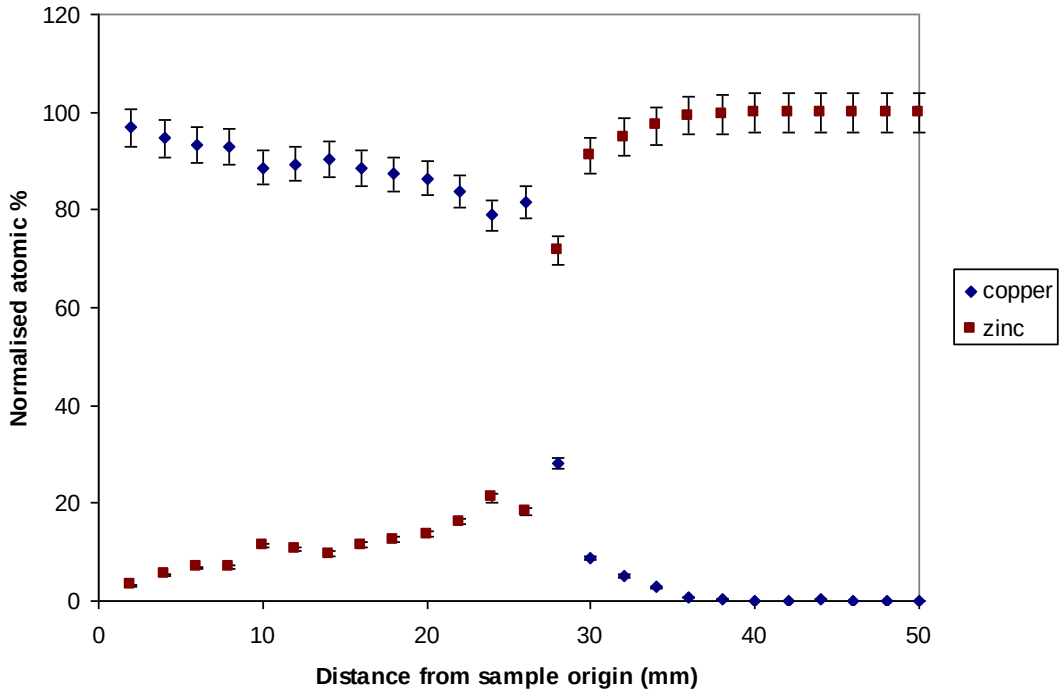

Figure 4.12. EDS calculation of the elemental composition of the ZnCu graded sample (2569) with respect to position on the substrate. The error bars represent the equivalent to one standard deviation.

The example shown in figure 4.12 was deposited onto Pilkington Tec 15 tin oxide coated glass. The tin oxide has been shown to allow the formation of a consistent layer in terms of both thickness and morphology for a range on films. The Tec 15 layer also allows good adhesion of electro sprayed films. The ZnCu was chosen as an example of a rapidly changing composition.

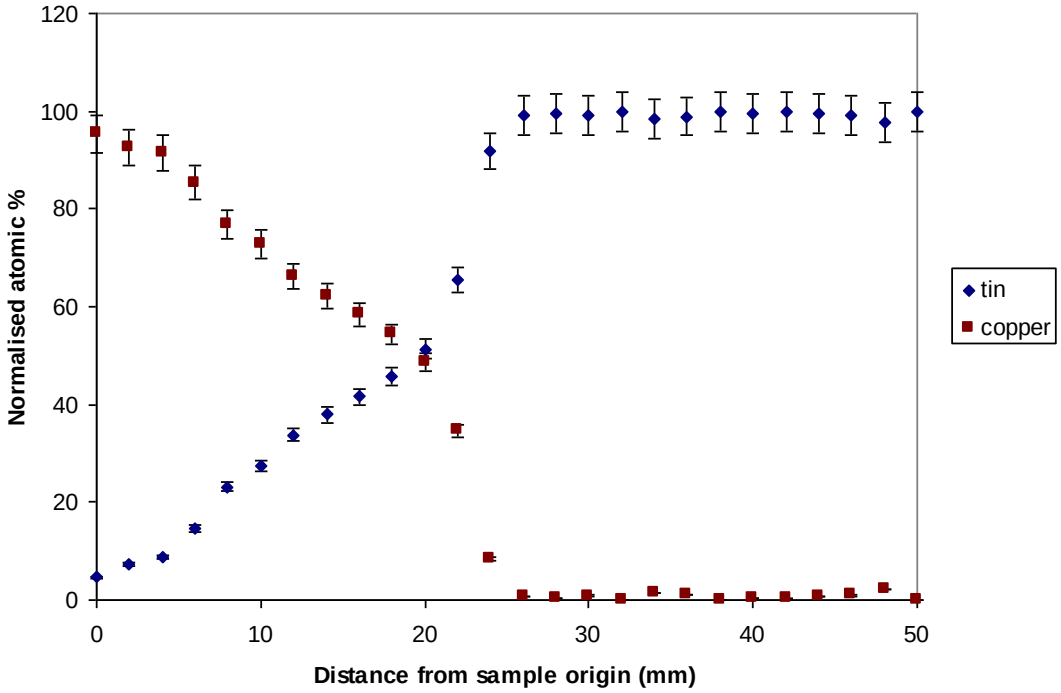

Figure 4.13. EDS calculation of the elemental composition of the SnCu graded sample (191009) with respect to position on the substrate. The error bars represent the equivalent to one standard deviation.

The tin-copper system has been made with a slower gradient. This has been given a larger physical distance in which any alloy phases will be present and available for detection. The 0 – 20 mm positions in figure 4.13 illustrate the successful employment of a milder gradient.

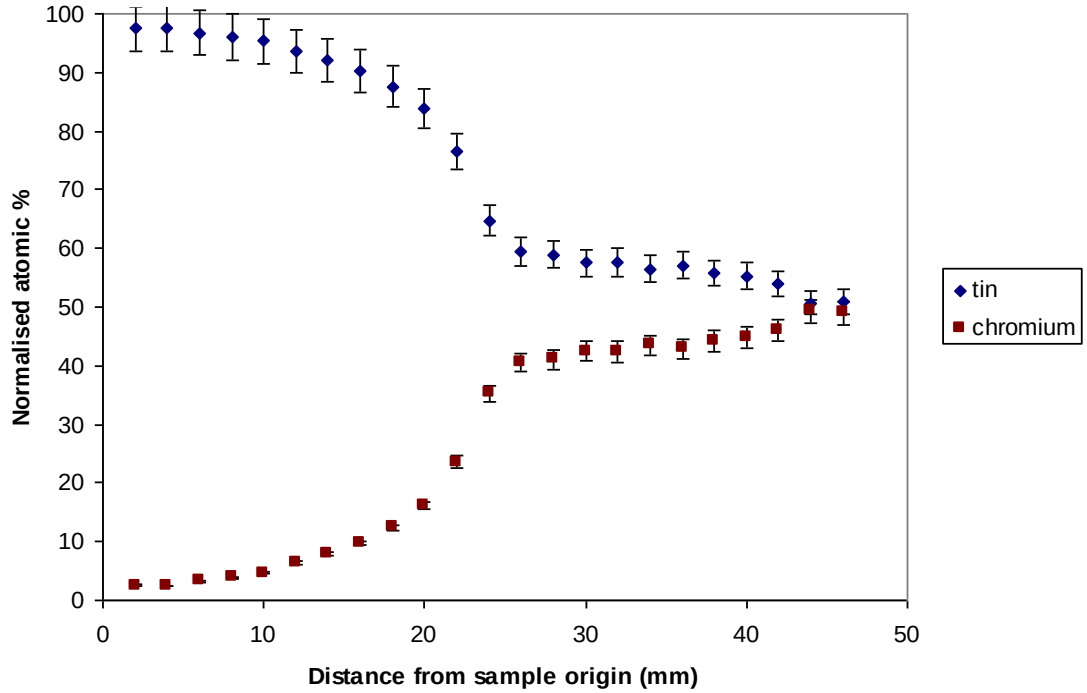

Figure 4.14. EDS calculation of the elemental composition of the SnCr graded sample (251009) with respect to position on the substrate. The error bars represent the equivalent to one standard deviation.

As shown in figure 4.14 a smaller range of elemental compositions has been chosen for the tin-chromium library. As the materials are largely immiscible, no binary compounds are therefore expected [138]. The elemental compositional gradient have been examined by EDS and XRD has been used for a semi-quantitative determination of the elements by establishing signal intensity ratios.

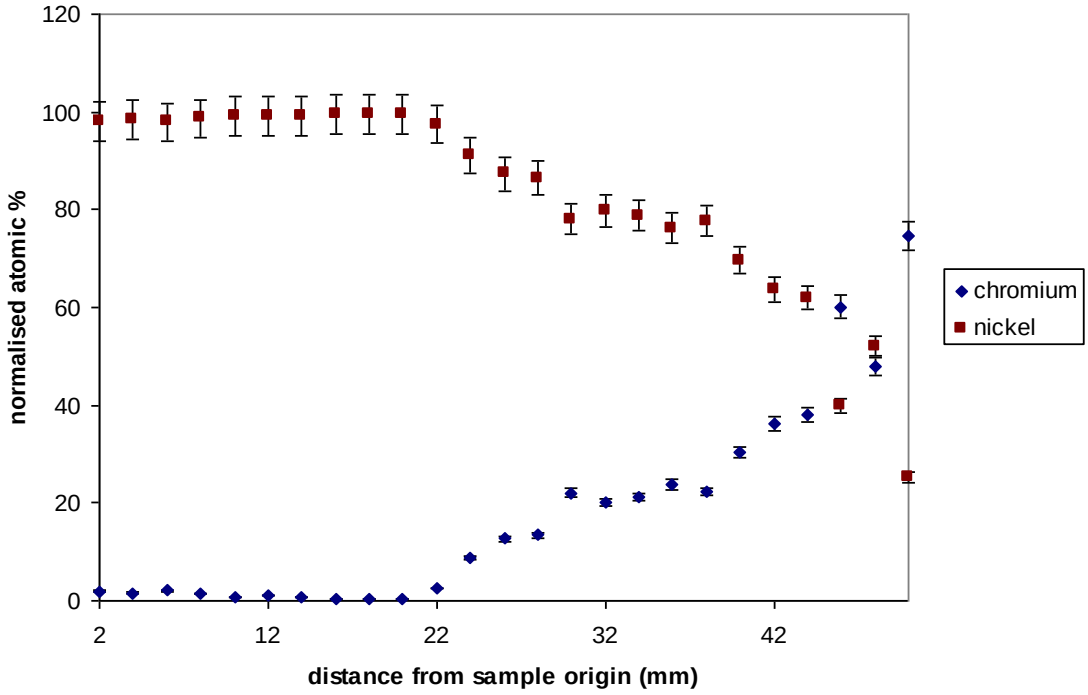

Figure 4.15. EDS calculation of the elemental composition of the CrNi graded sample (1769) with respect to position on the substrate. The error bars represent the equivalent to one standard deviation.

The nickel-chromium system has been chosen as an example where the ratio of the elements changed only slowly with movement across the sample. As seen in figure 4.15, the percentage of the nickel decreases from 92 % to 62 % over 20 mm where the change in compositional ratio is linear.

4.2.3 EDS results for sputter deposition

For the sputtered libraries, the copper-aluminium system was produced with a unique geometry but the other sputtered systems have been made to conform to a standard pattern. The differences in the thickness profile of the sputtered components are a function of the positioning of the virtual grid relative to this standard pattern. Other factors that will affect

the compositions are the individual sputtering efficiencies of the elements. Effects caused by differences in the shape surface finish of the elemental targets have been reduced to the point where they are not apparent.

Binary sputtered systems

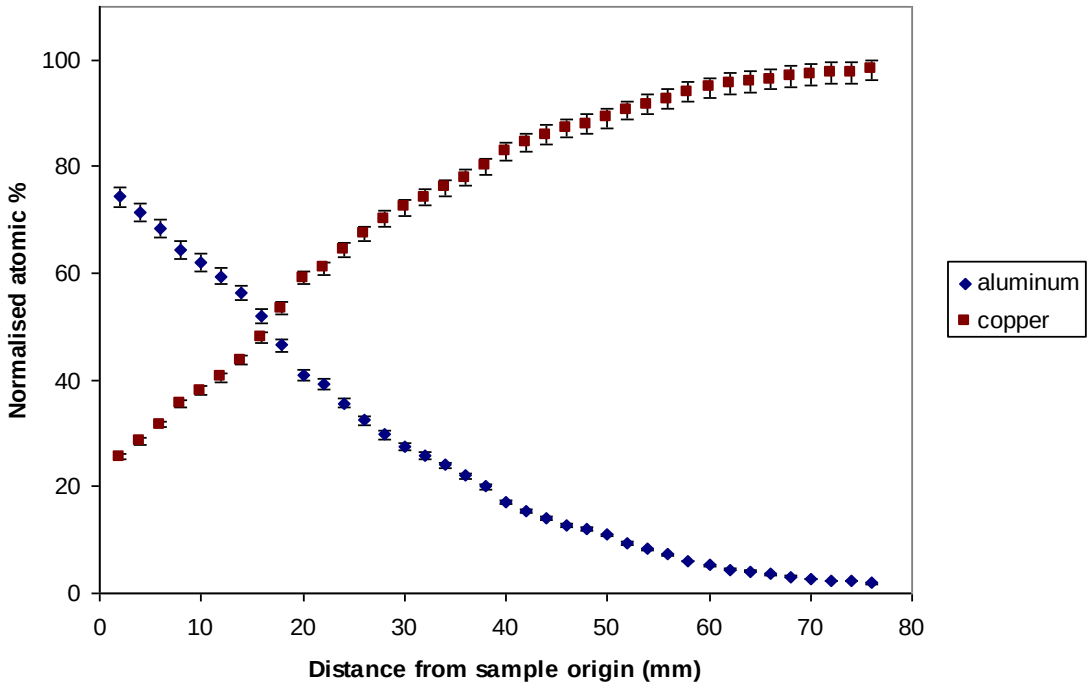

Figure 4.16. EDS quantitative elemental compositions for the sputtered AlCu binary system. The error bars represent the equivalent to one standard deviation.

The non-linear ratio change between the elements is evident in the aluminium-copper library, figure 4.16. This is produced by the characteristic deposition sputtering profiles where flat elemental targets are used. A substrate close to the magnetron will be deposited with a film that has a thickness profile that is broadly flat topped with an expediential decay in thickness.

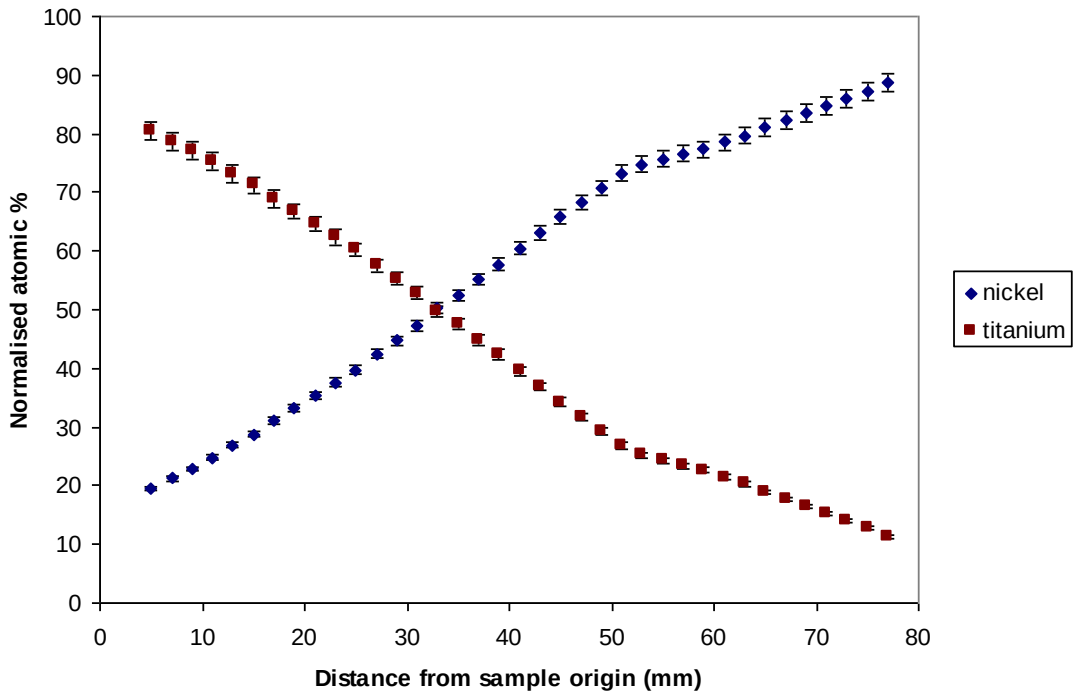

Figure 4.17. EDS quantitative elemental compositions for the sputtered NiTi binary system. The error bars represent the equivalent to one standard deviation.

The elemental compositions of the nickel-titanium binary sputtered libraries shown in figure 4.17 have a more linear gradient as the data collection is carried out away from the direct focus of the planer magnetrons. The part of the library between 5-51 mm from the sample origin is particularly useful due to this linear distribution R^2 = 0.997 for each line in this range. The total change in relative composition in this range is 2.38 %.

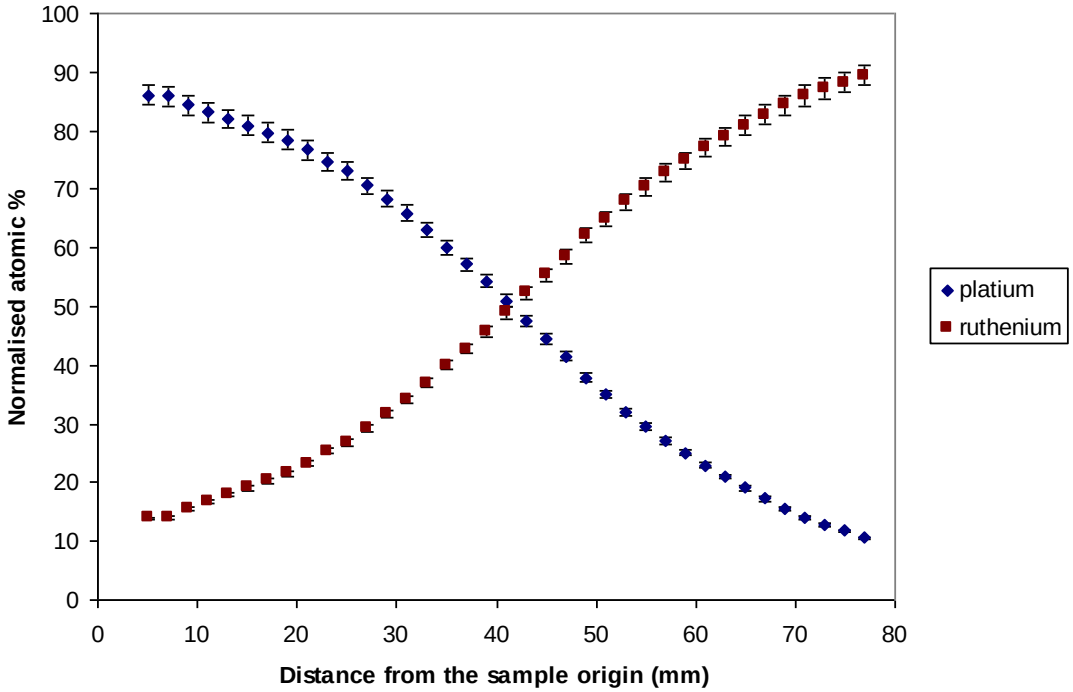

Figure 4.18. EDS quantitative elemental compositions for the sputtered RuPt binary system. This example is from the 135° sampling position. The error bars represent the equivalent to one standard deviation.

The platinum-ruthenium library was produced on a circular substrate and the EDS data was carried out from all four sample origins. The 135° sample origin start shown in figure 4.18 was chosen for data collection by the other analytical methods as it gave the largest compositional range of the four angles. The same logic was used for the choice of sample origin for the EDS collection from the lead-platinum library, results shown in figure 4.19. This sample is the same as the Pt-Ru except that the geometry is inverted through an axis running along the 0° data collection line.

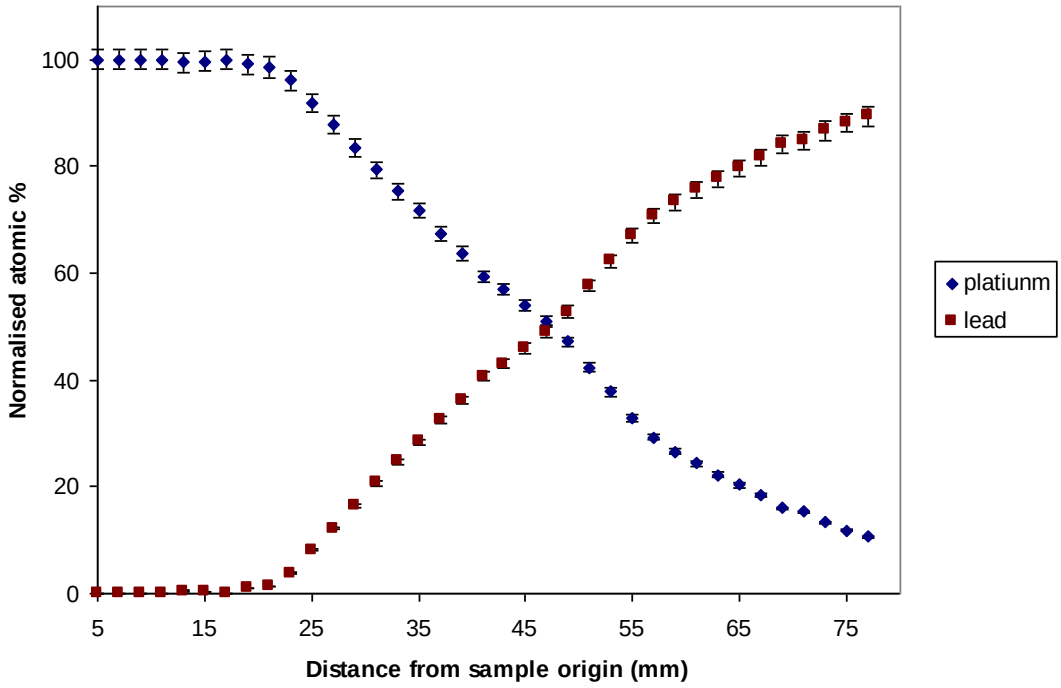

Figure 4.19. EDS quantitative elemental compositions for the sputtered PtPb binary system. The error bars represent the equivalent to one standard deviation.

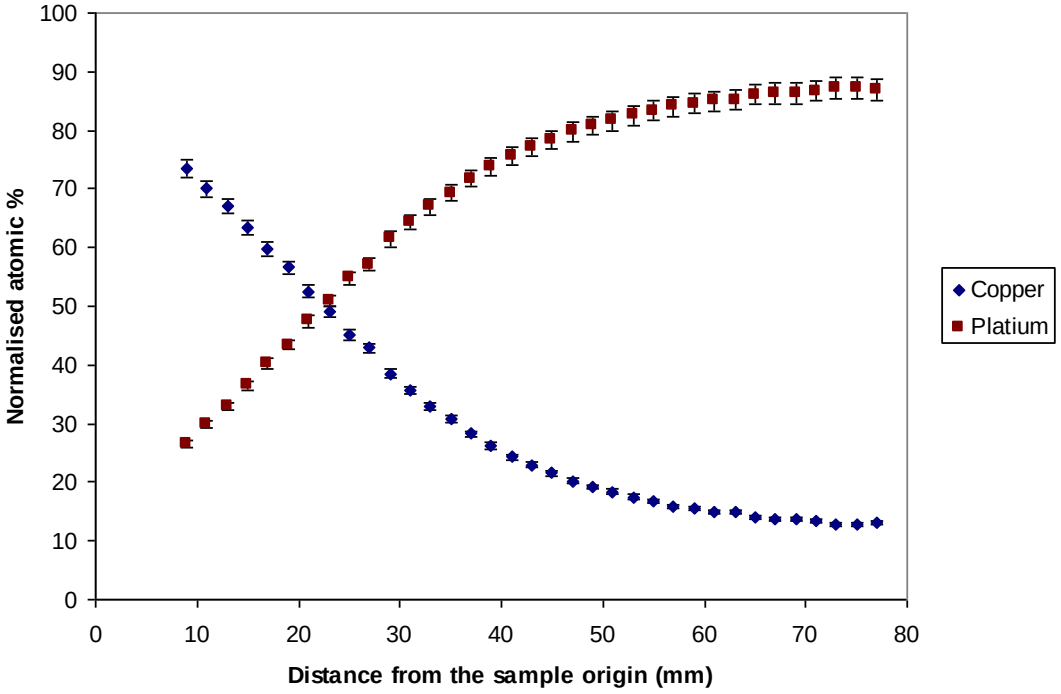

Figure 4.20. EDS quantitative elemental compositions for the sputtered CuPt binary system. The error bars represent the equivalent to one standard deviation.

The results of the EDS analysis of the copper-platinum are shown in figure 4.20. The geometry of this system is different to the other examples as the source directly above the

substrate is used for the deposition of the platinum. This source choice explains the low compositional gradient in the 41-77 mm part of the library.

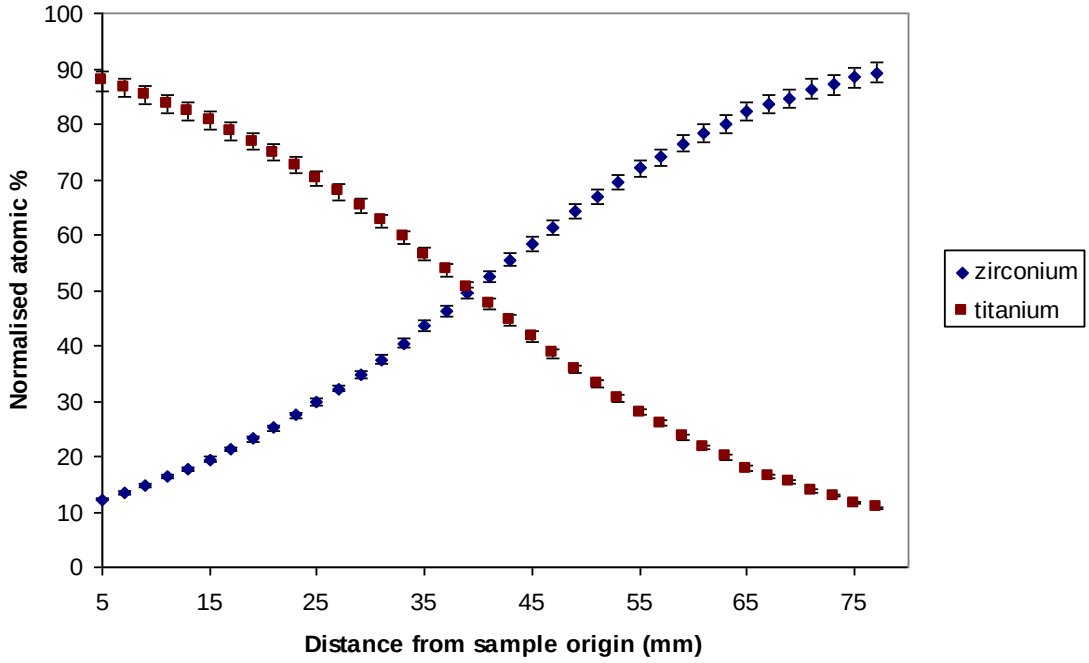

Figure 4.21. EDS quantitative elemental compositions for the sputtered ZiTi binary system. The error bars represent the equivalent to one standard deviation.

The EDS elemental analysis of the zirconium-titanium system identified in figure 4.21 shows a large compositional swing, with an average gradient of 2.11 % mm^{-1} over the whole substrate. This was achieved using the A and C magnetron source positions and a data collection at 90° from the sample origin.

Ternary sputtered samples

For the ternary samples, simple composition graphs do not well describe the elemental composition of the samples. One way that this information can be displayed is by the use of false colour information using red green blue (RGB) pigmentation to show the elements. The data points collected by EDS determination are represented in the top images of figures 4.22, 4.23 and 4.24. Extrapolation between the data collection points means that a colour map representative of the whole surface of the substrate can be produced; this is shown in the bottom image of 4.22, 4.23 and 4.24. Gremaud et al [139] among others have used false colour representation of elemental composition, with Takeuchi et al also using a variation on this theme [109]. For the BiCuSb sputtered library the individual elements have been assigned colour Bi = green, Cu = red, Sb = blue.

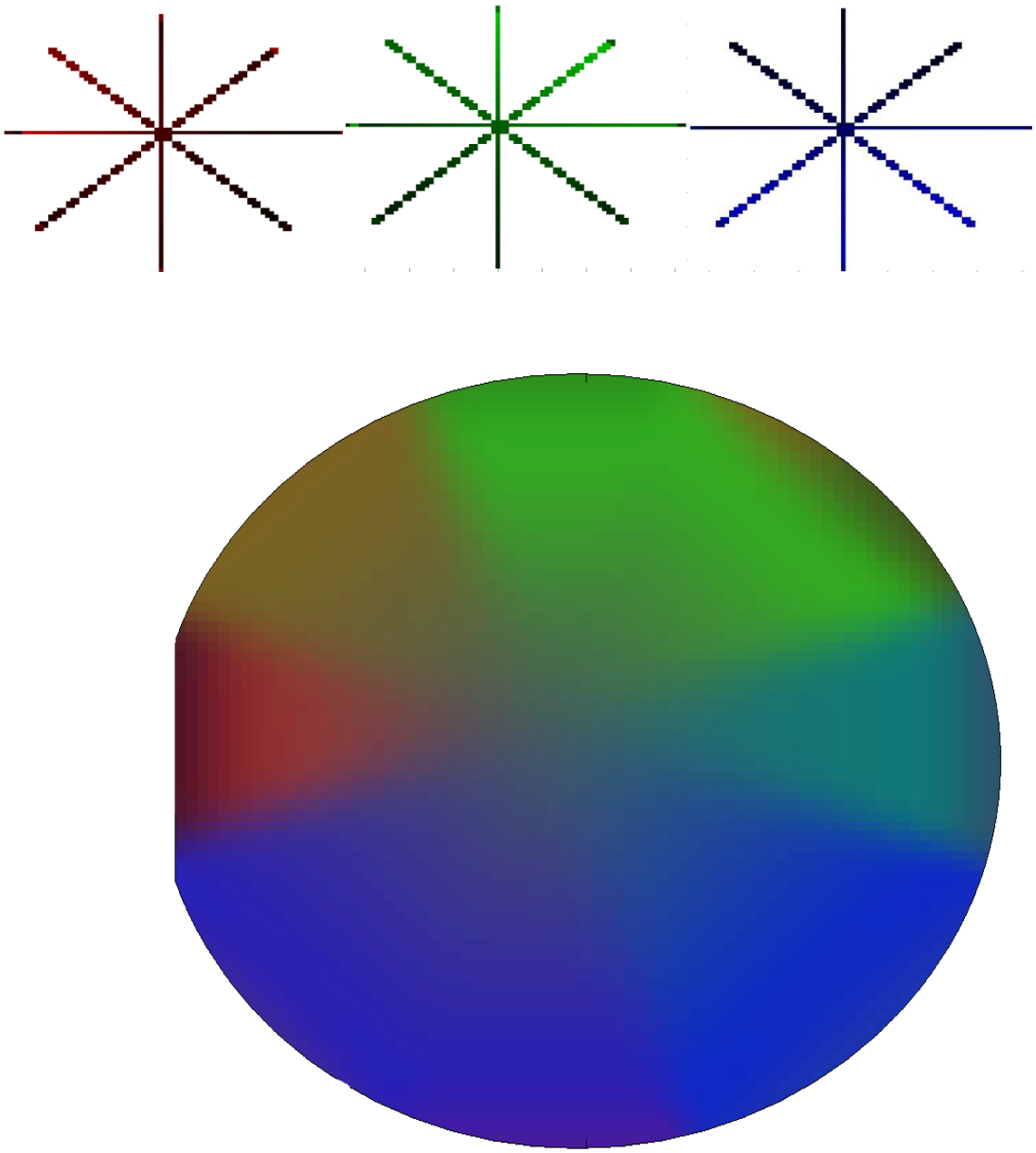

Figure 4.22. The BiCuSb elemental compositions are shown as colour intensities (above) and are then combined and interpolated to represent the full surface of the substrate as a RGB colour map (below).

For the RhPtSn sputtered library the individual elements have been assigned the individual colours Sn = blue, Pt = red, Rh = green

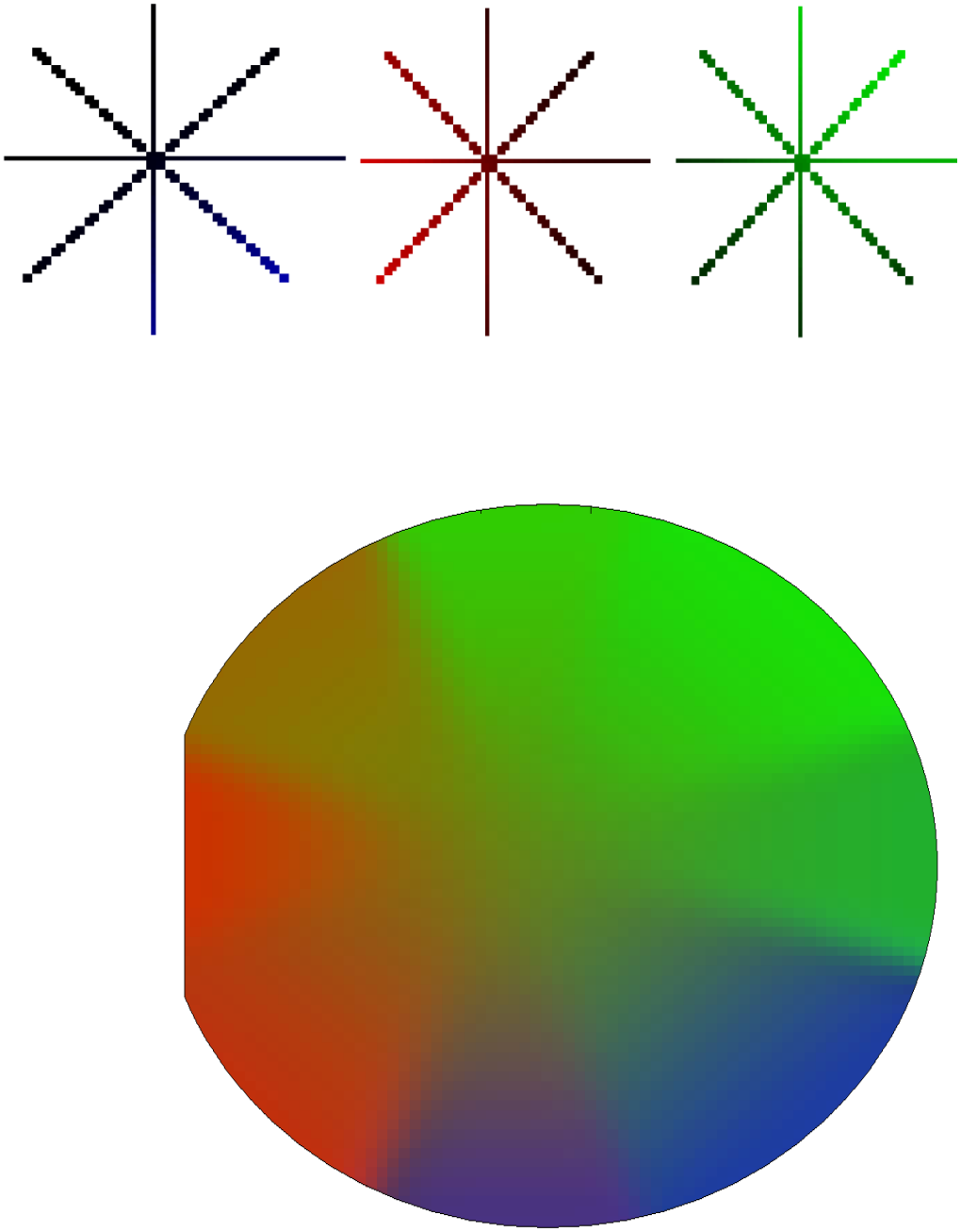

Figure 4.23. The RhPtSn elemental compositions are shown as colour intensities (above) and are then combined and interpolated to represent the full surface of the substrate as a RGB colour map (below).

For the RuPtPb sputtered library the individual elements have been assigned the colours Pb = blue Pt = green Ru = red.

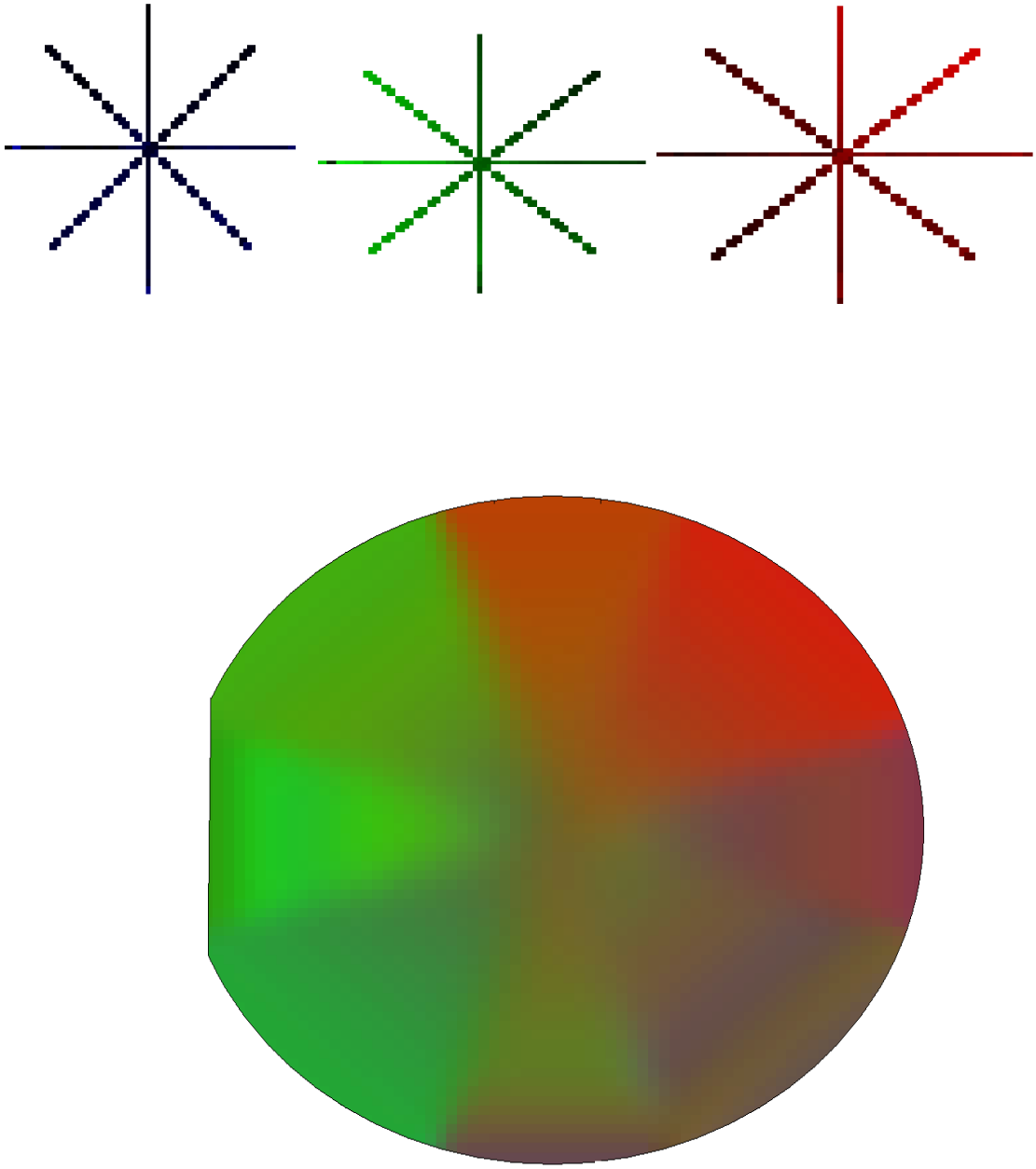

Figure 4.24. The RuPtPb elemental compositions are shown as colour intensities (above) and are then combined and interpolated to represent the full surface of the substrate as a RGB colour map (below).

The way that these figures (4.22, 4.23 and 4.24) vary shows that angle is not the only factor contributing to the compositional spreads. The characteristics of the individual elemental targets affect both the rate and spread of that material. Target erosion patterns that are archetypal of the individual materials have significant consequences on sputtering patterns, as well as film quality [140].

4.2.4 Rutherford Backscattering spectrometry

Here is illustrated an example thicknesses calculation for two of the sputtered samples. As the modelling to calculate thickness requires simultaneous modelling of the composition this information is also provided and compared quantitatively with the judgment of elemental composition produced by EDS analysis.

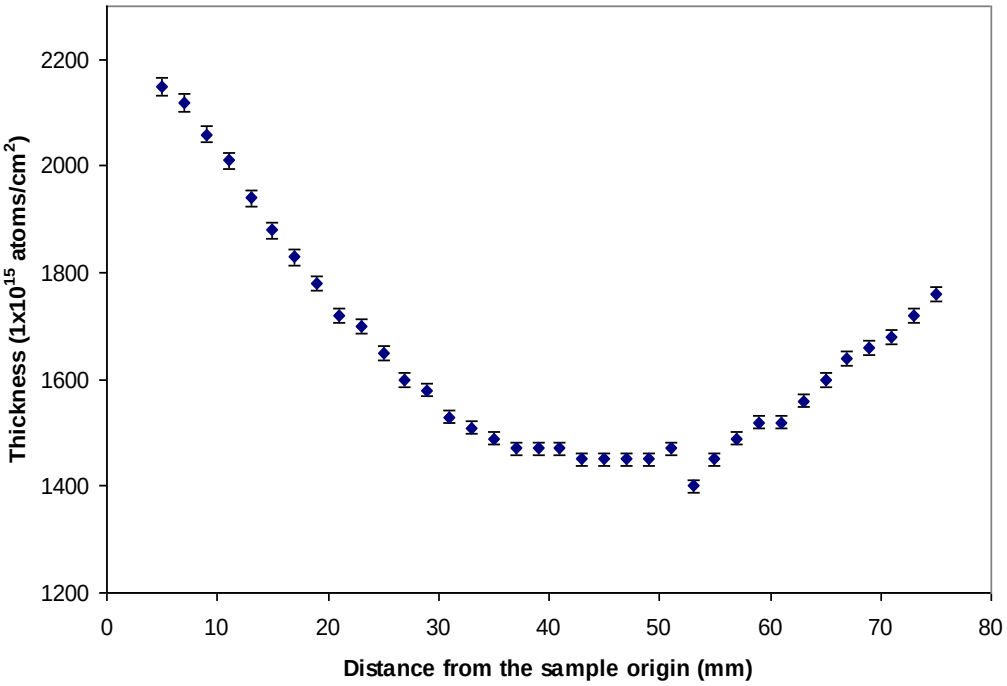

Figure 4.25. These are the thicknesses for the ZrTi. The Ti rich side is represented by the results on the left of the image.

The ZrTi is deposited with the A and C guns as the thickness measurement was taken from the 90° position and shown in figure 4.25. Thus as the measurements moved from the focus point of one of the sources towards the other the shape of the thickness profile is the characteristic the parabolic bowl which is a product of the two overlaid Gaussian distributions with centre points approximately 100 mm apart. The RuPt thickness measurements revealed in figure 4.26 are an example of different geometry, this sample was made with the A (Ru) and B (Pt) guns. The collection at the polar co-ordinate 135° starts at the Ru focus point but does not go through the Pt maximum and this explains the asymmetrical profile.

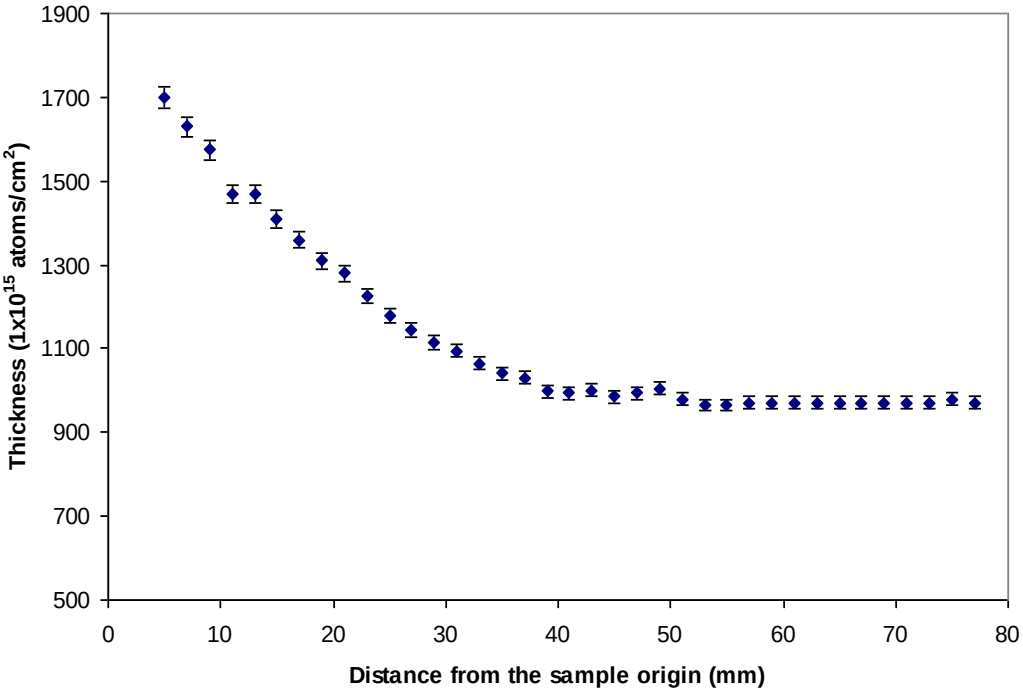

Figure 4.26. This graph shows the RuPt thicknesses across the substrate. The Ru rich side is represented by the results on the left of the image.

The figures are quoted from the Rutherford backscattering spectroscopy as calculated from the amount of channel numbers filled by the film of interest. These have not been converted into nm thicknesses as the exact densities of the alloys are not known.

To help visualise the films two example have been converted using

$$\frac{\frac{\rho}{N_A} * RAM}{D}$$

Where ρ is the thickness in atoms per cm^2, N_A is Avogadro's number, RAM is the relative atomic mass and D is the density.

If the first point on the TiZi library was assumed to have the density of elemental Ti the thickness would be

2200 atoms per cm^2 = 389 nm

If the first point on the RuPt library was assumed to have the density of elemental Ru the thickness would be

1700 atoms per cm^2 = 231 nm.

For the electrodeposited samples thickness information was more difficult to calculate. The RBS analysis using protons as the ion beam gave an indication of thickness but due to the substantial, irregular surface roughness and the likelihood of porous regions the density of the materials and therefore the thickness could not be estimated.

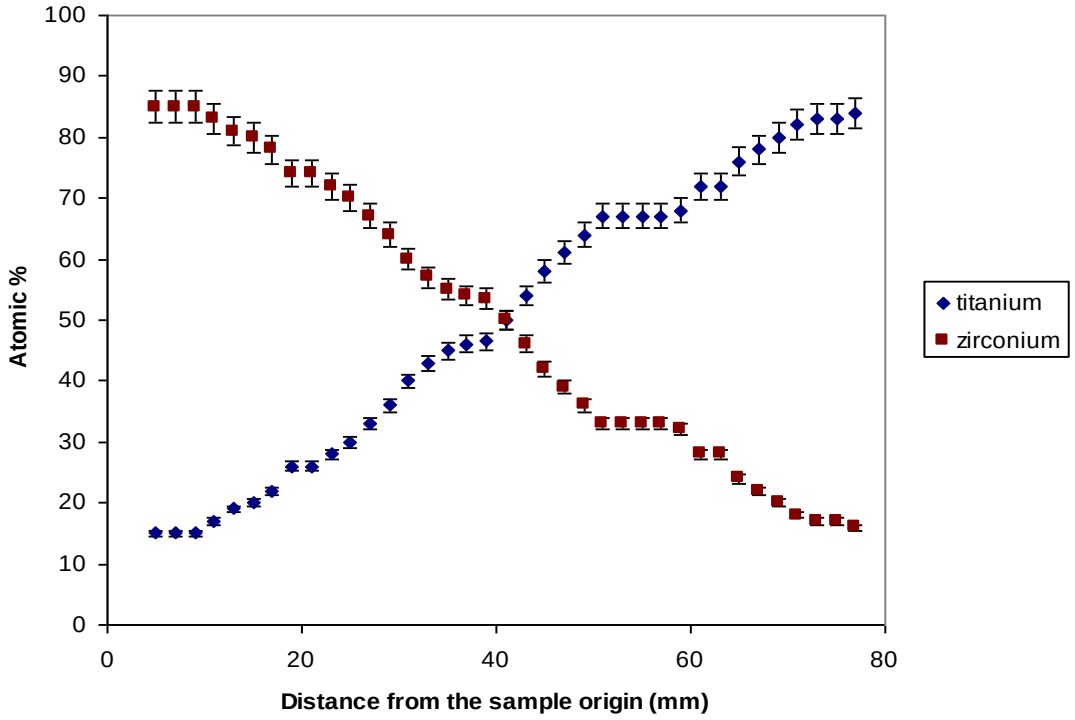

Figure 4.27. Composition of the titanium zirconium library as measured by Rutherford backscattering spectroscopy.

The compositions of the samples at different points in the library as determined by RBS are shown in figure 4.27 for the Ti-Zi system and figure 4.28 for Ru-Pt. For the most productive use of the two methods EDS and RBS it is important to show that the elemental compositional results that come from both methods do not contain statistically significant differences.

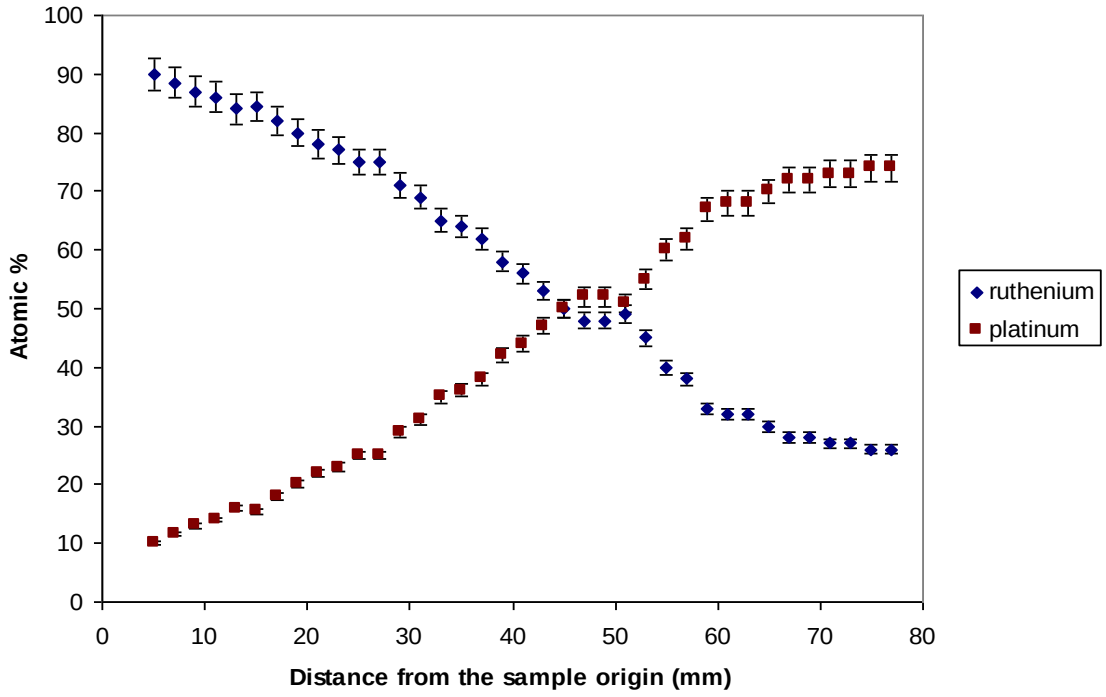

Figure 4.28. Composition of the ruthenium platinum library as measured by Rutherford backscattering spectroscopy.

It is difficult to compare the RBS and the EDS directly especially in the cases where there is only one measurement. Indication of the commonality can be reached in the cases where multiple results have been collected for each point. This was done for two points on each of these systems. Both the EDS and RBS results have been shown to be normally distributed as explained in section 4.2.1. so it is now possible to perform a two tailed student t-test on the four data sets. In all cases they are not significantly different to 0.05, this is an indication of agreement.

4.3 Structural Analysis

4.3.1 X-Ray Diffraction

The following XRD images are displayed as whole libraries of the portions of the individual libraries that are of interest. A contour map combining all of the raster scanned diffraction profiles has been collated for straightforward comparison to the extended beam. A Matlab™ script has been produced to input the multiple 2θ versus intensity profile from the D8 radial integration of each raster point and produce an x, y, z matrix containing the same 2θ position on the sample. The conversion used Braggs' law to create this intensity information position

against d-spacing. As this is the same as the partitioning output it allows the data to be compared directly.

Electrodeposited libraries

Some of the chemical libraries are shown in their as deposited form (figures 4.30 and 4.34) and at stages in the heat treatment to show the effect on the diffusion and the alloy formation. Where applicable, the graphs also illustrate the initial alloy formation caused by the energy of the deposition process. Also the effect of the ongoing room temperature alloying that occurs in some systems is illustrated. In the cases where interesting phases are only present in the final system the preliminary stages are omitted.

Here in figure 4.29 is illustrated one third of the conventional diffractograms collected from the raster scanning of the as deposited copper-zinc library along with the same library displayed using the contour method, figure 4.30. In the contour plots, the data from all the raster points have been displayed so all the information collected is available to the reader. Displaying this number of conventional diffractograms in one plot is often unclear.

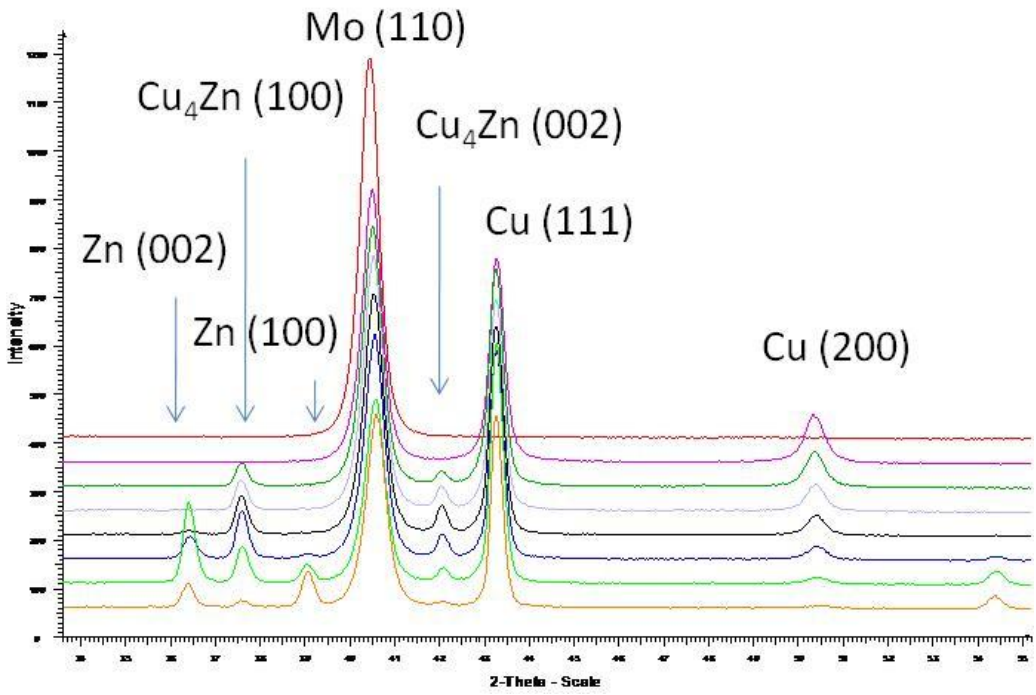

Figure 4.29. Compilation of the conventional raster collected diffractograms collected from the copper-zinc library. Every third diffractogram is shown starting from the first position at the top.

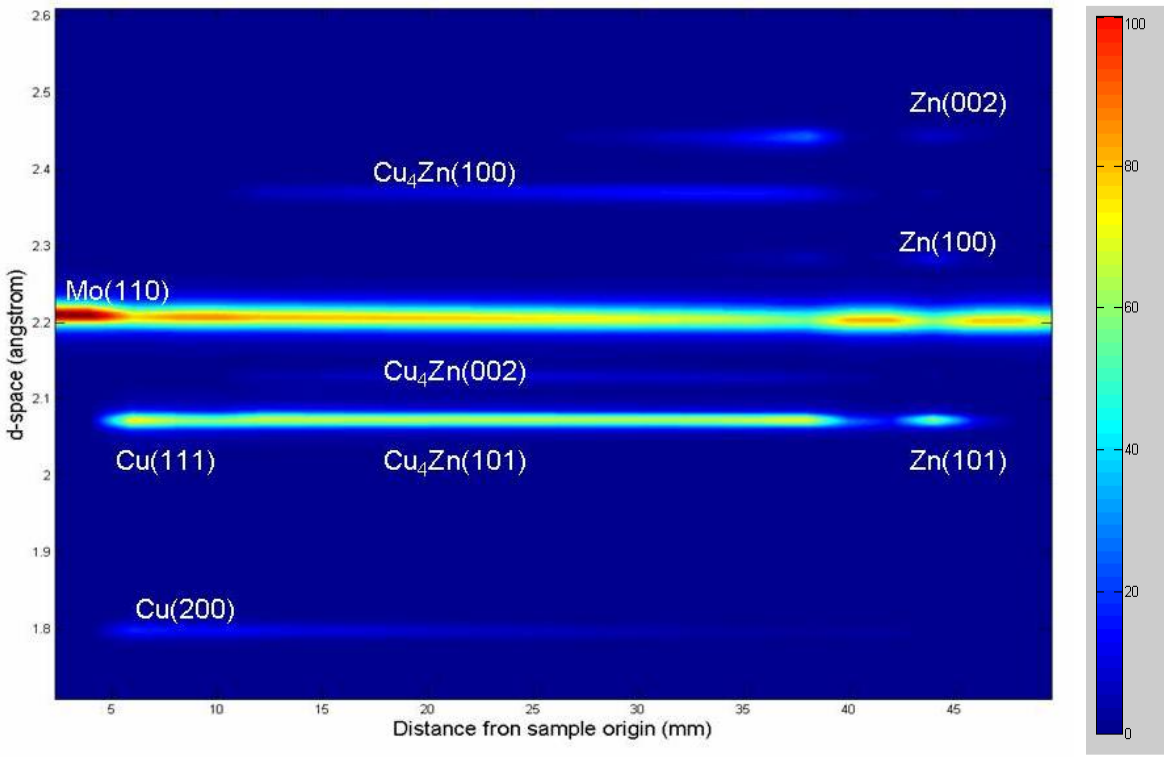

Figure 4.30. The CuZn binary layered system on a molybdenum substrate. This is an example of the diffraction patterns compilation achieved by raster scanning before heat treatment.

A diffraction pattern consistent with hexagonal Cu_4Zn has been detected over a large compositional range. This is present as well as the elemental signatures shown in figures 4.29 and 4.30. The combination of these separate diffraction signatures indicates that most of the material is still in the original layers. This is to be expected when considering the low energy deposition conditions. The use of Matlab© allows a large degree of freedom when producing a graphical representation of both the raster scan compilations and the extended beam partitioned data. For consistency area contours plots have been chosen is all cases. In this example (figure 4.30 legend) and in all other cases unless otherwise stated the colour key is proportional to the maximum intensity registered during that data collection.

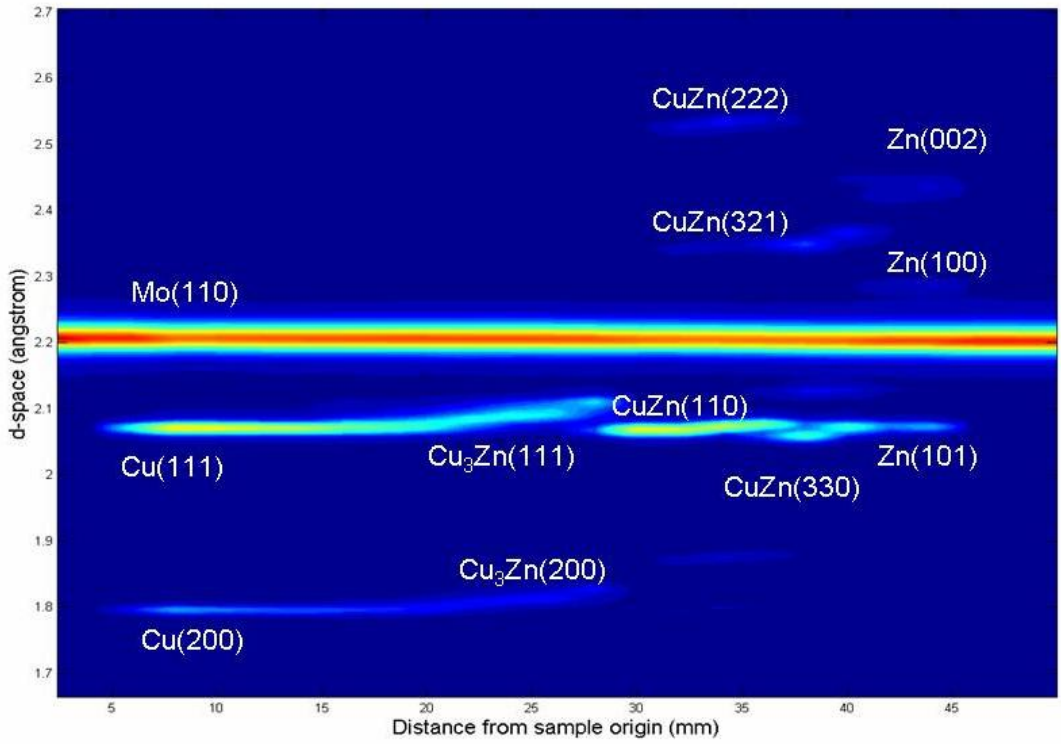

Figure 4.31. This XRD raster scan compilation image shows the electrodeposited CuZn on a molybdenum substrate after heat treatment.

When heat-treated and cooled quickly from 500°C a multiphase section of the diagram common to the literature is formed. Comparison of the results shown in figure 4.31 with the literature yields phase identification. Compositions quoted by Spencer [141] give these main phases as β and γ with CuZn having a ratio showing a mix of these. The d-spacing seen in the Cu_3Zn implies that it is in the transition between α and β phases. From the EDS, it can be confirmed that the atomic ratio of zinc never exceeds 80 % hence the ε is not expected.

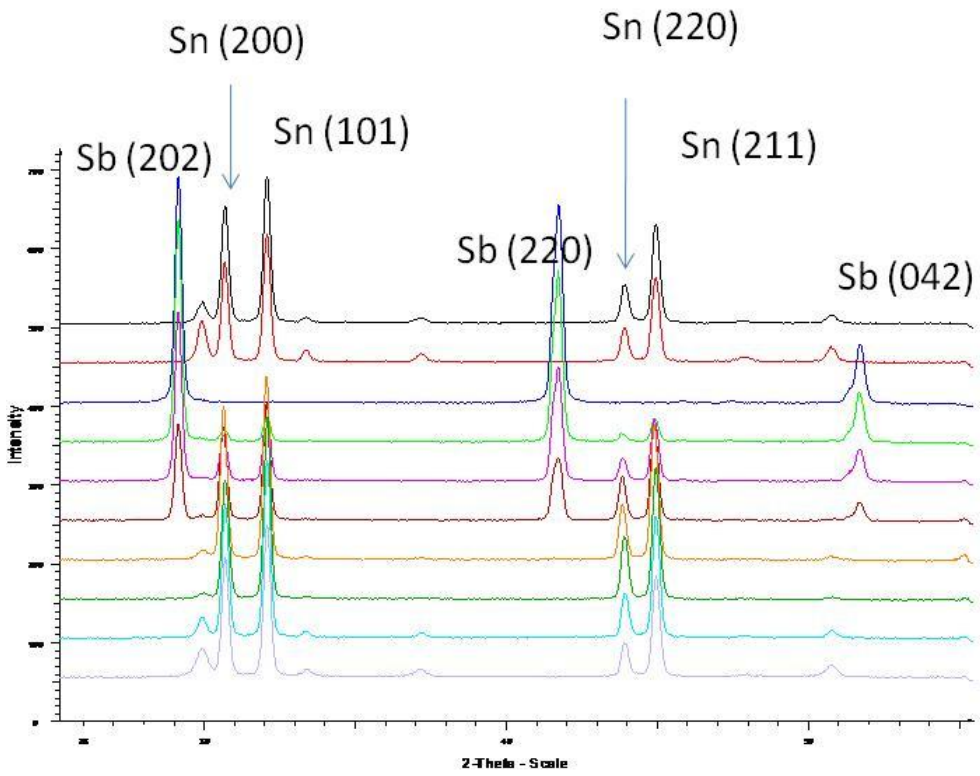

Figure 4.32. Compilation of the conventional diffractograms collected from the antimony-tin library. Every fourth diffractogram is shown starting from the first position at the top.

The conventional diffractograms for the raster scans of the antimony-tin library compiled for figure 4.32 show the presence of antimony as the major component in the 15-45 mm section of the library with tin dominating the other positions. The contour plot, figure 4.33, contains the same information. In the contour plots, the relative intensities are less clear but the positions of the peak in terms of position on the substrate is more easily apparent. Both methods indicate the 2θ/d-spacing values precisely.

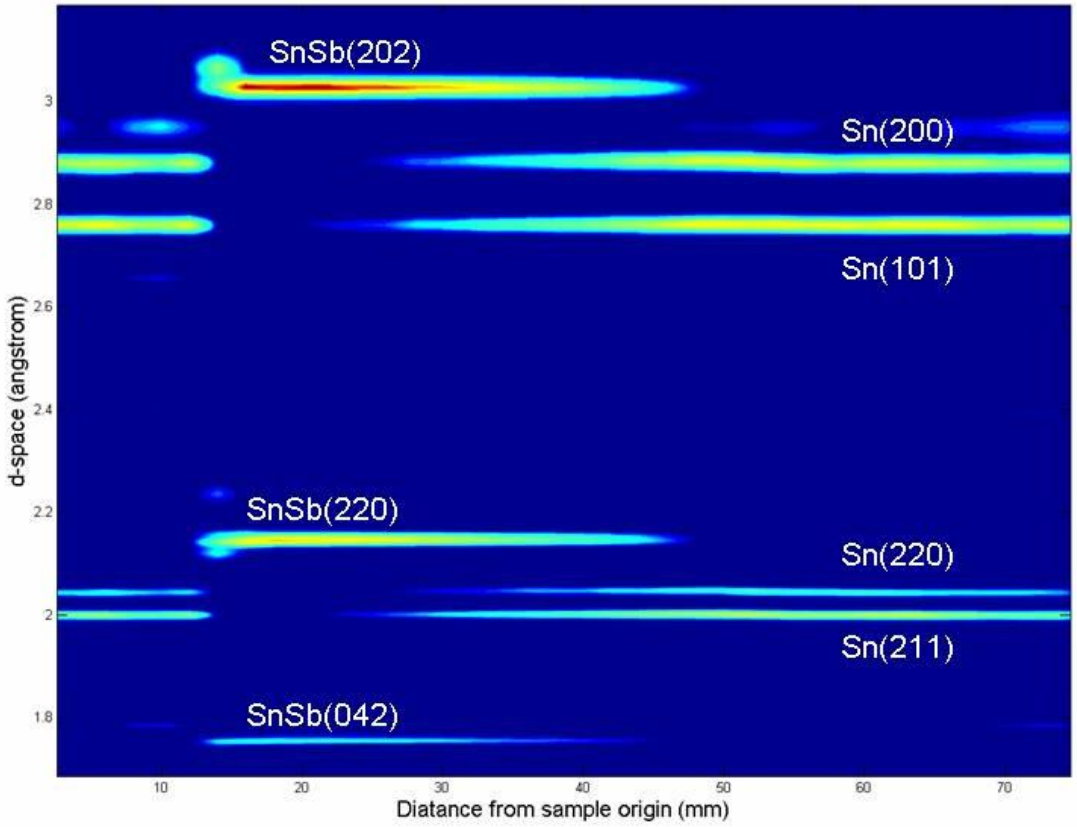

Figure 4.33. The XRD raster scan compilation of the SnSb sample after layer electrodeposition and heat treatment.

The lack of elemental antimony and the formation of the SnSb phase shown by the XRD results in figure 4.33 indicates an excess of tin over most of the library and this is in agreement with the EDS results that calculate the Sb atomic ratio to exceed 40 % for < 6 mm of the substrate. The SnSb is identified as the face centred cubic β-phase from the binary phase diagram. [142] The Miller index identifications are taken from the search match card 1-830.

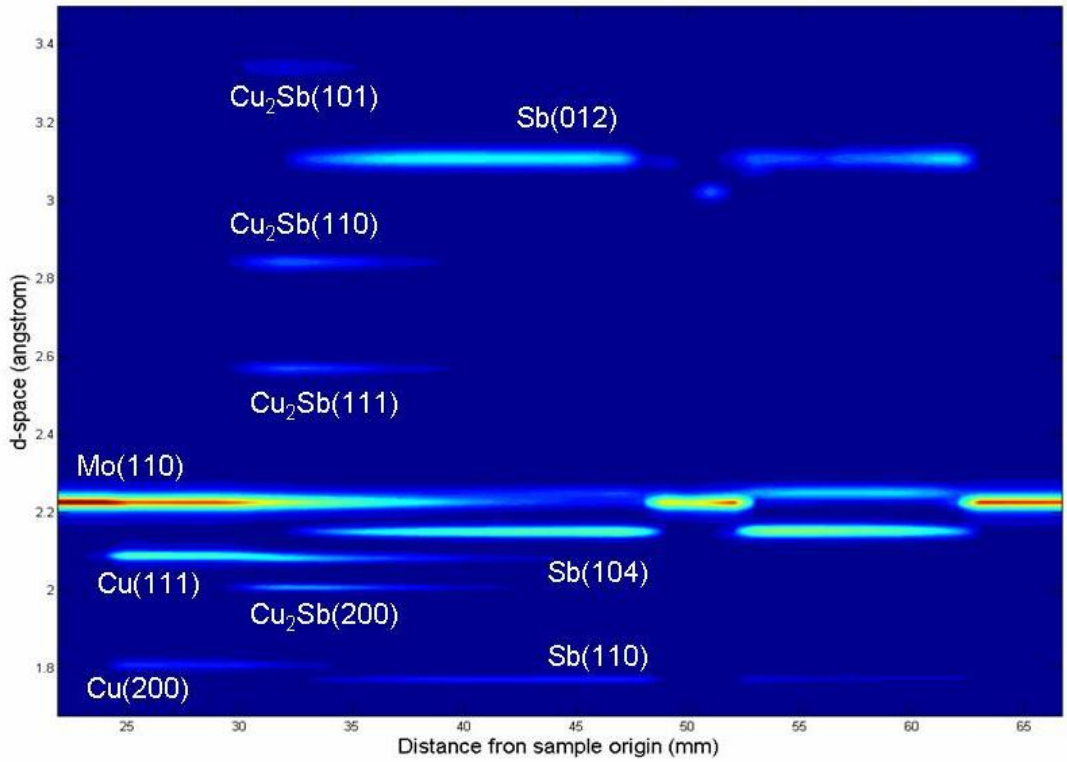

Figure 4.34. The XRD raster scan compilation of the CuSb sample electrodeposited in layers. This is as deposited.

The XRD raster scan contour plot, figure 4.34, indicated that, even in the room temperature deposition conditions of the electrolytic bath Cu_2Sb forms readily. This is persistent after heating. Figures 4.35 and 4.36 show that the major addition in these conditions is $Cu_{11}Sb_3$.

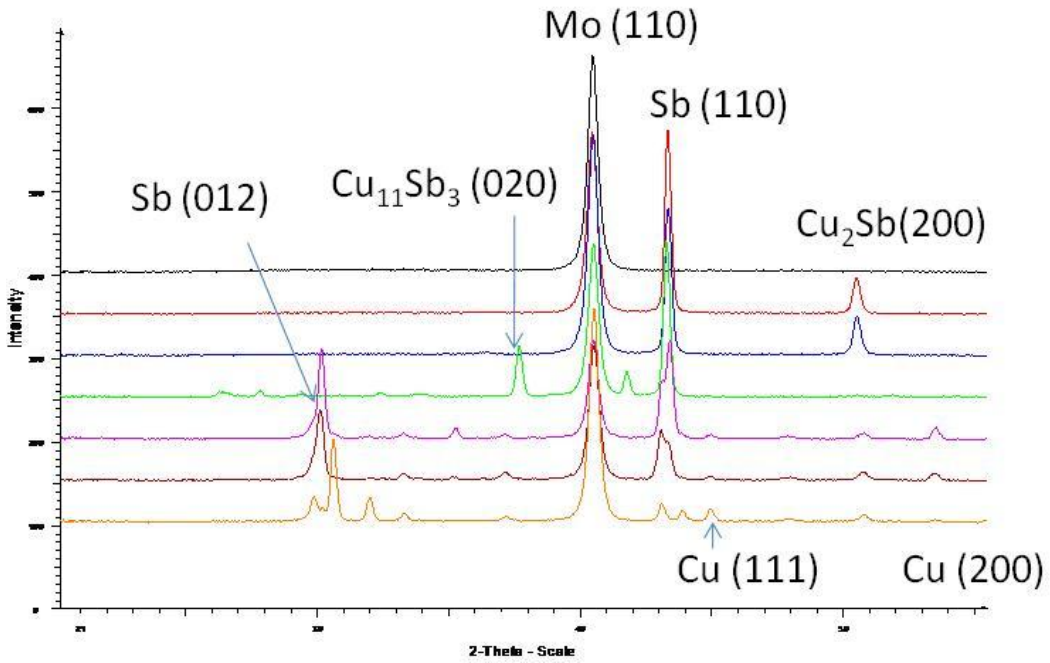

Figure 4.35. Compilation of the conventional diffractograms collected from the copper-antimony library. Every third diffractogram is shown starting from the first position at the bottom.

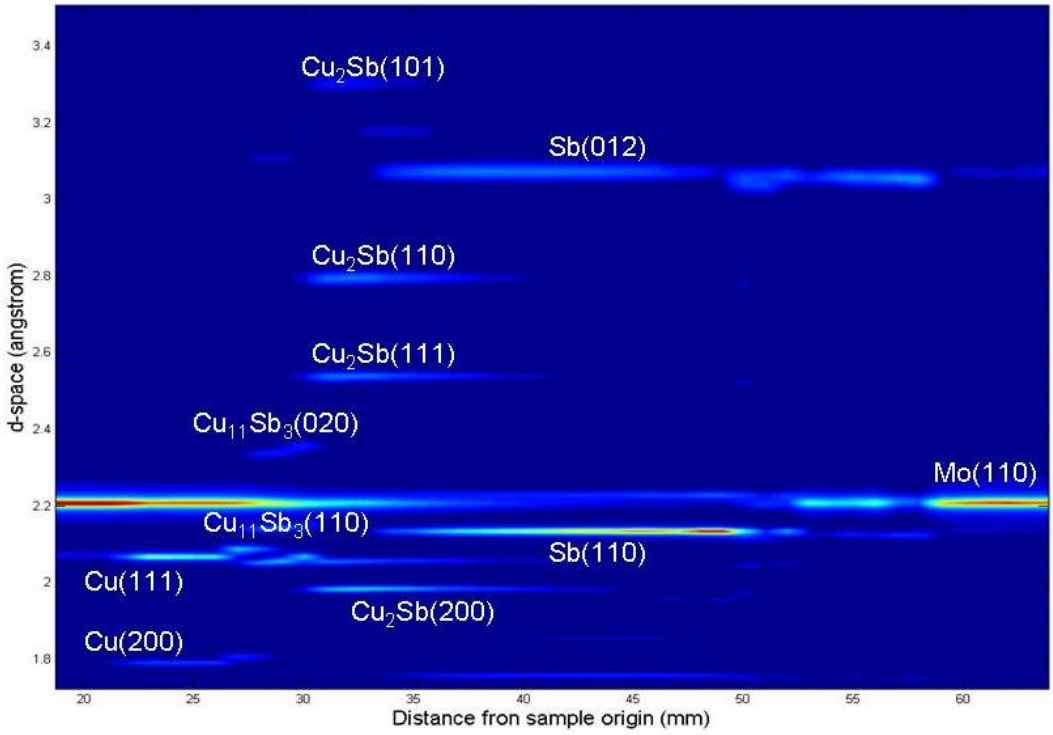

Figure 4.36. The XRD raster scan compilation of the CuSb sample electrodeposited in layers after heat-treatment.

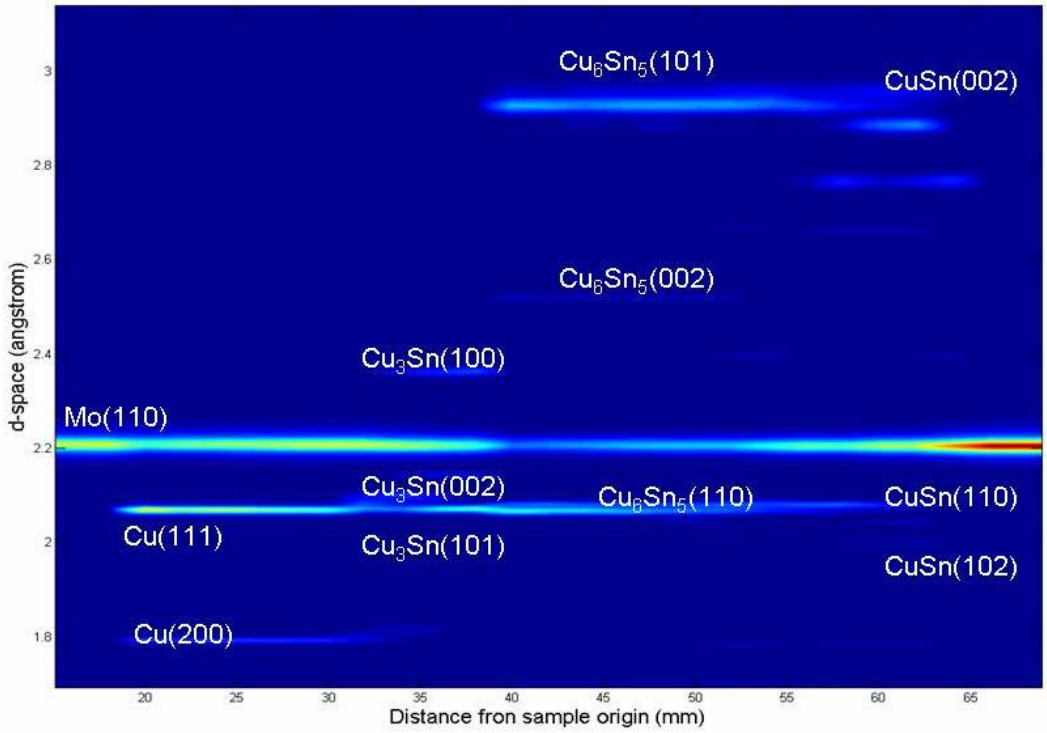

Figure 4.37. The XRD raster scan compilation of the CuSn electrodeposited sample after the 200°C heat-treatment.

Both Cu_3Sn and Cu_6Sn_5 can be seen in figure 4.37. This is expected as their formation is thermodynamically favourable and has been recorded in a number of examples where the stoichiometry of the alloy is not fixed. Fujimara [143] coated bulk copper with a layer of tin and found that both compounds were formed along with $Cu_{10}Sn_3$ which was not identified in the investigation. The formation on these materials indicates the mutual diffusion of the elements that would be expected at higher temperatures this is in contrast to the one way diffusion of copper into the tin matrix that produces tin rich interstitial phases that are formed at lower temperatures. [144]

Other investigators have shown that Cu_6Sn_5 forms readily at lower temperature while Cu_3Sn will only form at higher temperatures. The elemental compositions of this library suggest that Cu_4Sn should be formed but it has not been detected as the majority material in any position. The formation of this material is only favoured at high temperatures as seen by Tu et al [145].

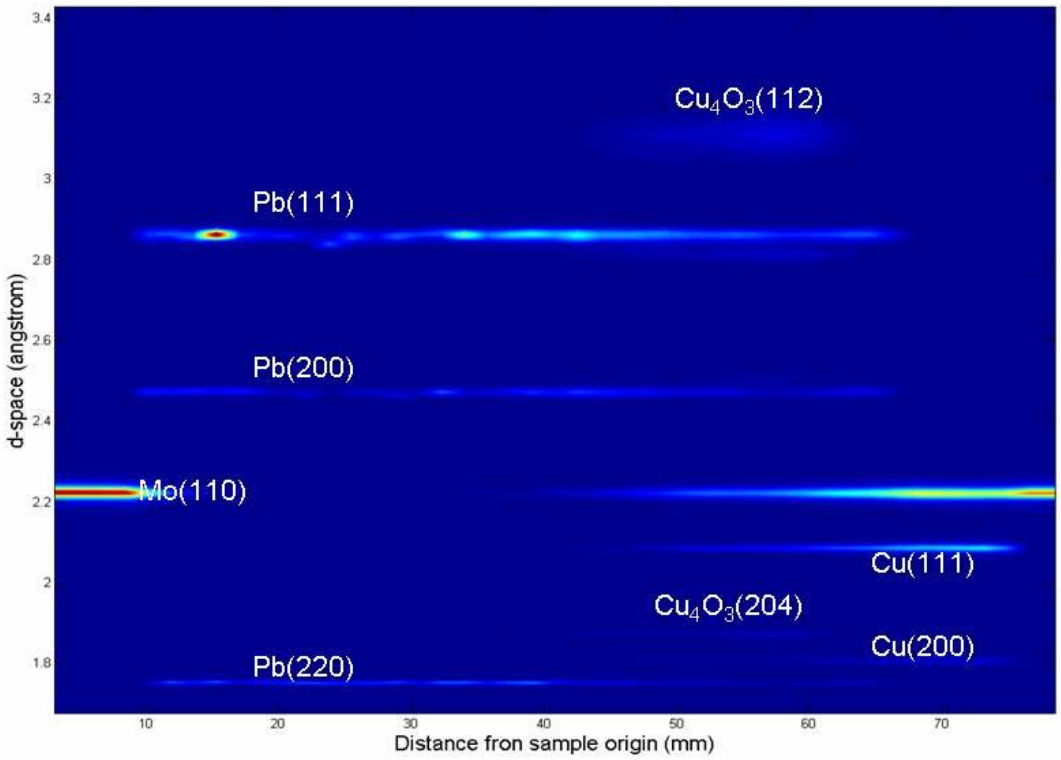

Figure 4.38. The XRD raster scan compilation of the electrodeposited PbCu system after heat treatment.

Copper and lead are not generally miscible and have no metastable compounds. A high level of mixing only being achieved where the Cu/Cu + liquid boundary temperature is exceeded in temperature [138]. This library would be expected to show the signatures of the elemental phases with varying relative intensity with position, this is indeed the case. Additionally oxygen incorporation to form Cu_4O_3 has been recorded, in addition to CuO and Cu_2O, this is a common oxide of copper. Not immediately apparent on the contour plot figure 4.38 but clear on to GADDS single frame output figure 4.39 is the large grain size (> 1 µm) seen in the elemental lead, the effect of this is discussed in section 6.4.

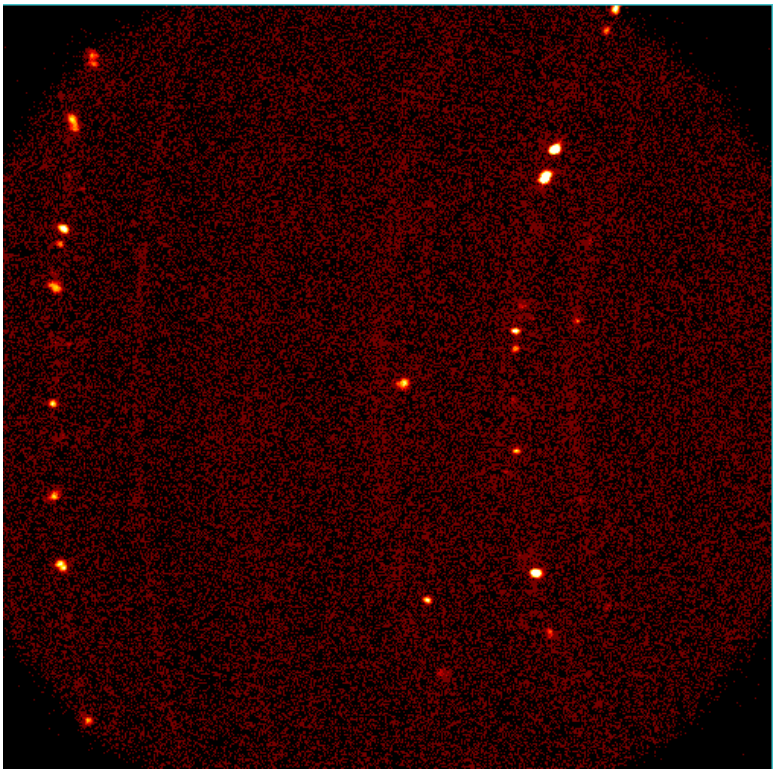

Figure 4.39. A single frame X-ray diffraction image taken from the GADDS showing small numbers of very large grains in the lead of the PbCu library.

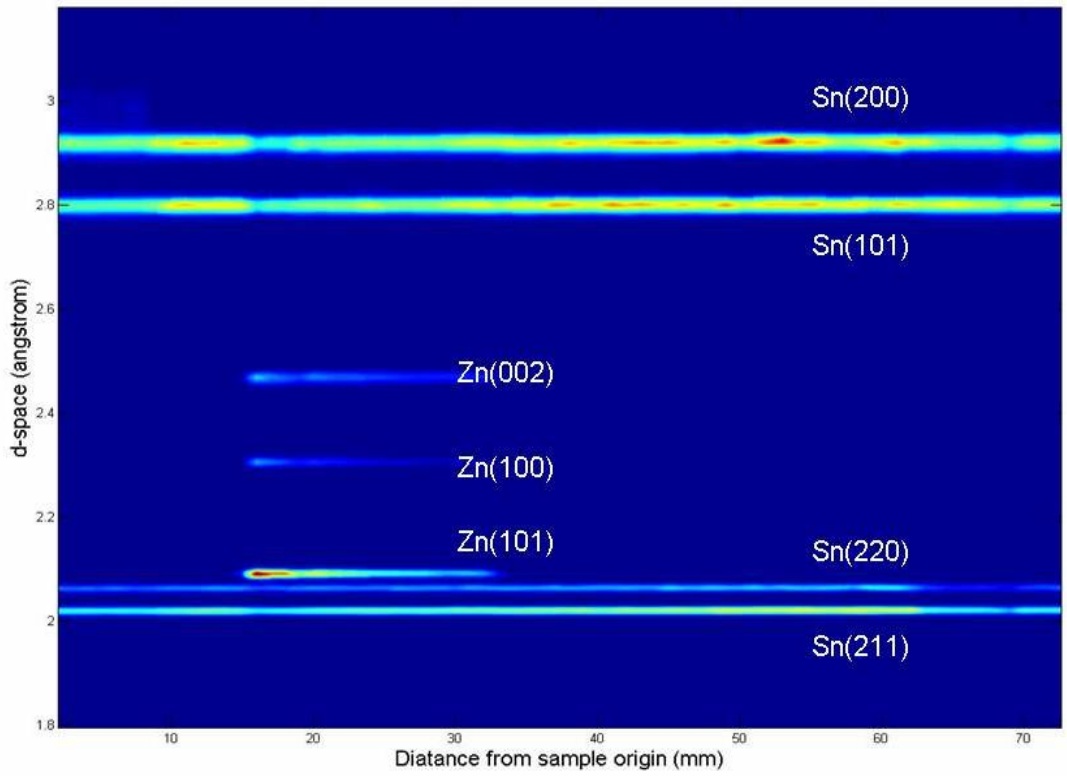

Figure 4.40. This is the compilation of raster XRD results for the SnZn system before heat treatment.

The tin-copper system is a simple eutectic type characterised by the mutual insolubility of the elements [146]. As expected no stable Sn-Zn compounds are formed. The heat treatment in figure 4.41 shows a change in the tin from the normal metallic allotrope tetragonal β-tin (white) to the less stable cubic α-tin (gray) [147]. This occurs in the presence of zinc.

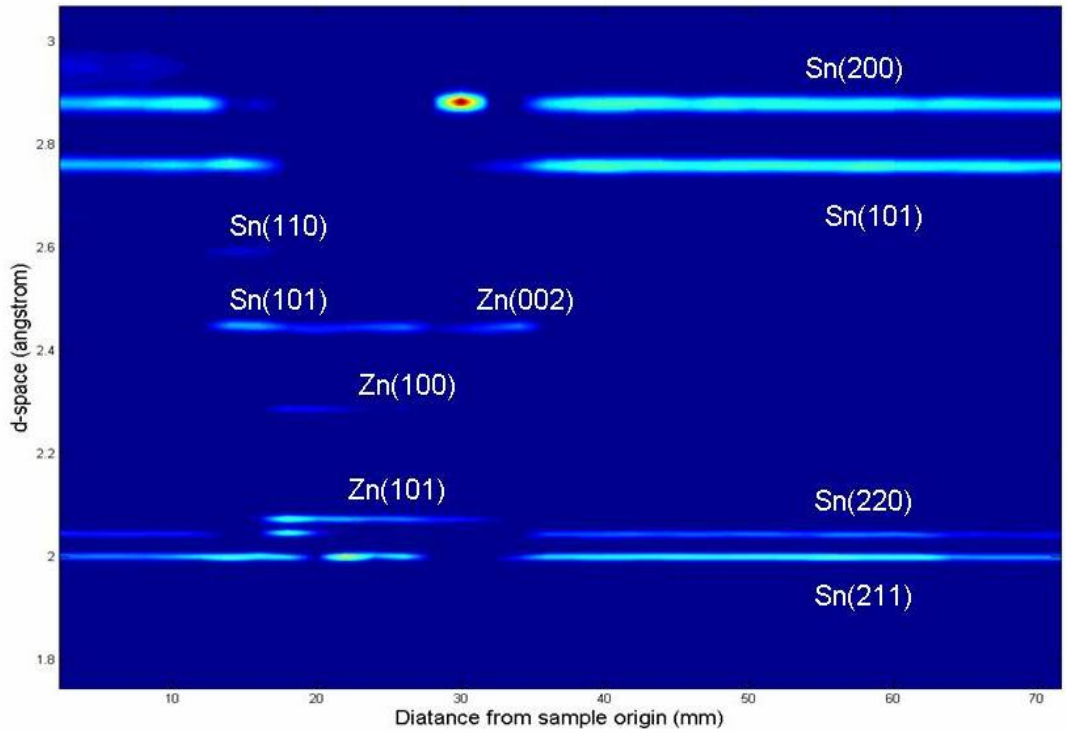

Figure 4.41. The XRD raster scan compilation of the SnZn system after heat treatment. The elemental tin phase on the left of the image is a new phase formed during the heat treatment.

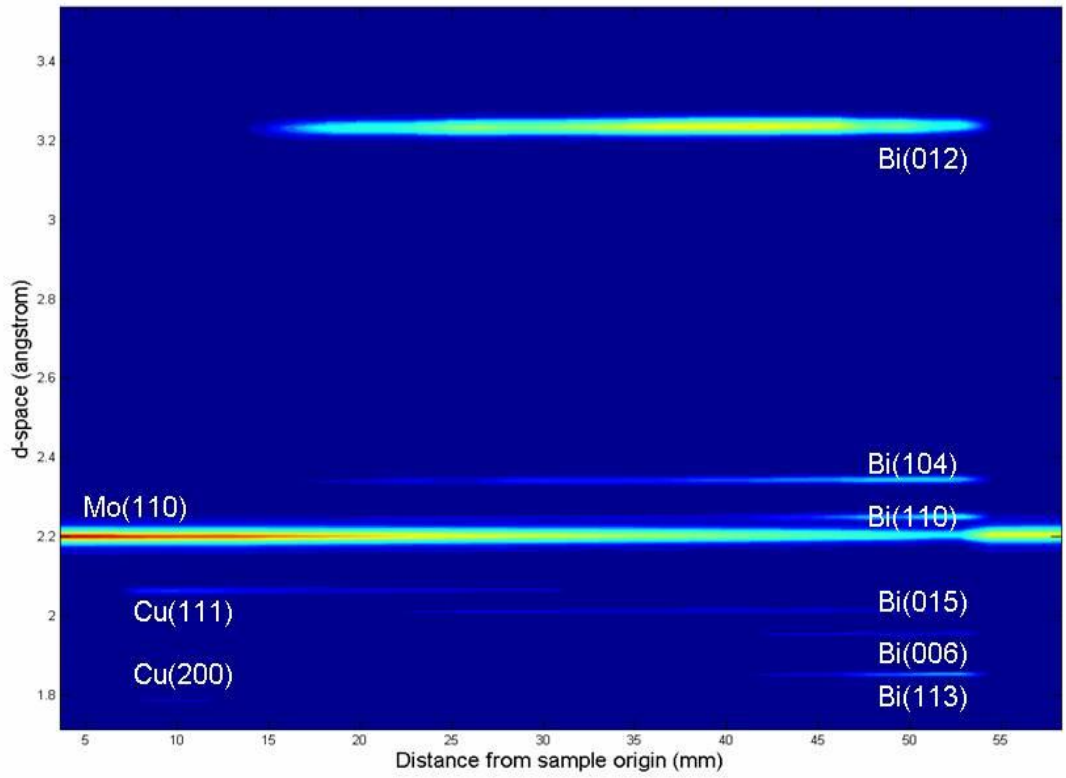

Figure 4.42. The XRD raster scan compilation from the copper-bismuth system after heat treatment. This showing no differences to the as deposited sample after 24 hours.

Raster scanning of the copper-bismuth library shown in figure 4.42 produces simple elemental diffraction patterns over the whole range of compositions studied. The EDS shows almost 100 % of each element at different positions on the substrate indicating that the largest possible compositional range has been produced. The main interest in the copper bismuth system is as a precursor material to the CuBiS and CuBiSe libraries. One feature of interest is the effect of composition of the perception of the underlying molybdenum substrate. Even though the thickness of the film remains broadly constant the increased X-ray attenuation of the bismuth rich parts significantly reduces the diffraction response of the Mo (110) peak.

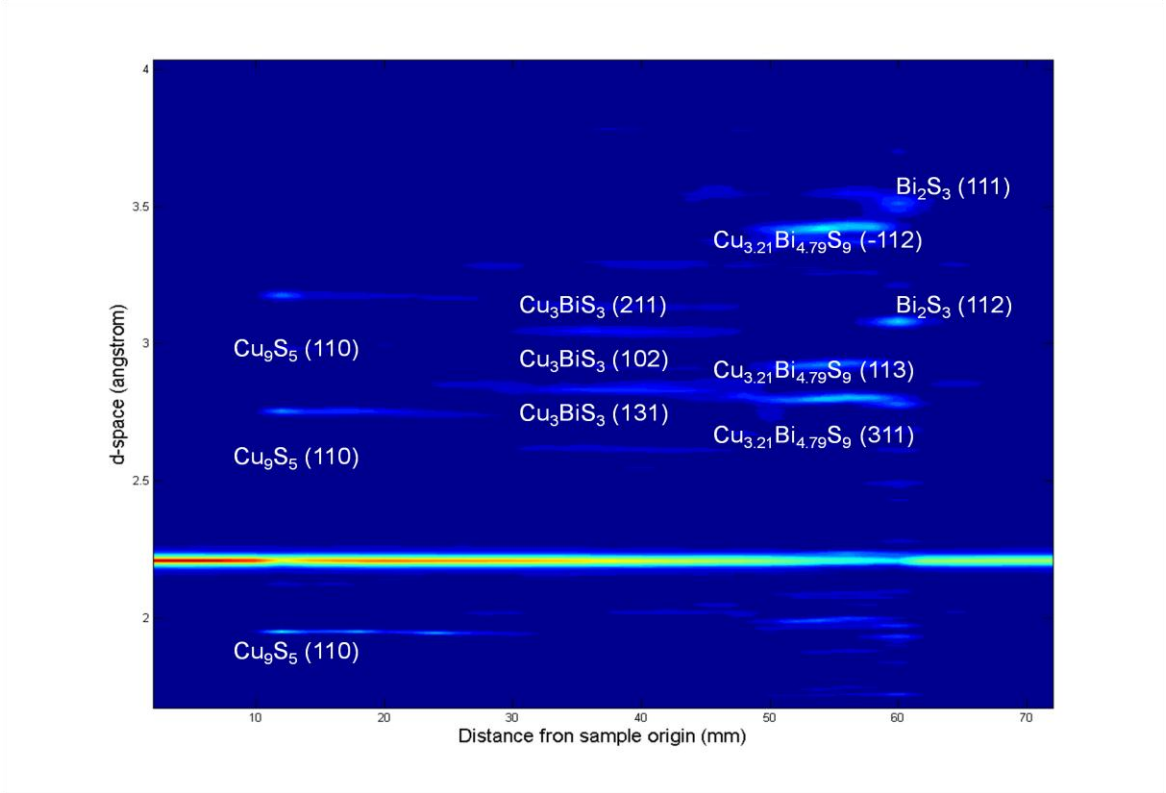

Figure 4.43. The XRD raster scan compilation from the copper-bismuth library diffraction data collected after sulpherisation step.

Two of the phases of interest in this sulpherised system are the Cu_3BiS_3 phase that has been mooted as a solar cell absorber [153] and $Cu_{3.21}Bi_{4.79}S_9$ which is another semiconductor. Diffraction patterns that closely match these phases can be seen in figure 4.43. Additional stable phase such as Cu_2S and CuS will form after longer heat treatment [148] but it is the ternary compounds that are of most interest.

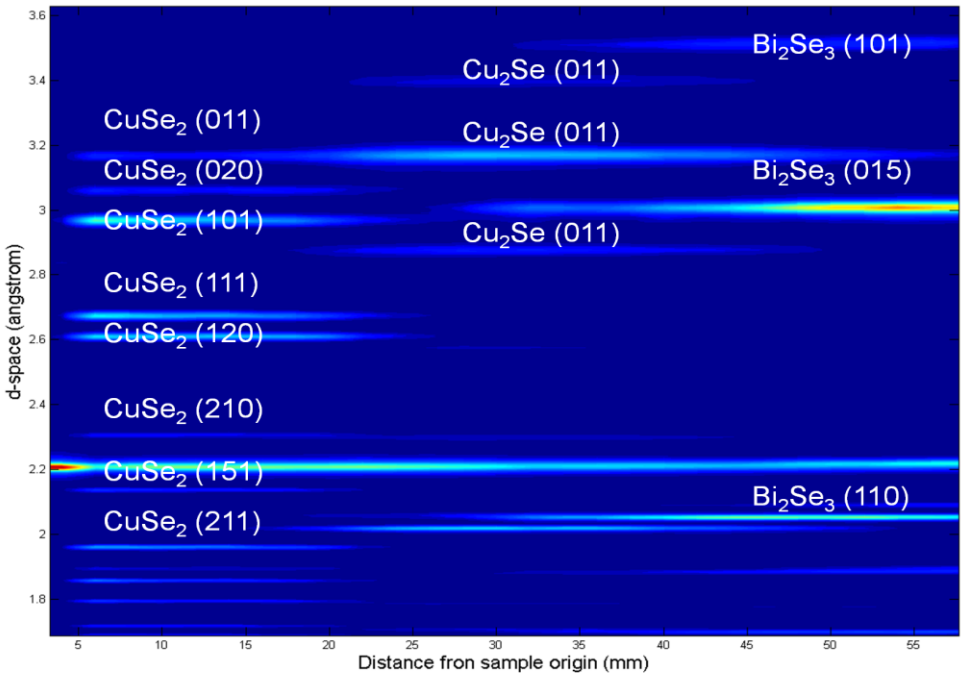

Figure 4.44. The XRD raster scan compilation from the copper-bismuth library after 450° C selenium treatment.

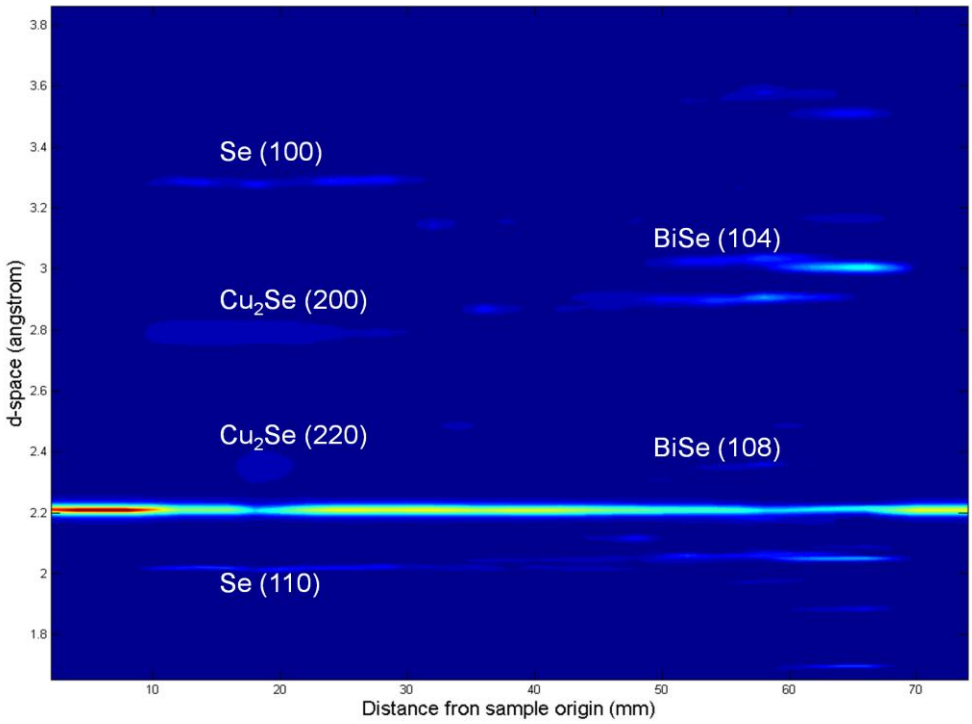

Figure 4.45. The XRD raster scan compilation from the copper-bismuth library after 250° C selenium treatment.

The formation of several of the CuBiSe ternaries are temperature dependent. In addition to the main phases that are illustrated in figures 4.44 and 4.45 the low temperature system contains minor phases such as $Cu_8Bi_{24}Se_{40}$ which exists only for a signal point, 58 mm from the sample origin. Loss of Bi in the high temperature and low pressure environment of the seleinisation chamber has been considered but no significant loss has been recorded. The covering of Se added under cooler conditions helped to prevent this loss.

Sputtered samples

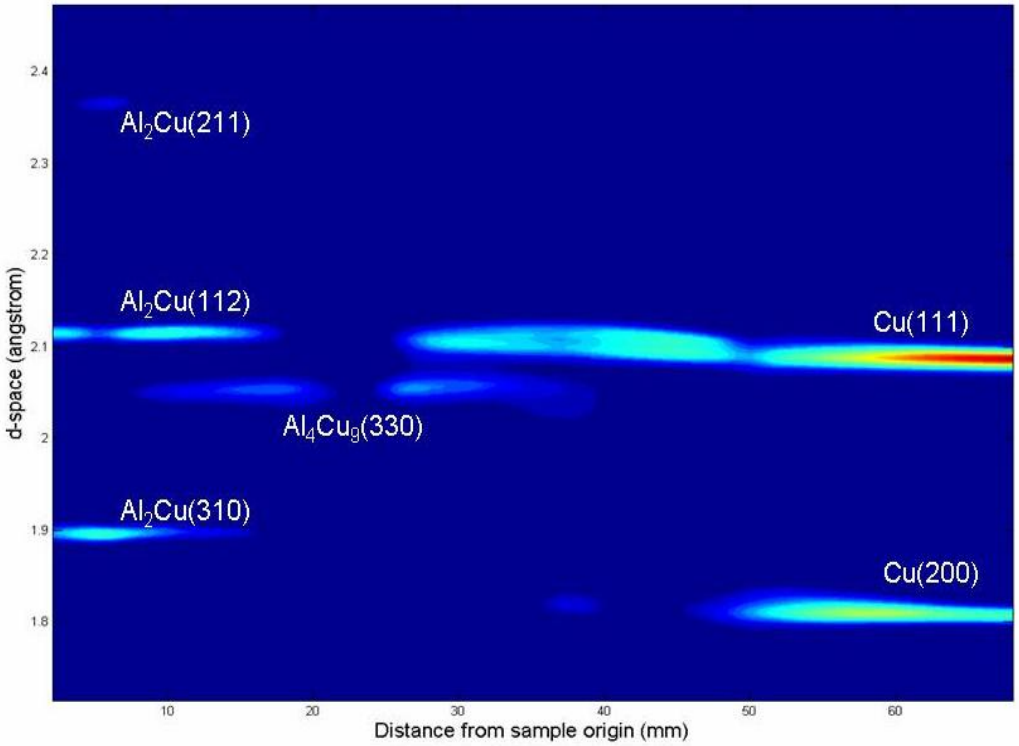

Figure 4.46. Compilation of the XRD diffractograms collected from the AlCu binary co-sputtered library after heat treatment.

In the temperature range used for this annealing, the AlCu phase diagram has 13 distinct regions [138]. The results of the XRD analysis shown in figure 4.46 indicate that 5 materials in 7 regions have been formed.

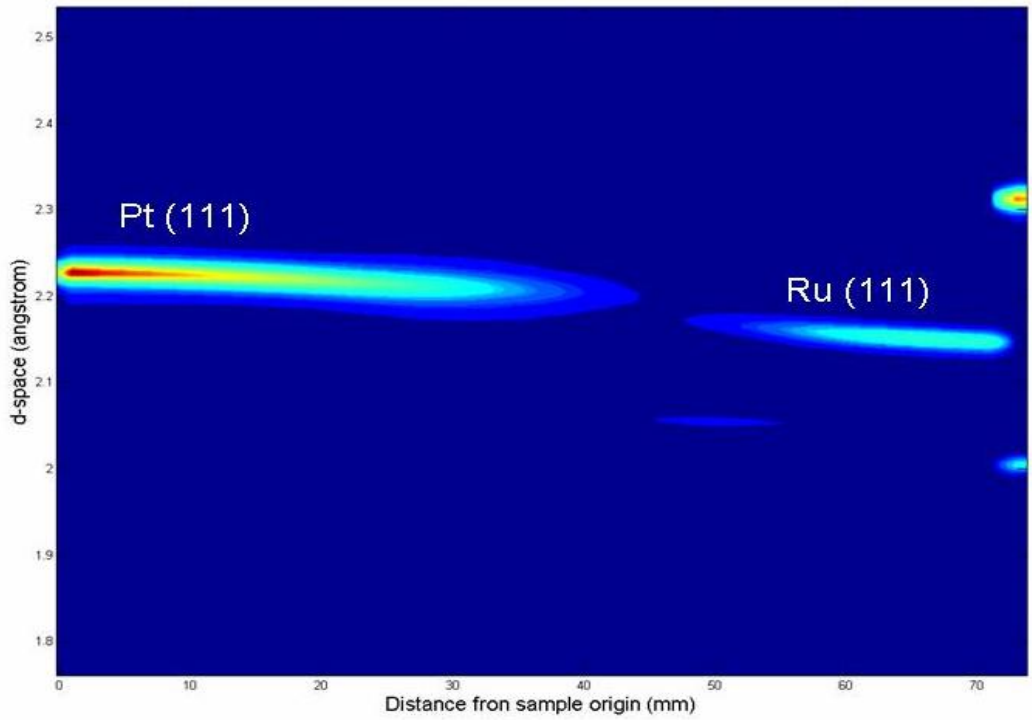

Figure 4.47. The XRD raster scan compilation of the RuPt binary co-sputtered library as deposited.

The RuPt phase diagram shows three low temperature phase regions, the central one being a mixture of the α and β phase that make up the other two parts. As is seen in figure 4.47 the diffraction from some portions of the compositional spread is weaker. The EDS suggests that the low intensity region is too Pt rich to be fully explained by this phase, so the reduction in intensity of this reflection cannot be explained by a phase change.

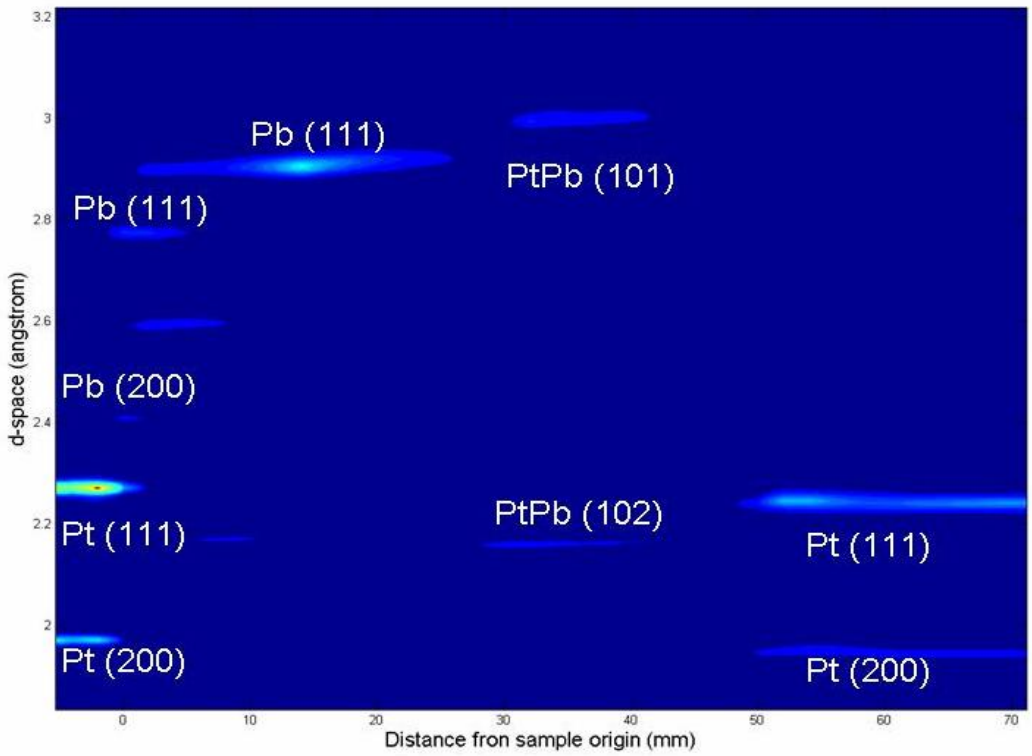

Figure 4.48. The XRD raster scan compilation of the PtPb binary co-sputtered library in its as deposited form.

Figure 4.48 shows the XRD results from raster scanning over the platinum-lead library with three of the four possible phases identifiable [138].

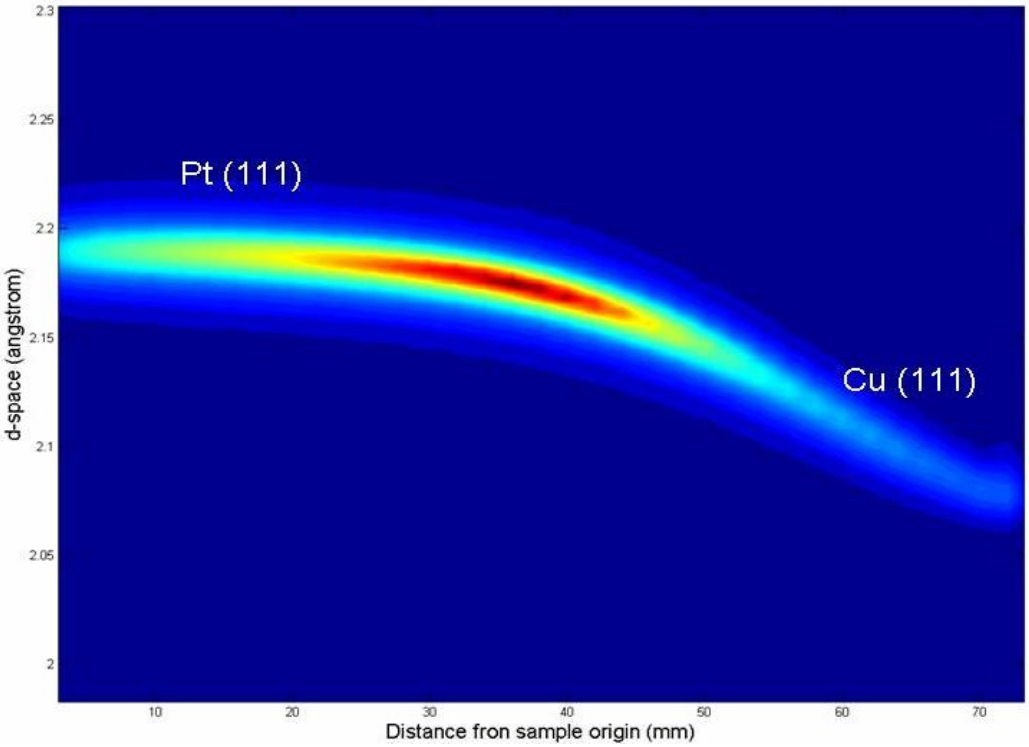

Figure 4.49. The XRD raster scan compilation of the PtCu binary co-sputtered library in its as deposited form.

As seen in figure 4.49, near the edges of the substrate the characteristic elemental phases can be seen with Pt in the <10 mm range and Cu at >70 mm from the sample origin. In the central part of the system does not show the expected phases. Three distinct phases are described in the literature Cu_3Pt, CuPt and $CuPt_3$ exist together over a large temperature range [149] and the lack of these phases can be explained by the low temperature production methods employed.

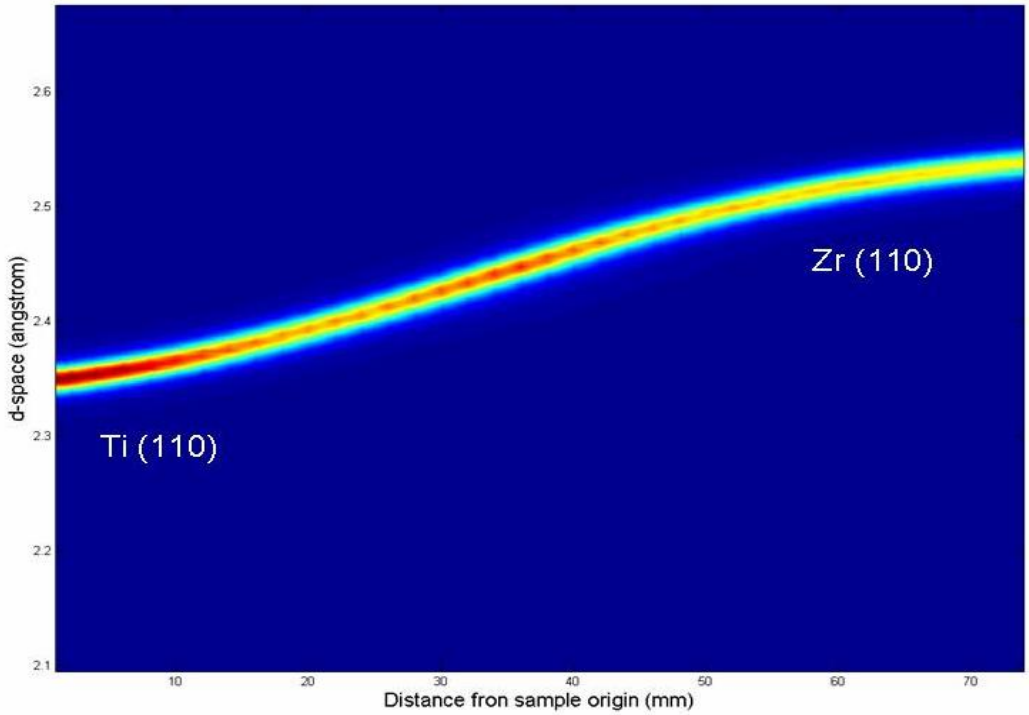

Figure 4.50. The XRD raster scan compilation of the TiZr binary co-sputtered library in its as deposited form.

The titanium zirconium system exists in a fully miscible solid solution. At temperatures under 605°C both the titanium and zirconium are in the α allotropic form and the material exhibits a close packed hexagonal arrangement throughout the compositional spread [138]. This constant phase with the associated lattice parameter shift as the composition changes is demonstrated in figure 4.50. The other interesting property of this film that can be shown from the X-ray diffraction results is the high level of preferred orientation. Hence only the (110) plane exhibits strong diffraction and the incomplete form of the Debye ring is revealed in figure 4.51.

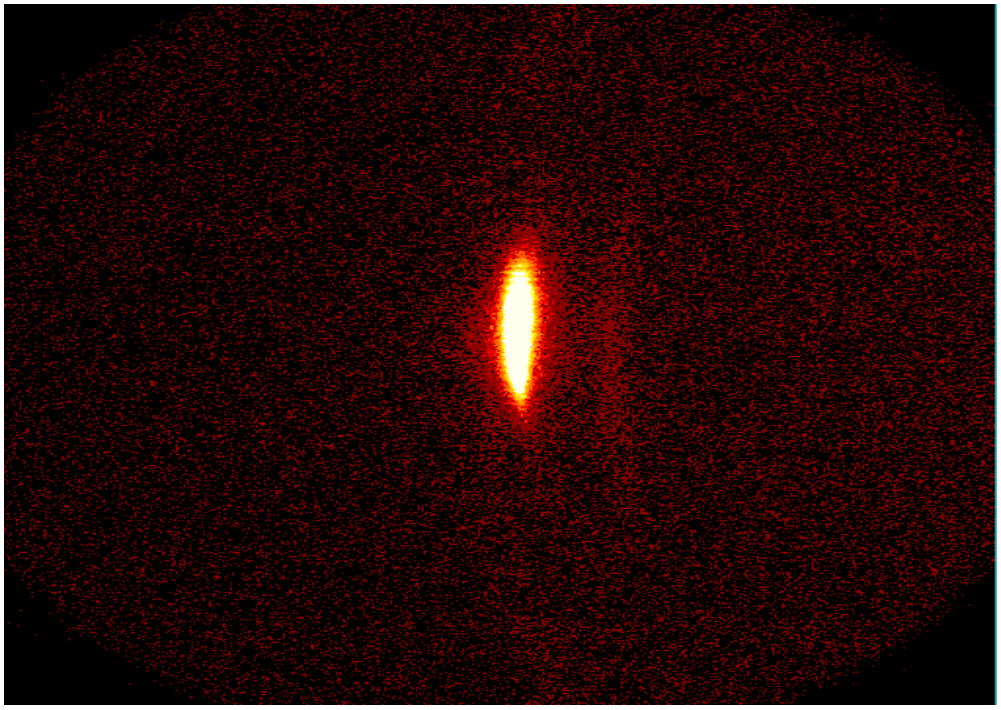

Figure 4.51. Area detector (GADDS) image for the TiZr library from position 34 mm from the sample origin. This shows the large amount of preferred orientation for the alloy and is representative of a large number of the sputtered samples.

Electrostatically sprayed samples

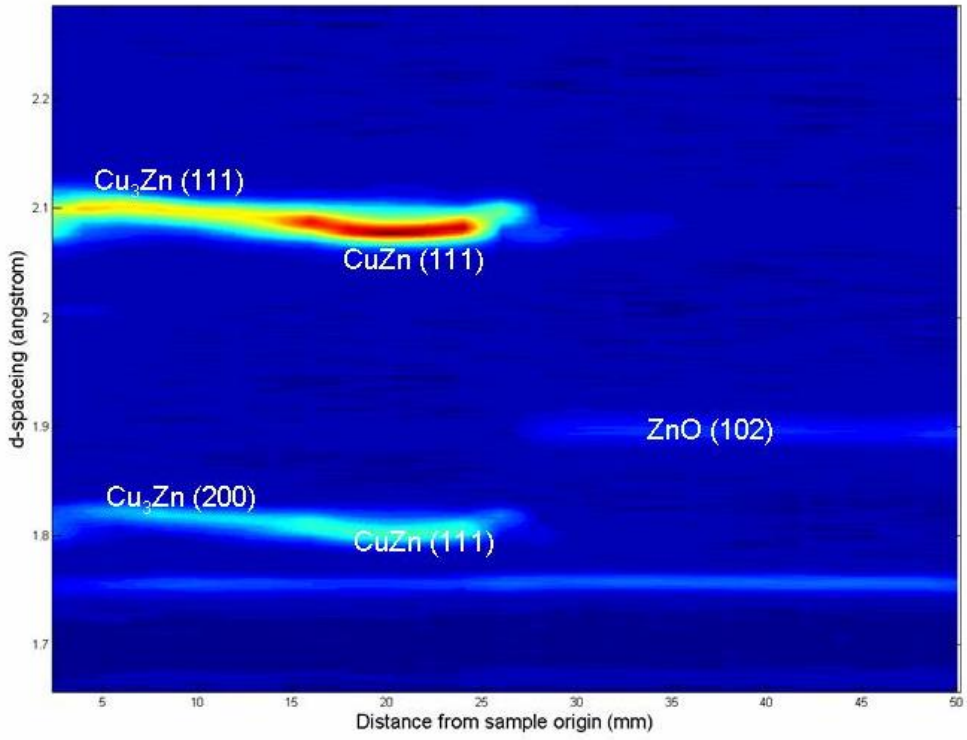

Figure 4.52. The XRD raster scan compilation of the ZnCu256 library. This sample was deposited on an inert SiO_2 substrate.

The library formed by electrostatic atomisation differs from the sample formed by electroplating in two main ways. The shallower gradient of the spread sample and it being skewed in favour of high zinc compositing means that the elemental copper signatures are not present; this is confirmed by figure 4.52. Additionally the incorporation of oxygen into the film is recorded. As the other zinc containing samples have been heated in the same forming gas filled oven the incorporation has come from the deposition process. This is not unexpected as it is known that ZnO forms readily at 475 K when zinc acetate is atomised by the similar mechanical spray pyrolysis method [150].

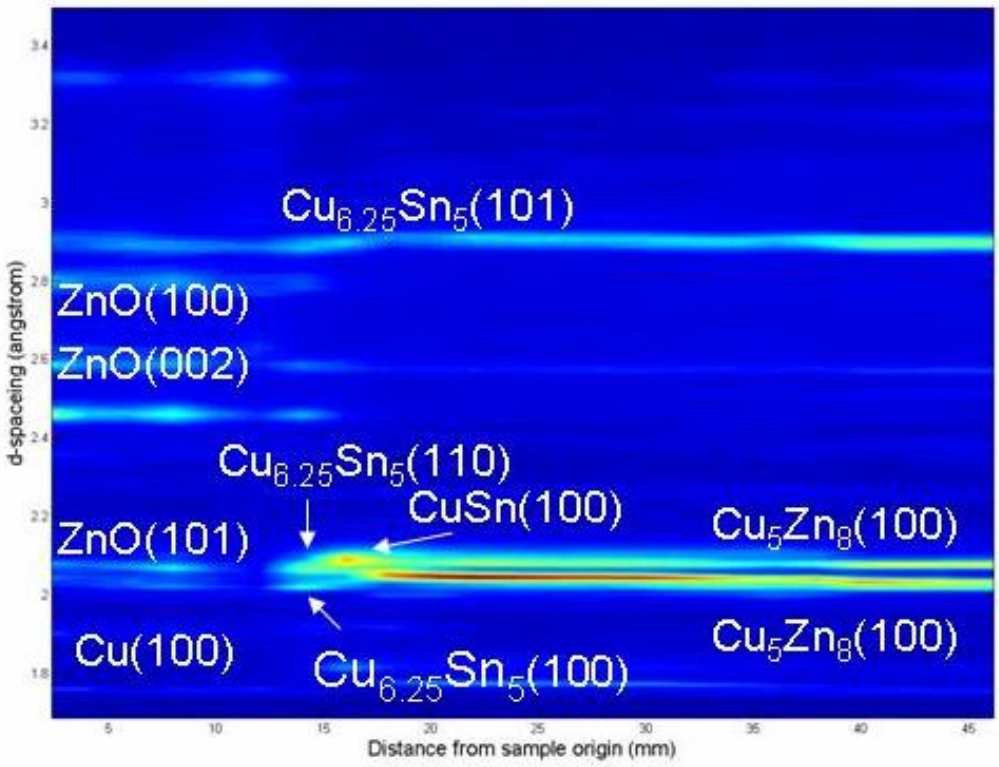

Figure 4.53. The XRD raster scan compilation of the ZnCu2569 library after heat treatment. This sample was deposited on TCO.

In figure 4.54 the XRD data collected from the Zn-Cu library is displayed. This data indicates that the tin oxide substrate used in this deposition of copper and zinc is not inert under the dissociation conditions. The tin has been included in the library forming a number of ternary systems with weak diffraction peaks. The strength of these peaks indicates that these are always minor components. All of the strongly diffracting phases have been matched to binary systems. Peak broadening combined with their low signal to noise ratio meant that positive matches of the minor components proved elusive. As these low signal peaks were assumed to

be beyond the resolution of the extended beam partitioning no further identification attempts have been made.

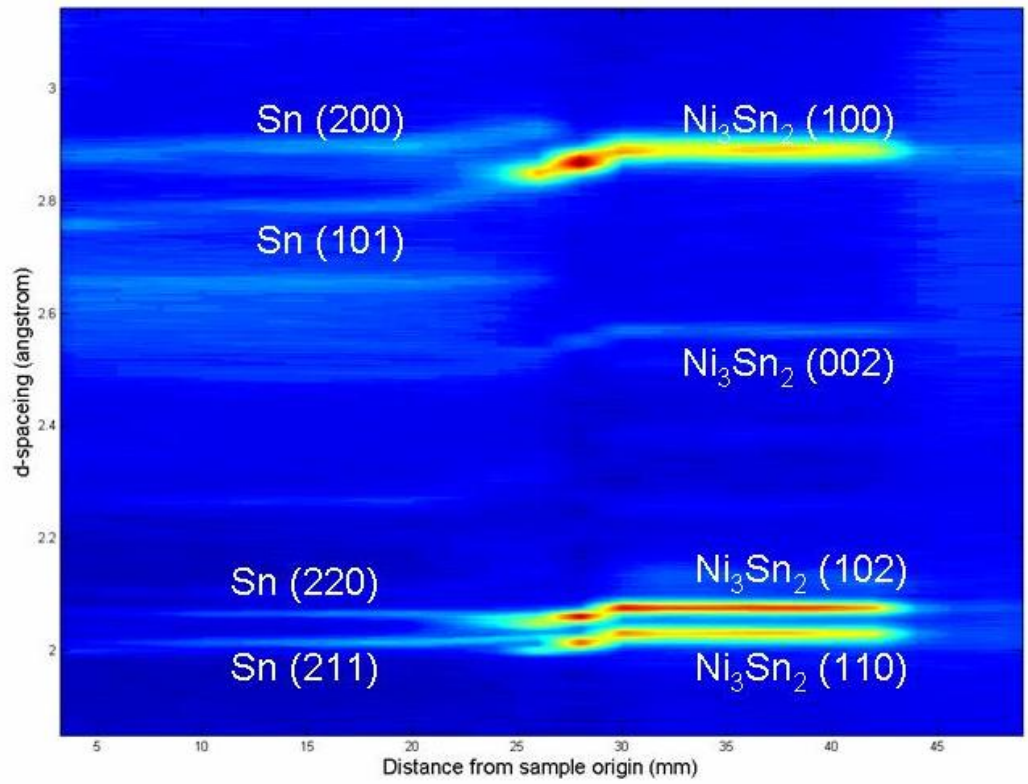

Figure 4.54. The XRD raster scan compilation of the SnNi251009 electrostatically sprayed library on uncoated glass.

XRD analysis of the tin- nickel shown in figure 4.54 gives signals closely matching Ni_3Sn_2. Examination of the SnNi binary phase diagram shows that the Ni_3Sn_2 phase only exists as single phase for a small compositional range but it exists as one phase in a two phase region for between 26-56 atomic percent tin. As the compositional spread in the 30 mm to 45 mm rejoin of this library represent significantly less than this compositional range the findings are consistent with expectations. The strong signal from the Ni_3Sn_2 phase throughout this region is explained by the mixing of phases through these points. The proportions of the different phase in this area can be determined by adoption of the lever rule [151].

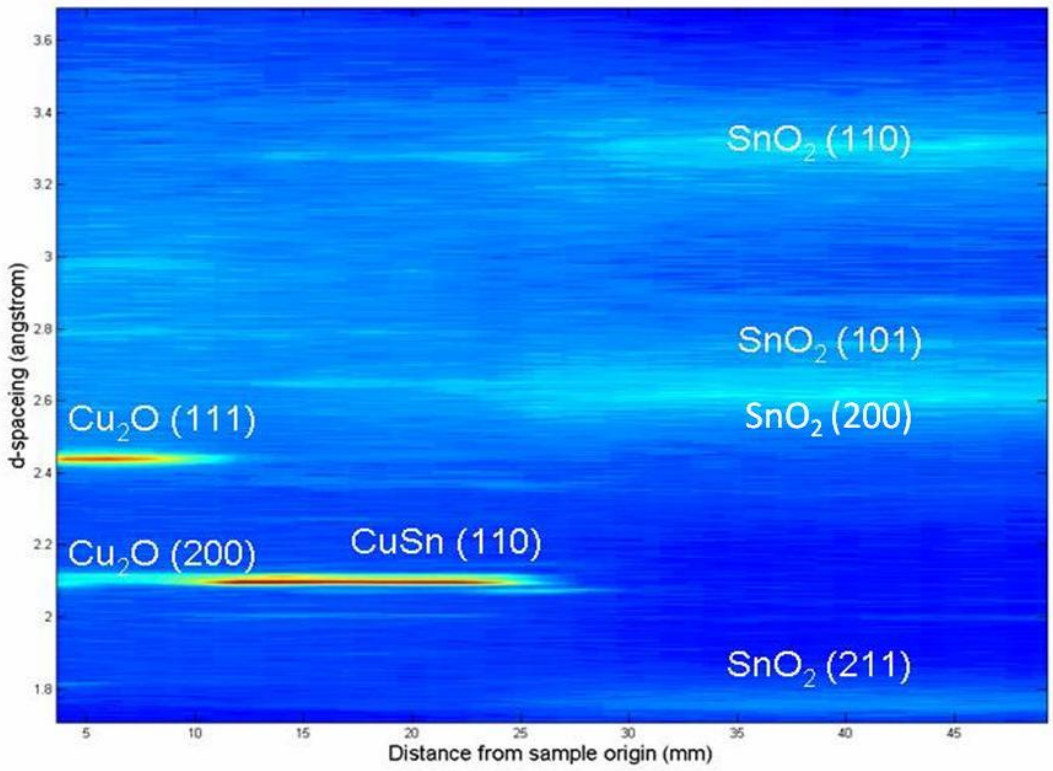

Figure 4.55. The XRD raster scan compilation from the SnCu191009 electrostatically sprayed full library with the diffuse contour mapping representing the wide peaks.

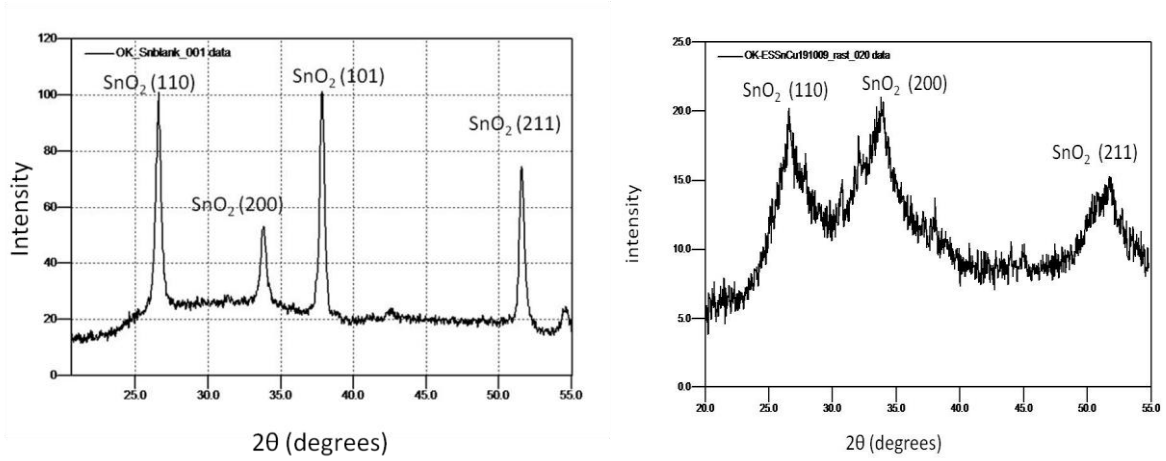

Figure 4.56. Showing commercially produced SnO_2 (left) and an example of an individual diffractogram of the electrostatically sprayed SnO_2 indicating the wide peaks (right).

The copper rich part of the electrostaticaly produced copper-tin system can be seen in figure 4.55. This contains diffraction returns characteristic of a low strain system but on the low copper portion clear peak broadening can be observed. The cause of this is likely to be a combination of the small grain size of this material and internal microstrain in this portion of the film. Both of these characteristics are known to be expressed as large symmetrical broadening of the peaks [106] [152]. Figure 4.56 contrasts the sample with commercially

deposited tin oxide and illustrates the effect of this broadening and also the change in relative intensities of the peaks produced by different planes.

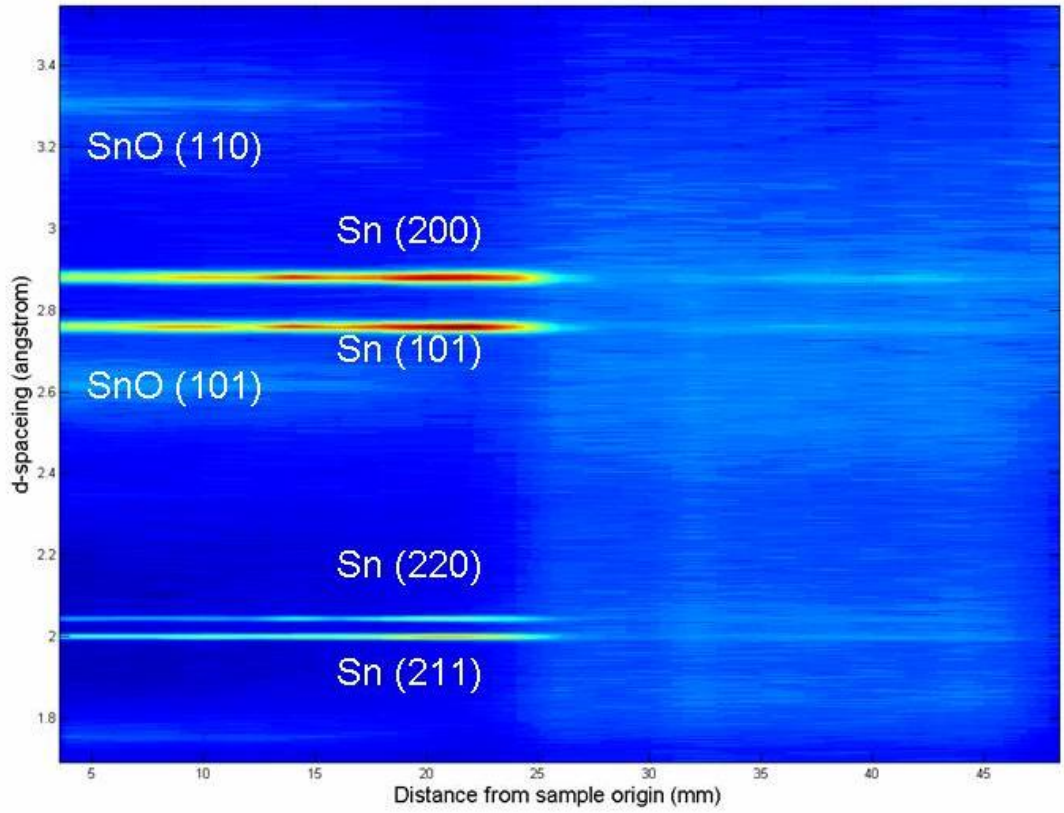

Figure 4.57. The XRD raster scan compilation from the SnCr251009 electrostatically sprayed library.

In the case of the tin-chromium library described in figure 4.57 the two tin phases are crystalline but the chromium containing phases are more amorphous. No diffraction peaks however broad can be identified. The composition of this area can be determined by EDS analysis to range between 10 – 60 % tin in the crystalline region.

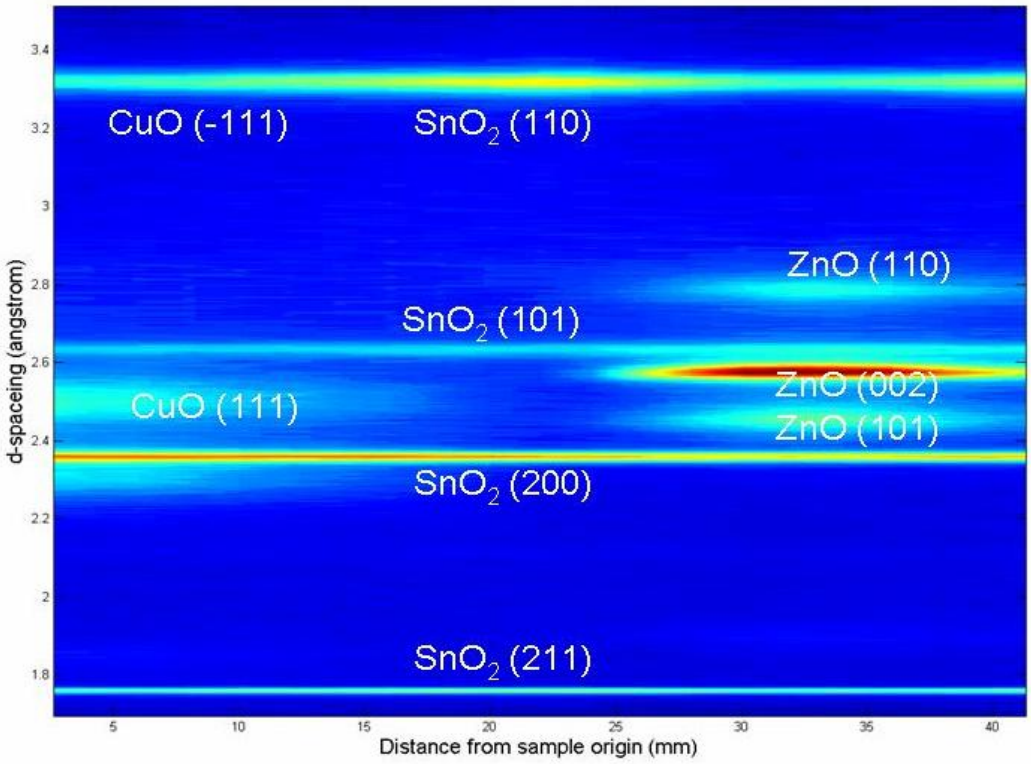

Figure 4.58. The XRD raster scan compilation from the CuZnQ electrostatically sprayed library.

The image in figure 4.58 clearly shows the different widths of the peaks from different components of the CuZn library. The broad ZnO and CuO signatures are contrasted against the tightly defined peaks of the TCO. The wide peaks in this region are probably caused by strain broadening. The sample thickness in this library is very low, < 200 nm on average. The middle of the library is thinnest and produces a signal that is insignificantly small compared to the TCO substrate. The elemental composition of the centre of the library can be measured with EDS which is known to be more sensitive and has a much smaller penetration [119].

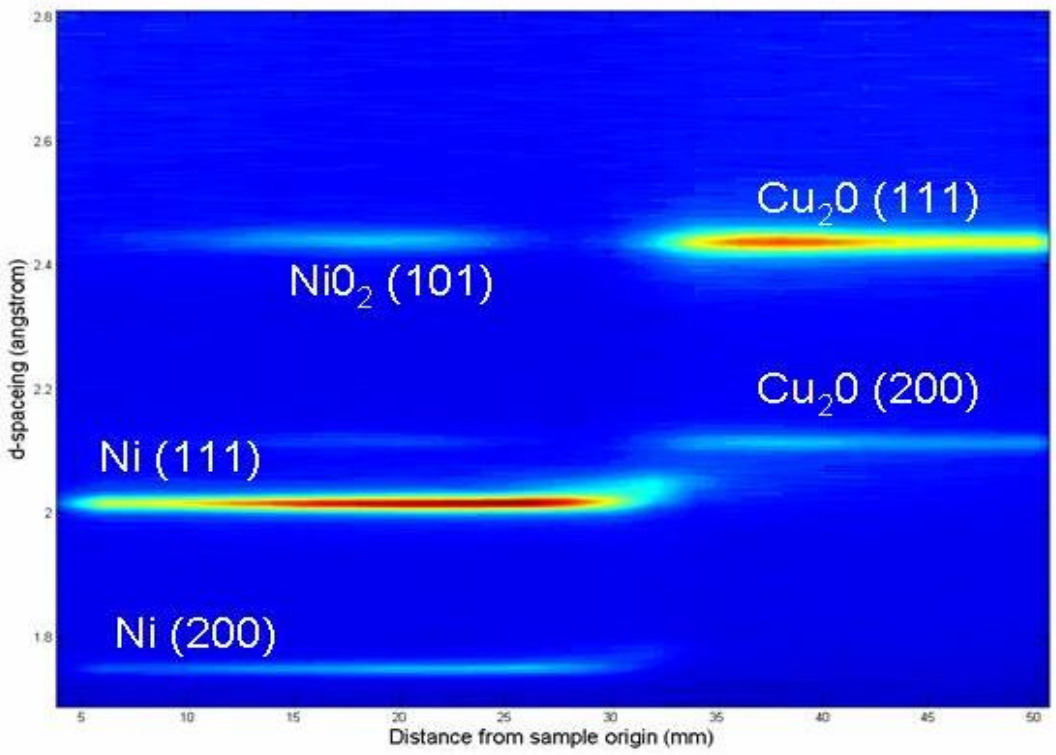

Figure 4.59. The XRD raster scan compilation from the CuNi250908 electrostatically sprayed library.

The diffraction results of the electrostatically sprayed copper-nickel library, figure 4.59, shows peak patterns that match to both elemental nickel and nickel oxide. The larger proportion of the oxide visible in the middle may be due to the reduced thickness of the underlying metallic layer in this area. This would suggest an external source of oxygen and not the acetate pyrolysis products. Diffraction results characteristic of copper nickel alloying have been detected over a small compositional range.

Diamond Light Source Synchrotron data collection

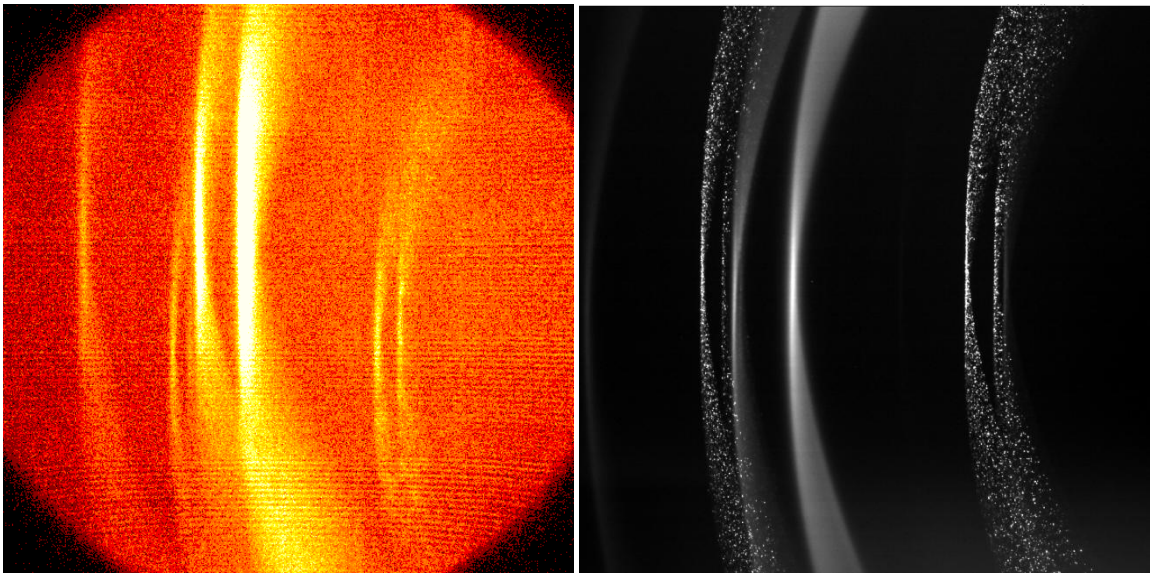

Figure 4.60. CuSn libraries as seen in the X-ray tube based systems left and synchrotron data collection right.

In figure 4.60 the main difference between the GADDS detector and the photonic science X-ray image star 9000 used for data collection at the synchrotron source is the positioning in relation to the sample. During the synchrotron data collection 12 keV X-rays were used, hence from Planks rule [112] the wavelength is calculated as 1.03 Å. This shorter wavelength means that for the same d-spacing the 2θ angle would be smaller increasing the curvature of the Debye arcs.

The tin in the copper-tin samples have undergone room temperature re-crystallisation between the data collections so larger grains can be seen.

The data from the diamond synchrotron was collected and saved as tiff images. By applying the same partition algorithm used on the extended beam samples to the rastered samples an effective radial integration of the sample is produced. An example of this is shown in figure 4.61 where an Al_2O_3 standard exposed to point source illumination has been partitioned. The quantatitive results of this process can be seen in table 4.2. This can be done over only one pixel line if only a conventional diffractogram is required. If the whole intensity map is required the normal partitioning of the 3056 pixels can be measured. This also gives us an indication of how the partitioning will work without the overlaying peaks and the additional detector noise that is present.

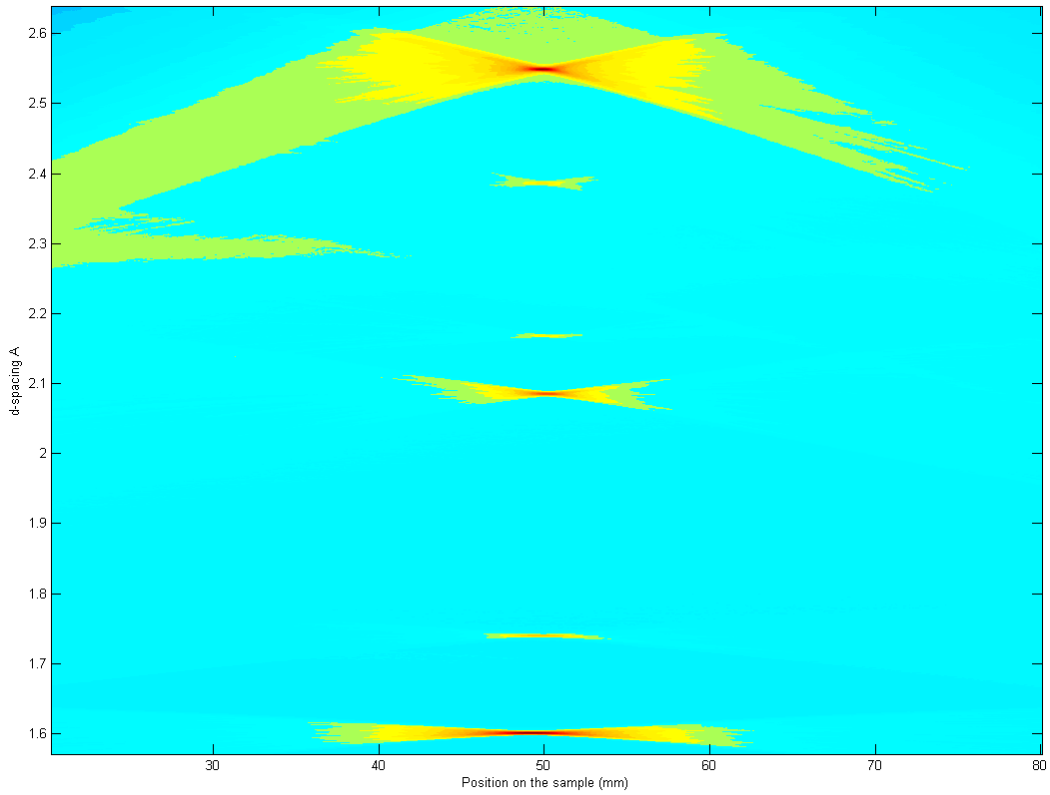

Figure 4.61. Displayed is the result when the partition is carried out on a sample of Al_2O_3 when illuminated by a conventional pencil beam.

Al_2O_3 d-spacing (NBS 640c)	Al_2O_3 d-spacing (partitioned)
2.5508	2.549 ± 0.002
2.3795	2.386 ± 0.002
2.1654	2.170 ± 0.002
2.0853	2.086 ± 0.002
1.7401	1.740 ± 0.002
1.6016	1.601 ± 0.002

Table 4.2. The d-spacing input data from literature (NBS 640c) and the output data from the partitioning.

The partitioning values should be exactly the same as the actual Al_2O_3 standard as the d-spacing values are first input as the calibration. The calibration standard is then partitioned in the same way as a sample and the d-spacing extracted directly from the resulting tiff image.

Single Composition Samples

In figures 4.62 and 4.63 are represented the XRD results for conventional single composition samples produced by electroplating and post deposition sulpherisation. In both cases, the desired compounds have been manufactured on the first attempt as the correct conditions

were confirmed in advance by the presence of and the positioning of the phases in the original combinatorial libraries.

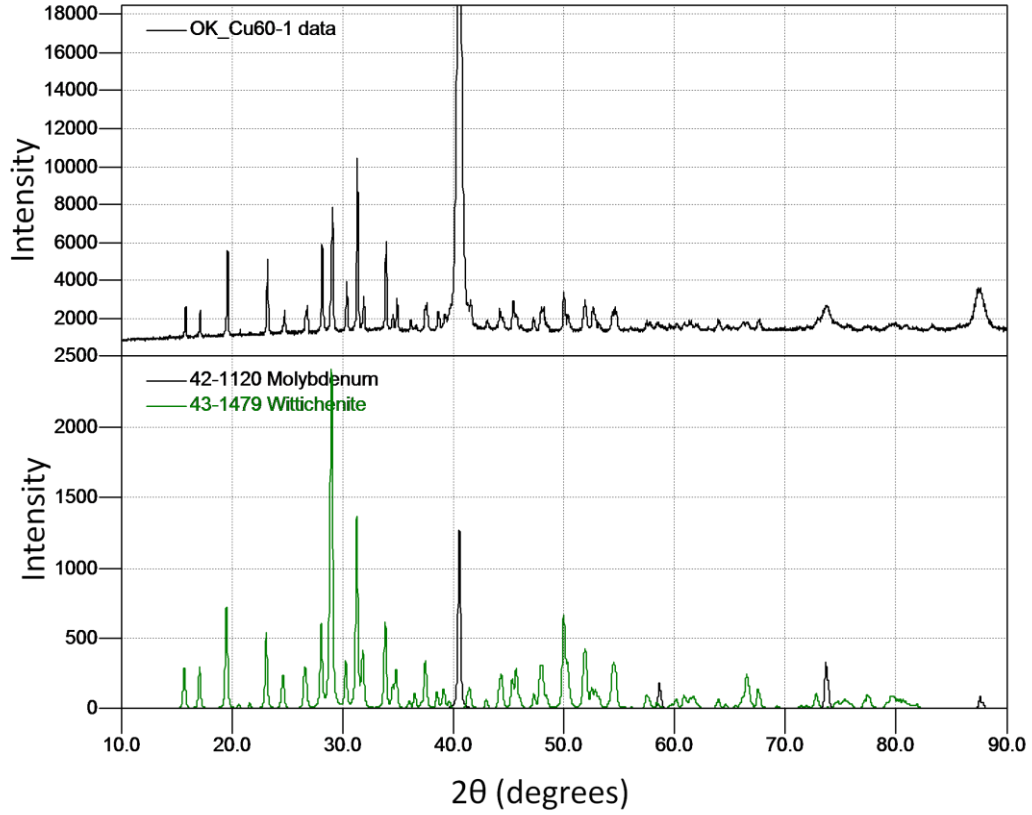

Figure 4.62. Conventional XRD patterns showing the electrodeposited sample Cu60 and the search match card of Cu_3BiS_3.

If the elemental ratio of a target material is known as in Cu_3BiS_3 and $Cu_{2.94}Bi_{4.8}S_9$ the correct thickness of the layers could easily be calculated without the combinatorial library but in these cases the other conditions would have to be optimised separately. The use of the combinatorial method is most effective where the system is not generally known and targeting specific phases without an indication that they will form under the chosen conditions would have a low probability of success.

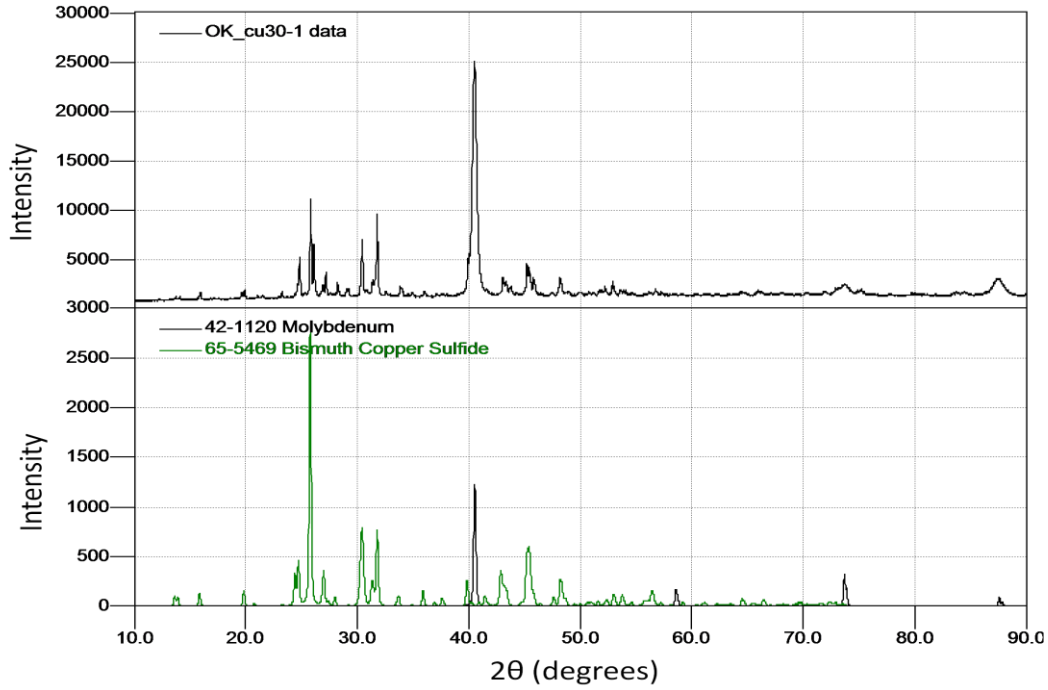

Figure 4.63. Conventional XRD patterns showing the electrodeposited sample Cu30 and the search match card of $Cu_{2.94}Bi_{4.8}S_9$.

As with the $Cu_{2.94}Bi_{4.8}S_9$ this phase could be picked from the library for conventional production. The knowledge of the layering of the precursor material and the post deposition treatments allowed efficient formation of the desired material. The XRD in Figure 4.63 demonstrates it to be the only phase of note in the sample.

4.4 Electro Optical Properties

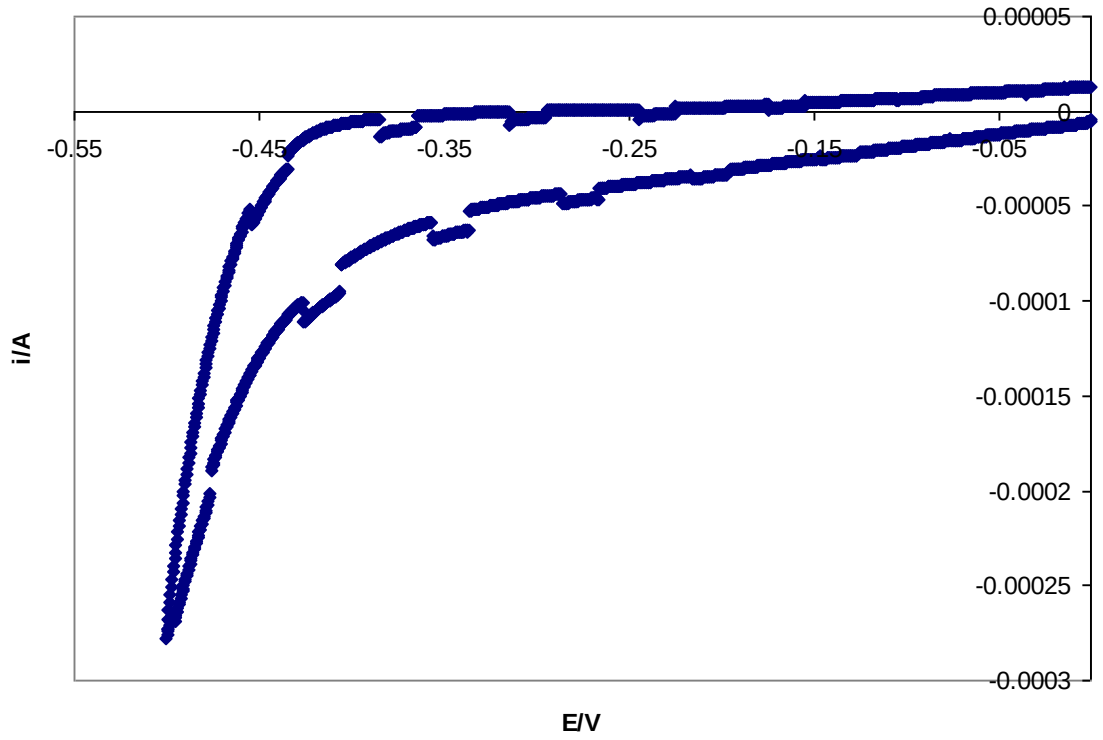

Figure 4.64. The cyclic voltammetry results for the conventionally produced Cu_3BiS_3 sample.

Cyclic voltammetry shows a minor photo response with the Cu_3BiS_3 sample, as indicated in figure 4.64. This is expected from the literature [32] [153], However the response is too small (< 10 mA) for full quantitative determination. The $Cu_{2.94}Bi_{4.8}S_9$ did not have a response sufficient for this measurement.

Chapter 5

5 Extended Beam X-ray Diffraction

5.1 Application of partitioning to theoretical images

The partitioning method allows a virtual arc of any dimension to be used to make the regional intensity sum calculation. When deciding these dimensions, the type of sample needs to be considered. For samples with a high degree of random orientations of the grains, a virtual arc with a length covering the whole detector collection area is thought to give the largest potential true positive signal with the noise being proportionally at its smallest. This is used in all cases for partitioning in this investigation.

In terms of the virtual arc thickness a judgement has to be made in relation to the width. As the arcs from actual samples will inevitability have some width an idealised virtual arc occupying a single data point in the matrix (one pixel on the simulated detector) would not create the close match required for the strongest possible positive signal so because of this, a thicker virtual arc may be chosen. In most situations where the partitioning is to be used the maximum possible resolution is expected. Due to this the arc movement increments in most cases would be set as small as possible, one pixel in both axes. If the increments in the arc movement was smaller than the width of the arc this would produce an over sampling effect that would widen the peaks in the partitioning output and reduce the d-spacing resolution. In the examples that follow the width of the virtual arc was set at an idealised one pixel unless otherwise stated.

5.1.1 Preparation of simple simulated examples

For the theoretical study a simulated standard equivalent to the Al_2O_3 standard used in the library samples was produced. The size of the virtual grid used in the simulations matched the pixel density of the GADDS on the Bruker diffractometer. The geometry of this virtual system was also set in a way such that the pixel number versus d-spacing on the simulated images would match the real arc position to d-spacing calculations for this detection geometry.

In both the simulated and the collected results the terminology has been kept consistent. The direction along the gradient of the binary systems and, therefore, along the length of the extended beam is referred to as ‘position on the sample’. This is the ‘y’ direction. The other side of the Cartesian grid is the x direction on the physical sample or ‘the d-spacing direction when the XRD contour plots are considered. Z displacements are always used to talk about changes in the sample height.

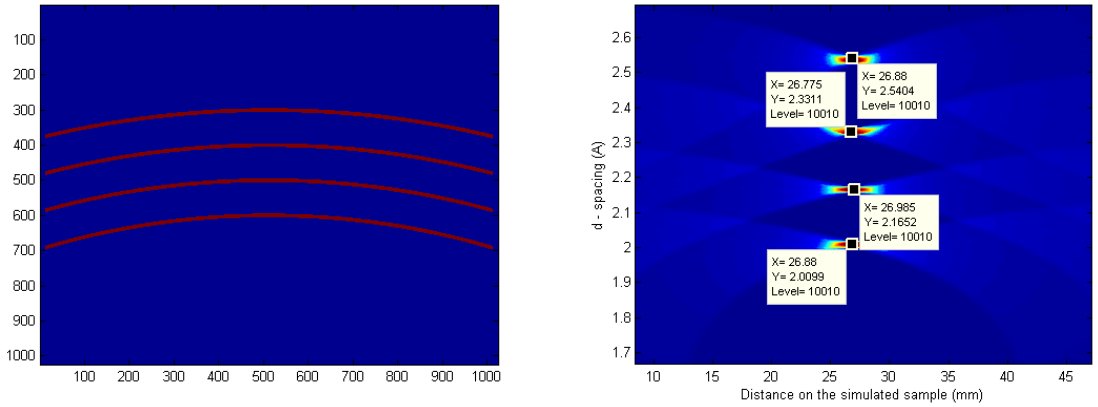

Figure 5.1. Calibration for the simulated arcs and the partitioning results when this is analysed as a sample.

Results of running virtual standard as a sample		
Pixel position	**Input d-spacing**	**Output d-spacing**
301	2.010	2.010
399	2.165	2.165
499	2.330	2.331
599	2.540	2.540

Table 5.1. Input verses output results for the simulated standard.

This confirms that the algorithms that calculate the centre point of the arcs and then link the radius of these arcs (the distance to the position of the primary beam) to material d-spacing are working correctly.

5.1.2 Simple example with different sample position

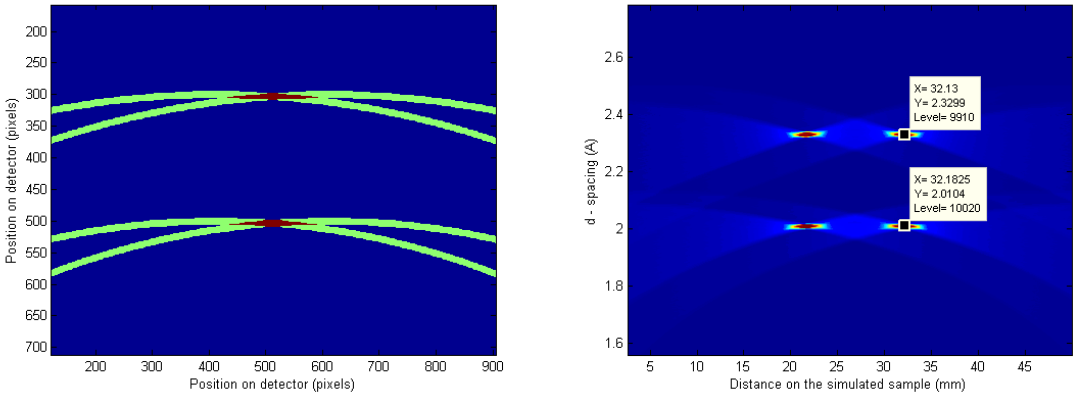

Figure 5.2. Simple two source system the produced simulation and the partitioning results.

This is the simulation of two of the arcs that could be produced if two point sources offset by 200 pixels (10.5 mm) were overlaid. This pattern would be produced if an extended beam was used to illuminate two 1 mm samples separated by 9.5 mm of poorly diffracting substrate.

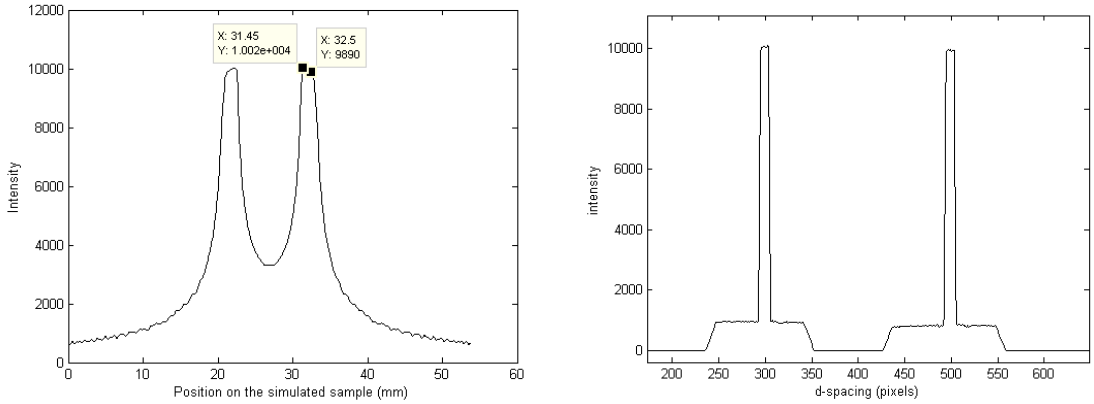

Figure 5.3. Intensity profile through the maximum peak, the left showing change with sample position and the right changes with d-spacing calculation.

A cross-section of the partitioning intensity against position output means that the size of the sample along the direction of the extended beam and the amount of non diffracting material between can be shown.

5.1.3 With different sample position and d-spacing

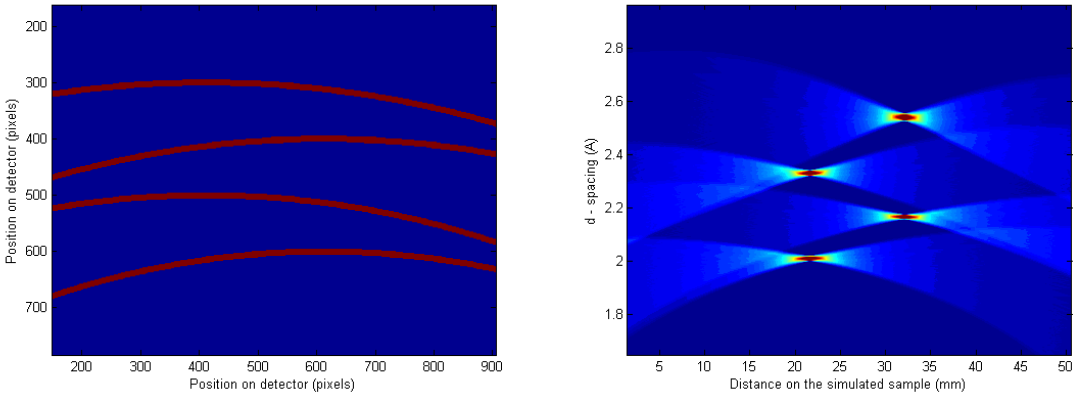

Figure 5.4. Simulation of two different point source materials and the partitioning results.

The results of the partitioning in this case show both the position of the two diffraction sources and also the d-spacing difference between them. The d-spacings are all correct to 0.01 Å when less than 2.6 Å. At smaller diffracted angles the pixel to d-spacing calculation means that this calculation is more strongly affected by the whole integer nature of the data.

Simulated illumination of larger samples

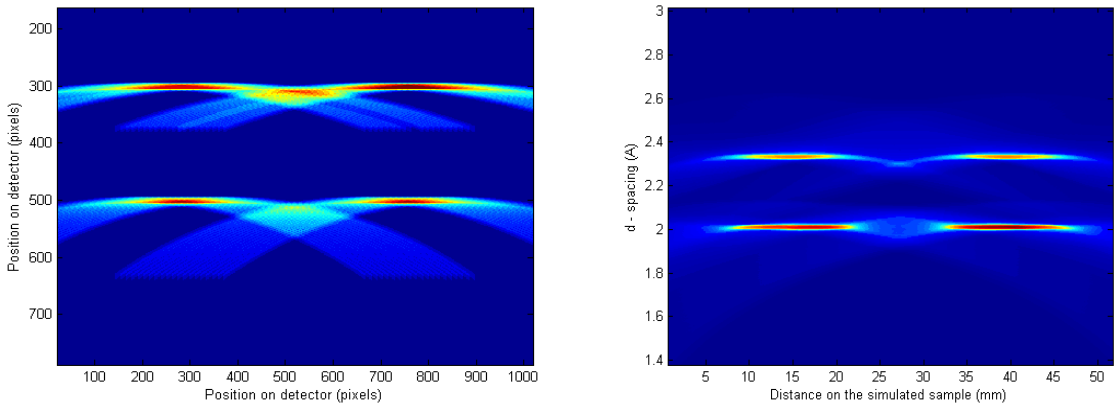

Figure 5.5. Simulations of the extended beam illumination of two 12 mm samples.

Truncated versions of the Debye rings are shown for clarity for description, in this case the simulation of two 228 pixel of diffraction response regions between 228 pixel of non-diffracting materials. This resolution is expected on the GADDS detector from two 12 mm samples and a 12 mm gap. At 90% of maximum peak intensity the size is calculated at 12 mm ± 0.2 mm.

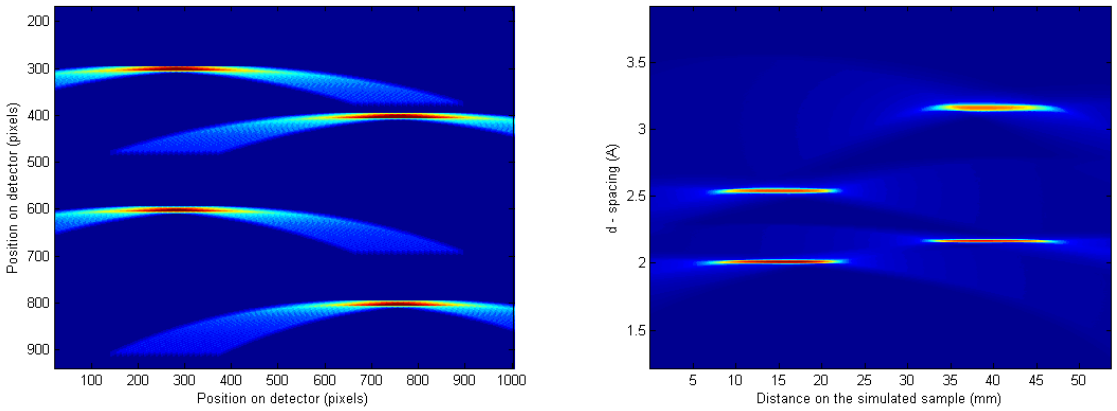

Figure 5.6. Simulation of two different 12 mm materials and the partitioning results.

As in the point source samples the position on the substrate and the angle of diffraction are clear. In all four cases the sample size can be correctly calculated to 1 mm on the substrate using the 90 % of the maximum peak strength as the boundary.

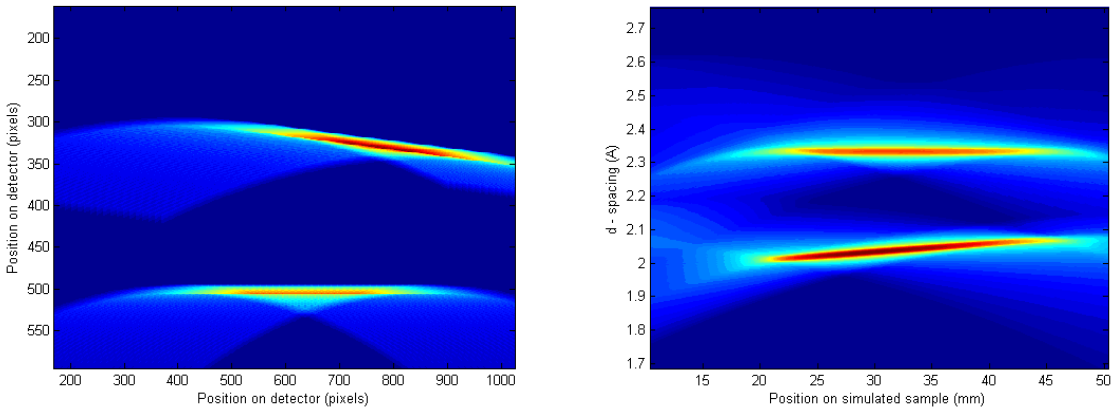

Figure 5.7. Simulation of two different sets of diffraction arcs and the partitioning results. One set of arcs is unchanged while the other has been simulated with a gradual d-spacing shift.

The aim of this simulated pattern was to demonstrate a material with a gradual d-spacing shift, this is common for samples where a gradient of elemental composition is achieved by either substitutions or interstitial additions. The size of the crystalline lattice changes with atomic substitutions as the materials obey Vergard's law. For illustrative purposes only one of the two sets of arcs has been transformed to show this effect the other having a constant d-spacing. Both the sets of arcs have been simulated so that they have the same centre point, that is, they come from the same position on the sample. Interestingly, even in this simple sample simulation where a visual inspection could give the general trend this would be unwise as the positions look distorted. The simulations look separated spatially but the two

sets of arcs are known to have the same origins but this is only apparent in the partitioned image.

5.2 Preferred orientation effects.

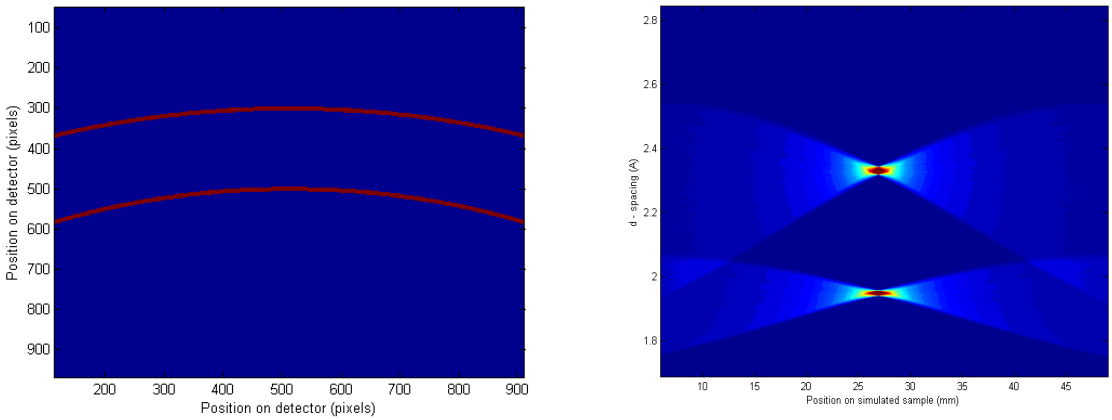

Figure 5.8. Two simulated point source arcs illustrating the results from ideal randomly orientated crystals.

Two arcs single point source ten pixels wide are shown, they have no preferred orientation. If this simulation was set to match the Bruker resolution and the angle geometry that was used to collect the real libraries the centre of the detector would be at 38° at this point the 10 pixel width would equate to a 0.019 Å total width.

Earlier tests have shown that the partitioning is more robust to preferred orientation effects when the preference of the plane concentrates most of the intensity of the Debye ring in the centre of the detector. For this reason the extent of the preference has been exaggerated in the simulations in comparison to the other ring, the two cases are still displayed together. Another characteristic of the simulations is that while that the positions of the arcs are changed it has been decided that there was no change in their intensity. This policy does not affect the ratios of the peak to background as the simulations have a perfect flat base line and therefore the principle of adding to the data collection time to improve signal does not apply. The effects demonstrated in this section are misalignment artefacts and are always proportional to maximum intensity.

Consultation of the results displayed in figure 5.8 shown the calculated d-spacings are 1.95 Å and 2.33 Å for the input. The partitioning output found this to be the case ± 0.01 Å.

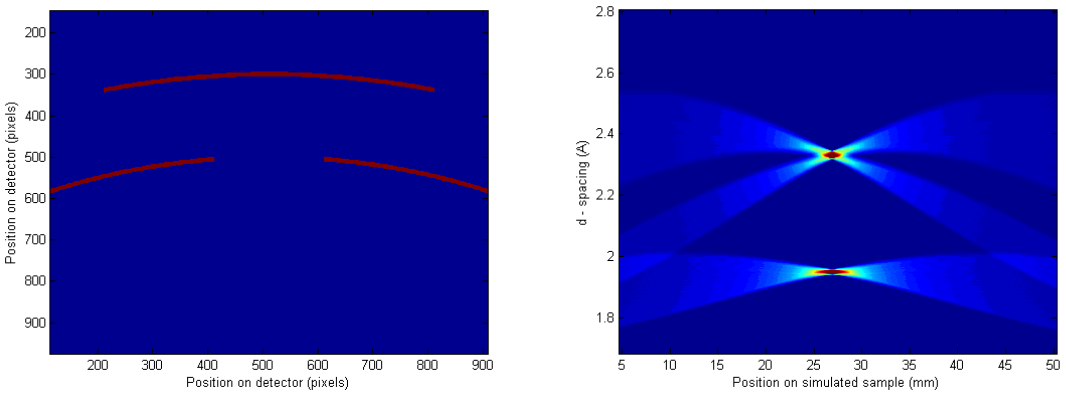

Figure 5.9. Point source simulations that demonstrate 75 % detector coverage by the Debye arcs and the corresponding partition data.

The simulation presented in figure 5.9 was produced with higher 2θ arc at 75% of the ideal and the lower 2θ arc is also at 75% of the ideal case. The d-spacing of the peak was set at 1.95 Å and 2.33 Å for the input simulation. The partitioning calculation, from the maximum, output the same result with an error of only ± 0.01 Å.

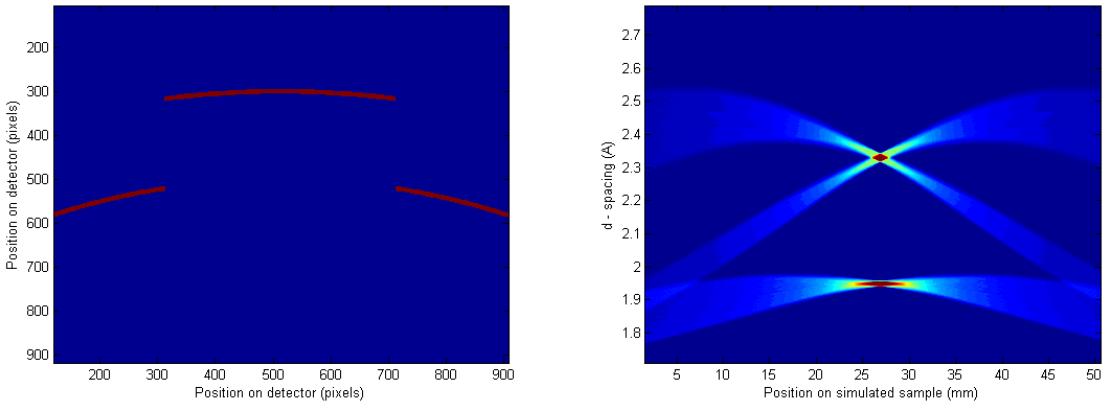

Figure 5.10. Point source simulations that demonstrates 50 % detector coverage by the Debye arcs and the corresponding partition data.

In the simulation presented in figure 5.10 both arcs were produced at 50 % of an ideal diffraction arc. The calculated d-spacing of the peak are input at 1.95 Å and 2.33 Å. Form the max intensity, the partitioning output found this to be the case with an error less than ± 0.01 Å.

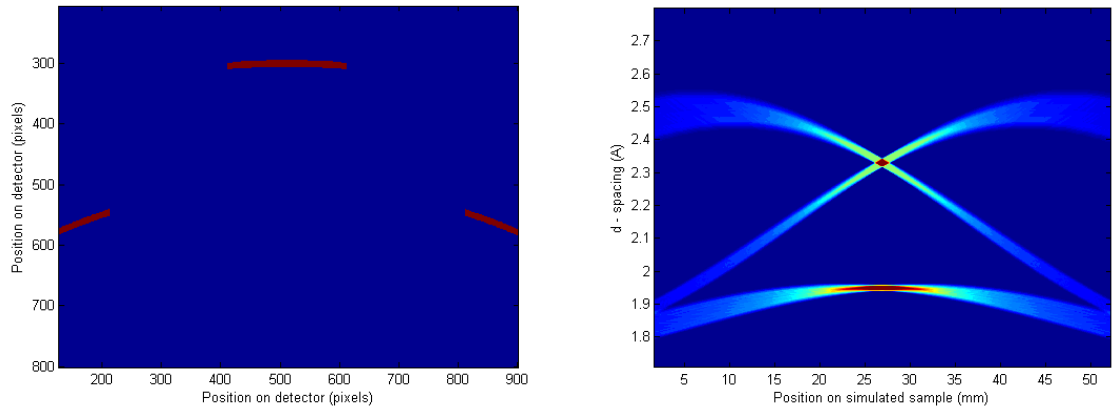

Figure 5.11. Point source simulations that demonstrates 25 % detector coverage by the Debye arcs and the corresponding partition data.

Figure 5.11 shown an input simulation with both arc at 25 % of the ideal case. When the partitioning was used to calculated d-spacing form the maximum intensity of the peak, the results are still 1.95 Å and 2.33 Å correct to ± 0.01 Å. These results are correct despite the clear change in the distribution of the partitioning artefact and a change in its intensity.

The following are simulations of a sample with the same arrangement and scale of preferred orientation as seen in the proceeding point source examples but this time under the extended beam illumination. Figure 5.12 shows the idealised sample arrangement with a totally random crystalline arrangement. Figures 5.13 – 5.17 show an increasingly pronounced orientation in the crystal structure.

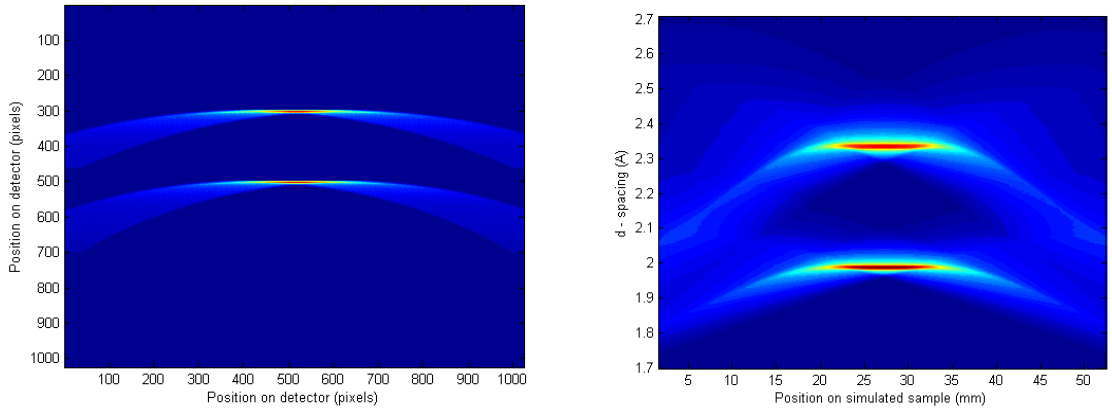

Figure 5.12. A simulated set of superimposed idealised Debye rings as would be expected from 12 mm extended beam illumination.

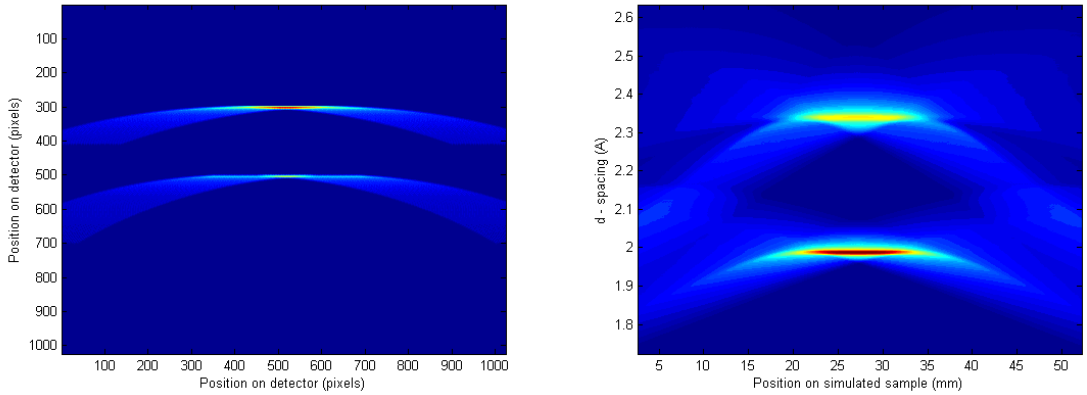

Figure 5.13. Simulations of higher angle diffraction with 83.3 % of the original arcs and the lower angle with 91.6 % of the arcs displayed.

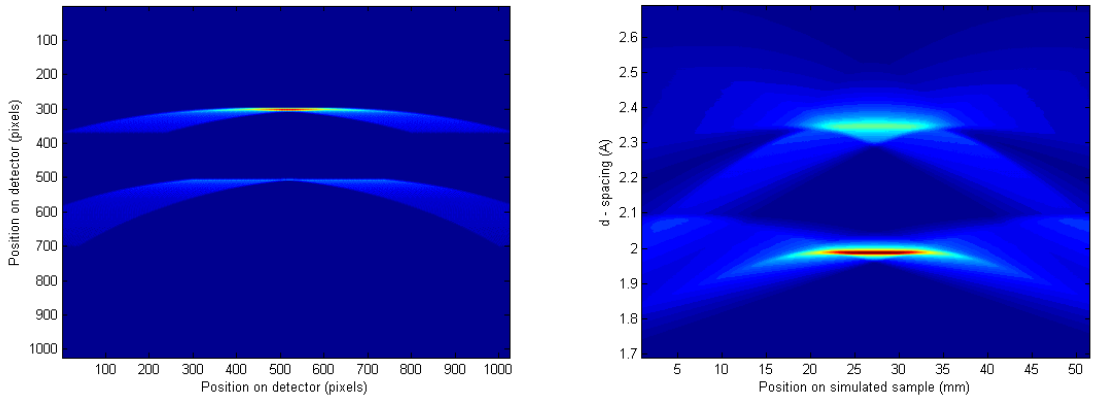

Figure 5.14. Simulations of higher angle diffraction with 66.6 % of the original arcs and the lower angle with 83.3 % of the arcs displayed.

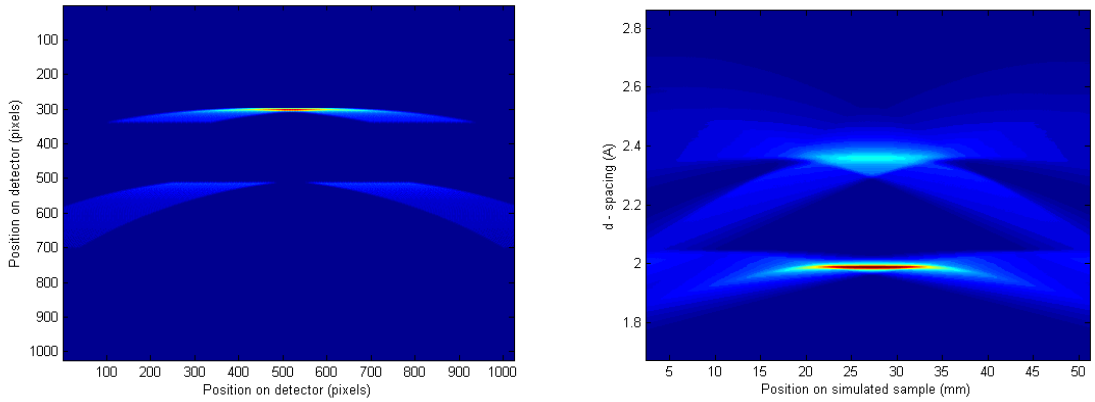

Figure 5.15. Simulations of higher angle diffraction with 50 % of the original arcs and the lower angle with 75 % of the arcs displayed.

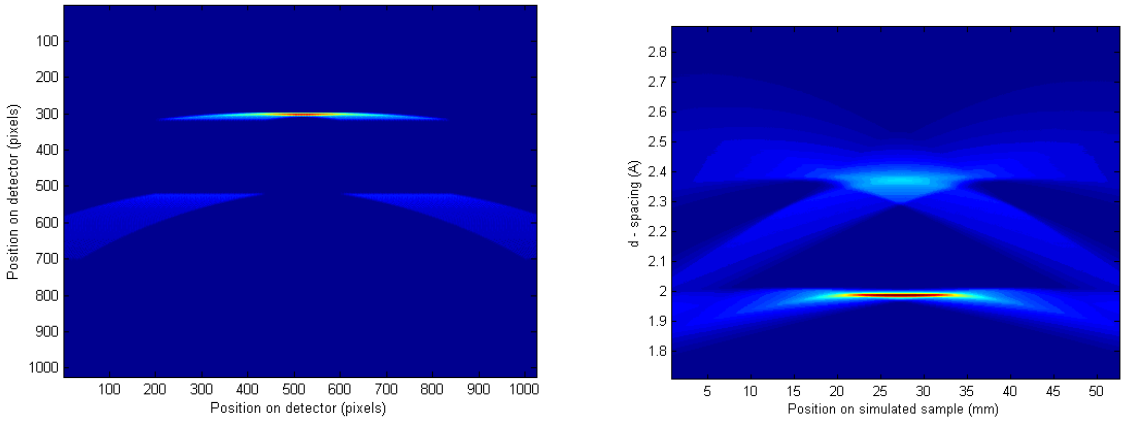

Figure 5.16. Simulations of higher angle diffraction with 33.3 % of the original arcs and the lower angle with 66.6 % of the arcs displayed.

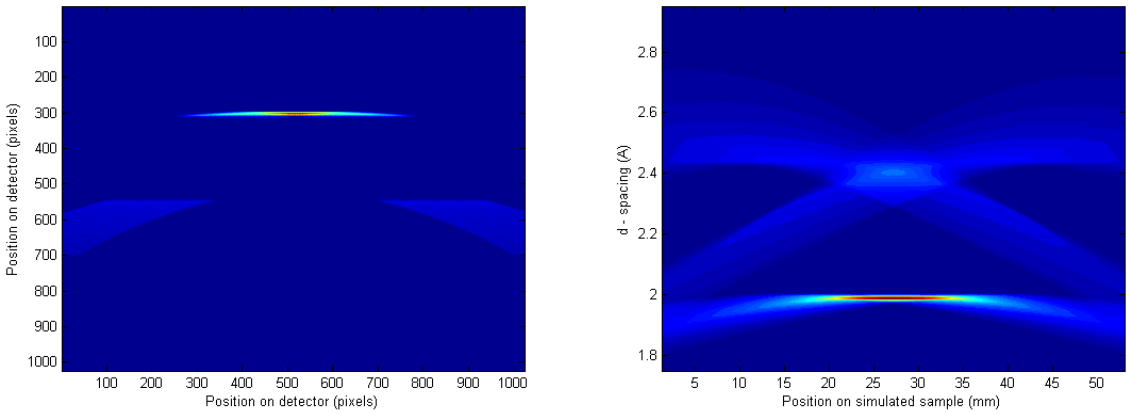

Figure 5.17. Simulations of higher angle diffraction with 25 % of the original arcs and the lower angle with 50 % of the arcs displayed.

Direct observation of the partitioning outputs (figure 5.12 to 5.17) shows a change in both the position and intensity of the artefacts that are present in addition to the desired results.

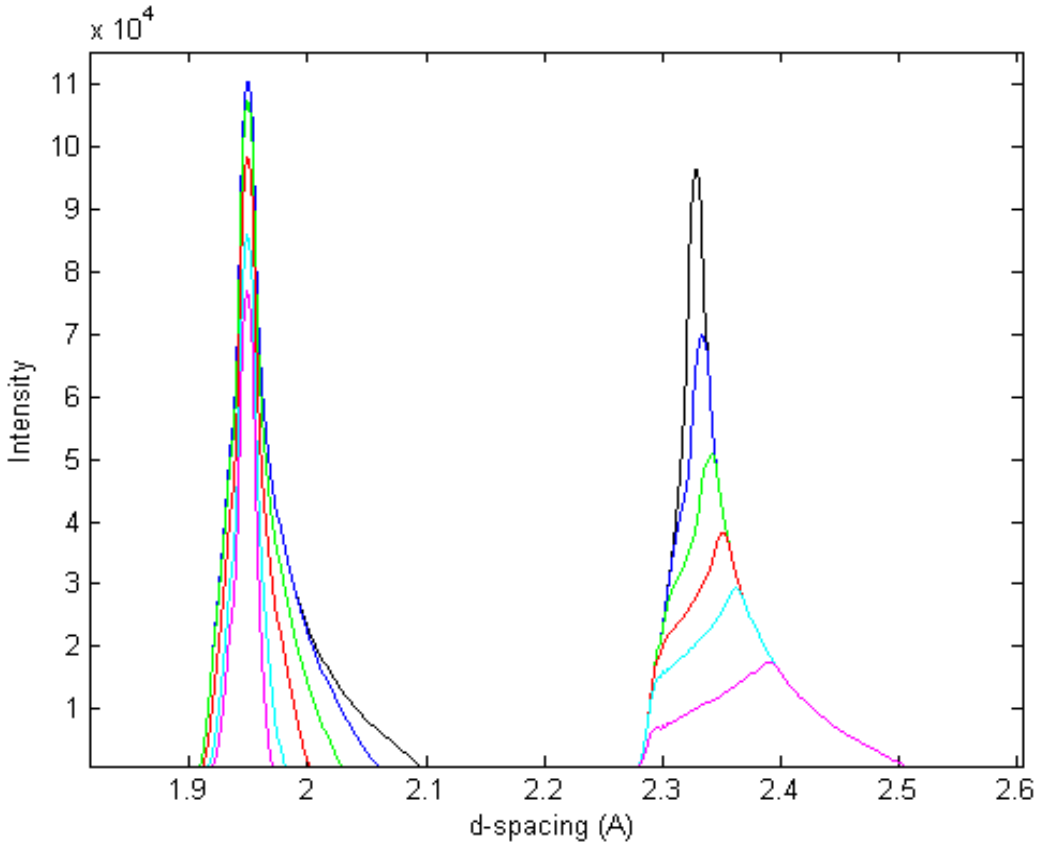

Figure 5.18. Compilation of the intensity versus d-spacing calculation for all cases.

This left series in figure 5.18 shows a cross-section of the non-orientated sample (black) and the orientated examples from 83.3% (blue) to 25% (pink). The right series shows the non-orientated example (black) and the preferred samples ranging from 91.6 % (blue) to 50 % (pink). The d-spacing calculation taken from the peak maximums are tabulated below.

Diffraction pattern confined to the middle of the detector		**Diffraction pattern confined to the edges of the detector**	
Amount of ideal arc present (%)	**d-spacing (Å)**	**Amount of ideal arc present (%)**	**d-spacing (Å)**
100	1.95	100	2.331
83.3	1.95	91.6	2.334
66.6	1.95	83.3	2.341
50	1.95	75	2.353
33.3	1.95	66.6	2.360
25	1.95	50	2.391

Table 5.2. How the percentage of the Debye ring on the detector effects the calculation of d-spacing.

5.3 Application of partitioning to Phantom Samples

5.3.1 Profile of the beam

Here are displayed the results used to calculate the length, shape and the intensity profile of the extended beam on the samples. The measurements have been made using the diffraction profiles on standard samples rather than direct measurement as it is only the primary beam that illuminated the sample intensely enough to give rise to measurable diffraction through the partitioning method that is of interest.

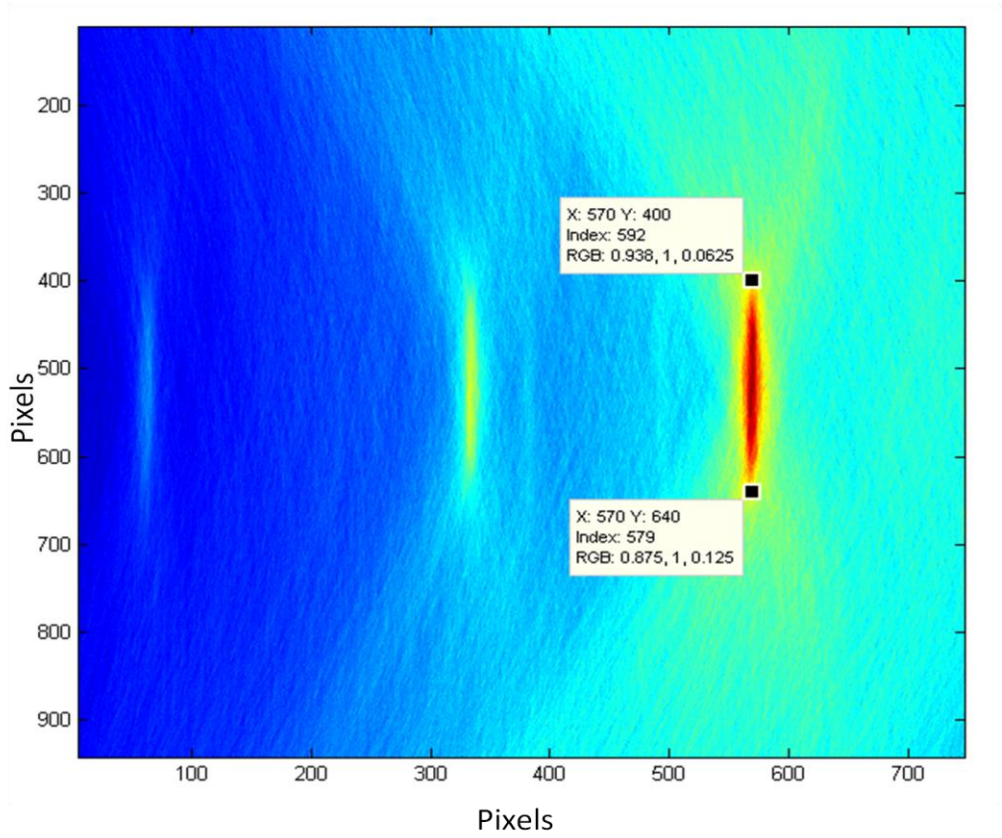

Figure 5.19. Partitioning result from an extended beam illumination of Al_2O_3 standard.

Figure 5.19 shows the diffraction profile from a 12.6 mm section of Al_2O_3. This is so that the intensity of the beam, when producing diffraction off a standard substrate, is shown. In this case the illuminated area available for diffraction is only half the estimated beam length. So here the sample is the limiting factor in the diffraction profile.

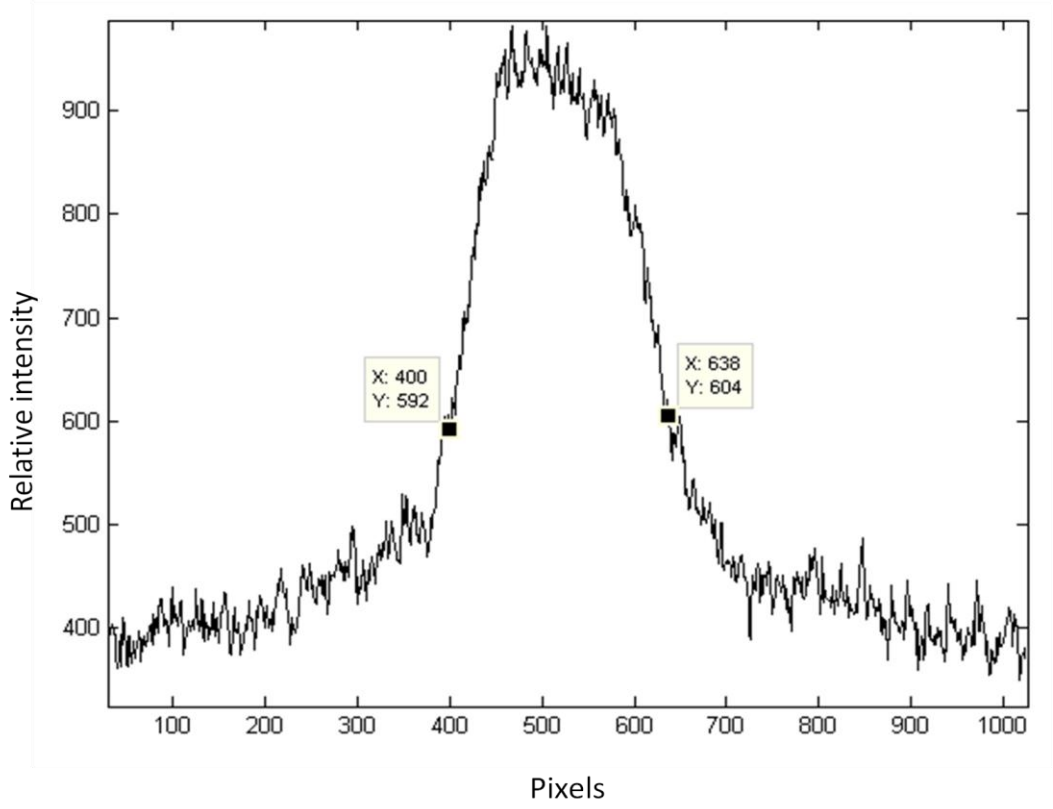

Figure 5.20. Partitioning result from an extended beam illumination with the intensity cross-section through the most intense peak (miller index 116).

The intensity cross-section at pixel 570 was chosen as this line contains the matrix maximum. The value of pixels that most closely relates to the actual width of the sample is at 60 % of the peak maximum.

Assuming a homogeneous sample, any intensity variation at constant d-spacing would indicate variations in intensity along the interrogating X-ray beam and this could be used subsequently as a correction factor.

5.3.2 Calculation of the extended beam length

The calculation of the extended beam length has been carried out in two ways. This first way is directly and is independent of pixel to true distance calculation. An aluminium oxide plate is rastered through the beam along its extended direction this was carried out in 2 mm increments. The starting and ending positions were chosen where they were too far to the

sides of the beam to be illuminated. From the first and last positions that diffraction occurs the length of the extended beam can be calculated.

Debye rings are first detected at position 9 and last detected at 43 which gives a 68 mm difference. The plate is 45.4 mm long so the beam length was calculated as;

22.6 mm < extended beam length < 26.6 mm

The second method of calculation is a measurement of the beam length calculated directly from the partitioned data. This method requires a pixel to distance conversion that has been calculated to be 52.5 µm per pixel from earlier experiments.

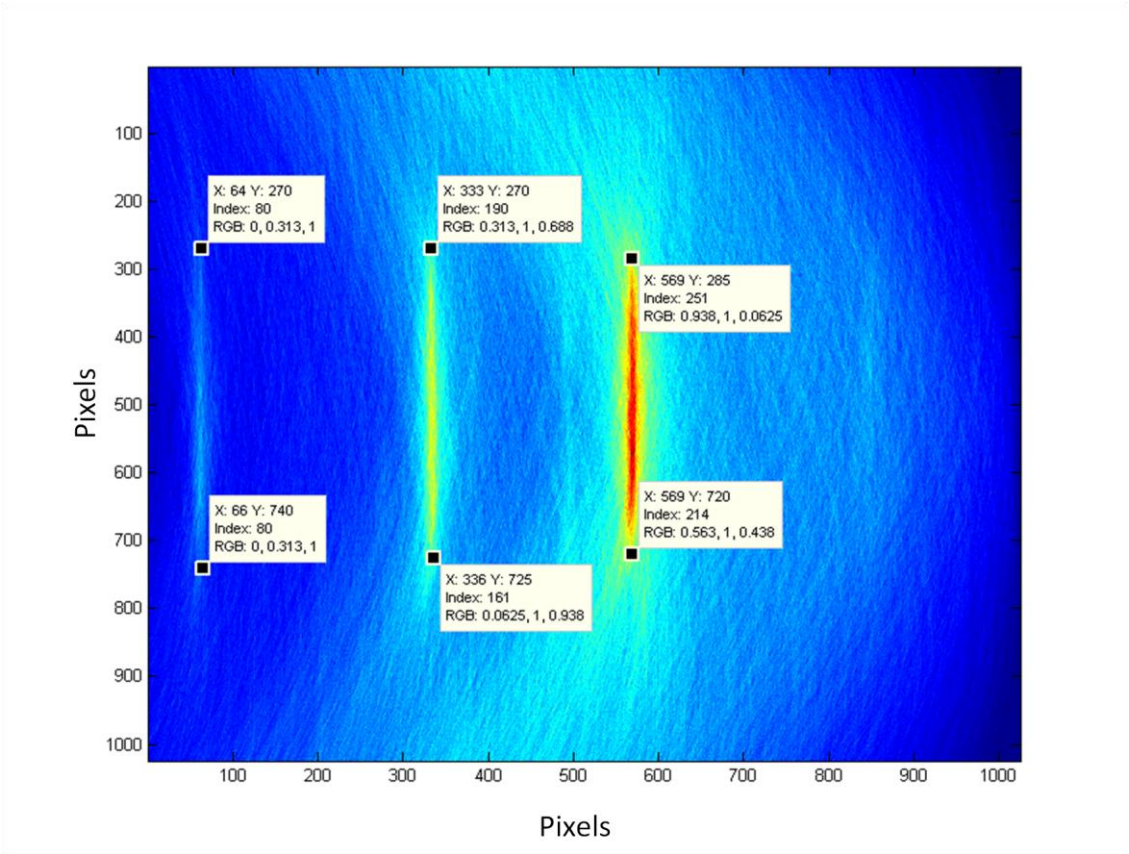

Figure 5.21. Extended beam illumination of Al_2O_3 standard that is larger than the beam length.

The calculation was carried out on the three main peaks of the Al_2O_3 with 5 repeats of each. The graph displayed in figure 5.21 is an illustration of the median result.

Peak	Beam length average (pixels)	Beam length average (mm)
Al_2O_3 (104)	435	22.84
Al_2O_3 (113)	455	23.89
Al_2O_3 (116)	470	24.68

Table 5.3 Beam length calculation from different diffraction peaks.

5.4 Choosing the size of the virtual arc

In the simulated cases, the width of the virtual arc was kept thin so as to achieve maximum resolution. However, in real samples, the some of the Debye rings are thick and otherwise imperfect. The results of overlaying an ideal arc may not give the best results. Inconsistencies that are present in real rings can be smoothed by making the virtual arcs from which the intensities are summed thicker. This may match the more closely match the Debye rings and therefore avoid artefacts picked up by an overly precise methodology.

The advantage gained by changing the size of the overlaid arcs will inevitably have to be balanced by the adverse affects on the resolution. So as an optimised compromise can be made the effect of changing the virtual arc is shown.

The slices taken through the intensity contour map (figure 5.22) were taken as a 5 pixels thick average plot. This was done as a one pixel thick section has been found to be unrepresentative of its neighbours, in some cases.

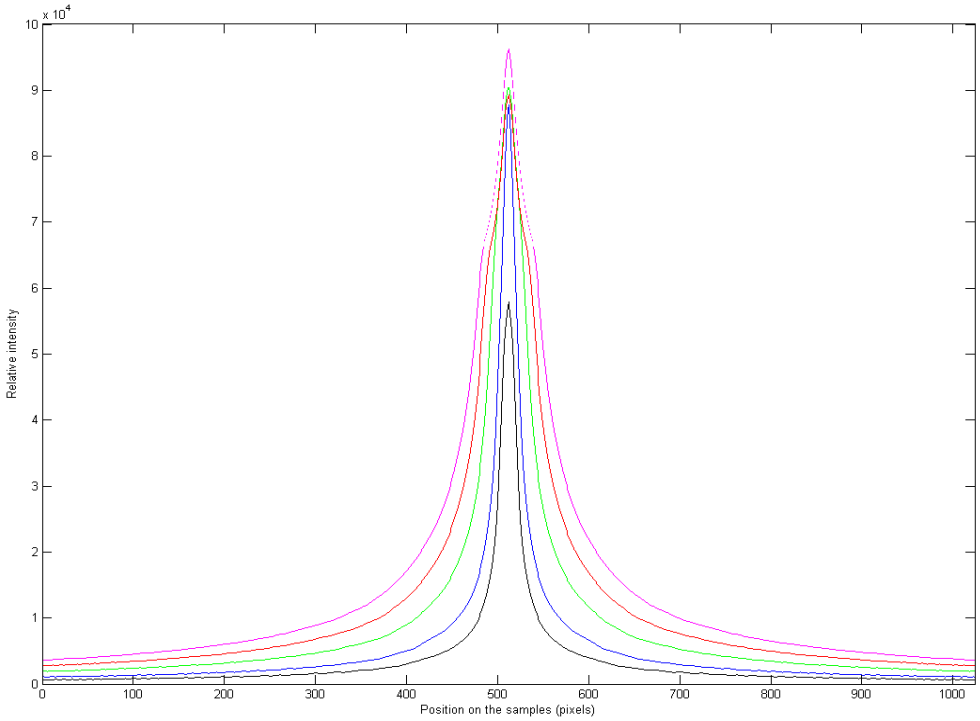

Figure 5.22. Effect of virtual width arc on the partitioning position resolution. 2 pixels shown in black, 4 pixels blue, 8 pixels green, 16 pixels red and 32 pixels purple.

Figure 5.22 shows the effect of different virtual arcs with respect to sample position resolution. In all cases the position indicated by the centre of the peak was correct to one pixel but the peak widths varied significantly. A quantitative measure of these increasing peak widths is displayed in table 5.4.

Width of overlaid arc in pixels	Width of resulting response peak (full width half maximum)	
	pixels	Distance on sample for Bruker GAADS
2	12	0.630 mm
4	22	1.155 mm
8	42	2.200 mm
16	60	3.150 mm
32	78	4.100 mm

Table 5.4 Quantitative calculation of resolution under different virtual arc conditions.

The same resolution test was carried out for the calculation of d-spacing, as figure 5.23 shows. For this the intensity map was cross-sectioned along the axis in such a way that the position on the sample value remains constant. The results show an increase in the output peak widths with respect to d-spacing as the virtual arc width increases

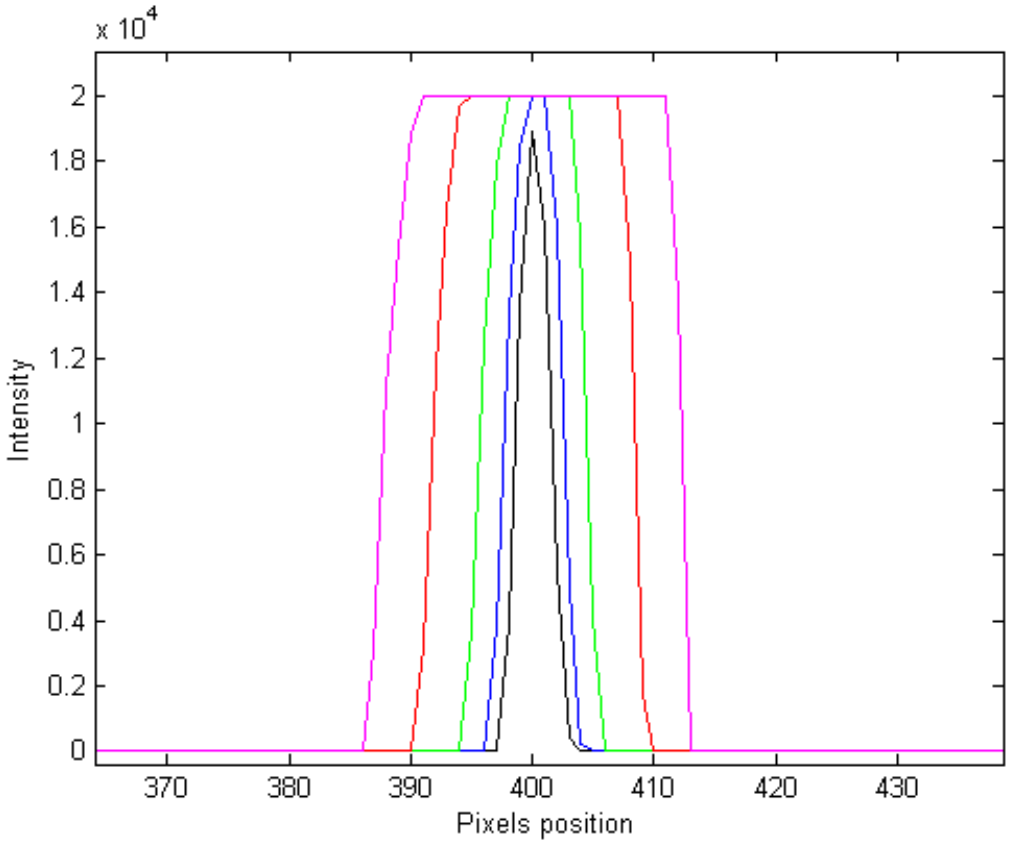

Figure 5.23. Effect of virtual arc on the partitioning d-spacing resolution.

This increasing width has been shown to be linear for pixels but this is not linear for d-spacing due to the sin function in Bragg's law. Because of this an example d-spacing of 2.55 Å has been used to illustrate this effect. The results of this case are listed in table 5.5.

Width of overlaid arc in pixels	Width of resulting response peak (full width half maximum)	
	pixels	d-spacing calculation for Bruker GAADS (at 2.55 Å)
2	3	0.003
4	5	0.005
8	8	0.008
16	16	0.016
32	32	0.032

Table 5.5. Quantitative calculation of d-spacing resolution for a 2.55 Å peak, under different virtual arc conditions.

5.5 Optimisation of the beam incident angle

The series of diffractograms seen in figure 5.24 are examples of the partitioning results from an aluminium oxide sample that has been illuminated with a range of different incident angles. In all cases the two dimensional intensity output has been sectioned at a fixed position on the sample to give an output analogous to a conventional diffractogram. From this how the incident angle effects characteristics such as signal to noise ratio and peak widths can be determined.

30 degrees

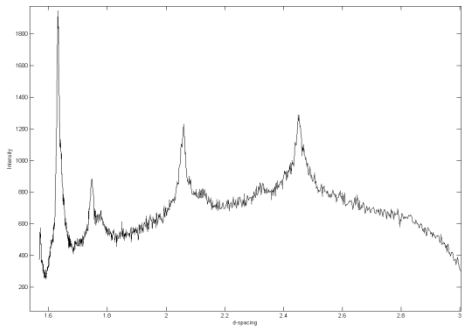

25 degrees

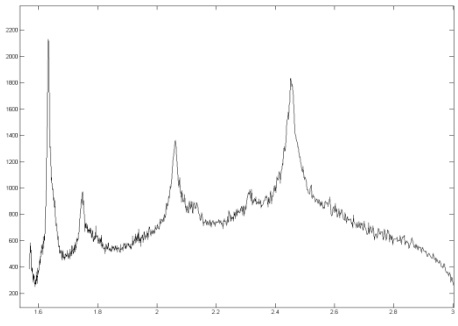

20 degrees

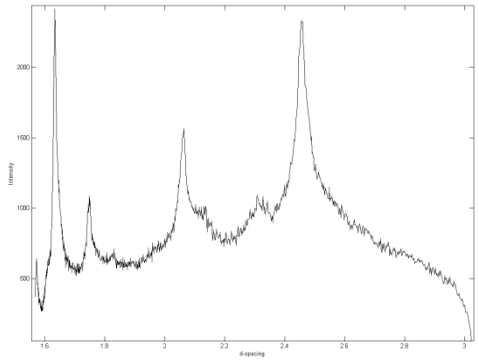

15 degrees

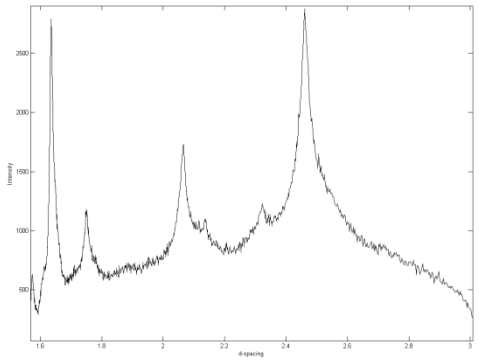

10 degrees

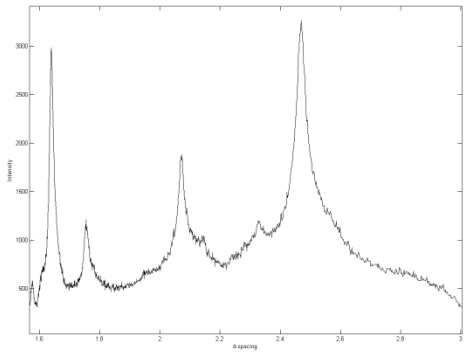

5 degrees

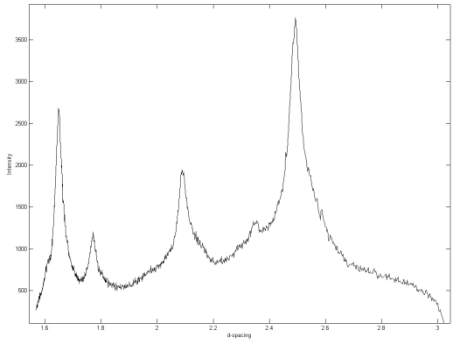

Figure 5.24. Graphs illustrating the effect of incident beam angle.

Incident angle (degrees)	FWHM of peak Al_2O_3 (104) in Angstrom	FWHM of peak Al_2O_3 (116) in Angstrom
5	0.053	0.018
10	0.048	0.014
15	0.049	0.010
20	0.053	0.009
25	0.044	0.009
30	0.041	0.010

Table 5.6. Two examples of the quantitative effect of incident beam angle on peak widths.

Changes in the relative intensity of the different planes can be seen as the sequence of diffractograms examined in figure 5.24. This effect is due to the lack of homogeneity with depth in the sample chosen. Table 5.6 gives an indication of the widths of two intense peaks under the varying incident angle. No significant trends in peak resolution are seen the small

change in the width of the peak from the 116 reflection can be explained by its change in intensity.

One area where incident angle can be seen to be significant is the analysis of samples that are not correctly aligned with the instruments focusing point.

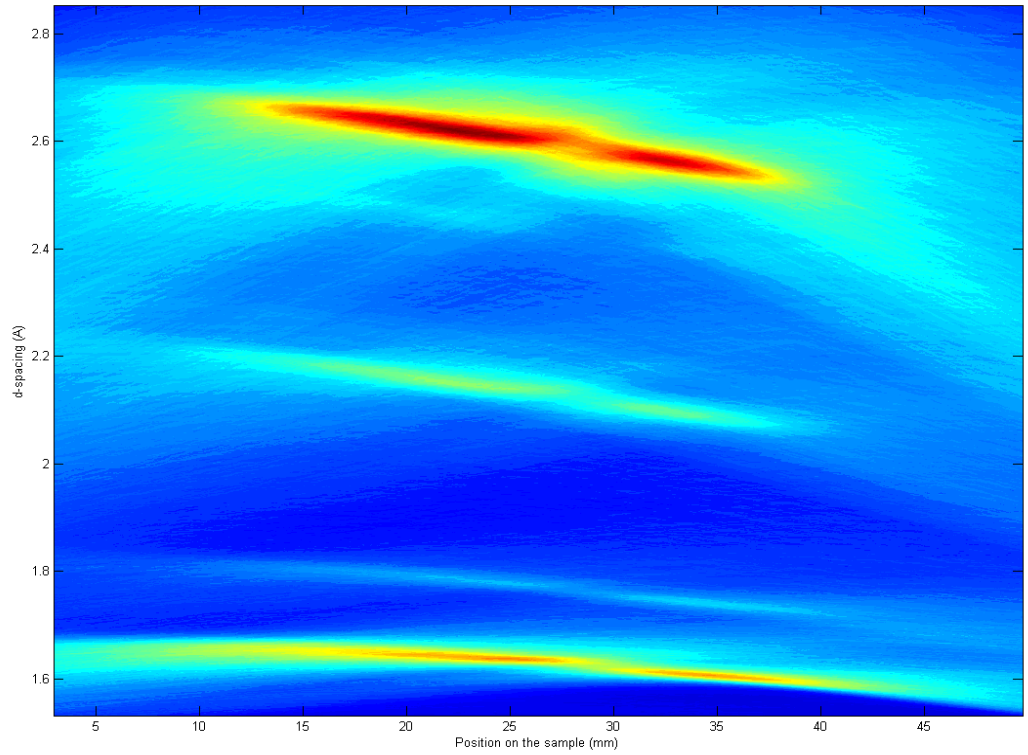

Figure 5.25. Illustration of a sample displacement error of 2° with an incident angle of 5°.

Figure 5.25 shows that an only 2° tilt on the sample produces the marked effect when an incident beam angle of 5° has been chosen. In cases of low incident angle sample alignment should be prioritised.

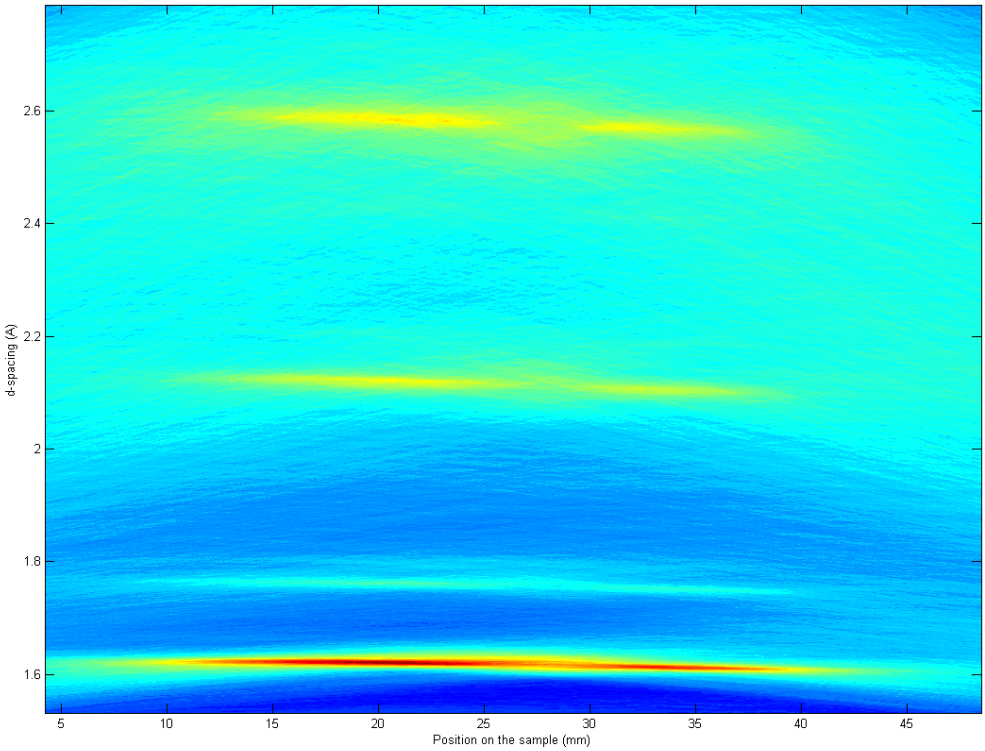

Figure 5.26. Illustration of a sample displacement error of 2° with an incident angle of 30°.

Figure 5.26 shows the same 2° misalignment but from 30° incident angle. With this geometry the movement of the X-ray illumination and the corresponding displacement error is smaller.

5.6 Addition of a knife edge

A lower signal to noise ratio has been observed in extended beam illuminations. This includes the illumination of a conventional point sample with the extended beam. Improvements to the signal have been shown with the use of a knife-edge scatter reduction method. Figure 5.27 shows the reduction in noise that can be achieved for a variety of positions.

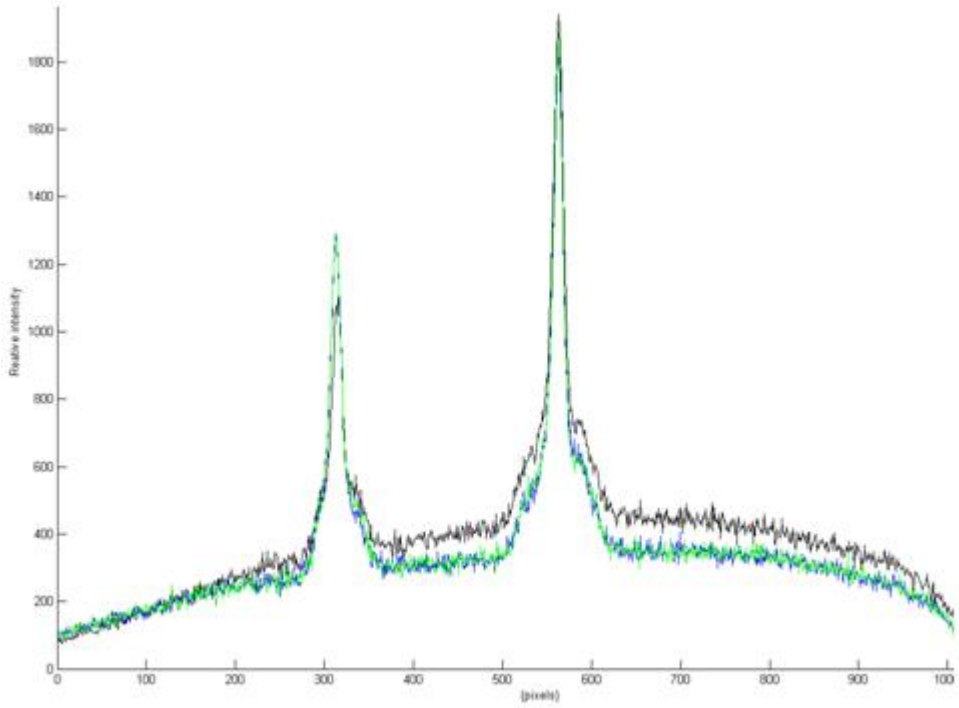

Figure 5.27. Graph of a typical diffractogram without knife edge (black), at a height of 2 mm (blue) and at 1 mm (green) from the sample.

Knife-edge position	Max intensity to background ratio
None	4.63
2 mm from sample surface	5.48
1 mm from surface	5.38

Table 5.7. Quantitative effect of the knife edge height.

The results shown in table 5.7 give an indication of the small but still useful improvements in signal strength that can be achieved with the knife edge in a central position.

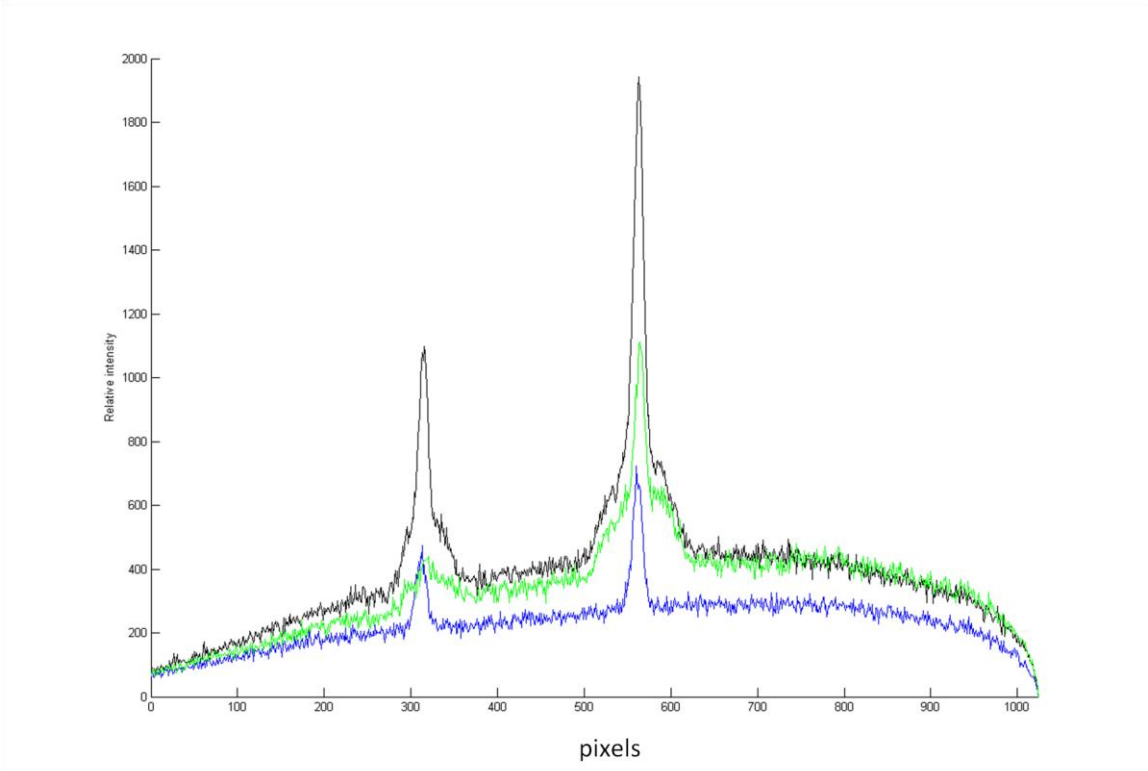

Figure 5.28. Graph of a typical diffractogram with knife edges at three positions across the sample.

When examining figure 5.28 it can be seen that position one (shown in blue) blocks some of the incoming beam and reduces the intensity generally. Position two (shown in black) blocks scatter only and has a small positive effect. Position three (shown in green) reduces the desired diffracted peaks and in an example of bad positioning the interference effects the higher angle diffraction more.

5.7 Resolution characterisation

Resolution characterisation using the Si powder between Al_2O_3 plates arrangement. The plates start 1.929 mm apart with the didtance between then and therefore the amount of Si illuminated being reduce to 1.074 mm. A rapid drop off in the signal intensity over this range is clearly demonstrated in table and figure 5.29.

Sample number	Si powder sample size (mm)
1 (black)	1.929
2 (blue)	1.693
3 (green)	1.490
4 (red)	1.311
5 (pink)	1.074

Table 5.8. The sizes of the Si powder section.

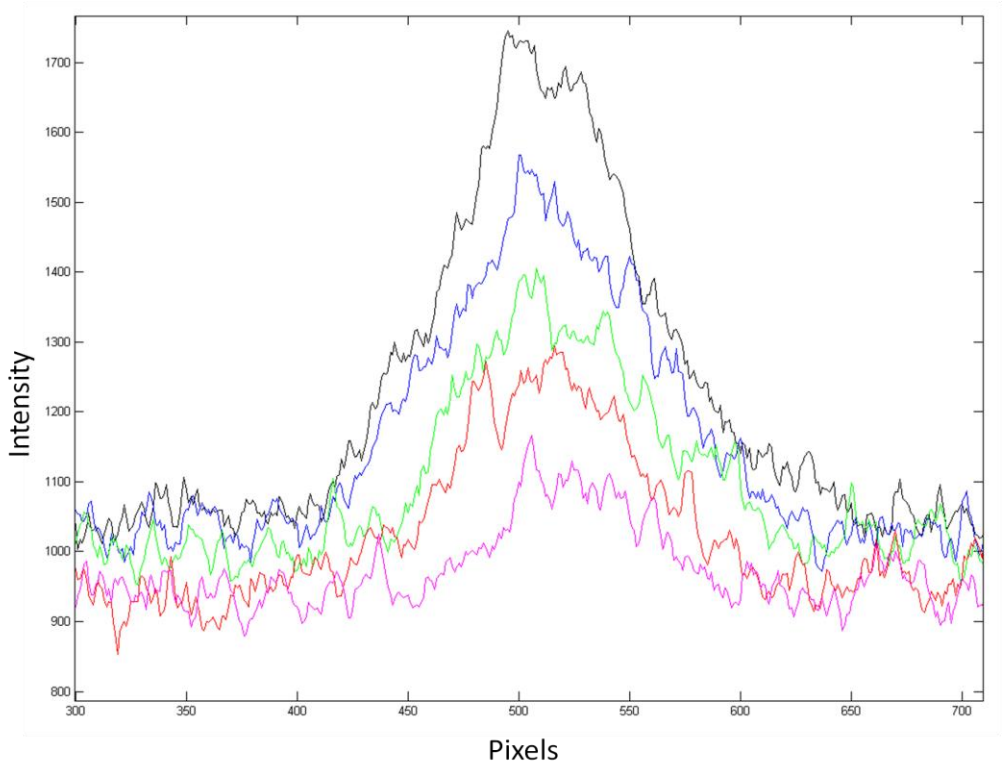

Figure 5.29. Examples of diffraction peaks for the size of the diffraction material.

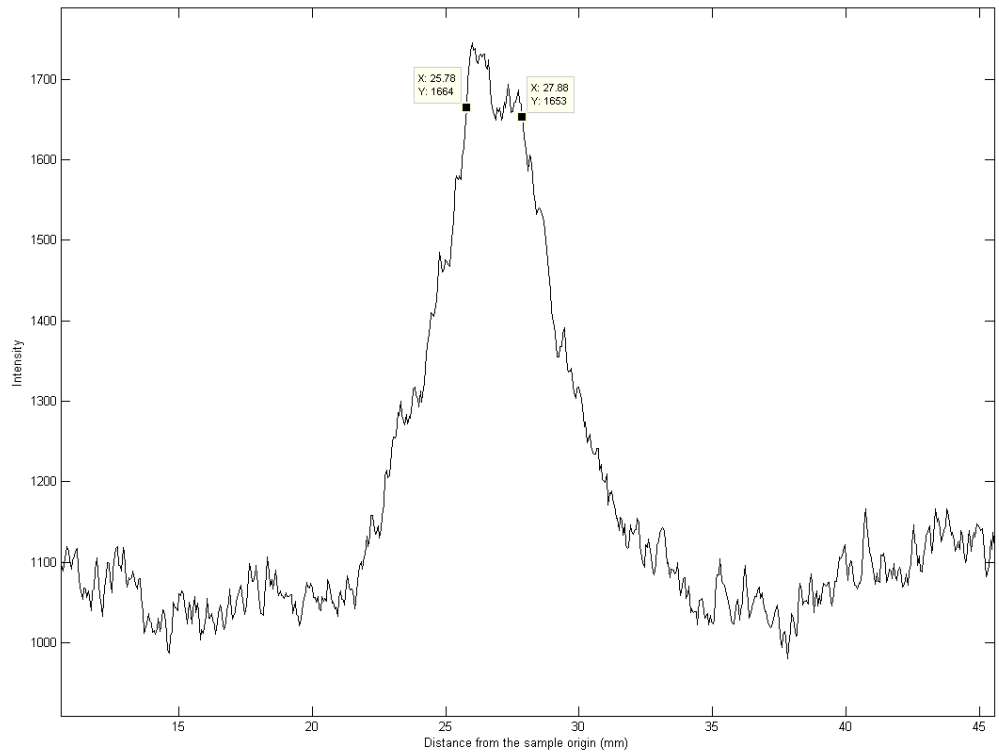

Figure 5.30. This shows the result of a 1.9 mm gap. The 90% intensity value gives the correct width that corresponds to the real sample.

As the sample intensity profile of the partitioned data does not have a clear edge as would be seen in conventional raster scanned data. From these Si Al_2O_3 samples the intensity that characterises this edge can be determined. An illustration of this is displayed in figure 5.30.

Slit width investigation

The results here demonstrate the width of the slit masking the X-ray source and its effect on the data collection time and the resolution of the partitioning method. This has been investigated for both d-spacing and for position on the substrate calculation. Here is compared data collected from a slit of 0.05 mm with the intensity of the signal achieved in 60 seconds of data collection on two Al_2O_3 standards separated by a non-diffracting area. Both the diffracting areas are 5 mm long separated by a 5 mm gap.

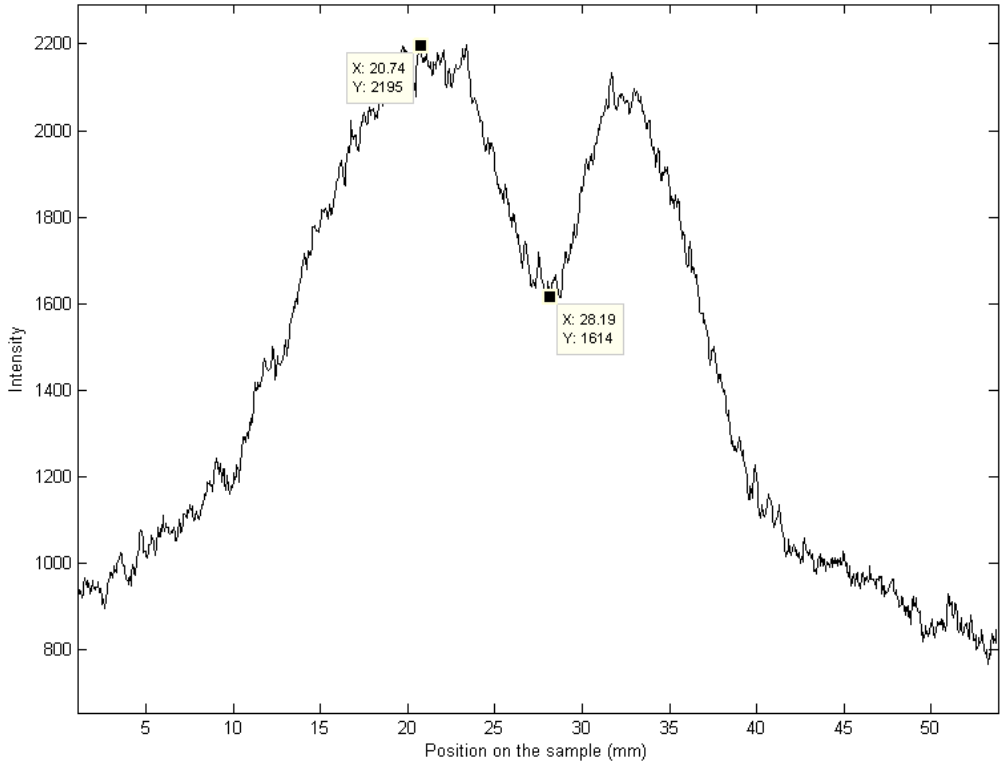

Figure 5.31. This shows the profile along the substrate at a fixed d-spacing for the Al_2O_3 (116) peak under 0.05 mm illumination.

As with the simple test of the resolution in the previous section a ratio between the relative intensity of the central amorphous region and the diffraction standards can be produced. This time the changes in the ratio have been considered in relation to changing the primary beam collimation. The poorly diffracting area gives an intensity of 73.53% of the diffraction peak maximum for the 0.05 mm slit. The graph figure 5.31 shows the position on the sample

resolution. The d-spacing resolution for the 0.05 mm slit is given by figure 5.32 and table 5.9 gives the measurement of these peak widths.

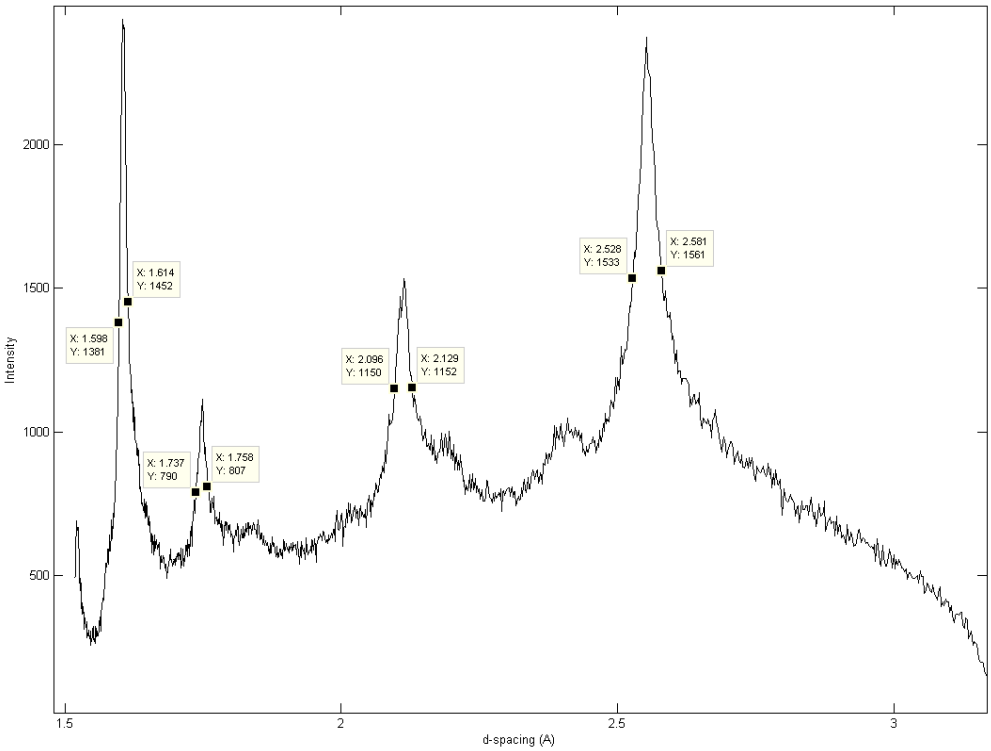

Figure 5.32. This graph shows the d-spacing resolution for the 0.05 mm slit.

D - spacing resolution for the 0.05 mm slit	
Peak	**Full width half maximum (Å)**
Al_2O_3 (104)	0.016
Al_2O_3 (113)	0.021
Al_2O_3 (024)	0.033
Al_2O_3 (116)	0.053

Table 5.9. D-spacing resolutions for the Al_2O_3 under 0.05 mm slit illumination.

The same resolution experiment was carried out but this time with a 0.2 mm slit, the diffraction results of this experiment are display in figure 5.33 for the position on the sample resolution and in figure 5.34 when the d-spacing resolution was considered.

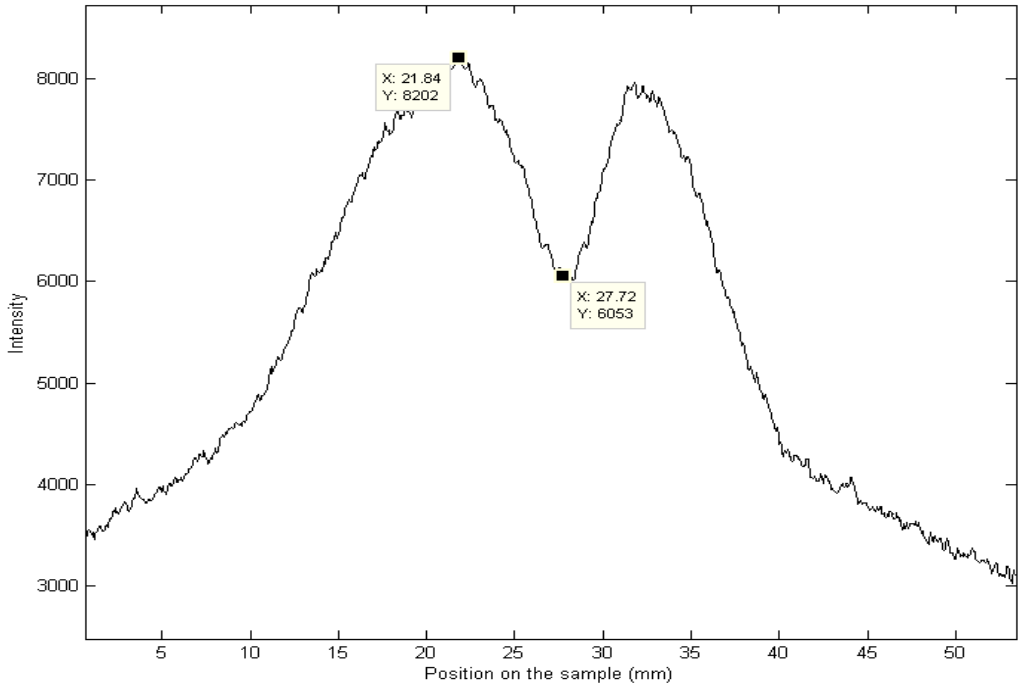

Figure 5.33. This shows the profile along the substrate at a fixed d-spacing for the Al_2O_3 (116) peak under 0.2 mm illumination.

When the position on the sample resolution was investigated the non-diffracting area was found to be 73.80% of the peak maximum, as shown in figure 5.33. The ability to resolve the two separate Si cells is not affected by the change in X-ray illumination footprint.

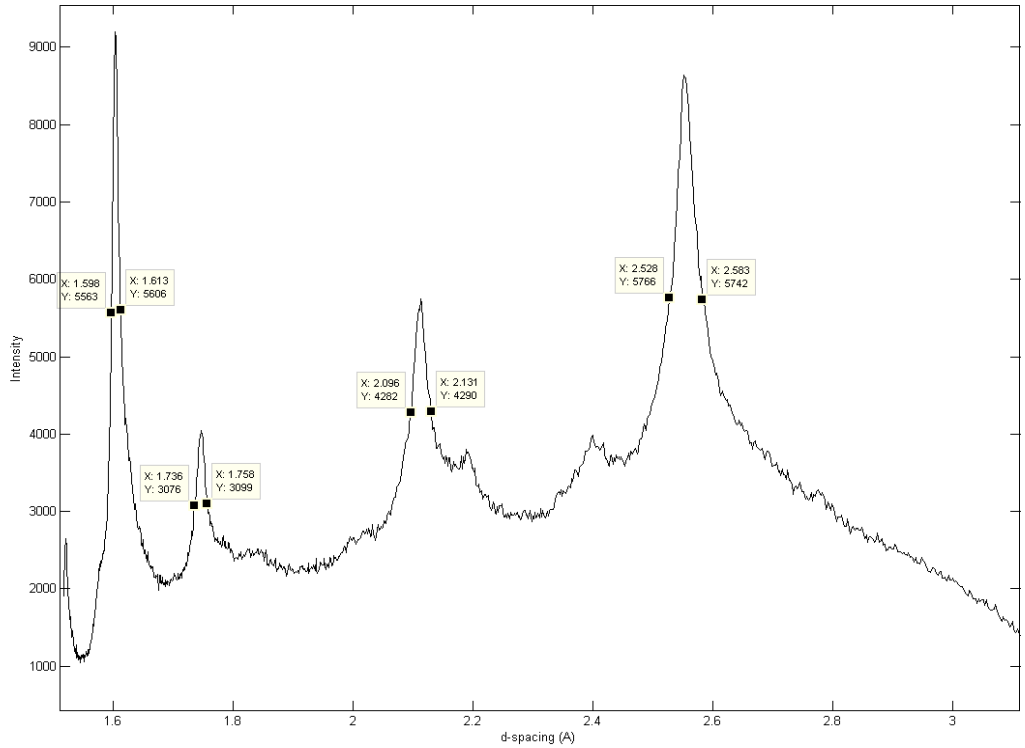

Figure 5.34. The graph shows the d-spacing resolution for the 0.2 mm slit.

As expected, the total photon count is higher when the sample is illuminated with the larger slit. This was seen when the 0.2 mm slit (figure 5.34) was compared with the 0.05 mm colimation (figure 5.32).

d - spacing resolution for the 0.2 mm slit	
Peak	**Full width half maximum (Å)**
Al_2O_3 (116)	0.015
Al_2O_3 (024)	0.022
Al_2O_3 (113)	0.035
Al_2O_3 (104)	0.055

Table 5.10. The d-spacing resolutions for the Al_2O_3 under 0.2 mm slit illumination.

Comparison of the widths of the diffraction peaks collected with the two areas of illumination (table 5.9 and 5.10) shows that there is not a marked difference in the two approaches. From this it can be deduced that the extended beam portioning method is robust with regard to this variable, and therefore the approach allows flexibility when optimising this aspect of the experimental setup.

5.8 Matching the standard detector angle to the data collection angle

This is a geometric effect that can mean that the virtual arc and the collected diffraction arcs do not fully overlay. This gives inaccuracies when the detector is different for the data collection of the samples and the production of the standards.

This image is the Si powder between two Al_2O_3 plates. The graph shown in figure 5.35 is as expected for the 38° collection. The effect of the miss fitting can be illustrated in the second (46°) collection, figure 5.36, where the peak produced by diffraction from the Si (111) plane is distorted.

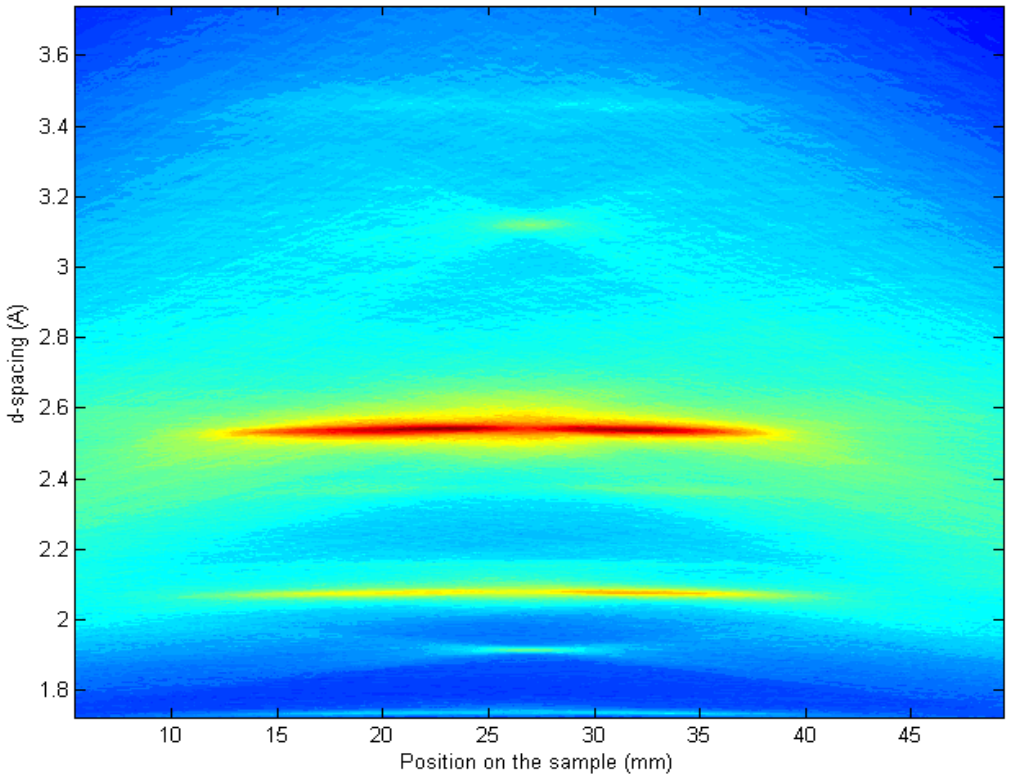

Figure 5.35. Mixed Al_2O_3 and Si phantom sample collected with the detector at 38° and partitioned with the 38° Standard.

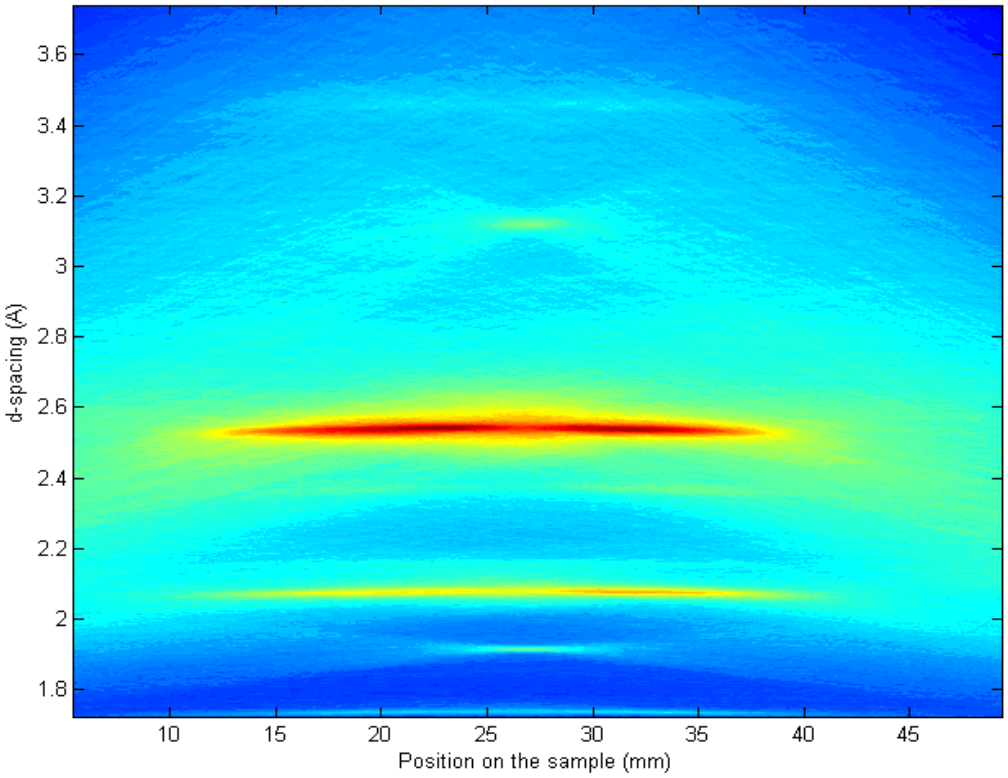

Figure 5.36. Mixed Al_2O_3 and Si phantom sample collected with the detector at 46° and partitioned with the 38° Standard.

Resolution data can be seen in figure 5.37 this is the Al_2O_3 (104). For clarity the data set has been smoothed using least-squares digital polynomial smoothing filters (Savitzky-Golay) with a third order polynomial spread over 51 data points. This method is popular in the processing of diffraction data as Savitzky-Golay filters achieve high levels of stationary white noise reduction while preserving peak maximum position. [154]

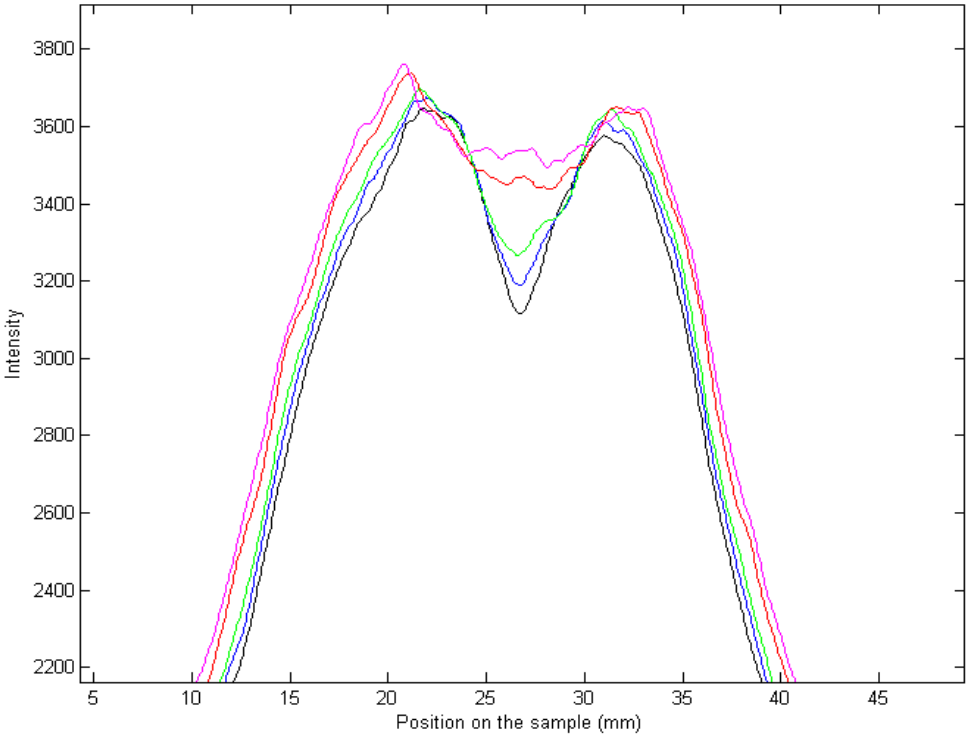

Figure 5.37. Cross-section of the Al_2O_3 (104) indicating the intensity with position under the different detector angle collection conditions.

The same Savitzky-Golay smoothing filter with a third order polynomial spread over 51 data points has been used in the displaying of the Si (111) peak shown below.

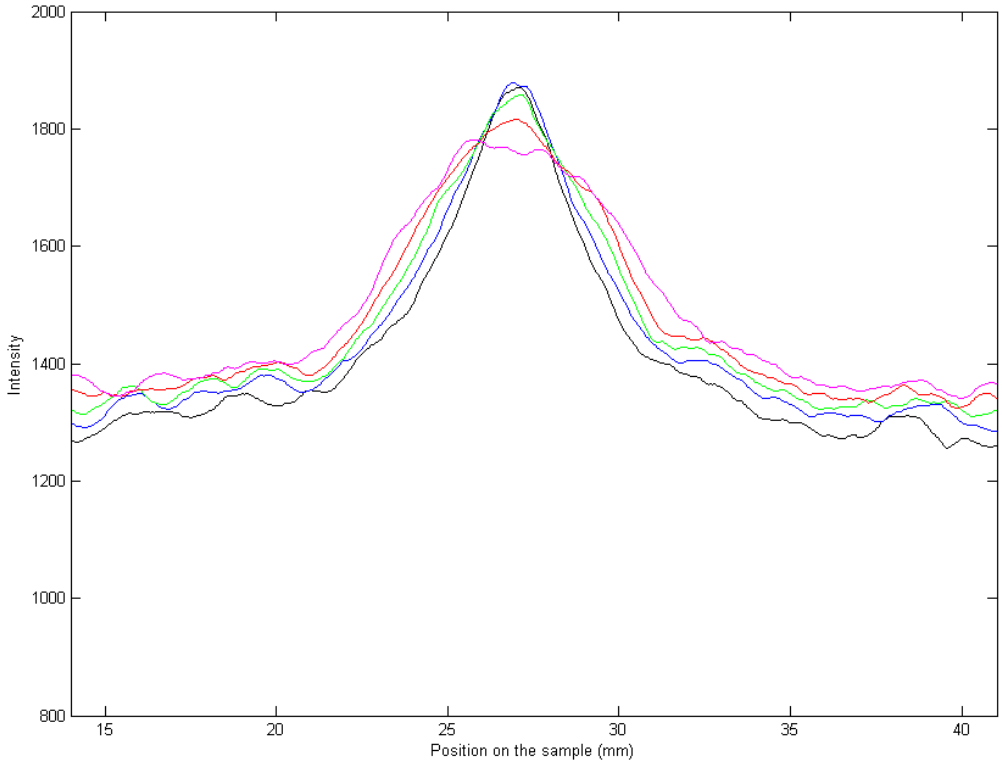

Figure 5.38. Cross-section of the Si (111) indicating the intensity with position under the different detector angle collection conditions.

The peaks		
Collection angle	**Si (111) peak FWHM (mm)**	**Al_2O_3 (104) peak (height to trough ratio)**
38 (black)	4.9	85.56%
40 (blue)	5.5	86.79%
42 (green)	5.7	88.58%
44 (red)	6.0	93.10%
46 (pink)	7.1	94.07%

Table 5.11. The effect of data collection to calibration angle on both single and double peak sources.

Now that the characteristics of the partitioning have been identified the way that useful diffraction information can be extracted from the extended beam illumination can be presented clearly.

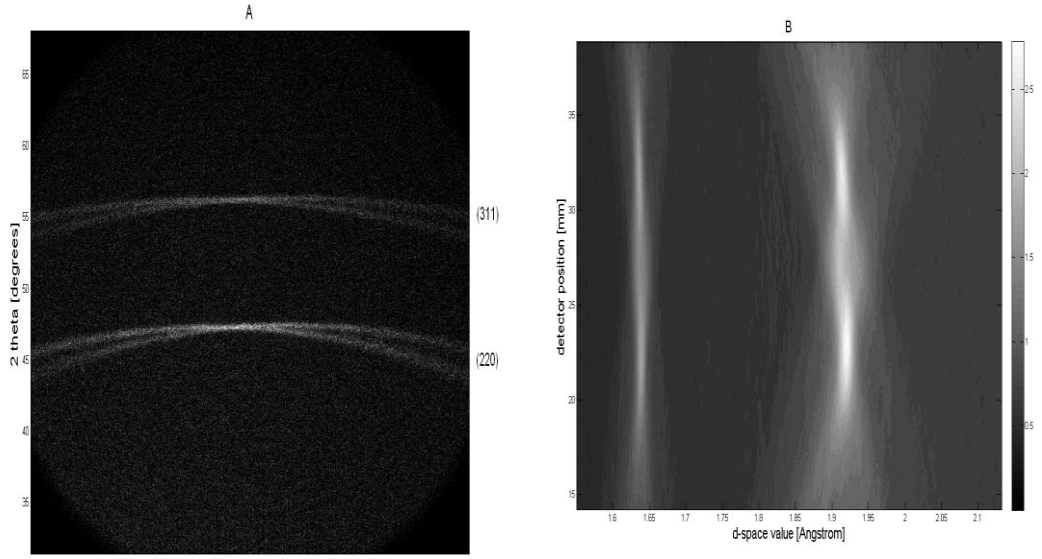

Figure 5.39. Two Si powder filled cells illuminated with the extended beam, the diffraction image as collected (A) and the partitioned data (B).

Figure 5.39 shows both the direct diffraction profile and the partitioning results of the linear array. Two silicon powder samples are separated by an unfilled well, i.e. two sources of diffraction with the same diffraction patterns but with the respective sample centres separated by ≈10 mm ± 0.1 mm along the library principal axis. This was the experimental equivalent of the previously simulated case shown in figure 4.65. As with the equivalent simulation, the transformed maxima are extended in the 'y' direction, which is to be expected due to the finite sample size of 5x5 mm.

The sample separation was determined to be 9.89 mm (± 0.13 mm) when calculated from the peak maxima. The d-spacings were determined to be 1.931 Å for the (220) and 1.642 Å for the (311) planes. Lattice parameter calculations for this material give a = 5.45 Å (± 0.01 Å). The NIST certified values for the corresponding maxima are 1.920 Å for the (220) and 1.640 Å for the (311). The lattice parameters calculated from measurements by conventional powder diffraction techniques gave a = 5.435 Å ± 0.006 Å when calculated from these maxima only.

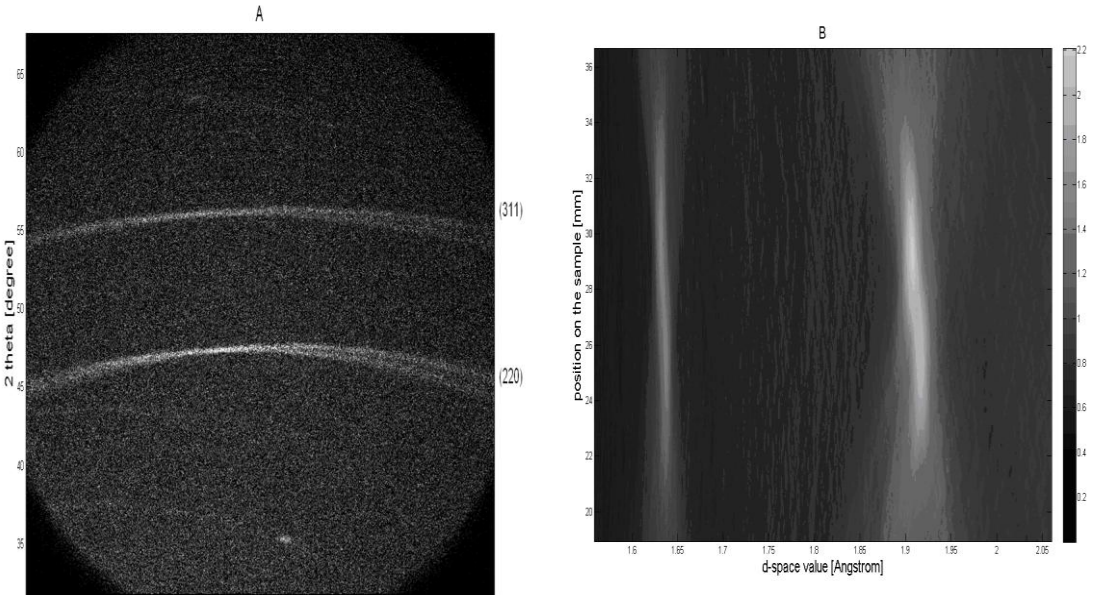

Figure 5.40. Two Si powder filled cells with a 0.34 mm displacement error, the diffraction image as collected (A) and the partitioned data (B).

In figure 5.40 we see the results for the samples where the Si powder were offset from each other. The steps were separated by 4 mm along the illuminated area and were displaced in height by 0.34 mm. The resultant transformed data is shown in figure 5.40 B, from this intensity distribution the distance between the steps was determined to be 3.9 mm ± 0.1 mm. The transformed data was used to calculate differences in d-spacings from each of the cells of 0.008 Å for the (220) and 0.005 Å for the (311). The results of this deliberately introduced displacement error are in agreement with those calculated from,

$$\Delta 2\theta = -2s\cos\theta/R$$

Where s is the displacement R is the sample to detector distance and θ is the diffracted angle expressed in radians [106].

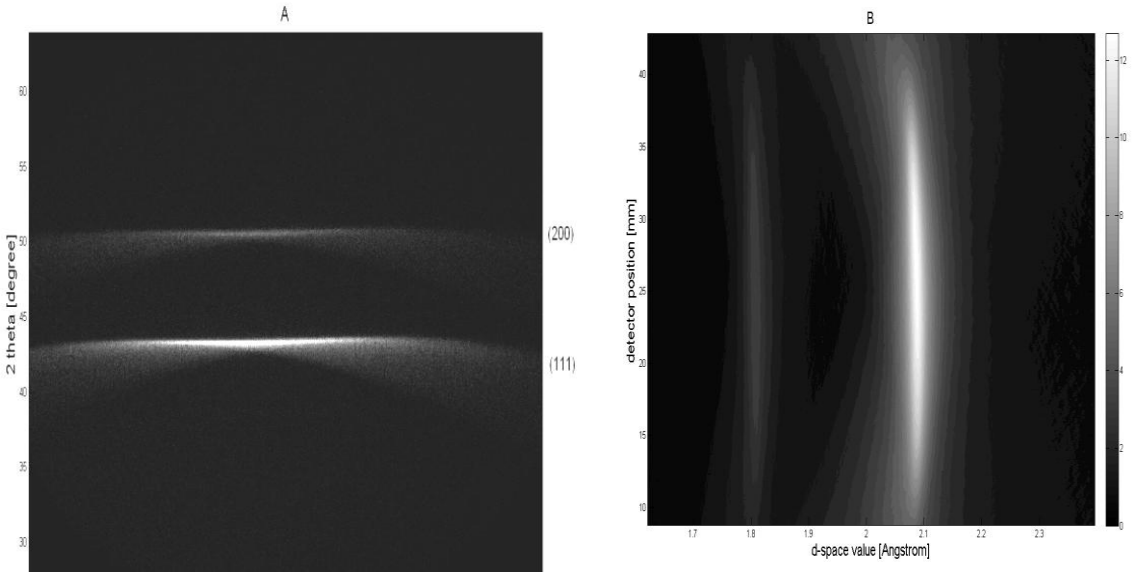

Figure 5.41. Patterns created from polycrystalline copper thin film held parallel to the detector, diffraction image (A) and the partitioning results (B).

The scattering data and the partitioned data from a homogeneous Cu thin film deposited upon a glass slide and illuminated with the elongated source is shown in Figure 5.41. The detector was positioned to receive scattering from the (111) and (200) crystal planes. As expected two intensity maxima extended in the 'y' direction for a length equal to that of the illuminating beam but each with a constant d-spacing corresponding to the (111) & (200) of Cu.

To experimentally simulate scattering from a library possessing a continuous lattice parameter gradient, data from the copper thin film was collected following a rotation of the sample by 1° thus creating a displacement error gradient. This was calculated to produce a change in d-spacing of 0.015 Å and 0.011 Å across 24 mm for the (111) and (200) maxima respectively. The consequent scattering data and the corresponding transformed data is presented in Figure 5.42. The d-spacing changes measured from the transformed data were 0.015 Å and 0.010 Å for the (111) and (200) respectively. The apparent lattice parameter gradient of 9.911×10^{-11} (equivalent to 9.911×10^{-4} Å per mm) has been measured. This is more precise than that required for the characterisation of most materials.

The additional effect of this procedure is that the z displacement shift changes the position of the footprint of the X-ray beam. Moving it in the x plane has a minor effect here due to the 25° incident angle. The effect on examples where the incident angle is smaller is discussed in section 6.3.

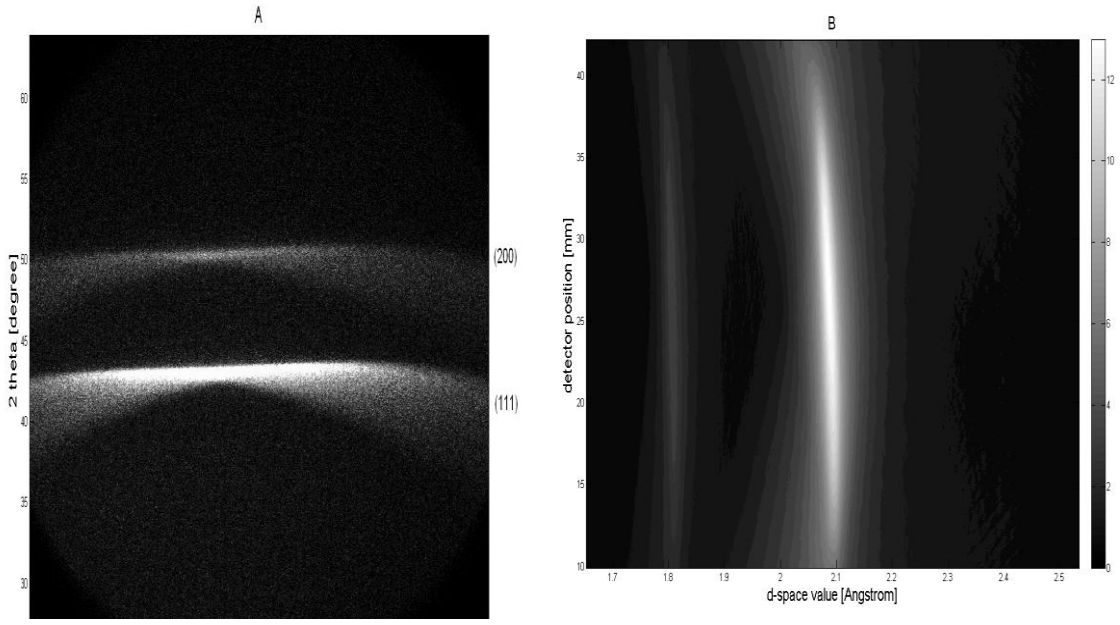

Figure 5.42. Patterns created from polycrystalline copper thin film held with 1° tilt with respect to the detector, the diffraction image (A) and partitioning results (B).

5.9 Application of the partitioning to High Density Chemical Libraries

5.9.1 Electrodeposited libraries

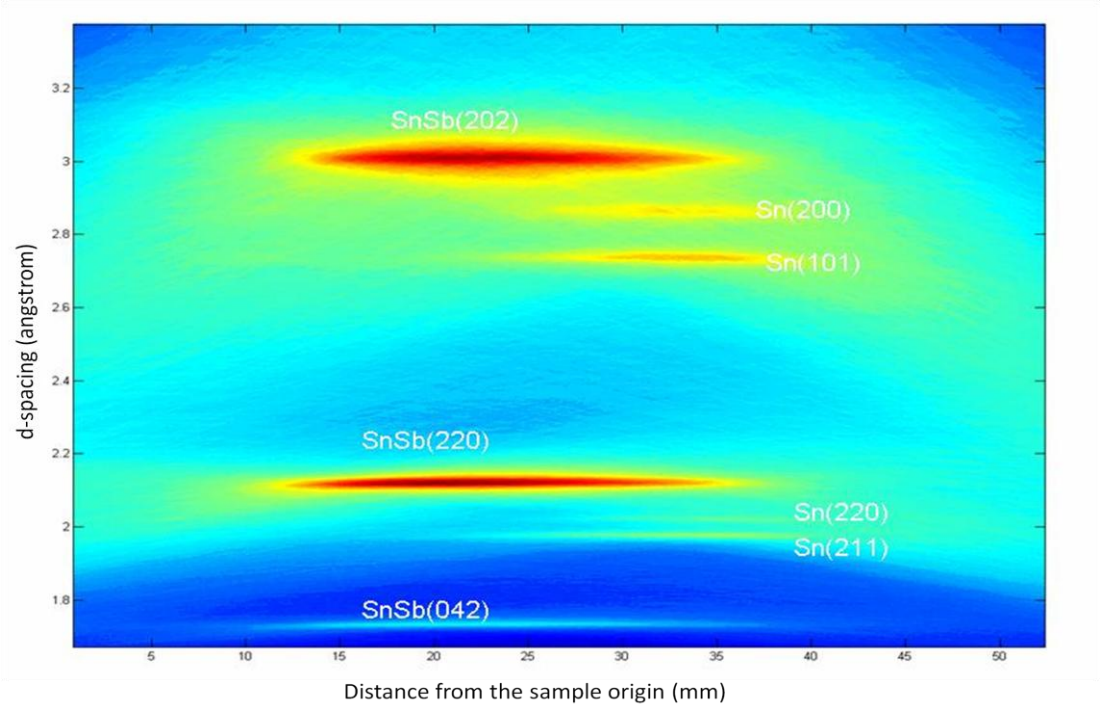

Figure 5.43. Extended beam partitioning of the electrodeposited tin-antimony library.

Data corresponding to the SnSb library are shown in figures 4.32 and 4.33 for the raster point collection and 5.43 for the extended beam. Seven discrete Bragg maxima are visible in the 2θ range measured. These have been assigned as Sn and SnSb. The intensity distributions in both figures are visually very similar. Maxima corresponding to Sn were observed only within the upper section of the library, between 45 and 22 mm. Across this region, the intensity of the Sn maxima decreases. The SnSb peaks are visible across the entire library although their intensities are greatest at around 15-20 mm. The simultaneous presence of the Sn and SnSb peaks between 22 mm and 45 mm suggests the co-existence of elemental tin and tin-antimony alloy in this part of the library. The absence of the Sb phase is due to the total conversion of the metal into the SnSb alloy.

Phase	Miller Indices	Raster scan d-space (Å)	Extended beam d-space (Å)
SnSb	101	3.02832 ±0.0002	3.0114 ±0.0009
Sn	200	2.88133 ±0.0003	2.8712 ±0.0008
Sn	101	2.75832 ±0.0001	2.7308 ±0.0007
SnSb	110	2.14570 ±0.0001	2.1170 ±0.0007
Sn	220	2.05000 ±0.0003	2.0305 ±0.0003
Sn	211	2.00030 ±0.0005	1.9758 ±0.0006
SnSb	021	1.75334 ±0.0004	1.7363 ±0.0006

Table 5.12. The observed d-space values determined from extended beam partitioning are compared with those obtained during the raster scan measurements.

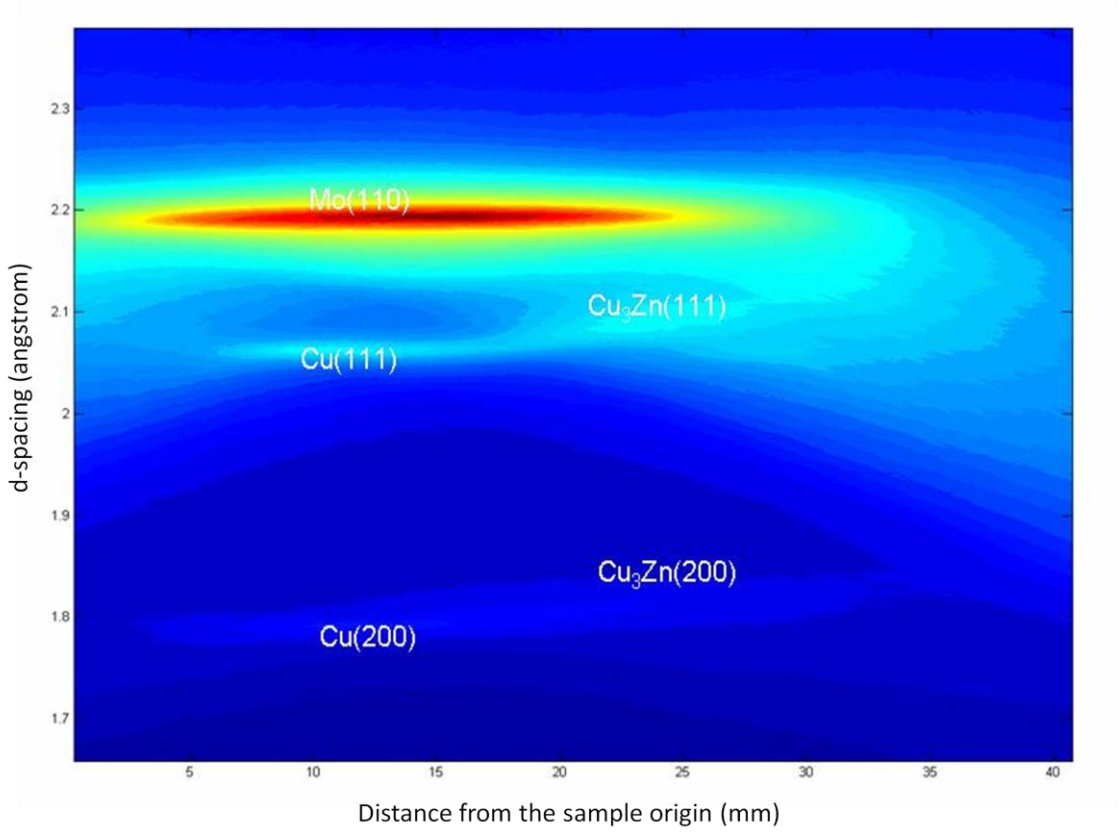

Figure 5.44. Extended beam partitioning of the electrodeposited copper zinc library.

The result of the partitioning of the copper-zinc library is shown in figure 5.44. This illustrates the way the extended beam technique is limited by the length of this particular beam. The perceived length of the beam is limited by the diffraction off the substance in question; in this case the continuous layer is the molybdenum. The attenuation of the over layers reduced the intensity profile and as the beam is not totally uniform the perceived length can appear different depending on the diffraction characteristics of the materials to be tested. The perceived length of the beam is lower in this case.

The widths of the peaks and the low intensity in contrast to the molybdenum substrate mean that a quantitative comparison to the raster scans in figure 4.31 was not chosen in this case. This is true of both of the data collection methods and not a short coming of the diffraction. The transition between the Cu and the Cu_3Zn can be seen clearly in both the raster scanned data and the extended beam partitioning figure 5.44 where the d-spacing shift is indicated.

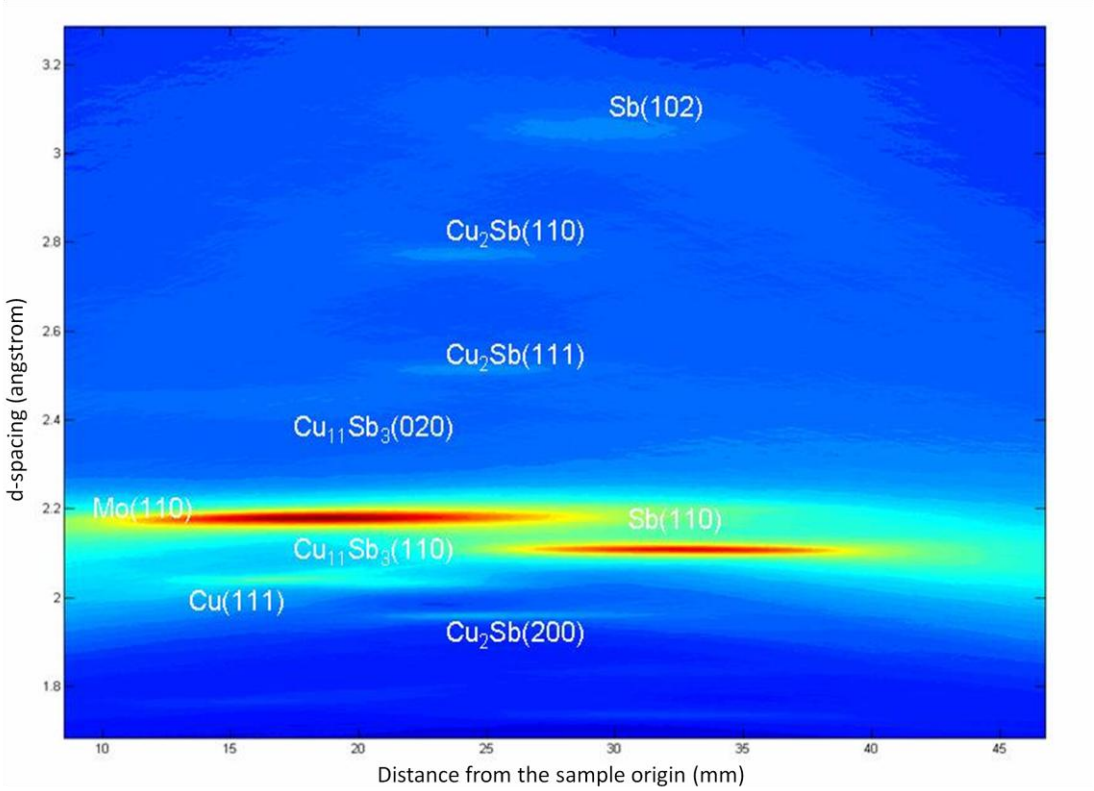

Figure 5.45. Extended beam partitioning of the electrodeposited copper antimony library.

This case shows the abilities of the extended beam partition at its best. Figure 5.45 demonstrates that five different phases at four different samples positions spread over >25 mm can be recorded from one data collection. Data collected from extended beam figure 5.45 and raster scan compilation figure 4.36 are contrasted in table 5.13.

Phase	Miller Indices	Raster Scan	Extended beam
		d-space (Å)	d-space (Å)
Mo	110	2.209	2.1906
Cu	111	2.068	2.0505
$Cu_{11}Sb_3$	110	2.0908	2.0954
$Cu_{11}Sb_3$	020	2.3425	2.3389
Cu_2Sb	110	2.8003	2.7933
Cu_2Sb	111	2.5368	2.5235
Cu_2Sb	200	1.9862	1.9645
Sb	012	3.0712	3.0607
Sb	110	2.135	2.122

Table 5.13. Summary of the d-spacing for the identified phases of the copper antimony system measured using both raster scan and extended beam partitioning methods.

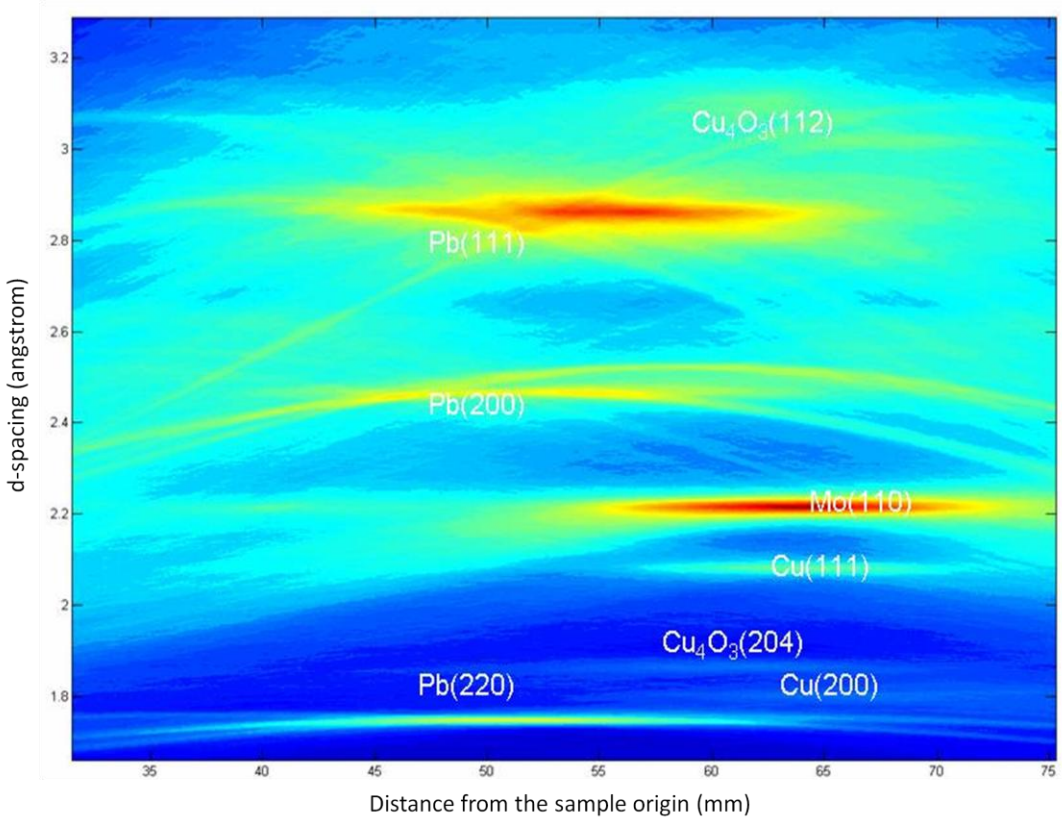

Figure 5.46. Extended beam partitioning of the electrodeposited copper lead library.

In the analysis of the extended beam in figure 5.46 the part of the library between 35 and 75 mm from the sample origin can be seen. All of the phases in this part of the library that can be identified in the raster scanned results (figure 4.38) can still be found. If appropriate cross-sections are taken, the main peaks are correctly positioned with regard to both d-spacing and position on the substrate. The visual differences are discussed in section 6.4.

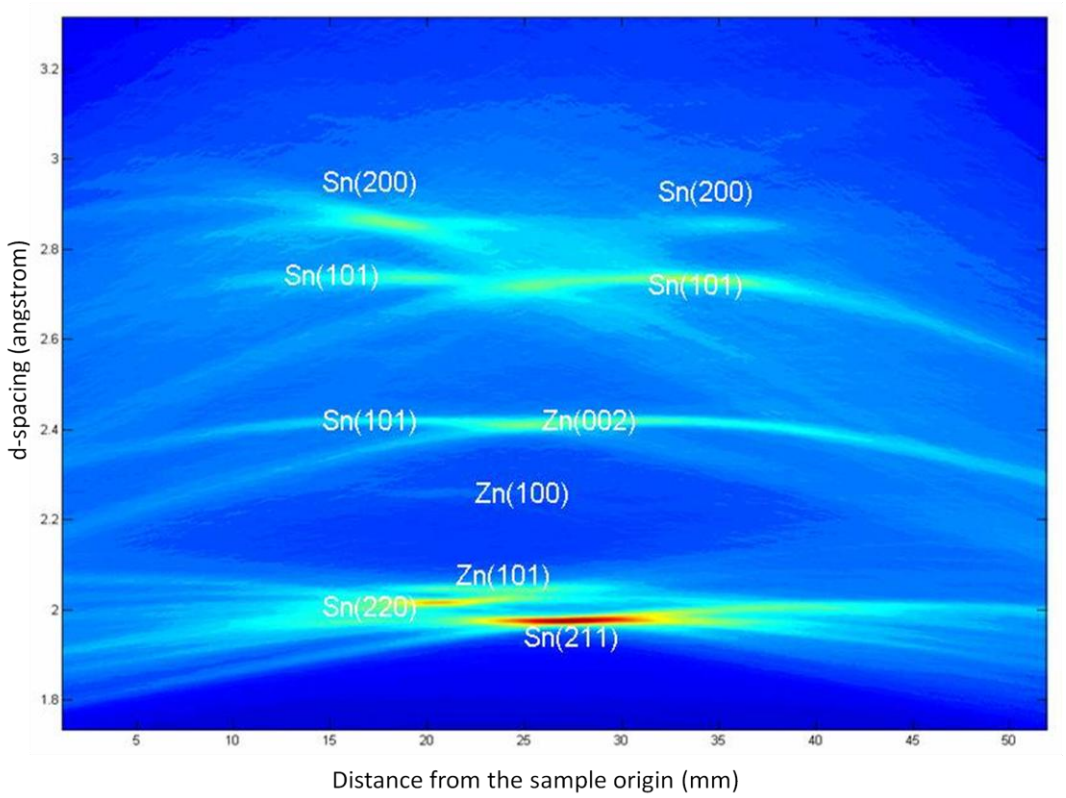

Figure 5.47. Extended beam partitioning of the electrodeposited tin zinc library.

In the same way as in the copper-lead system the tin-zinc partitioning data from figure 5.47 can be used as an overview of the part of the substrate that is illuminated. Comparisons to figure 4.40 show that all of the key phases can be identified and the d-spacing accuracy is generally high if the highest intensity points of the peaks are taken. The observation of position on the sample is distorted with the consequence that the low intensity area of the tin where the zinc is overlaid is not detectable as a continuous pattern of any significance in comparison to the local background.

This can be explained by the fact that the tin-zinc system has lots of preferred orientation which can be seen in the arc shaped artefacts. The mechanism for the formation of these arc shaped artefacts in section 5.1.

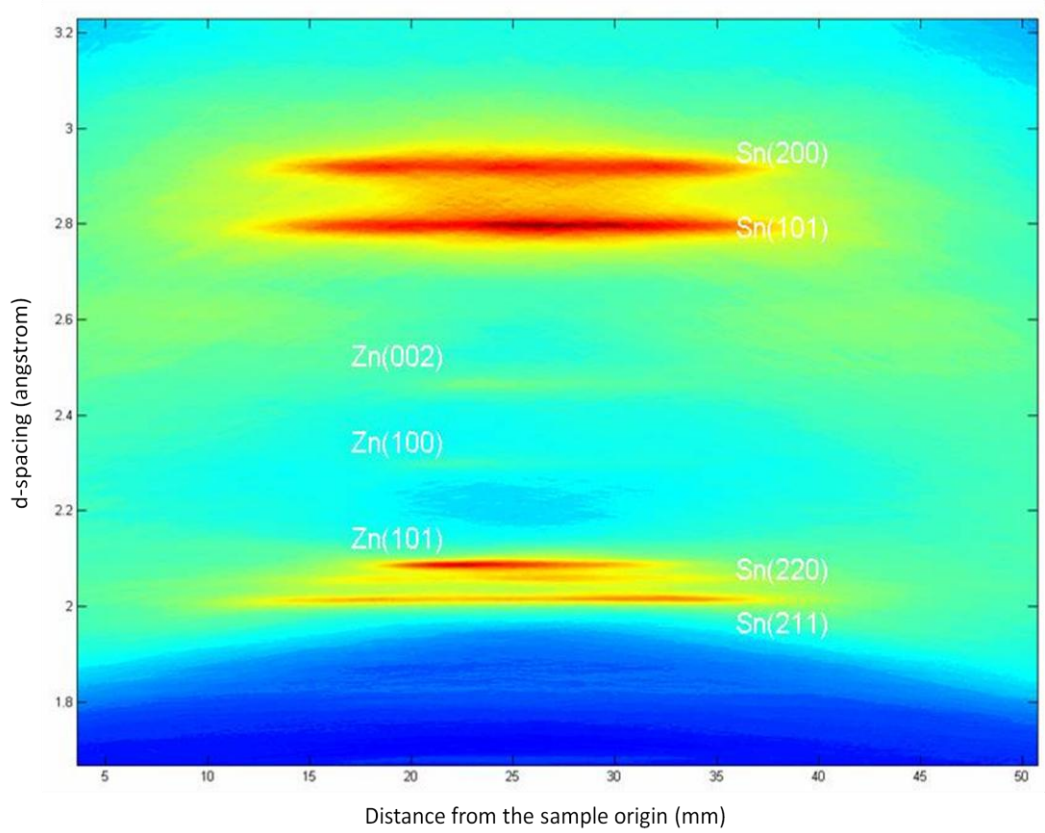

Figure 5.48. Extended beam partitioning of the electrodeposited tin-zinc library.

The SnZn library was made again to try to reduce these effects. The results can be seen in figure 5.48. As a thinner sample deposited on to an amorphous substrate has been found to produce less preferred orientation for a range of materials [155] [156] , the total sample thickness was reduced. This included the sputtered tin conducting substrate and the relatively high energy of the sputtering process in known to produce strongly preferred films at a wide range of power inputs, temperature conditions, gas pressures and film types. [157] Conventional XRD measurement shows that in the samples or even parts of the libraries where the preferred orientation reduced the extended beam partitioning more closely matches the raster scan compilation contour maps.

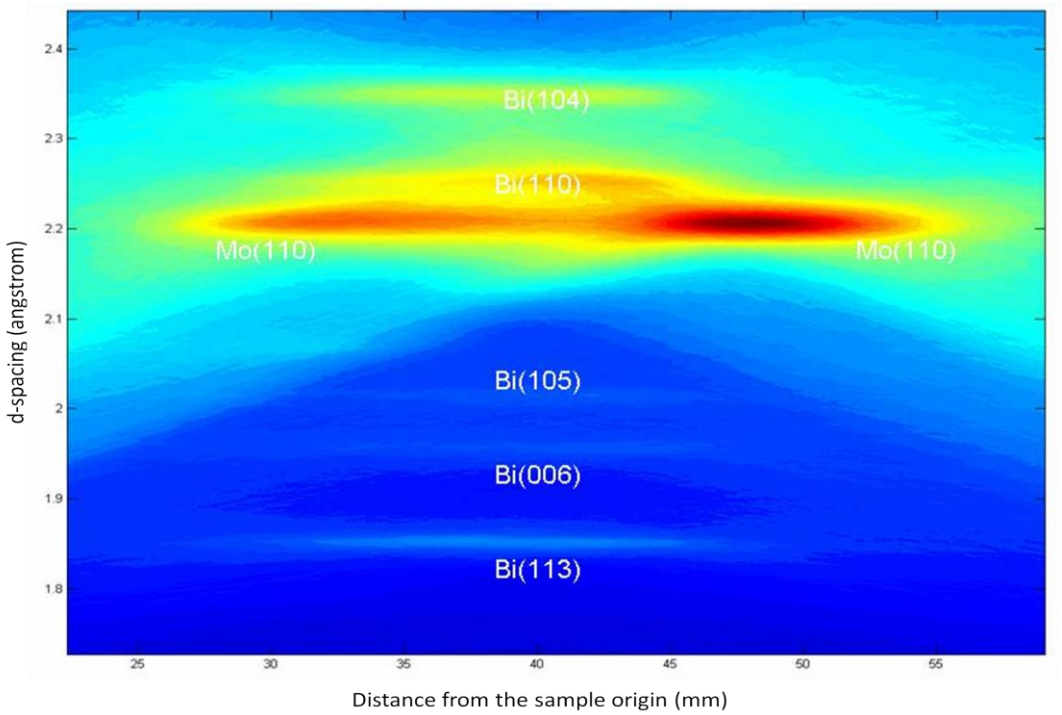

Figure 5.49. Extended beam partitioning of the electrodeposited copper-bismuth library.

The extended beam contour plot is shown in figure 5.49. This can be compared with the raster scanned data in figure 4.42 over the same area. Cu-Bi has a eutectic point close to pure bismuth. However, the extremely restricted solubility of bismuth in copper and copper in bismuth means that as predicted no alloy formation was apparent within the library. Both plots show the intense Mo peak which traverses the entire library. Bismuth peaks are apparent in both the measurements from 30 mm to 50 mm. These results indicate the reliability of extended beam measurements in the determination of the d-space and the position and length of the intensity maxima in terms of its sample position.

Phase	Miller Indices	Raster Scan	Extended beam
		d-space (Å)	d-space (Å)
Bi	202	1.85183(1)	1.8400(8)
Bi	006	1.95544(1)	1.9535(5)
BI	015	2.01724(3)	2.0207(7)
Cu	111	2.20691(2)	2.2014(7)
Mo	110	2.21122(2)	2.2051(8)
Bi	110	2.25031(3)	2.2600(6)
Bi	104	2.35088(1)	2.3639(6)
Bi	012	3.25121(3)	3.2493(7)

Table 5.14. Summary of the d-spacing for the identified phases for the copper and bismuth library, measured using both raster scan and extended beam partitioning methods.

5.9.2 Sputtered libraries

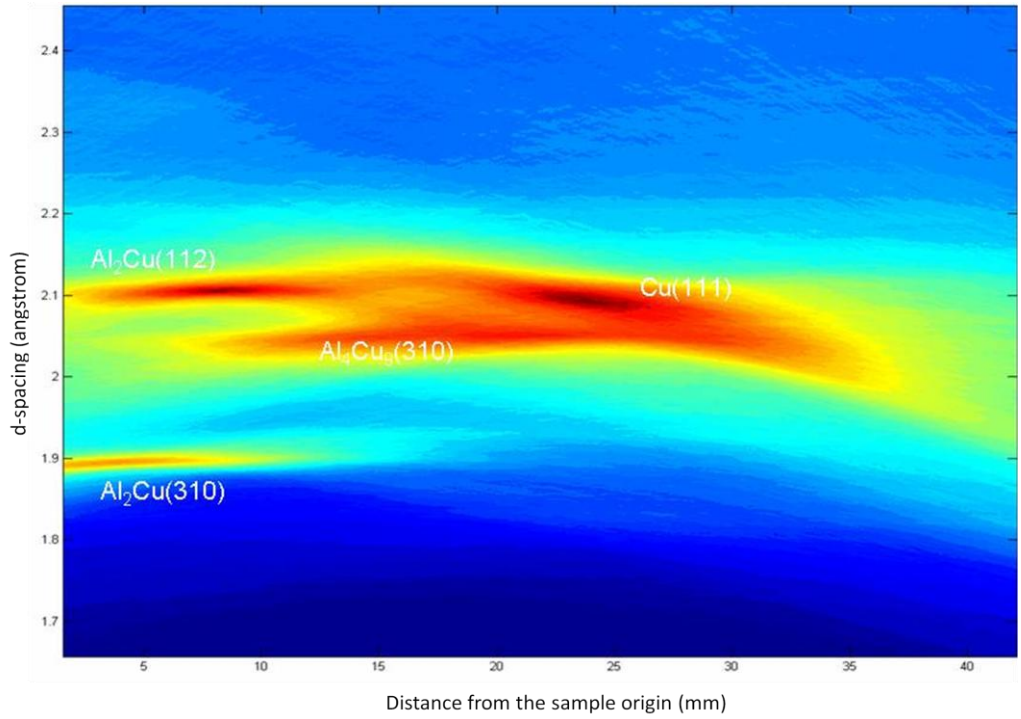

Figure 5.50. Extended beam partitioning of the sputtered copper-aluminium library.

Data corresponding to the CuAl library is shown in figure 4.46 for the raster scans and figure 5.50 for the extended beam. These contour plots of the CuAl system are qualitatively very similar. In the first 5 mm of the library, Al_2Cu is the only alloy detected. From 6 to 18 mm this alloy coexists with cubic Al_4Cu_9. The signal from the Al_2Cu being weaker, the apparent co-existence distance could be measured as being shorter. The only phase detected between 19 and 23 mm is Al_2Cu_3 and above this within the library elemental Cu is also observed. The relative closeness of the peaks used for the identification in terms of d-spacing and the large overlapping areas of different phases within the library are a considerable test for the partitioning system, notable the similarity of the d-spacing measures by the two method is still high. Table 5.15 shows these similarities.

Phase	Miller Indices	Raster Scan	Extended beam
		d-space (Å)	d-space (Å)
Al_2Cu	310	1.89927(7)	1.8981(2)
Al_4Cu_9	330	2.02783(4)	2.0345(2)
Al_2Cu_3	102	2.05658(1)	2.0494(3)
Cu	111	2.10803(1)	2.0988(4)
Al_2Cu	112	2.11661(9)	2.1025(2)

Table 5.15. A summary of d-spacing obtained by raster scan and extended beam partitioning methods for AlCu library.

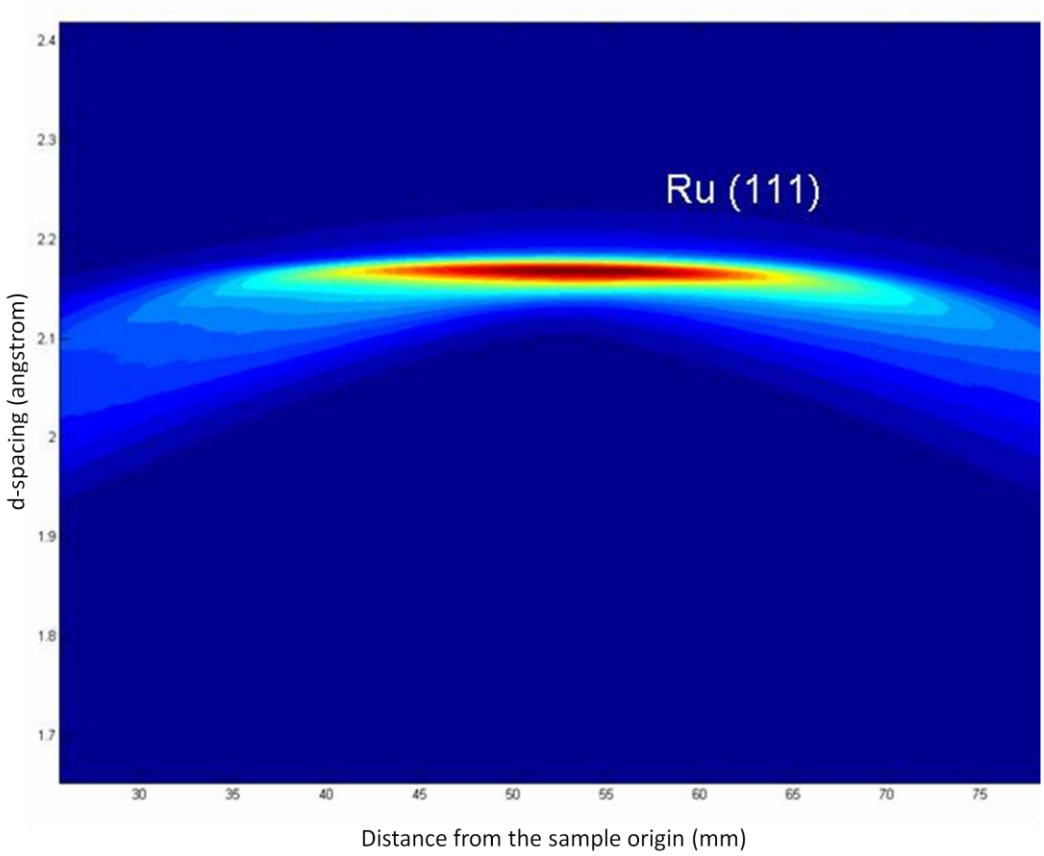

Figure 5.51. Extended beam partitioning of the sputtered ruthenium-platinum library.

The RuPt library illustrated in figure 5.51 is a three phase system at all of the temperatures possible in the investigation [138]. The preferred orientation of the sample means that only one peak can be measured with accuracy, the raster scanned contour plot in figure 4.47 exemplify this. This phenomenon means that the best way to examine this sample is to look at only one of the phase regions at once and inspect the solid solution in this compositional range.

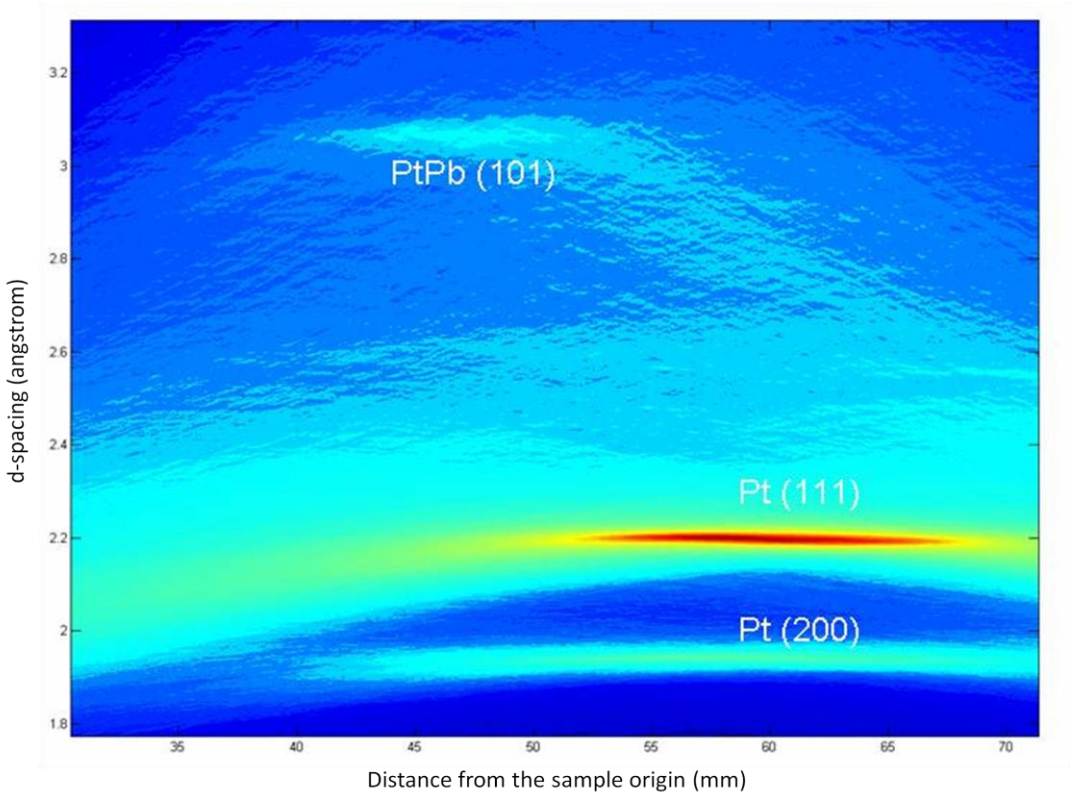

Figure 5.52. Extended beam partitioning of the sputtered lead-platinum library. In this case the extended beam was used to characterise the area covered by the higher raster scanned positions.

The area covered by the extended beam figure 5.52 covers two phase rejoins. This is expected as it is seen in figure 4.48. The intensity of the PtPb (102) plane combined with the fact that it is close to the intense Pt (111) plane means that it is hard to discern. In ideal samples this combination would not produce such a manifest interference but the distortion due to the preferred orientation of the platinum and the coincidental positioning of the PtPb (102) combine to amplify the swamping effect. Other information to be extracted from the partitioning profile is the relative peak intensities the ratio between Pt (111) and (200) planes is 12% on average the corresponding raster collection is also 12 % over the nine points that most closely correspond to the extended illumination but with a greater variation within the sample set.

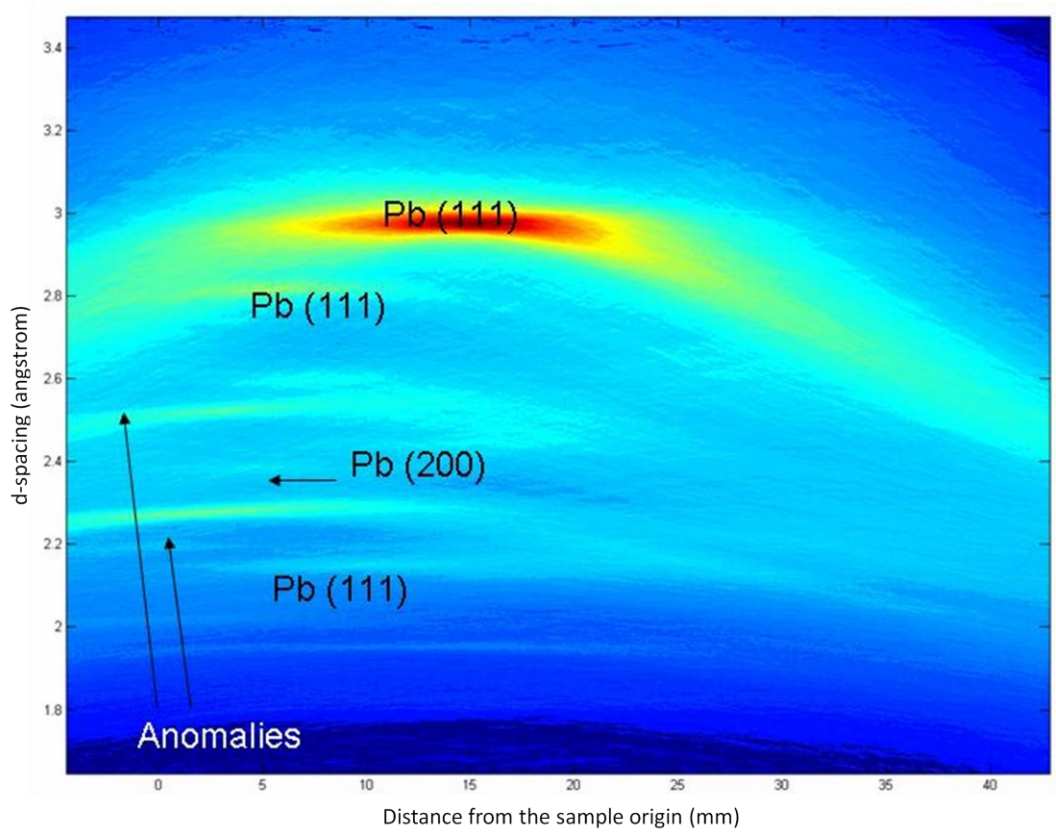

Figure 5.53. Extended beam partitioning of the sputtered lead-platinum library. The other side of the library also required characterisation so the extended beam was used to cover the area corresponding to the higher raster scanned positions.

Generally figure 5.53 has the expected phases from figure 4.48 can be seen but there are two additional intensity maxima that were not expected. The peak at ≈ 2.25 Å can be explained by the uncovered platinum at the edge of the libraries this is thought to originate on the first raster point but its strong orientation causes the artefact present for some of the sampling distance. The other at ≈ 2.5 Å has not been identified but is thought to be produced by the same mechanism. The reason why it has not identified by the point source illumination can be explained by its short-lived positioning being missed by the non-continuous data collection method.

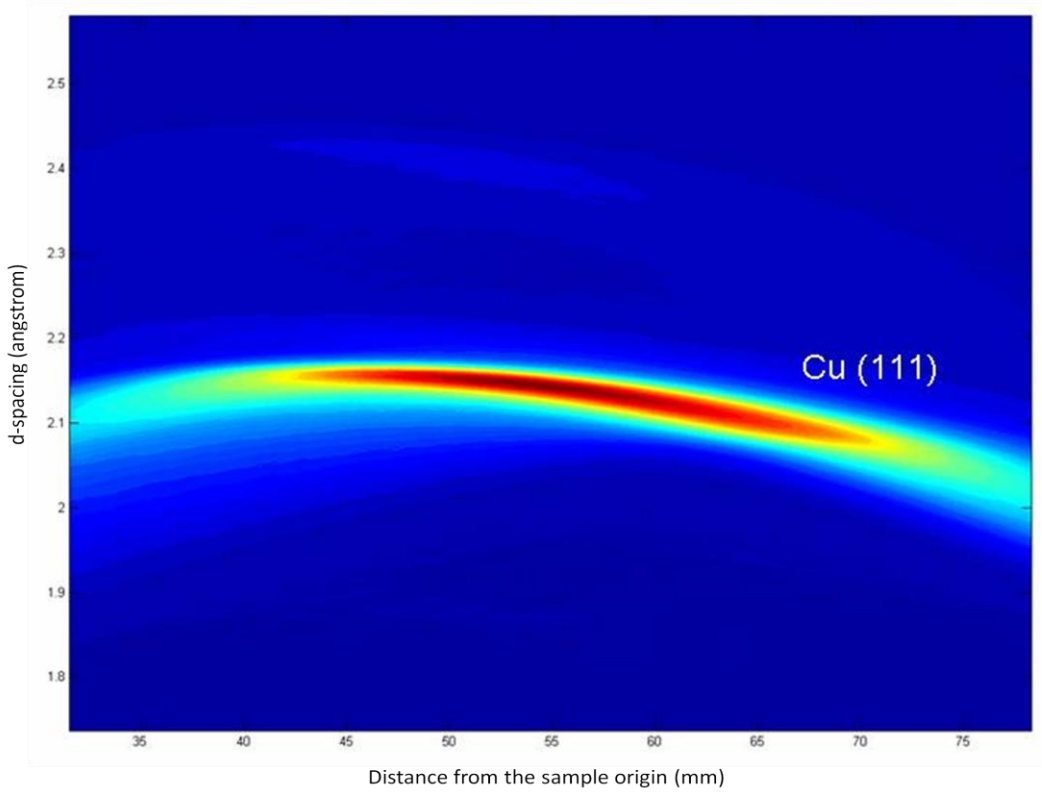

Figure 5.54. Extended beam partitioning of the sputtered copper-platinum library.

The partitioned data of the copper platinum library shown in figure 5.54 matches well to the pencil beam scanned data (figure 4.49) collected over the same range. The d-spacing calculations remaining consistent between two methods if the maximum peak intensities are considered. This CuPt sample along with the TiZr has been found to have a highly preferred structure the result of this is a perceived bowing of the partitioning arcs that follow an opposite profile to the virtual arc. This characteristic effect is described in section 5.1. With this knowledge it is possible to use the partitioned data alone to show that the samples are exhibiting preferred orientation. The partitioned intensity plot also give information on how the diffraction area is positioned on the detector. This information is present in the raster scans when an area detector is used but is lost when the image is radial integrated into a conventional diffractogram.

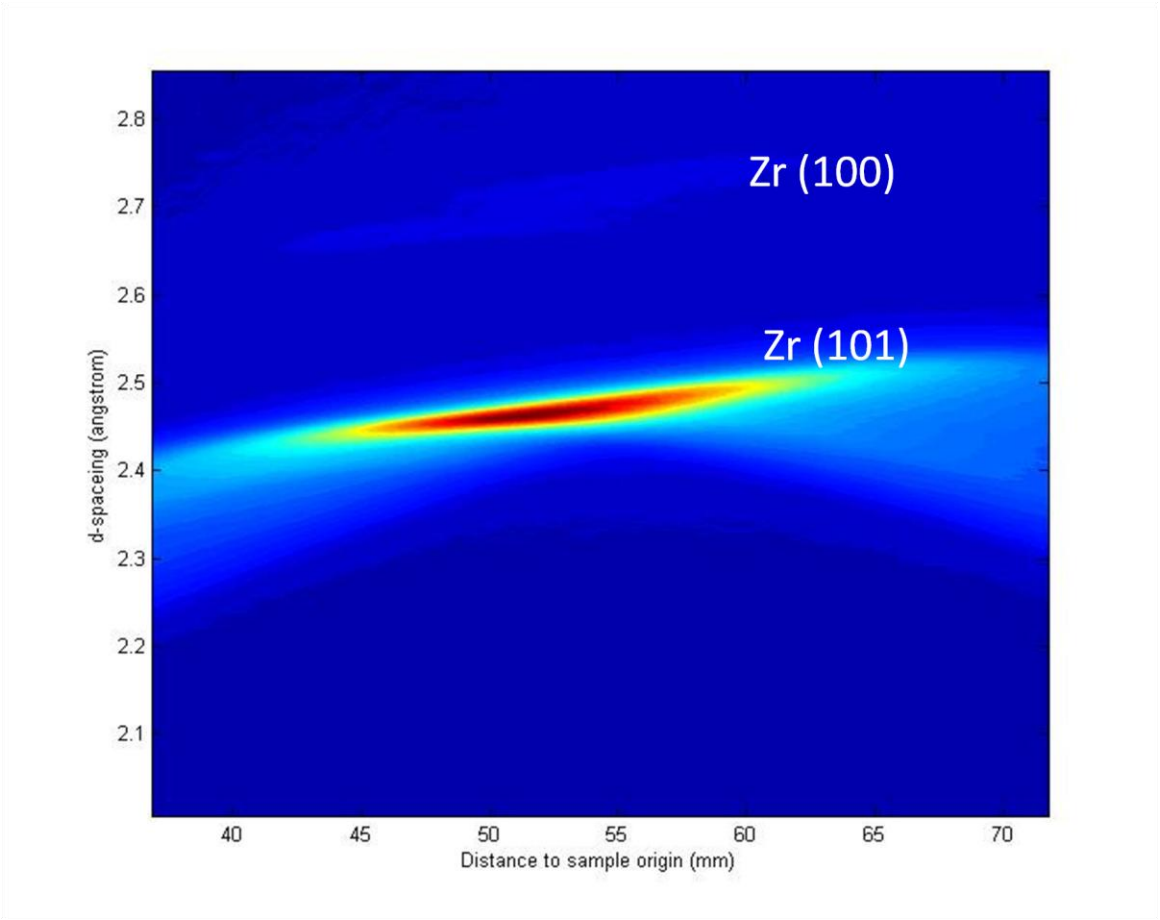

Figure 5.55. Extended beam partitioning of the sputtered zirconium-titanium library.

The partitioning result figure 5.55. is in agreement with the raster scanned data in figure 4.50 and the expected ZrTi phase diagram both of which indicate complete solubility of the two elements [138]. No additional alloy phases were observed. Both the contour plot of the raster scan data and the partitioned results show the 101 reflection is the only one in the measured range. As expected, the plot shows a continuous change of d-spacing across the library which is an indication of the substitution of one of the elements by the other. While the extended beam illumination only covers the 45 mm to 70 mm the treads in d-spacing shift can be seen. The d-spacing of the reflection increased from 2.36 Å at 10 mm to 2.48 Å at 70 mm in the raster scanned example. For the extended beam results the change of d-spacing was from 2.40 at 45 mm to 2.49 Å at 70 mm.

Due to the nature of partitioning process the full width half maximum is larger than the corresponding raster scan data. However this results in an error typically at the fourth decimal place and it is not considered significant. The corresponding Vegard coefficients for each

interrogation method, 0.2590 Å (raster scan) and 0.2591 Å (extended beam) are not significantly different.

5.9.3 Electrostatically produced samples

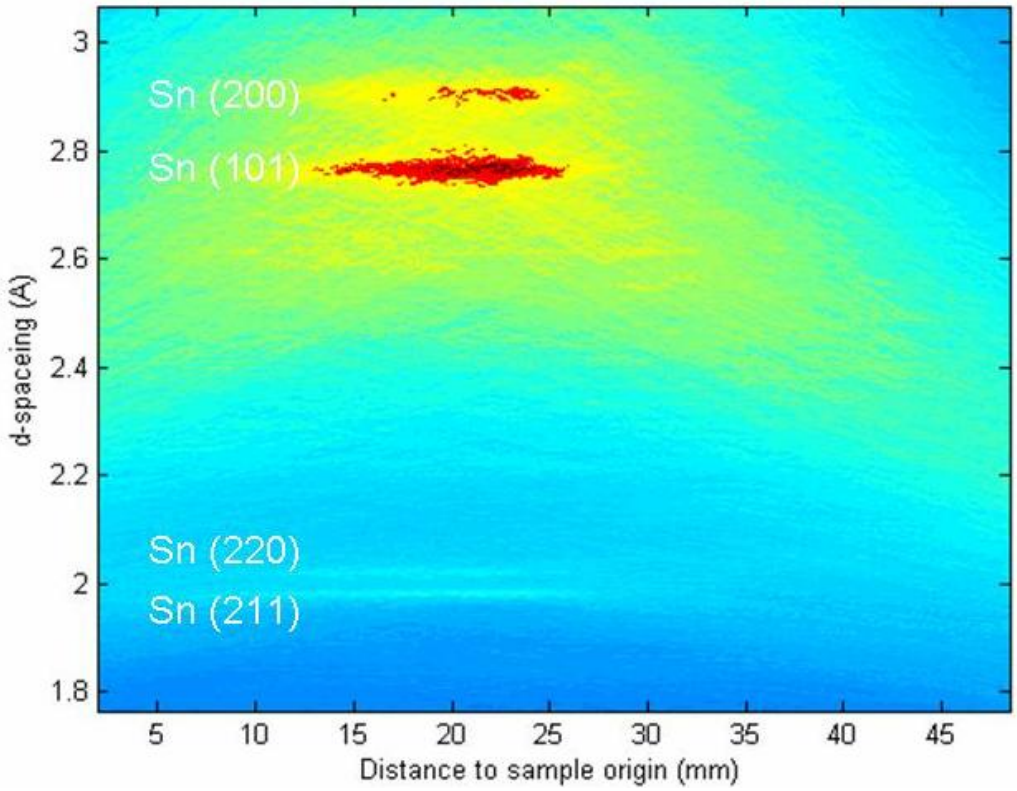

Figure 5.56. Extended beam partitioning of the electrostaticaly deposited SnCr251009 library.

The partitioning results for the SnCr library are shown in figure 5.56. The extended beam used in this data collection illuminated the area approximately 12-37 mm from the sample origin. It can be seen that the partitioning reveals no measurable peaks between 25-37 mm even though this part of the sample is illuminated. This is expected as the Cr side of the library is amorphous, as confirmed by the raster scanned data.

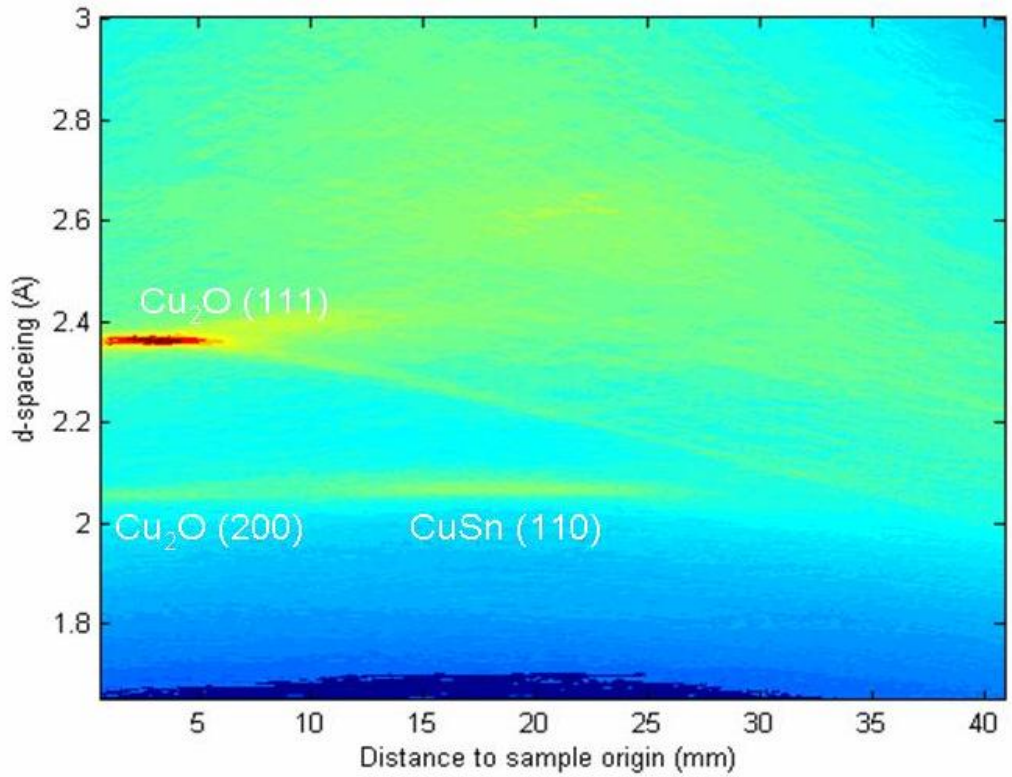

Figure 5.57. Extended beam partitioning of the electrostaticaly deposited SnCu191009 library.

The Cu_2O and the CuSn seen in the raster scan of the SnO_2 peak (figure 4.55) is not fully clear because the partitioning method, results of which are shown in figure 5.57, is affected more by the increase in peak widths than the normal method. This should be thought of as an extreme example as the raster scan of the SnO_2 peak having a FWHM of 0.2 A. changing the virtual arc of partitioning may make this peak visible but it would detract from the precision in locating the narrower ones.

Results achieved when using synchrotron radiation source

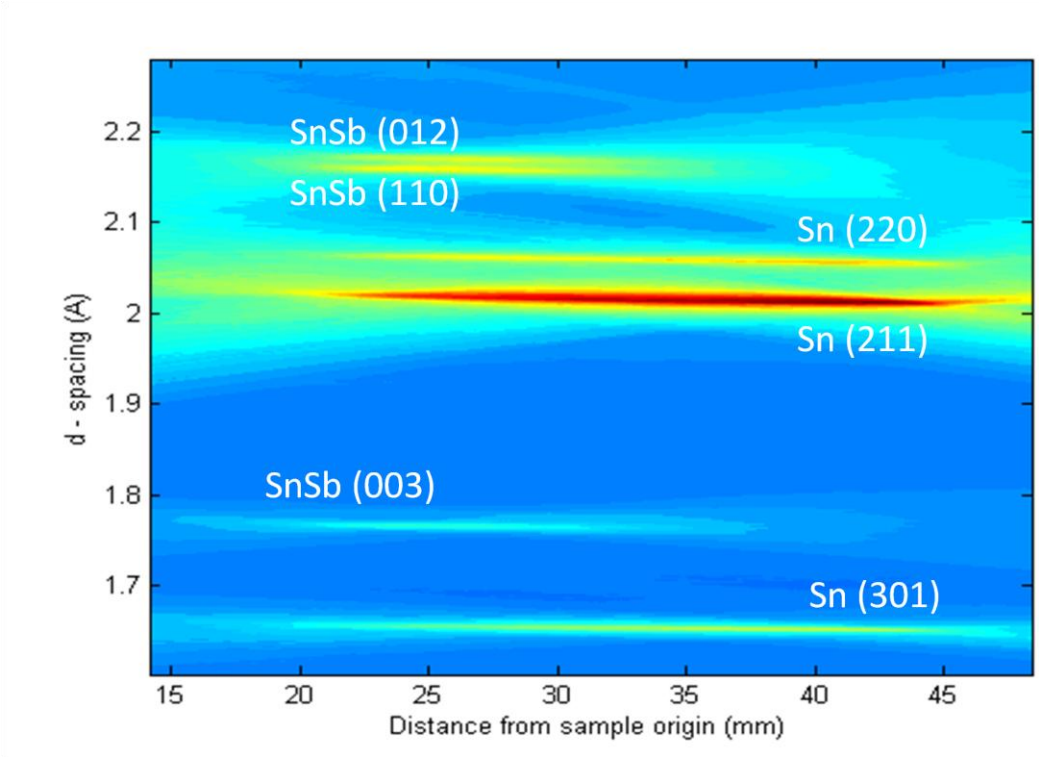

Figure 5.58. Partitioned extended beam illumination of the tin-antimony library, with the data collected from the synchrotron.

When the results of the synchrotron experiment are examined both the direct diffraction intensity profile and the resulting partition in figure 5.58 show a clarity of image that is not achieved with the D8 diffractometer. The main reason for this is that the detector employed has a 3056 x 3056 pixel array. The spatial contrast of this detector is almost three times better than the GADDS in both directions. This allows the detector a greater field of view in both directions as well as improved resolution. In the dimension where position on the sample is measured the field of view cannot be fully exploited as the beam is a finite length (≈25 mm). This would become more significant if the extended beam could be made as long as the whole library of area of interest. The partition was carried out with a resolution of 1:2 pixels so the quality could be improved further.

The resolution can be clearly illustrated by looking at the two peaks from planes SnSb (012) and SnSb (110). These are clearly distinguishable in the partitioning image. The difference is clear when contrasting this with the D8 diffractometer results; even the conventional point source collection cannot clearly separate the two.

The importance of this is highlighted by the fact that, in this case, the subtle changes serve to promote some previously unconsidered search match cards. Consultation of these cards changes the identification of some of the miller indices. The identification of this sample from search match card 33-118 differs from the some of the other SnSb alloy identifications that most closely match 1-830.

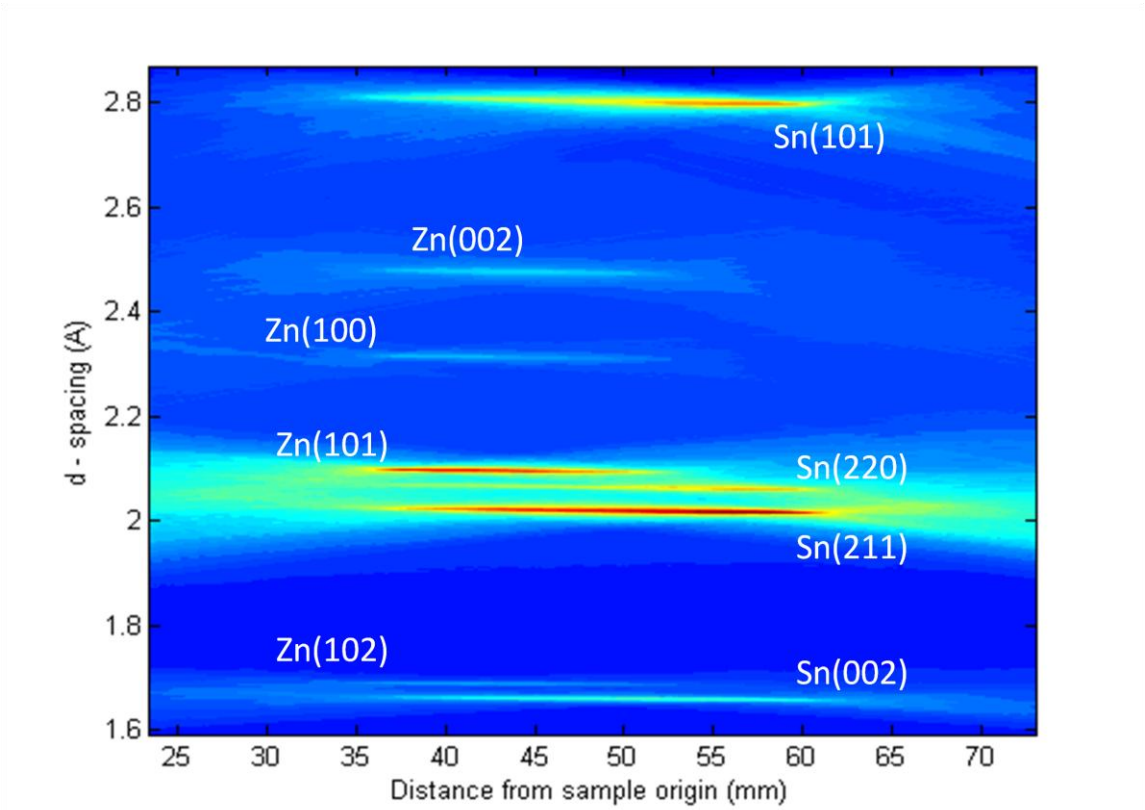

Figure 5.59. Partitioned extended beam illumination of the tin-zinc library, with the data collected from synchrotron source X-rays.

The tin-zinc system illuminated by the synchrotron X-ray source and highlighted in figure 5.59 can be directly compared with the extended beam illumination of the same sample achieved with the X-ray tube source and shown in figure 5.48.

Chapter 6

6 Discussion

This chapter comprises three main parts. Section 6.1 deals with the production of the chemical libraries explaining the positive and negative aspects of the three chosen production methods. In this section, the physical and chemical characterisation of the libraries has been carried out using well established techniques. Sections 6.2 and 6.3 deal, primarily, with the newly developed extended beam partitioning method and its application to simulated diffraction samples and ideal phantom libraries. These sections clarify the theoretical constraints of both the data collection procedure and the chosen partitioning algorithm, with potential future modifications. Section 6.4 demonstrates the application of the extended beam method to the combinatorial samples that have been produced during this investigation. The focus will centre on the comparison between the compilation maps from the conventional XRD raster and the partitioned data.

6.1 Production and conventional analysis of libraries

The energy dispersive X-ray spectroscopy (EDS) calculations rely on the assumption that the materials to be tested were homogeneous within the sampling volume [119]. The libraries produced for this study are homogeneous with respect to depth after this heat treatment, unless otherwise stated. This enables the calculation of composition to be carried out using the standard corrections for the atomic number effect (Z), absorption (A) and fluorescence (F). For the co-deposited samples the nature of production gives homogeneity with depth without heat treatment, this being one of the advantages popularising the method. [47] [158]

The illumination area of the electron beam used for the EDS data collection points was chosen to match the other analytical methods footprint. All the analytical probes have been made to illuminate an area of approximately 500 µm along the gradient of the library. This allows direct comparison between the different methods.

For the EDS collection the sampling volume was limited to a depth less than the film thickness so that no underlying substrate signal is detected and the assumed homogeneity is

accurate. The applied voltage was chosen for each library with consideration of film thickness and the electron attenuation characteristics of the materials. The aim was to achieve the required excitation energies for the relevant elements with a 50 % excess in acceleration voltage to ensure efficient excitation. The inevitable compromises for the EDS accelerating voltages are particularly apparent when characterising libraries which contain the high Z number elemenst. Pt, where the $L\alpha_1$ is 9.44 keV and Pb, where the $L\alpha_2$ 10.55 keV, [159] need particularly high electron energy for efficient excitement, leading to detectable penetration into the substrate. Use of $M\alpha_1$ X-ray lines alone is not preferred as the peaks in this low energy part of the spectrum are difficult to integrate with the accuracy required for quantitative analysis. Changing the accelerating voltage from 15 to 20 keV with the corresponding increase in substrate penetration has been examined. The normalised atomic ratios recorded at the two voltages are unchanged within the accepted experimental error.

The compositions of the co-sputtered ternary systems deposited are shown in figure 4.22 for the BiCuSb, figure 4.23 for RhPtSn and figure 4.24 for the RuPtPb. In each library there are positions where the concentration of the major component exceeds 80 %. This means that >60 % of the ternary phase diagram could be potentially be present. Using an additional target could produce some quaternary phases but this limited as any chosen geometry will exclude large compositional ranges. An alternative method such as layering or masking would be preferential if a large variety of compositions was required. The masking approach has been studied by Cheverrier and Dahn [160]. Using our systems a move to pseudo-quaternary systems with one element in a constant quantity is another potential solution.

The study of the Cu-Bi-S is well suited to combinatorial processes due to the large numbers of factors that affect final structure. Many of the systems are paragenetic with some structures requiring chemical stabilisation and only occurring in the presence of other complimentary materials. The formation of some materials occurs at specific points in the reaction chain and therefore only exists for a brief time [161]. For this reason time dependent investigations could be a useful addition to the study. Other factors must also be considered as the gas phase sulpherisation method is more effective at the surface and produces a film that is anisotropic through the film as well as the expected gradient along the substrate. This is particularly prevalent if the treatment time is short [162]. This, to a certain extent, precludes the formation of short lived phases as a minimum time to produce homogeneity through the layer is required. The formation of the Cu_9S_5 recorded at 5 – 29 mm from the sample origin in figure 4.43 is known to form preferentially to several Cu-Bi-S ternary compounds due to

the strong affinity of elemental copper for sulphur [161]. Lower temperature processes have been found to produce $Cu_{10}Bi_2S_{13}$ and $Cu_5Bi_2S_8$ coexisting with the Cu-S binaries [161]. Even with these limitations at least eleven different phases have been detected in only 60 mm of substrate. While this density of different materials is desirable and justifies the combinatorial procedure, it combines with the co-existence of multiple phases at a number of positions to make the extended beam partitioning ineffective in this case.

Transition from the combinatorially produced libraries to the conventional samples could be achieved by measuring the time exposed to the electrolytic solution at the point of interest. However the compositional ratio of the precursor is not directly related to the composition of the target material, due to annealing losses of one component [148]. This is compensated for in this study by using the information from the libraries and not the expected precursor ratio. In the same way when high order systems are being investigated unknown compounds can be reproduced for further study by adopting the production variables discovered combinatorially. This is effective even if the material of interest has not been fully characterised.

As with the sputtering method the multi-source electrostatic spray process allows a choice of either sequential or simultaneous deposition. The example shown in figures 4.7 and 4.8 indicate that the sequential deposition offers improvement over the co-deposited samples in terms of the extent of the elemental ratios that have been produced. In general, the differences are not great, and can with reference to other experiments be attributed to characteristics of the particular film and substrate combinations investigated. The broader spray interactions often quoted where multiple sources are employed [79] were only ever a minor factor effecting the deposition distributions. Production of a uniform copper film seems to be highly dependent on the substrate; a zinc/zinc oxide layer allows a high quality copper/copper oxide to form. The production of zinc/zinc oxide film forms readily from the zinc acetate precursor solution under a wide range of conditions [163]. From this it is proposed that the ratio of copper in the copper rich parts of the library is reduced by the lack of the zinc's binding properties. This reduction in the overall compositional gradient can be seen in the differences between figures 4.7 and 4.8.

As discussed in section 4.1 the effect of grinding the needles before the electrostatic spray deposition had been detected and quantified. This grinding has only a small effect in these cases while the results from the un-ground needles are slightly steeper gradients. Comparing

figures 4.8 with 4.10 the rate of change in elemental ratio increases from 7.5 % mm^{-1} for the ground to 9 % mm^{-1} for the un-ground needles when measured over the 10 mm of maximum gradient of each library.

This result shows that capillary end shape is not the major factor determining the spraying modes. This finding is similar to that of Choy and Su [164], who demonstrated that increases in the flow rate of $CdCl_2$ solution are the primary caused a transition between cone-jet and multi-jet spraying. A multi-jet arrangement giving complex spraying interactions and generally more unpredictable depositions are undesirable when using a geometric approach to combinatorial production. This explains the difficulty of increasing the deposition rate of one component to compensate of the more intense signal from some elements.

For the un-ground needles, a very marked effect is recorded when distance from the substrate is altered. Figures 4.9 and 4.10 show that needles 6 cm away from the substrate give a much smaller gradient than at 4 cm. This matches expectations as these needles are more likely to spray from a single source and are more directional.

Changing the distance between the needles has a relatively small effect in the range of positions investigated. This is thought to be due to the cone interaction effects. These were found to be minor at larger distances but are increased when the electrostatic sources are very close. It is this static repulsion that resists the greater mixing expected when the sources are closer together.

When co-depositing by electrostatic spray there are serious compromises to be made when optimising the deposition temperature. Two different materials with different pyrolisis rates and oxidisation affinity were both catered for by a single substrate temperature. The physical properties of all the precursor solutions also required optimisation. If the chosen solutions evaporate too readily, they would deposit the element or oxides already dried. This dry deposition gives a fine powder that exhibits no significant adhesion to the substrate. Powdered samples produced in this way have also been shown to produce poor diffraction patterns. Sn-Ni figure 4.54 and Sn-Cr figure 4.57 produce more intense patterns when deposited at 200°C.

The most successful libraries in terms of both adhesion and compositional gradient were deposited at 200° C and then heated to 500°C to remove the remaining acetate. Annealing under a slightly reducing atmosphere prevented complete oxidation thus libraries with a

number of elemental and metallic phases have been produced. Signals from these phases could be seen in a number of the XRD data collections, demonstrated in figures 4.52, 4.53 and 4.54. Also alloys demonstrating lattice parameter shifts caused by atomic ratio changes as illustrated in figure 4.52 have been produced. A negative aspect of the lower temperature depositions are that the film is wet when it is deposited because a significant amount of the solvent reaches the substrate. The film will later dry and contract often cracking under heat treatment.

Single needle deposition was carried out initially so that the substrate adhesion and crystalline structure could be investigated. In these single needle cases the higher temperature depositions produced the more consistent films. For the combinatorial systems optimisation of the deposition methods led to a lower temperature method with a separate pyrolisis step being adopted. This change is due to the difficulty of compensating for the different evaporation rates of the two solutions used simultaneously. High temperature deposition generally leads to films that were deposited either dry or wet depending on the precursor solution the low temperature method ensures that both materials arrive at the substrate with some solvent still present removing this unwanted variable.

As long as a temperature above the pyrolyisis temperature of the acetates is achieved at some point in the production the desired elements will be released. For example 300°C is required for the complete thermal decomposition of $Cu(CO_2CH_3)_2$ [165]. However, the change to a lower deposition temperature with a separate heat treatment negates the pyrolisis of the ethanol solution, the ethanol instead evaporates. It is this ethanol pyrolisis mechanism which produces CO a reducing agent that is responsible for removing oxygen from the system [166]. In this way, the choice of post deposition annealing can increase the oxygen content of the film.

The 50 x 50 mm substrates, used here, allowed the study of the film characteristics as the deposition moves away from the needle focus point perpendicular to the compositional gradient. The film in the area > 25mm from the needle often failed to adhere to the substrate. The smaller quantity of material deposited in this area likely allowed full evaporation of the solution before contact with the substrate, reducing the adhesion. Particles at the edges of the cone are also generally smaller than those in the centre [80]. This will also produce a higher evaporation rate.

The deposition method informs the choice of substrate. Electrostatic methods require a conducting surface to ground the sample [167] for this reason, TCO coated glass were chosen. TCO coated glass is regularly used for solar cell applications where a superstrate deposition order has been used [168]. Results collected during this investigation show that the uncoated glass is conductive enough to fulfil the required grounding so the TCO could be replaced for some depositions. The films produced on the plain glass had strong elemental gradients and a uniform texture. The finding that uncoated glass is suitable for the production of combinational spreads increases the potential for this form of deposition. The coated glass has been established to improve adhesion by incorporation of the newly deposited elements into the conducting film during heat treatment. Despite this improved adhesion given by the SnO_2 layer more useful libraries were fabricated by eliminating the TCO coating.

One of the aims of the depositions was to produce precursors for gas phase addition of chalcogens. Electrostatic spraying allows direct deposition of sulphur into the film by spraying $CS(NH_2)_2$ (thiourea) and the metallic precursors simultaneously [169]. The use of thiourea can be used to achieve either combinatorial additions or a uniform layer independent to the compositional gradient. This gives the advantage of removing the post deposition annealing required for sulphur addition to electrochemically deposited or DC sputtered libraries.

The specific electroplating deposition process employed in this investigation is little used and possibly unique in combinatorial production. The few combinatorial electrochemical production methods found in the literature used a Hull cell type geometric arrangement where a current density difference across the substrate produces CCS samples [71]. All other published methods employ numerous separate reaction vessels where the conditions are varied between each producing arrays of distinct samples [170]. The method developed during this investigation is more desirable than either of the two published methods due to its simplicity and flexibility. Any layer that can be deposited conventionally can be deposited with a controlled change in the film thickness. All eight of the binary systems attempted were deposited in such a way that the majority of the compositional range was available for analysis, or to be used as precursors for ternary systems. The thickness of the samples and the profile of the gradient were easily adapted to the primary function of these samples, testing the extended beam XRD procedure.

Total sample thickness in these layered samples was kept to < 3 μm total thickness to reduce the diffusion time through the samples. Diffusion to the extent where the desired alloys make up the majority of the recorded phases was accepted as complete in some cases. This acceptance stems from the fact that the concentration dependent diffusion rates, as described by Fick's first law of diffusion, could delay diffusion to a totally homogeneous state almost indefinitely [171].

$$J = -D\frac{dC}{dx}$$

Where J is the net flow of atoms, D is the diffusion coefficient and dC/dx is the concentration gradient.

Most of the samples fabricated show a complete absence of the original elemental precursors so, within the limits of detection of the XRD characterisation, these films can be said to be completely diffused. The increased rate of diffusion can be explained by the strong external driving forces, such as electric fields and stress effects, which are often a feature of thin film layers [171].

An important advantage of the new deposition method is the flexibility of the compositional gradient production which exceeds that of the other production methods examined. This is because the sputtering and electrostatic spray methods produce deposition profiles that conform to certain geometric progressions. With this form of electrodeposition, the solution level can be altered at will while plating the films. This can be used to produce the linear or exponential deposition profiles seen with the other methods or a chosen profile where the relatively thickness of the layers is changed rationally. Using the electrochemical method future libraries could be produced where the most desirable characteristics of both CCS and distinct cell libraries can be incorporated. For example, samples where compositional areas of interest are given a small gradient and therefore cover a larger area on the substrate could be produced. At the same time areas of the phase diagram where less information is to be collected can be compressed on the substrate without the need to truncate the system.

As was explained in the introduction (section 1.2.2), a highly conductive surface is required for electrodeposition. In several cases one of the components of the library was sputtered on glass to form the conducting substrate. The sputtered component will diffuse to become one component of the compositional gradient during post-deposition heat treatment. The

sputtering/electroplating method was used successfully in the production of the tin-zinc system shown in figures 4.5, 4.40 and 4.41 and in the tin-antimony system shown in figures 4.4, 4.32, 4.33. This produces simple systems where background interactions have been minimised.

The alternative solution, having an inert substrate that is not incorporated into the library has also successfully employed. A molybdenum substrate was chosen for this layer as the diffusion rates into the sample materials are small at the temperatures employed [56]. This is one of the reasons for the preference of Mo over Au or Pt for the back contacts of CIS solar cells [56]. The use of molybdenum in for example CZTS device structures increases interest in being able to combinatorially deposit over it [127].

The XRD analysis confirmed no detectable Mo alloy phases in any of the binary libraries characterised, only the elemental signatures being recorded. The more complex patterns produced by the addition of the characteristic molybdenum peaks are desired for development of the extended beam.

The addition of an elemental substrate was found to be useful as an internal calibration; initially this was achieved by measuring the exposed Mo at the ends of the library. As the XRD characterisation probe penetrates the over layers the Mo layer can be identified under the surface at any point of the library. The characteristic Mo peaks can, therefore, be used as a calibration throughout the library. This is especially useful where the compositions of the layers above give a lattice parameter shift. The underlying molybdenum remaining at constant d-spacing confirms that the shift observed in the libraries is due to lattice parameter shift only and not any instrumental effects.

Another major advantage of the new electrochemical production method is that, in binary systems, any section of the library taken perpendicular to the sample gradient will be consistent for composition, thickness and physical properties. This has already been shown not to be the case for electrostatically produced samples where the properties of the deposition cone change the substrate adhesion in this direction. In the case of sputtering, a movement on the substrate as described will move to an off-axis position and will reduce deposition rate. The consistency of the electroplated libraries in this respect allows them to be applied to other combinatorial processes. An example of this is where a binary system is turned into a 2-D ternary system by applying different physical conditions such as a temperature gradient to the other axis during deposition or annealing [21].

Copper-tin-zinc alloys have applications in the thin film solar cell industry as precursor materials for the production of Cu_2ZnSnS_4 absorber layers [130]. The feasibility of producing this absorber material by sequential depositions of elemental copper, tin and zinc followed by the annealing in a sulphur atmosphere has been demonstrated by Kurihara et al [172]. Other Cu-Zn-Sn ratios could potentially yield photoactive semiconductors when annealed with sulphur or other chalcogens. The binary fractions of this system have, therefore, been produced as a relevant test of the combinatorial production process. These binaries are also desirable when validating the novel extended beam XRD method as they range from the simple eutectic with a very low degree of mutual solubility, as found in the Sn-Zn system, to the multiphase Cu-Sn and Cu-Zn systems. [173]

The copper-zinc library exemplifies some of the compromises required for the chosen deposition technique. When measured by alpha step at the exposed ≈2 μm thick elemental region the copper was found to be deposited in a uniform manor. No measurable variation in thickness was found when measured perpendicular to the gradient. The mirror like surface is an indication of the lack of nanoscale surface features in the copper layer. The zinc layer is much less evenly finished with tide marks visible to the naked eye. While every effort has been made to make the solution movement over the sample as continuous as possible erratic movements of the meniscus is inevitable, this is more evident during the zinc deposition, most likely due to the properties of the solution used. It is this discontinuous movement of the level of the solution that creates the macro scale tide marks.

The surface of the zinc could be seen to hold on to solutions used in the deposition and cleaning process. The absorption of liquids or gases indicating a porous film, as is measured by surface acoustic wave measurement devices [174]. The surface of the as deposited zinc has been found to be more delicate than would be expected from electrochemical deposition. This fragile surface reduces the scope for direct profiling thickness measurements by the physical Alfa step device. The low reflectivity of the zinc surface means that it is generally unsuitable for interferometer measurements. These two factors combine to make direct quantitative measurements of the physical characteristics of the film difficult. Indirect thickness measurements can be inferred from EDS elemental ratio measurements, which show the elemental percentage of zinc changing by < 1 mm^{-1} parallel to the gradient as opposed to an average of 3.1 mm^{-1} along the gradient. This data is presented in figure 4.3. Additionally, parallel to the gradient the change is a random variation around the mean, while the intended gradient conforms to clear trend. The conclusions to be drawn from this is that,

even with the least consistent element deposited the variation measured perpendicular to the intended gradient was smaller than for sputtered targets.

When XRD was employed the patterns from both elemental copper and zinc were detected co-existing with Cu_4Zn in the as deposited sample (figures 4.29 and 4.30). After heat treatment the material transitions to Cu_3Zn between 15-25 mm as seen in figure 4.31. The same transition is seen in the extended beam partition results figure 4.104. These alloys are both produced from the same α phase with the difference in composition seen on the EDS results occurring by increased atomic substitutions. The diffraction profile for common high brass Cu_3Zn_2 [151] was not matched with any the major components at any point despite the elemental ratio matching this 40 mm from the sample origin. CuZn, a component in the β + γ mixed phase can be clearly identified over positions 27-37 mm.

Another potential material in the photovoltaic field is $CuSbS_2$. This has been mooted as a replacement for the $CuInS_2$ absorber material. [175] A potential mechanism for the production of this material is the gas phase sulphurisation of a CuSb elemental layered precursor material. For this reason an attempt was made to produce an isothermal section of the Cu-Sb phase diagram combinatorially. The EDS results in figure 4.4 and the XRD data in figures 4.34, 4.35 and 4.36 show the presence of Cu_2Sb for a large part of the of the substrate which is to be expected as the ζ region of the binary phase diagram that exists for 60 % of the compositional range is a mixture of Cu_2Sb and Sb phases. [176] For the as deposited this material is seen to be skewed towards the copper rich end as a large amount of elemental copper is still present as an under layer. This is still the case in the heat treated samples indicating incomplete dissociation of the copper layer. The dissociation is more complete as can be seen by the formation of $Cu_{11}Sb_3$ and the associated waning of the diffraction patterns associated with elemental copper.

Sputtering is the only deposition method that is currently used for the production of continuous compositional spread (CCS) libraries. The widely stated positive attributes were evident in the samples characterised here. The mm scale consistency of the average sputtered samples exceeds that of its plated or sprayed alternative. This is illustrated by comparing the EDS elemental compositional results. For example contrasting the sputtered Cu-Al in figure 4.16 with electroplated Cu-Zn in figure 4.3 shows a smoother compositional profile with no discontinuities for the sputtered system. The smoothness of the surface finish and the adhesion to the substrate is also superior for the sputtered examples. This is expected as the

higher energies of the method reduce dendrites and porosity [48] [177]. The preliminary production attempts by electroplating compared positively with the established and highly optimised method. Layer ordering and diffusion time constraints produced by the sequential nature of the elemental electrodeposition were the only significant disadvantages confronted.

The direct current sputtering method was expected to produce graded films in terms of elemental composition [6] [57]. The EDS results presented in section 4.2 demonstrate this to be the case in all the libraries offered. Polycrystalline films suitable for XRD have resulted from the sputtering method in many studies [58] [59], section 4.4 illustrates that this is the case in the samples made for this investigation. The characteristics of the extended beam partitioning when applied to different sample morphologies is best understood by applying it to samples created by this well established fabrication method.

To summarise both the electrostatic spray and the electrochemical bath depositions produce composition spread libraries suitable for both EDS and XRD analysis. Electrostatic spray libraries production is viable for multiple needle simultaneous depositions of several materials. The interactions of the separate charged sprays are not detrimental to the formation of elemental gradients. The changes in composition over the majority of the substrate is small meaning the process could be employed in the study of subtle dopents in established systems. Improvements to the film adhesion could be made by changing the substrate. The presence of trace amounts of chlorine detected by EDS could be eliminated by using an organic acid (that is thermally unstable) to resist the hydroxide formation in the precursor solution.

The electrochemical bath production method proved flexible in controlling both the compositional spreads and film thickness. The method was easily adapted for the production of ternary systems as a third material can be added perpendicular to the binary gradient. This geometry is most practical when using a Cartesian sampling grid as it avoids wasted data collection points.

Post-deposition annealing of the electrochemically produced libraries produced the alloy phases desired for the diffraction method development. The addition of chalcogens during this heat treatment produced compounds known to be semiconductors. These were limited to portions of the compositional spreads and had clearly defined limits. Materials existing for a small physical distance on the substrate show that this method can be used to investigate specific short lived high order phases.

Mechanical stirring to equalise the concentration in the ions in the electrolytic solution is not practical with this set up as it disturbs the surface of the solution. An alternative to stirring is desired as using diffusion based equalisation alone reduces the consistency of the surface finish. Plating efficiency is also inevitably reduced as the concentration of the metallic anions next to the substrate surface and available for deposition is reduced during the process [63].

6.2 Extended X-ray beam methods

Validation of the partitioning process has been carried out on simulated samples and simple phantom samples so the characteristics are fully understood before it is applied to the combinatorially produced libraries.

6.2.1 Simulated data

In both the simulated point source examples (figures 5.1 – 5.4) and in the simulations of the extended beam (figures 5.5 – 5.7), the d-spacing and the position on the substrate calculations are accurate to the nearest grid point. This is important as subsequent deviations from this calculation can be attributed to changes in the characteristics of the input data and not to the partitioning algorithm. As the abstract grid points used in the simulations have no physical dimensions the exact quantification of the effect has been left in grid point units. A direct conversion to detector pixels is possible, in these cases the resolution results would be a function of standard diffraction geometry. This gives a linear relationship to distance in the y axis ‘position on the substrate’ and will conform to Bragg’s law for the d-spacing calculation.

The simulations establish a robustness of the method within the calibration range. With the centre point of the diffraction rings (the point where the illumination beam would reach the detector if sample transparency allowed it) fixed, the d-spacing calculation remains accurate to 0.02 Å at any diffraction angle. The one-to-one correspondence of sample position and detector position means that no calibration is required for this parameter. This remains true for any degree of extension to the simulated beam.

In these simulated cases, the cross-section graphs, (figure 5.3), show a flat top profile when sectioned in the sample distance (constant d-spacing) direction. The intensity profile rises with the sudden transition from a weakly diffracting material to a material with intense

diffracting peaks at a fixed point. Similar flat topped peaks are detected when the cross-section of the intensity profile is taken along a line of constant sample position. This is an artefact of the idealised top hat profile of the original simulated diffraction arcs (figure 5.2). The flat top to the characteristic 'bow tie' feature of the partitioning is also marked in these simulations, (figure 5.3), due to the idealised sample.

6.2.2 Profile of partitioned results

The profile of the partitioned beam can be seen to be slightly asymmetrical, the randomly orientated results shown in figure 5.18 (black peaks) illustrate this effect. This can be explained if intensity map from an extended beam illumination producing multiple arcs is considered as a single thick arc. As the two sides are created by the opposite sides of two different arcs in different positions when this new arc is examined at its small angle side it appears to have a smaller radius than would be expected from its centre position. Conversely, if it is examined from the large angle side the radius is larger then would be expected of a true Debye arc at that position.

This means that the overlaid virtual arc being moved from low to higher angles will interact with this at an early stage leading to a gradual tailing to the intensity profile. On the higher angle side the rising angle of the virtual arc and its increasing radius work concurrently so that the detection of this unwanted intensity profile reduces more rapidly with the changing arc position.

This effect can be regarded as similar to the axial divergence distortions that are the principle cause of profile asymmetry in conventional powder diffraction [106]. The virtual arc is effectively a curved receiving slit for this purpose as its movement produces the intensity distribution. As with its parallel in conventional diffraction, the peak asymmetry produced by the partitioning is more pronounced at low diffraction angles.

Additional peak asymmetry is caused by the transition from a plot of 2θ to d-spacing. If this is problematic a non-linear d-spacing scale can be used to improve the visual representation of the results. This scaling is used, for example, in Eva diffraction software.

6.2.3 Preferred orientation (point source)

When considering the partitioning with respect to a simulated version of a standard point source sample the amount of preferred orientation or the way that the diffraction arc intensities are distributed does not change the accuracy or the precision of the d-spacing determination. Therefore the partitioning and linking this intensity maximum to the d-pacing of that plane is as robust as the conventional radial integration methods. In this study the raster scanned data from the Diamond synchrotron was collected as images, the partitioning algorithm being used as an in house radial integration method. It has been shown that the diffraction angle is correctly determined even in cases (Pt-Ru library for example) where the preferred orientation is very high.

For point source samples d-spacing is unaffected by orientation except for the rare case where only a single intensity point is produced for a given diffraction ring. This may be the case with the diffractograms from some single crystal samples. The opportunity for this exception to occur is further reduced as only the situation where diffraction spot is asymmetrical with respect to the virtual arc produces an inaccuracy in the d-pacing calculation. In all the symmetrical highly preferred cases the partitioning produced an artefact shapes like the reciprocal to the overlaid virtual arc (figures 5.09, 5.10 and 5.11) but with the intensity maximum still correctly positioned.

In diffraction results where the intensity profile on the area detector is highly confined and unsymmetrical the partitioning outputs a range of possible position and d-spacing combinations. The correct one cannot be calculated without additional information. This is because the results conform to an equation with two unknown variables, position on the sample and d-spacing. Nevertheless, this situation is not as problematic as would be first assumed. There is only one geometric situation that could reasonably fulfil these criteria, that is strongly preferred sample with a plane orientation allowing only one area of intensity for every detectible diffraction ring.

While the d-spacing is correct if the maximum intensity point is considered the shape of the peaks in the area intensity map is distorted by the preferred orientation. The extent of this is illustrated in figures 5.9, 5.10 and 5.11. The ‘bow-tie’ artefact is still detected but less of it is present as there are fewer positions where the interactions forming these artefacts occur. A

related consequence of the preferred orientation is the noise signal created by the unwanted interactions between the sample and the virtual arcs are proportionally larger compared to the true signal. The correct overlaying of the virtual arc and the diffraction ring will always give the best fit and therefore give rise to a response clearly discernable from the background. In this way the point of maximum intensity will give the correct d-spacing even in highly preferred of large grain size materials.

6.2.4 Preferred orientation (extended source)

For the extended beam situation a cross-section of the intensity map in figure 5.18 shows that, as in the point source examples, there is no change to the plane spacing when the preferred orientation limits the detectable diffraction intensity to the central region in the simulation. However, in cases where orientation of a particular plane means the centre point of the detector is not illuminated the d-spacing calculation is overestimated. The extent of this is shown in figure 6.1 where as the preferred orientation effect reduces the area of the detector covered by the diffraction arc (displayed as a percentage of an ideal randomly orientated arc) the error in recorded d-spacing increases. Figure 6.1 also confirms the systematic nature of the effect. To aid the perception of the scale of this effect the simulated system was scaled to exactly match the geometry of the Bruker D8 diffractometer used for library characterisation, hence the errors are quoted in Angstroms.

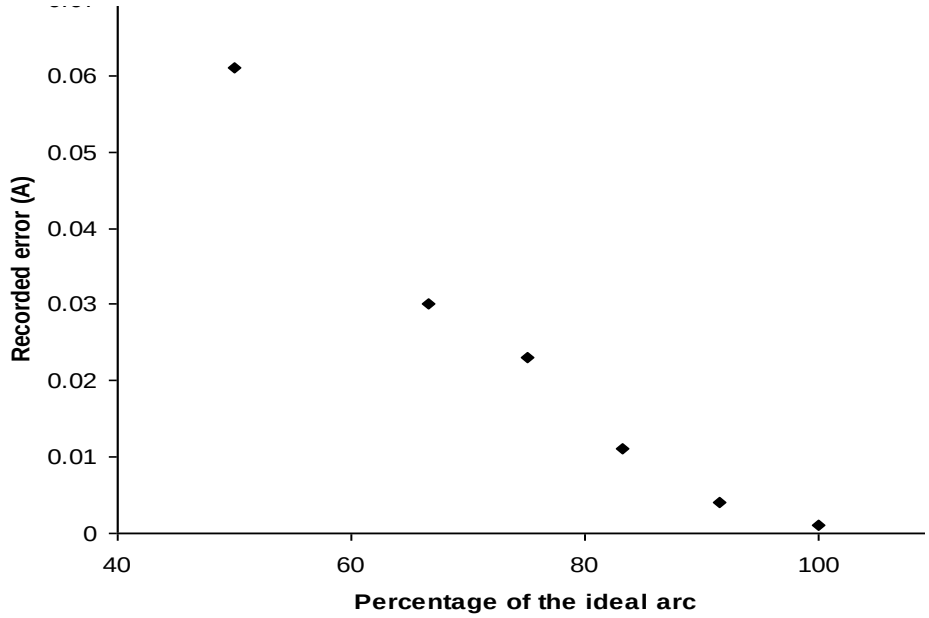

Figure 6.1. The systematic error produced by the partitioning of diffraction data from strongly orientated samples. The lengths of the orientated arcs are quoted as a percentage of the ideal arcs that cover the full width of the detector.

In materials that are strongly orientated detecting a plane that is parallel to the surface of the sample may actually be favoured over random orientations. This orientation arrangement does not affect the d-spacing calculation when the maximum intensity is used. The peaks partitioned from these orientated planes demonstrate greater sharpness, being narrower at both FWHM and at the base. This is true even after considering the reduction in intensity which is a function of the reduction of total intensity in the simulated matrix. The reason for this sharpness is that the intensity profile described here gives less opportunity for arc mismatch errors.

The advantages calculating the d-spacings from highly preferred samples should be considered cautiously. The improved results described above are achieved using the peak maxima positions only. This specific way of determining result precision would not ideally be considered in isolation. When the 2-dimentional intensity map is examined as a whole it is clear that where the mismatching does occur it is more problematic. The intensities of the artefacts shown in figures 5.12 - 5.17 are a larger proportion of the main signal. This is because these false responses are more concentrated than the artefact seen in randomly orientated samples. This means that they are more likely to conceal other weak diffraction peaks especially if these have different origin positions.

Where a randomly orientated sample is illuminated the symmetrical nature of the artefacts helps to determine the position of the samples physical limits. In strongly orientated samples this does not occur so the end of the sample is less well defined.

Where most of the intensity of the diffraction ring is concentrated at the edges of the detector, such issues are more significant; figures 5.12 – 5.17 also illustrate this situation. In addition to the shift in calculated d-spacing quantified in table 5.2, the cross-section shows that the peaks appear wider and more markedly asymmetrical as shown in figure 5.18. The signal to artefact intensity ratio over a large range is also smaller. These factors are all due to the larger mismatch effect that exists in these situations, which can also produce false positives over a long range of sample positions. This makes the identification of low intensity secondary peaks less likely.

6.3 Ideal samples

6.3.1 Profile of the beam

To fully explain the results of the partitioning it is imperative to first fully characterise the extended X-ray beam. It is clear that many of the features of this method could arise from the specific character of the illumination source. It is also important to distinguish between limitations arising from our particular setup and theoretical limitations that cannot be overcome with different instrumentation.

The length of the beam when using the pixel dependent method, explained in section 5.2, was calculated as 22.84 mm, 23.89 mm and 24.68 mm for the different reflections. This is the preferred method of beam length calculation as it comes directly from the results of the partitioned data and will, as a result, be most closely linked to the real diffraction data collected from the libraries. The disparity in the three results is due to the way in which the diffraction profiles are slightly intensity related. The intensity of the extended beam drops slightly towards its ends, so the beam appears 4 mm shorter at 90 % of the maximum intensity than when the 50 % level is used. Due to this in poorly diffracting materials or in very thin films were the interaction volume is significantly restrained the footprint of the beam will appear smaller. In the same way it is seen that even in the case of a strongly diffracting standard the planes that exhibit diffraction with lower relative intensity will also register a smaller perceived beam size. An approximately 0.5 mm reduction from each end is observed when moving from Al_2O_3 116 to the 104 reflections. In the course of the study, this issue was considered with regard to its effect on the various samples but it needs to be made clear that this variation in the photon flux at different points along the extended beam comes from the collimation of this particular X-ray source and is not fundamental to the method. Figure 5.20 shows that the variation in the photon flux along the extended beam is uniform for the purposes of this experiment, with a < 10 % variation over the central 200 pixels (21 mm).

The second method of determining the length of the extended beam is explained in section 5.2. This is independent of pixel size and this independence constitutes its major advantage as it can be used as a check for the conversion factor. The other advantage of calculating the

beam length in this way is that it is less sensitive to X-ray intensity. Any diffraction that can be perceived on the detector was determined as a positive result calculating the beam length from this premise gives a maximum value of 26.6 mm.

6.3.2 Optimisation of the beam incident angle

Flexibility in choosing the incident angle is important when using this method on certain thin films. It is also useful when analysing 3 dimensional libraries with layered structures using variable angle profiling. For these reasons, a measure of the robustness of the partition method to changes in incident angle are useful.

Changes in the incident angle are known to produce different penetration profiles with lower angles illumination giving less penetration [112]. For thin film samples where the thickness of the homogeneous layer is small, a fixed low incident angle may be preferred as this will limit substrate interactions. Table 5.6 shows that a low incident angle for the X-ray illumination does not have a major detrimental effect on the d-spacing calculation when using the extended beam. None of the peaks show a systematic increase in width as incident angle in reduced. The low angle method can therefore be fully exploited when using the partitioning method.

When the result of reducing the incident angle on the characteristics of the diffraction peaks was studied efforts were taken to minimise other factors such as substrate interactions. A bulk diffraction standard was therefore used in these determinations. However subtle changes in the structure of bulk materials between the surface layers and the rest are still detectable. These results are weighted by the intensity of the diffraction profile at their particular depth. In this sample changes in preferred orientation with respect to depth are apparent. This explains the changes in the relative intensity of different planes recorded in table 5.24. This finding neatly demonstrates the usefulness of being able to change the incident angle.

One of the characteristics of the extended beam approach is of course the larger area on the substrate from which the data collection is achieved. This means that positioning the sample correctly can be more important. For example having a flat sample with small displacement errors (> 10 µm) across ≈25 mm is required. For the raster scanned samples it is possible to reposition the sample between scan positions, thus the requirement of a sample of consistent

height is removed. As the method is envisaged for thin film samples large fluctuations in sample height are only likely to occur if the substrate moves off the focal point of the illumination.

The positions of the Cartesian axis quoted in this discussion are related to the physical sample or the 2 dimensional partitioning profiles in the same way as in section 5.1 where it is explained fully. Ensuring that the extended beam keeps a constant angle to the surface of the sample is important. If this is not the case the interaction of the beam and sample will occur at different x positions and being a different distance from the detector will give an error in the d-spacing. This effect is larger where the incident angle is small as the same displacement moves the footprint of the beam over a larger distance. Figure 5.25 shows the effects of a 2° tilt at an incident angle of 5° and figure 5.26 shown the same effect at 30°.

For the 30° incident angle a 2° tilt acting over the typical beam length of 25 mm would give a 1.55 mm error in the x position using the equation as described by Dicken et al [178]

$$2\theta_{obs} = 2\theta_{std} - \sin^{-1}(r_1 \sin(180 - 2\theta_{std})/R$$

Where R is the sample to detector distance, r_1 is the x axis displacement error and θ_{std} is the expected angle. Using the Al_2O_3 (104) plane ($2\theta = 35.1°$) as an example, the error would be approximately +0.34° 2θ at this angle. This would be a lesser component to the error caused by the accompany Z displacement error highlighted in section 4.5.2 this would be +0.63° 2θ.

When the incident angle was moved to 5° the applied 2° shift acting over 25 mm of the sample y axis gives an x direction error of 10.29 mm. Using the same conditions as above the effect would be 2.25°. However, eliminating this source of error by calibration with homogeneous sample is straight forward and will allow the use of the method at small incident angles.

6.3.3 Matching the calibration detector angle to the data collection angle

Peak smoothing was carried out to aid the data presentation in this section. A Savitzky–Golay smoothing method was used as this does not change the peak position. A 51 position smoothing was chosen as this leaves the data is such a way that the short range data quality

can still be observed. The trend (shown in figures 5.37 and 5.38) is that as the as the detector position angle error increases the noise seen in the intensity profile will increase.

In the single peak example Si (111) (quantified in table 5.11) the process is robust. The main difference is a spreading of the peak along the position on the sample (y) direction. This is due to the radius mismatch between the collected diffraction pattern and the virtual arc used for the intensity summing of the partitioning mechanism. As the angle of the detector position increases the peaks will be lower on the detector than would be expected from their radii. In these cases, the virtual arc overlaid will be too small in radius to match fully and it is this process that is the mechanism for the spreading. The process means that the calculation for the width of the Si powder that is initially calculated correctly as 5 mm (± 0.1mm) will be over estimated at approximately 0.33 mm per degree of detector position offset.

The peaks of the Al_2O_3 are more prone to this effect as the diffraction peaks are present for ≈ 10 mm on each side of the Si. This larger presence in the 'position on substrate' direction means that there is a larger amount of overlaid diffraction arcs caused by the Al_2O_3. This produces a greater false signal in situations where the arc fitting is poor.

Where the detector position for the data collection and the detector position in the partitioning differ by 8°or more the ability to detect the low intensity trough in the Al_2O_2 signal has been lost. Therefore under these conditions determining the position of the absence of the aluminium oxide is not possible from this partitioning. The detection resolution has become poorer than 5 mm in this case. It should be noted that this is only true when considering the Al_2O_3 (104) in isolation. When the partitioning data from the sample is considered in its entirety the correct positions of the materials can still be correctly surmised even in this extreme situation.

This finding is interesting as different detector positions have been shown to have a marked detrimental effect on the resolution of the partitioning especially with respect to position on the sample calculation. This is contrary to the expected results that assumed that the position on the sample resolution errors would be small. The d-spacing calculation can be easily compensated for but this is of little significance as the other findings rule out the use of a standard angle for the calibration.

6.4 Application of the results to phantom samples

In samples such as the Si and Al_20_3 composite sample, the results of which are shown in table 5.8 and 5.29, the rising of the intensity at one characteristic position and the lowering of intensity profiles at other d- spacing is observed. This means that the resolution in terms of position on the sample is easily to define.

For samples such as the two Si filled well samples (results shown in figure 5.39), the potential resolution of the method when it is employed to measure this type of samples is less well established. In these cases, the position of the edge of the samples in relation to the substrate is linked to a judgement on the level of intensity that yields a positive result. Calibrations with known samples show that 90 % of the maximum intensity is representative of the presence of sample materials used during this investigation. The continuation of the intensity profile after this point is caused by the partitioning mechanism. Reduction to the unwanted intensity profile in this region could be achieved by altering the frequency of the partitioning. This is currently at 105 µm but as the ultimate resolution of this type of sample is ≈ 1.5 mm this choice of partitioning frequency represents a form of oversampling, spreading the intensity profile in the position on the sample direction. Changing this to for example 1.575 mm, a 1 in 15 pixel sampling is possible without a large reduction in resolution. While the resolution would be reduced slightly the results would be still comparable with a raster scan collection of an average density. The methods would have two advantages. The edges of the sample would be more clearly defined and the time taken to partition the results would be reduced.

6.5 Application of the partitioning to High Density Chemical Libraries

Here is presented the characteristics of the partitioning method when applied to specific high density chemical libraries. The examples have been chosen to indicate the effect of different physical properties of the libraries, specifically how these characteristics alter the comparison between the various extended beam results and their raster scan compilation equivalents.

6.5.1 Electrochemical bath

The copper-zinc library is a multiple phase system. Both the extended and pencil beam methods show both abrupt phase changes and the lattice parameter changes that are caused by atomic substitutions or additions.

The change in d-spacing when calculated from the raster point scans are for the Cu/Cu_3Zn (200) 1.7970 Å ±0.0007 Å at point 16 mm changing to 1.8181 Å ±0.0007 Å at point 26 mm and for the Cu/Cu_3Zn (111) the change was from 2.0707 Å ±0.0009 Å at the 16 mm to 2.0991 Å ±0.0009 Å at the 26 mm position. When calculated from the wide beam partitioning Cu/Cu_3Zn (200) 1.7991 Å ±0.0014 Å at point 16 mm changing to 1.8150 Å ±0.0014 Å at point 26 mm and for the Cu/Cu_3Zn (111) the change was from 2.0744 Å ±0.0016 Å at the 16 mm to 2.0974 Å ±0.0016 Å at the 26 mm position. From these plane d-spacings, the lattice parameters were calculated and results of typical cases are displayed in table 6.1.

Data collection type	Cu (position 16 mm)	Cu_3Zn (position 26 mm)
Raster scanned	3.591Å ± 0.0058	3.636 Å ± 0.0003
Extended partitioning	3.599 Å ± 0.0005	3.631 Å ± 0.0020

Table 6.1. Calculation of the lattice parameter shifts for the Cu to Cu_3Zn transition, errors quoted to one standard deviation.

The fact that the lattice parameters calculated from the extended beam are not statistically different constituted confirmation of the methods effectiveness under these conditions. As the lattice parameter calculation is key to the effectiveness of XRD characterisation [99] [101]. This is an encouraging result in its own right and as an indication that similar low stress systems would be correctly characterised.

Expanding on these results it is possible to link the elemental composition of the library to the lattice parameters of the phases detected by the XRD. As only the EDS and the extended beam partitioning data are required this information can be gathered in a reduced time. Figure 6.2 shows the lattice parameters of the main phases, for the hexagonal zinc phase both a and c are displayed.

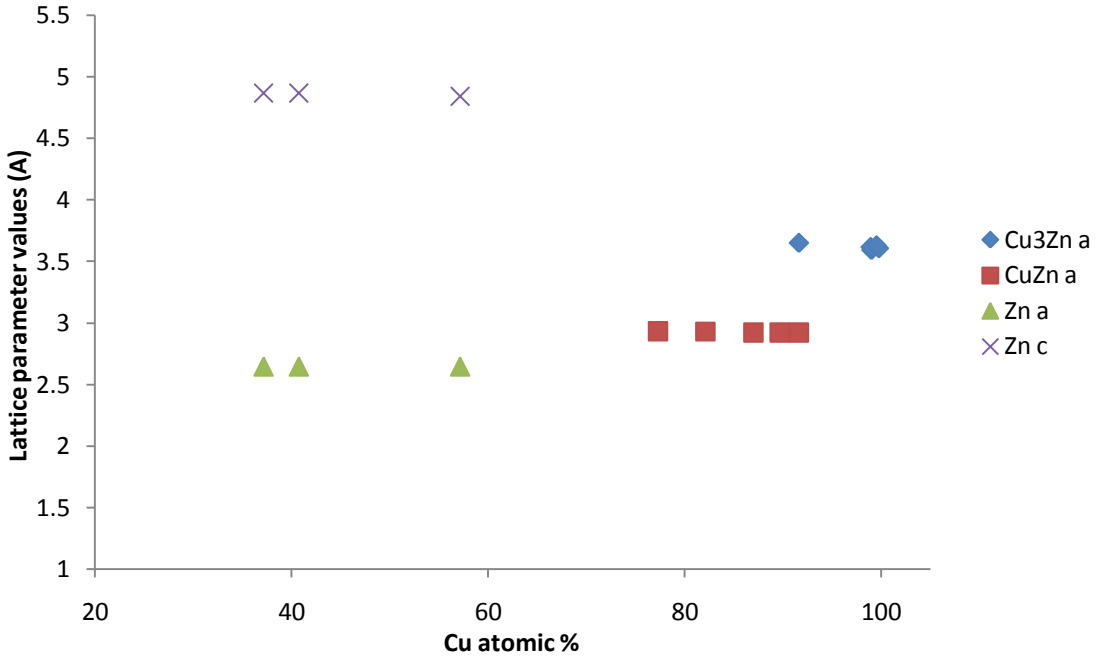

Figure 6.2. Combined EDS and extended beam XRD results for the copper-zinc library. Here is illustrated the link between elemental composition and lattice parameters.

Anomalous results from the extended beam partitioning method are shown in the Cu-Pb library. The compilation of the raster scans are shown in figure 4.38 with the corresponding extended beam partitioning shown in figure 5.46. Comparison with this graph and the one from the compilation of the raster scans gives a different overall profile. The diagonal lines that are present on the intensity map of the partitioned data are known to be inconsistent with the true diffraction profile. Complications to the analysis of the sample have occurred in this case as the nature of the sample adversely affects the partition. It is not the materials as such but instead the morphology. A small number of large grains in this library mean false positive signals are produced. This occurs anywhere the virtual arc overlay interacts with these grains, rather than only a match of the whole diffraction arc. A similar but smaller effect that creates the 'bow tie' artefacts in the partitioning of randomly orientated samples, this effect is more marked. This would be the case in any situation where an unusually large grain size in detected. The extreme case achieved with the lead in this system best illustrates the phenomenon. In figure 4.39 taken from the conventional point source data it can be seen that over the angle covered by the detector some of the Debye rings have only two intensity points. For this reason the usual partitioning artefact profile has been replaced with false arcs that map these few intense areas. The positioning of the false positives signal follows the same mechanism as the point source highly preferred simulated samples illustrated in figure

5.11. The false positives therefore produce an arc opposite to the overlaid virtual arc. From this it is possible to calculate the cause of the interference as a position on the sample vs. d-spacing function. It is not possible to solve for these two unknowns.

The results for the Sn-Sb library has been listed in table 5.12. The observed d-space values determined from the extended beam are compared with those obtained during the raster scan measurements. The similarity of the results indicates the reliability of the transformation algorithm in this and similar cases. In addition to the confirmation of the d-spacing consistency, an important result is the correspondence of the peak lengths in terms of their distance measured across the sample. An example of this is the Sn peak with d-spacing 2.75 Å is detected 20-45 mm from the sample origin. This can be obtained by either of the two methods (figure 4.33 for the raster scans and 5.43 for the partitioning). This is an important finding because it allows the confirmation of the presence of chemical species for each position of the library using the extended beam alone. Applying other analytical techniques it would therefore be possible to associate elemental composition to the position on the library and therefore obtain an isothermal line of the phase diagram.

The copper-antimony system shows the partitioning ability to determine both of these two factors quickly and accurately. Table 5.13 shows the d-spacing determination for all the detected peaks to be well within the precision required for phase determination. Figure 5.45 shows that the position on the sample calculation of phase position agrees with point source collected data for every position when 90 % of the maximum peak intensity is used as an end point. This shows the resolution of the partitioning in respect to the sample position smaller than 2 mm. The area of the Cu-Sb library illuminated by the extended beam is a multiphase part of the system and the fact that this can be partitioned with accuracy is a positive indication of the results that would be achieved when characterising similar systems.

6.5.2 Sputtering

The aluminium-copper library shows a number of phases that should be suitable for both data collection methods. The two sets of results are displayed in figure 4.46 for the raster scans and in figure 5.50 for the partitioning. Both identify the peaks and also display the d-spacing with a precision to quantify the lattice parameters. Using the tetragonal Cu_2Al system as an example the lattice parameters are a = 6.0261 Å ± 0.0395 Å and c = 4.8757 Å ± 0.01003 Å

for the raster calculation at 6 mm from the sample origin. Lattice parameters a = 6.0139 Å ± 0.0737 Å and c = 4.8453 Å ± 0.0194 Å have been calculated when the partitioned data equivalent to 6 mm from the origin is used.

The tetragonal structure of the Cu_2Al allows the lattice parameters to be calculated using several independent d-spacings [99]. The errors quoted are one standard deviation from the mean of these results. Even this relatively small deviation is large in comparison to the difference between the averages of the two different methods. This gives confidence that the results from the raster scanner date collection and the extended beam partitioning are not significantly different.

The results from this example are important this particular library has two characteristics that present a stern test for the partition method. Firstly is contains multiple closely positioned peaks in terms of d-spacing. Secondly there is significant d-spacing axis smearing caused by the orientation of the constituent phases, which reduces the perceived intensity of the lesser peaks. Despite these factors the lattice parameter calculations are consistent with the established method.

EDS results in figure 4.16 show 64 % copper at the 10 mm point, at the same position the majority component from the XRD is matched to Cu_2Al these collate well, although it is important to recognise these findings are the result of several coexisting phases θ and η_1 [138]. At 16 mm from the origin the Cu_2Al overlaps with diffraction profiles that match Al_4Cu_9, the elemental composition in this area is what would be expected from these two matches (figure 4.16). The presence of elemental copper traces is also inferred with observed diffraction peaks being matched to this material.

The Pt-Ru library has been examined due to its different structure. The alloy formed in this case is in the form of a solid solution over much of the compositional range, as can be seen in figures 4.47 and 5.51. When these results are considered with regard to the d-spacing shift the results are not exactly the same when measured by the two methods. For the area covered by the extended beam, the d-spacing change is recorded at 0.08 Å over the 25 mm of the extended beam as opposed to 0.12 Å that is determined by the raster scans.

The differences are explained by the lack of intensity in the diffraction from some points in the library as can be seen in the raster scanned data. This means that a 25 mm trend can only be calculated with confidence for data collected from the 52 mm to 77 mm positions on the

sample. The extended beam collected data is centred around 58 mm (i.e. from about 45-60 mm) these can only be compared directly if the lattice parameter shift is linear with the atomic composition change. It is known that the atomic size factor is not the only mechanism at work when considering d-spacing changes. Factors such as the change in the volume to valence electron ratio, Brillouin-zone effects and electrochemical differences between the elements will mean that, in most cases the composition effect will deviate from the linear relationship as described by Vergard's law [179]. Hence, the differences in the rate of d-spacing shift between areas on the substrate are expected and not a deficiency of the extended beam method. One finding is the reduction of intensity of some areas on the substrate is not immediately apparent from the partitioned results. This could be caused by an increase in photon flux with this method which would be a benefit. It may also be caused by sample morphology uncovering negative characteristics of the partitioning.

Preferred orientation evident in this library and measured by both diffraction methods has been linked to the insensitivity to the sample intensity. Preferred orientation should not in its self cause an inaccuracy in the partitioning. (The maximum intensity distribution of the remaining Debye in this sample has been shown to be in a detector position aligned with the area detector. That is caused by a plane orientated so that it lies parallel to the sample surface. This positioning has been shown not to effect the d-spacing calculation in section 6.2.) However, in this case, the reduction in the intensity of the diffraction from some parts of the library interacts with this orientation phenomenon. In this combination the maximum intensity is not caused by the expected position. Instead, the maximum intensity follows the profile of the virtual arc for the last ~10 mm of the extended beam incorrectly lowering the change in d-spacing calculation.

In the other examples all the point source positions have produced diffraction peaks of an acceptable intensity so that a direct comparison between the two different data collection methods is possible. This means that the effectiveness of the extended method in determining the lattice parameter shifts can be appreciated without making any assumptions towards the samples compliance to Vegard's law. That is if a non-linear relationship is detected in the raster scans it will also be detected by the extended beam.

Similar preferred orientation effects occur in the other samples such as the Zi-Ti and Cu-Pt systems; this is expected as these films have been produced with slow deposition rates and are less than 500 nm in all three cases. This type of growth onto an orientated substrate often

produces preferred films [111]. In this case the films grown on a single crystal Si wafer grow epitaxially. This mechanism is more likely to occur were the substrates temperature is low limiting atomic rearrangement. [180] In the cases of the Zi-Ti and Cu-Pt the preferred orientation does not adversely affect the ability of the partitioning to determine the correct d-spacing. This shows that it is only the unusual combination of preferred orientation and a large change in signal intensity with position on the sample that produces inaccuracies in the partitioned results.

As these results partitioning results have been found to be accurate, they can be linked to the elemental data in Figure 6.3. Use of the rate of lattice parameter shift to calculate the Vegard's coefficients is possible from these results. These were found to be +0.0048 Å/% with a pure titanium having a lattice parameter of 4.6513 Å if the relationship remained linear.

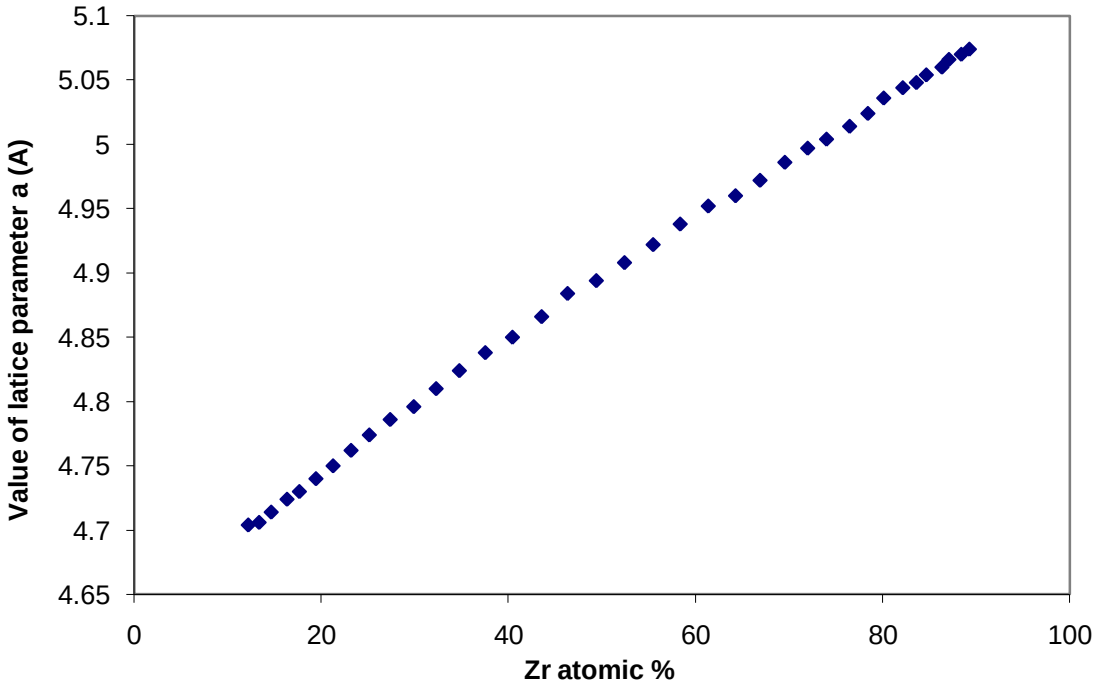

Figure 6.3 Results from the zirconium-titanium library linking the elemental composition with the lattice parameter calculated from the extended beam analysis.

Linking the lattice parameter value to the stoichiometry can be made with any partitioning data such as the copper-platinum library (figure 6.4). Here the Vegard's coefficient is found to be -0.0034 Å/% and the intercept (100 % platinum) would be 3.387 Å if a linear relationship was assumed throughout the range.

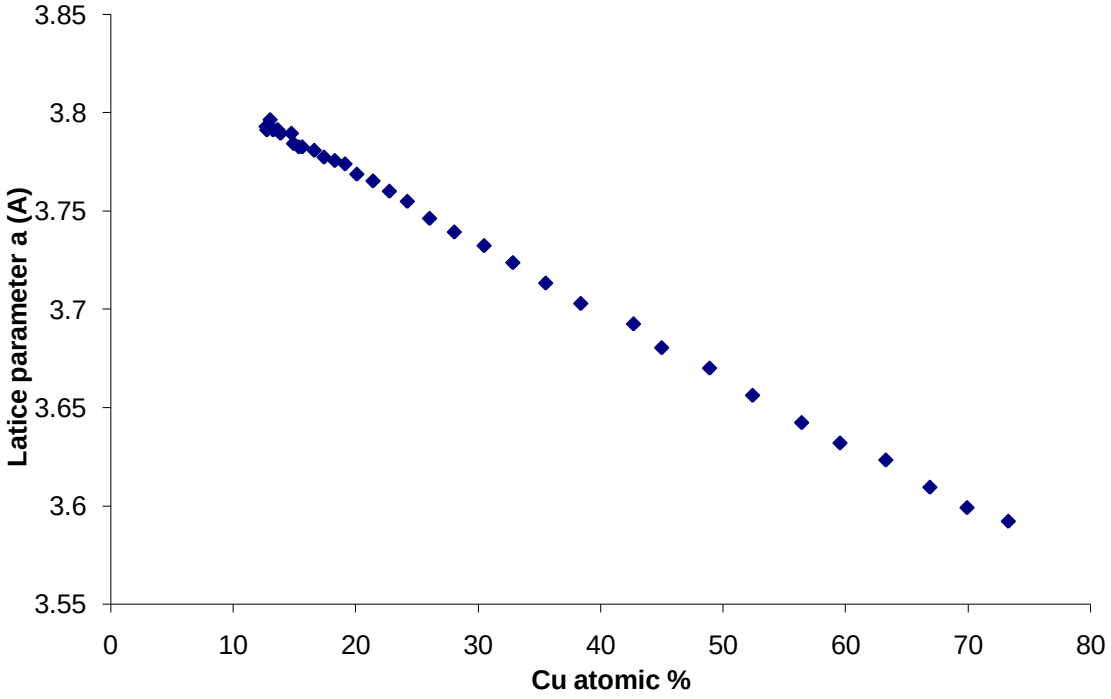

Figure 6.4 Results from the zirconium-titanium library linking the elemental composition with the lattice parameter calculated from the extended beam analysis.

6.5.3 Electrostatic spraying

When considering the electrosprayed Sn-Cr system in figure 5.56 two sides can be clearly observed. The intensity profile of the poorly diffracting side of the image can be seen to rise as the d-spacing increases. This intensity gradient is characteristic of air scatter [106]. While this effect is visible in the other diffraction images it is more apparent in this case because the intensity of the peaks present is very low. Additionally the intensity from the low intensity chromium part of the library is picked up by the virtual arc, this reduces the relative intensity of the true tin peaks in relation to the background. Also distortion of the shape of the peaks is observed. The result is that the peak widths are higher than would be expected, for most positions on the substrate.

While the quality of the information in this image is low however this should be considered in context, the raster scanned compilation also shows poor data quality. It is possible to extract the same information from either method, namely that the overall crystalline quality of the sample is poor and the chromium is almost amorphous. With both methods the tin can

be detected on the low numbers, up to about 25 mm from the sample origin, this can be matched to the pattern for the tetragonal β allotrope.

When comparing the raster scanned results for the electrostatically produced Cu-Sn systems (shown in figure 4.55) with the extended beam partitioning of the same system (figure 5.57) both similarities and difference can be observed. In this case the extended beam illumination is known to cover the 2-28 mm positions on the sample. This is correctly observed when the Cu_2O (200) and CuSn (110) peaks are considered. The Cu_2O (111) is positioned differently in terms, of position on the sample, this cannot be corrected by an intensity correction. Additionally the perceived d-spacing is lower for these peaks than would be expected. This is on first inspection strange as this was the only sample tested to exhibit this inaccuracy and the movement was not observed in any simulated examples. Only movement of the perceived peaks to higher d-spacing values can be explained by non-random crystalline orientations as shown in figure 5.18 and explained in section 6.3. A more detailed assessment of the partitioning profile reveals that the maximum intensity observation is caused by the interaction of several separated intensity arcs that happen to overlap and therefore sum at a lower d-spacing. The cause of the maximum intensity shift can therefore be attributed to a combination of two causes. Firstly that the sample in this region is strongly orientated with the Cu_2O (111) lying parallel to the samples surface and secondly that the diffraction signature and presumably the film that produced it is discontinuous. While this effect constituted a slight disadvantage of the partitioning method, careful analysis of the shape and position of the diffracting regions allows the correct d-spacing of the observed peaks to be calculated.

The reduction in the data collection time is the main advantage of the extended beam method. As the photon flux of the beam has the same density at every point as the pencil beam the improvements in data collection time should be equal to the number of conventional points covered by the larger beam. With this arrangement the data collection time would be x12.5 longer for conventional samples. In this study the data collection time for the extended beam was increased to 2.5 times longer than the point source collections reducing the collection time to an 5 fold advantage. This was done to improve the signal to noise ratio as this had been seen to be problematic with the wide beam illumination. When considering some weak peaks such as the peaks of the Ti-Zr figures 4.50 and 4.51 in comparison to the partitioned data figure 5.55 the weak Zr 100 reflection is more prominent against the background noise than for the raster scanned examples. This is expected due to the higher photon flux and

indicates that the additional data collection time is not required in some cases. Therefore the original 12.5 times data collection time saving is shown to be accurate. The time saving could be increased further by employing a longer beam, a 70 mm beam can be accommodated by the samples produced during this research therefore a 70 mm beam could lead to 14 - 35 times more sample area being analysed in the same time.

In complex libraries the advantages of the extended beam partitioning are reduced. In these complex patterns containing both very strong and weak diffraction peaks the lesser peaks cannot easily be partitioned from the background noise.

Noise problems can be considered as from two mechanisms. The first is background air scatter from the Compton mechanism that is present in both the extended beam and the point source diffraction experiments. This is exaggerated in the extended beam process because of the ≈50x increase in the X-ray output in these experiments. The extended beam is also less strongly collimated than the beam used to give the point collections. This scattering can be reduced with knife edge shielding of the detector. Such a system has been successfully employed and is illustrated with the ideal samples discussed in section 6.2.

The second mechanism is noise from the partitioning algorithm itself. In this case low intensity peaks can be masked by the artefacts from high intensity reflections. This can potentially occur were the maximum intensity of a diffraction ring - virtual arc match from a weak reflection is similar in intensity to a partial match on an arc from another reflection that occurs in the same area. Information is not necessarily lost as in most cases the true intensity is added to the artefact and is still detectable above the background. In some cases such as where strongly orientated and intense reflections are next to the weaker ones these can no longer be discerned. An example of this is shown in the copper-tin system, figure 5.57. This phenomenon is problematic at low diffraction angles (higher d-spacings) where the curvature of the virtual arc is more pronounced. Here the d-spacing range that the virtual are can potentially interact to produce a false maximum is higher.

The continuous nature of the data collection is an advantage of the extended beam illumination method. Investigations using the Al_2O_3 and Si composite samples help to quantify the extent of this advantage. The results from this experiment can be seen table 5.8 and figure 5.29. These results show that only 1.311 mm of Si on an Al_2O_3 substrate will produce a discernable Si diffraction pattern. When this is increased into the 1.49 mm to 1.693 mm range 5 peaks, all the peaks that are present on this detectors angular range are detected.

This is enough for confident matching to accepted patterns allowing phase identification. The resolution in this respect could be improved further by X-ray scatter reduction. If a raster system with a 2 mm grid in used a phase limited to an area of the substrate of < 1.5 mm could be missed by conventional point source collection but still detected by the extended beam.

While this continuous nature of the data collection constituted a major advantage it is also this property of the data that when expressed through the partitioning equation produces the noise that detracts from the method. One question to be considered is whether the chosen partitioning equation (explained in section 1.3.1) could be modified to improve some aspects of the data quality.

Possible alterations the partitioning equation above has both positive and negative implications. One area of potential improvement is in processing speed. Simplifying the equation is achieved by removing the normalisation of the intensity assigned to each point, thus leaving the results assigned to each point as the total intensity overlaid by the beam, i.e.

$$In(d,y) = \int_{\chi_1}^{\chi_2} I_{2\theta,y}(\chi)d\chi$$

This will increase the processing speed by ≈ 10 % but has the effect that intensity points where the virtual arc is only partially covering the detector will have reduced intensity. However if this change was adopted two points on the substrate producing two identically intense arcs with the same 2θ value could be assigned up to a 50 % reduction in intensity between the middle and edge of the detector solely due to this process. This may not constitute a major problem as if the detector is rectangular. At any y position the relative intensities of the peaks would remain constant, that is the relative intensities of the different reflections from one position on the substrate would not change.

The normalisation has the disadvantage of exaggerating the effect of interferences present in some positions on the detector. This can be explained by considering unwanted 'hot spots' caused by either large grains, as can be seen in the copper-lead system (figure 5.46) or faulty pixels that can occur on charge coupled detectors. If this was present in a corner of a rectangular detector it would be overlaid by a relatively short virtual arc. When the normalisation was introduced to compensate for this short arc the intensity of the false pixel would be amplified by the proportions of the differences in arc lengths.

$$\frac{\chi_{2max} - \chi_{1max}}{\chi_{2short} - \chi_{1short}}$$

Another possibility is to confine the azimuthal limits of the virtual arc in a manner unrelated to the detection area limits. During the completed partitionings these limits were set as wide as possible to give the largest possible contrast between a full or partial match between the diffraction ring and the virtual arc. Setting smaller limits would have the advantage of reducing processing time and could potentials reduce some mechanisms for interference. An example of this is that the 'bow-tie' artefact seem in the partitioned data would be reduced as the unwanted interactions that cause this effect will be reduced.

Confining the sweep of the virtual arc could be potentially useful in gathering additional information about the materials being characterised. The partitioning with open limits as has been carried out in the results depicted in this investigation could be complimented by the same partitioning carried out with a truncated arc. The comparison of the two results would give information on the orientation of the samples planes in a quantitative way. This would be superior to the qualitative study of partitioning artefacts discussed (section 6.4) in conjunction with the copper-lead system figures 4.38, 4.39 and 5.46.

For significant additional improvement, totally different alternative approaches should be considered. One of these approaches is the developments of an arc matching method where a series of potential pattern can be created. These simulations could be then matched against the extended beam illumination data collection image. Improvements to the simulated intensity profile in a way similar to a two dimensional Rietveld refinement is possible. In conventional diffraction this systematic improvement allows an efficient matching of the theoretical model to the collected data [106] [181]. Similar results are hoped for when using a two-dimensional system. As in the established Rietveld method the system envisaged uses peak position information calculated from first principles using lattice parameter and space group information. To fulfil the requirement for the extended beam work this calculation would have to be carried out for multiple y positions with the calculated diffraction arcs being overlaid. Additional information such as the particular elements included, their ionic state and position in the unit cell would be required to predict the relative intensities of the calculated peaks [182]. Taking this information from established diffraction standard cards would allow the introduction of these variables.

It is hoped that this method will produce a fast and accurate determination of the libraries content and will be able to compensate for morphological effects such as preferred orientation. Whether this approach could compensate for large grain size has not been established, this effect is too random potentially adding more variables than can realistically be simulated.

Chapter 7

7 Conclusions

The conclusions addressed here cover two main areas based on the experimental results. The first to be addressed is the production of the combinatorial libraries by various methods and their conventional characterisation. The second is the evaluation of the new extended beam X-ray diffraction method in a theoretical respect and in relation to the results obtained from chemical libraries. In addition to these, recommendations for future work that would compliment this investigation have been outlined.

7.1 Production of libraries

One of the key objectives of this investigation was to determine the practicality of using a range of production methods for combinatorial library fabrication. Direct current magnetron sputtering using a geometric arrangement is already well established in combinatorial thin film production [3] [6] [18]. In this context these samples serve as benchmarks to which the samples produced by novel methods are compared.

All of the production methods investigated produced at least some samples that are suitable for EDS and XRD analysis as excessive surface topography and defects such as pinholes are rare. Some of the combinations of elements produced sample regions that are prone to substrate de-adherance. While this is an accepted problem with combinatorial thin films [126], this finding still needs to be highlighted as a disadvantage of the process researched.

RBS depth profiling and subsequent modelling confirmed the homogeneity of the sputtered systems. It also illustrates the transition of a multilayer to a single layer arrangement for the electrodeposited libraries. Comparison of the EDS and RBS elemental composition calculations and the subsequent finding that the results obtained by both methods are equivalent within experimental error meant that these results can be quoted with a high degree of confidence.

Electrochemical deposition of metallic elements is already widely used for the production of uniform thin film samples [61] [71] so it was deemed desirable to adapt this method. The sputtered layer employed in all cases provided a conducting surface to allow deposition and a

surface alloying a strong adhesion between the entire library and the substrate. This showed that the sputtering and then electrodeposition combination used conventionally [64] is viable for this type of combinatorial fabrication. The deposition method used here, namely changing the level of the electrolytic fluid during the deposition, did not markedly change the deposition variables other than the intended variable, deposition time. This has been demonstrated by the production of CuBi layers as precursor materials for PV applications by conventional and combinatorial methods. In these cases, both the precursors and the final compounds had the same structural and elemental composition regardless of the fabrication method. The predictable nature of these depositions with no additional factors over the variables considered for uniform films has also been illustrated by its employment for a number of binary compositional spreads.

Only the zinc films showed artefacts from the combinatorial electrochemical production method. Tide patterns are thought to be caused by the irregular movement of the meniscus of the solution, possibly due to a high surface tension. A possible way to reduce this effect is by altering the composition of the solution to reduce the surface tension. However, for the purpose of this investigation having an efficient deposition solution with a high throwing power and effective diffusion rates were considered priorities.

The layers produced combinatorially have been shown to diffuse successfully and form alloyed thin films, with underlying substrate layers remaining inert. The formation of the metallic and intermetallic alloys relates to the position on the substrate. This shows that the ratio of the layer thicknesses are, as originally proposed, the major factor in the formation of a particular phase. Homogeneity of the films with respect to depth was not fully achieved at several points on some libraries. This is exemplified by the presence of elemental XRD signatures co-existing in alloy phase rejoins where they would not be expected. Changing the post deposition annealing conditions to impart greater energy would increase diffusion and through this homogeneity. However more aggressive annealing conditions can favour the production of certain alloy phases whose formation is limited by temperature. An example of this is the selenisation of copper-zinc-tin where the production of $CuSe_2$ Cu_5Zn_8 and Cu_6Sn_5 is favoured at 250 °C while a high yield of $Cu_2ZnSnSe_4$ is produced at > 370°C [183]. From this, we can infer that selecting a different temperature is not always appropriate. Even if the reduced temperature hold for a period was added after the high temperature cycle to speed alloying and before the final cooling the resulting spreads would not be representative of the desired isothermal sections of the phase diagram. This type of consideration is more pressing

for substrates that hold high density chemical libraries due to the requirement to consider all the potential compounds.

Electrostatic spray deposition of elemental compositional gradients has been partially achieved during this study. While a gradient has been achieved it has proved difficult to control the transition region, the interactions between cones from the different sources being a subtle but still significant obstacle to simultaneous deposition. The alternative sequential deposition detracts significantly from this method as it requires a more aggressive post-deposition diffusion procedure. Switching between the sources quickly to produce a densely layered structure is a possible compromise as stacks of very thin layers will interdiffuse more readily.

The precursor solutions based on the metal acetates have been chosen as these dissolved in the C_2H_5OH/H_2O solvent giving a solution of acceptably low surface tension. Sulphur was deposited from thiourea as this is known to undergo pyrolisis to leave elemental sulphur [169]. The change to low temperature depositions with post-deposition anneals was required to improve film quality and to reduce variation in film morphology. The negative aspect of the two step process is that it has added to the oxidation of the films. Films produced in this way were also more prone to macro scale cracking during the heat treatment process.

Samples produced with the electrospray method showed changing morphology effect as a result of the particle flight time and cone position differences employed to create the compositional gradient. This effect comes in addition to the effects of elemental composition and is measured even in samples where no stociometric gradients exist.

7.2 Extended beam method

The partitioning algorithm has been proven to be successful for idealised samples by the use of simulations. For idealised samples, measured inside a preset calibration range, the d-spacing calculation error was less than the value of one grid point. If this could be achieved with real samples, the error would be less than one pixel on the detector. The results for calculation of the position on the sample show only statistically insignificant differences from the original patterns when measured from the maximum intensity values. The simulated systems show a characteristic ‘bowtie’ artefact that is a product of this method of partitioning. This information could be used in future developments to compensate for this interference.

The effect of preferred orientation and large grain size was also investigated using the simulated diffraction patterns. The partitioning process has been shown to be robust in respect to most orientated samples. The characterisation of planes lying parallel to the surface of the sample actually improves the process, producing peaks with a smaller FWHM in respect to d-spacing. The measurement of both d-spacing and position on the sample of highly preferred samples cannot be accurately carried out for planes that lie close to perpendicular to the sample surface. This demonstrates a shortcoming of the technique.

Phantom samples have been used to show that the partitioning on the results of real samples has the same characteristics as those observed in the idealised simulated cases. The resolution in these examples has been shown (in the Al_2O_3/Si investigation) to exceed the 2 mm requirement for position on the sample detection and positioning. This resolution allows for direct comparison with the 2 mm raster scanned data collection. Using this principle a data collection speed of up to 12 times faster can be accomplished with this experimental setup. Changes to the experimental setup outside the scope of this investigation would lead to even greater time savings.

Application of the extended beam method to phantom samples has shown that the method is applicable to a wide range of incident angles. A low incident angle of 5° does not have a significant effect on the partitioning process and this finding adds to the types of thin film samples to which the method can be applied. The investigation has indicated that the partitioning can also be applied to data collections where the X-ray detector is in a large range of positions allowing the determination of peaks covering a wide angular range.

Application of the partitioning to the sputtered samples showed significant benefits over conventional point source data collections. These samples are generally consistent in surface topography over the illumination area. They also show similar diffraction intensity from a variety of adjacent positions over the characterisation area. This range of characteristics allows the most productive use of the demonstrated partitioning procedure.

When applied to the high quality sputtered samples, the calculation of d-spacing for a range of positions on the substrate has been shown to equal that of the point source collected data within an accepted experimental error. Highly orientated samples produced by deposition onto single crystal silicon substrates were also successfully characterised. The significant broadening of the diffraction peaks from the main reflections was no more extensive in the partitioned data than that seen in the point source compilations.

The application of the extended beam method to the electrodeposited samples had to overcome several different sample characteristics. The rapid transition between phases is advantageous for the new XRD method as the distinct phase profiles can be easily discerned. In addition a larger portion of the phase diagrams could be encompassed by a single data collection. The negative aspect to these rapid phase changes is that they are often accompanied by changes in reflection intensity. The abrupt changes in reflection intensity detract from the partitioning method as intense artefacts can obscure weaker diffraction peaks. However careful analysis of the resultant partitioned images produce minimal loss of data in most cases. Samples containing materials with a large grain size were produced by the electrodeposition method. Characterisation of these libraries using the partitioning process was problematic, the additional partitioning artefacts being considerable. These artefacts detract from the signal to noise ratio but the calculated d-spacing and positioning of the diffracting materials was unaffected.

Combining the extended beam diffraction results with EDS measurements gives clear and accurate measurement of the effect of the stociometric shifts on measured lattice parameters. Employment of the method to determine the compositions leading to a particular phase shift has been successfully carried out with the expected savings in data collection time. In the same way the extended beam method has been used to link lattice parameter and composition changes when analysing samples that exhibit Vegard's shifts.

Application to the electrostaticaly sprayed samples showed that the information obtained from the new method is comparable with the conventional raster scan compilations. The finding that the two diffraction methods yield the same results is inconclusive as for several libraries the electrostatic sample production encouraged characteristics detrimental to XRD characterisation. Factor such as microcrystalline material structure and low intensity X-ray reflections contributed to the paucity of quantitative data collected by either method.

Adapting the extended beam data collection method to a synchrotron X-ray source has been shown to be successful. Adaption of the extended beam to the synchrotron source was not fully optimised in the limited beam time available. These time constraints also limited the range of samples that were characterised. Considering this the results are positive with future improvements likely. A higher signal to noise has been seen in the results of samples when illuminated with the synchrotron source. This is most likely to be caused by the more highly collimated X-ray produced by this source. Higher resolution of the detector available was

also beneficial. Application of the method to the synchrotron is even more desirable than for X-ray tube based systems as the savings in data collection time are more important where the beam time to collect data is limited.

8 References

[1] Schuktz, P. G., Xiang, X-D. (1998). Combinatorial approaches to materials science. *Current Opinion in Solid State & Materials Science,* 3, p. 153-158.

[2] Wang, J., Yoo, Y., Gao, C., Takeuchi, I., Sun, X., Chang, H., Xiang, X-D., Schultz, P.G. (1998). Identification of a blue photoluminescent composite material from a combinatorial library. *Science,* 279, p. 1712-1714.

[3] Hanak, J. J. (2004). A quantum leap in the development of new materials and devices. *Applied Surface Science,* 223, p. 1-8.

[4] Pharr G.M. George E.P (2006) Development of combinatorial methods for alloy design and optimization. *U.S. depertment of energy publications.*

[5]Hanak, J. J. (1971). Compositional Determination of rf Co-Sputtered Multicomponent Systems. *The Journal of Vacuum Science and Technology,* 8, 1, p. 172-175.

[6] Xiang, X-D., Takeuchi, I. Combinatorial Materials Synthesis. Marcel Dekker Inc.
ISBN 0-8247-4119-6.

[7] Amis, E. J., Xiang, X-D., Zhao, J-C. (2002). Combinatorial materials science: what's new since Edison? *MRS Bulletin*, p. 295-300

[8] Koppitz, M., Eis, K. (2006). Automated Medicinal Chemistry. *Drug Discovery Today*, 11, 11/12, p. 561-568.

[9] Storer, R. (1996). Solution-phase Synthesis in Combinatorial Chemistry: Applications in Drug Discovery. *Drug Discovery Today*, 1, 6, p. 248-254.

[10] Klanner C. (2004) The Development of Descriptors for Solids: Teaching "Catalytic Intuition" to a Computer. *Angewandte Chemie International Edition*, 43, 40 p. 5347-5349.

[11] Chisholm B.J. Webster D.C. (2007) The development of coatings using combinatorial high throughput methods: a review of the current status. Jornal of coating technology research, 4, p. 1-12.

[12] Yajima, K., Ueda, Y., Tsuruya, H., Kanougi, T., Oumi, Y., Ammal, S. C.,Takami, S., Kubo, M., Miyamoto, A. (2000). Combinatorial Computational Chemistry Approach to the Design of deNO_x Catalysts. *Applied Catalyst A: General*, 194-195, p. 183-191.

[13] Corma, A., Diaz-Cabanas, M., Moliner, M., Martinez, C. (2006). Discovery of a New Catalytically Active and Selective Zeolite (ITQ-30) by High-Throughput Synthesis Techniques. *Journal of Catalysis,* 241, 2, p. 312-318

[14] Zhao, J-C. (2006). Combinatorial approaches as effective tools in the study of phase diagrams and composition-structure-property relationships. *Progress Materials Science,* 51, p. 557-631.

[15] Senkan S. (2001) Combinatorial heterogeneous catalysis – a new path in an old field. Angewandle chemie interational edition, 40, p. 312- 329

[16] Takeuchi, I., Lippmaa, M., Matsumoto, Y. (2006). Combinatorial Experimentation and Materials Informatics. *MRS Bulletin,* 31 p. 999-1002.

[17] Cekedaa, M., Panjan, P., Dolinsek, J., Zalar, A., Medunic, Z., Jaksic, M., Radic, N. (2007). Diffusion during annealing of Al/Cu/Fe thin films. *Thin Solid Films,* 515, p. 7135-7139.

[18] Zhao, J. (2001). A combinatorial approach for structural materials. *Advanced Engineering Materials*, 3, 3, p. 143-146.

[19] Rar A. Frafjord J.J. Fowlkes J.D. Specht E.D. Rack P.D. Santella M.L. Bei H. George E.P. Pharr G.M. (2005) PVD synthesis and high-througput property characterization of Ni-Fe-Cr alloy libraries. *Measurement science and technology*, 16, p. 46-53.

[20] Song R. Chiang M.Y.M. Crosby A.J. Karim A Amis E.J. Eidelman N. (2005) combinatorial peel tests for the characterization of adhesion behaviour of polymeric films. *Ploymer* 46 p. 1643-1652.

[21] Cawse J.N. (2002) Experimental design for combinatorial and high throughput materials development. *John wiley and sons inc*. p. 79-83.

[22] Lin S. Huang J. (2004) effect of thickness on the structural and optical properties of ZnO films by r.f. magnetron sputtering. *Surface and coatings technology*, 185, p. 222-227.

[23] Garrido J. Gerstenberg D. And Berry W. (1977) Effect of angle of incident during deposition on Ti-Pd-Au conductor film adhesion. *Thin solid films*, 41, p.87-103.

[24] Markvart, T. (1994). Solar Electricity. John Wiley and sons Ltd. ISBN 0-471-94161-1.

[25] Shah, A., Torres, P., Tscharner, R., Wyrsch, N., Keppner, H. (1999). Photovoltaic technology: the case for thin-film solar cells. *Science,* 285, p.692-698.

[26] Miles R.W. Haynes K.M. Forbes I. (2005) Photovoltaic solar cells: An overview of state-of-the-art cell development and environmental issues. *Progress in crystal growth and the characterisation of materials*, 51, p.1-42.

[27] Gratzel, M. (2005). Solar Energy Conversion by Dye-Sensitized Photovoltaic Cells. *Inorganic Chemistry,* 44, 20, p. 6841-6851.

[28] Hara, K., Horiguchi, T., Kinoshita, T., Sayama, K., Arakawa, H. (2001). Influence of electrolytes on the photovoltaic performance of organic dye-sensitized nanocrystalline TiO_2 Solar cells. *Solar Energy Materials & Solar Cells,* 70, p. 151-161.

[29] Gratzel, M., (2003). Dye-sensitized solar cells. *Journal of Photochemistry and Photobiology C,* 4, p. 145-153.

[30] Chopra, K. L., Paulson, P. D., Dutta, V. (2004). Thin-Film Solar Cells: An Overview. *Progress in Photovoltaics,* 12, p. 69-92.

[31] Nakamura, S., Yamamoto, A. (2001). Electrodeposition of pyrite (FeS_2) thin films for photovoltaic cells. *Solar Energy Materials & Solar Cells*, 65, p. 79-85.

[32] Gerein, N. J., Haber, J. A. (2005). Cu_3BiS_3, Cu_3BiS_4, Ga_3BiS_3 and $Cu_5Ga_2BiS_8$ as potential solar absorbers for thin film photovoltaics. p. 159-162.

[33] Chan, K-Y., Luo, P-Q., Zhou, Z-B., Tou, T-Y., Teo, B-S. (2008). Influence of direct current plasma magnetron sputtering parameters on the material characteristics of polycrystalline copper films. *Applied Surface Science,* 255, p. 5186-5190.

[34] Schurr, R., Holzing, A., Jost, S., Hock, R., Vob, T., Schulze, J., Kirbs, A., Ennaoui, A., Lux-Steiner, M., Weber, A., Kotschau, I., Schock, H-W. (2009). The crystallisation of Cu_2ZnSnS_4 thin film solar cell absorbers from co-electroplated Cu-Zn-Sn precursors. *Thin Solid Films,* 517, p. 2465-2468.

[35] Taunier, S., Sicx-Kurdi, J., Grand, P. P., Chomont, A., Ramdani, O., Parissi, L., Panhelux, P., Naghavi, N., Hubert, C., Ben-Farah, M., Fauvarque, J. P., Connolly, J., Roussel, O., Mogensen, P.,

Mahe, E., Gullemoles, J. F., Lincot, D., Kerrec, O. (2005). Cu(In,Ga)(S,Se)$_2$ solar cells and modules by electrodeposition. *Thin Solid Films*, 480-481, p. 526-531.

[36] Thelakkat, M., Schmitz, C., Neuber, C., Schmidt, H-W. (2004). Materials Screening and Combinatorial Development of Thin Film Multilayer Electro-Optical Devices. *Macromolecular Rapid Communications,* 25, p. 204-223.

[37] Neuber, C., Bate, M., Thelakkat, M., Schmidt, H-W., Hansel, H., Zettl, H., Krausch, G. (2207). Combinatorial preparation and characterization of thin-film multilayer electro-optical devices. *Review of Scientific instruments,* 78, p. 1-11.

[38] Mattox, D. M. (1998). Handbook of Physical Vapor Deposition (PVD) Processing William Andrew Publishing.

[39] Müller, J., Nowoczin, J., Schmitt, H. (2006). Composition, structure and optical properties of sputtered thin films of CuInSe$_2$. *Thin Solid Films*, 496, p. 364-370.

[40] Gordillo, G., Grizález, M., Hernandez, L. C. (1998). Structural and electrical properties of DC sputtered molybdenum films. *Solar Energy Materials and Solar Cells,* 51, p. 327-337.

[41]Fowlkes, J. D., Fitz-Gerald, J. M., Rack, P. D. (2006). Ultraviolet emitting $(Y_{1-x}Gd_x)_2O_{3-\delta}$ thin films deposited by radio frequency magnetron sputtering: combinatorial modelling, synthesis, and rapid characterization. *Thin Solid Films,* 510, p68-76.

[42]Black, M., Cooper, J., McGinn, P. (2005) Scanning electrochemical microchemical microscope characterization of thin film combinatorial libraries for fuel cell electrode applications. *Measurement Science and Techology,* 16, p174-182.

[43] Haber, J. A., Gerein, N. J., Hatchard, T. D., Versavel. M. Y. (2005) Combinatorial discovery of new thin film photovoltaics. p.155-158.

[44]Perkins, J. D. Taylor M.P., van Hest, M. F. A. M., Teplin, C. W., Alleman, J. L., Dabney, M. S., Gedvilas, L. M., Keyes, B. M., To, B., Readey, D. W., Delahoy, A. E., Guo, S., Ginley, D. S. (2005) Combinatorial optimization of transparent conducting oxides (TCOS) for PV. *Conference proceeding Photovoltaic Sciences (Florida)*.

[45] Ginley, D. S., van Hest, M. F. A. M., Young, D., Teplin, C. W., Alleman, J.L., Dabney, M. S., Parilla, P., Gedvilas, L.M., Keyes, B. M., To, B., Perkins, J. D., Taylor, M.P., Readney, D. (2005). Combinatorial exporation of novel transparent conducting oxide materials. *Conference paper NREL/CP-520-38999.*

[46] Van Hest, M. F. A. M., Dabney, M. S., Perkins, J. D., Ginley, D. S. (2005). High-mobility molybdenum doped idium oxide. *Thin Solid Films*, 496, p. 70-74.

[47] Vossen, J. L., Kern, W. (1978). Thin film processes. Academic Press Inc. ISBN 0-12-728250-5.

[48] Chan, K-Y., Tou , T-Y., Teo, B-S. (2006). Thickness dependence of the structural and electrical properties of copper films deposited by dc magnetron sputtering technique. *Microelectronics Journal*, 37, p. 608-612.

[49] Chan, K-Y., Teo, B-S. (2007). Investigation into the influence of direct current (DC) power in the magnetron sputtering process on the copper crystallite size. *Microelectronics Journal,* 38, p. 60-62.

[50] Chan, K-Y., Teo, B-S. (2006). Atomic force microscopy (ATM) and X-ray diffraction (XRD) investigations of copper thin films prepared by dc magnetron sputtering technique. *Microelectronics Journal*, 37, p. 1064-1071.

[51] Chen, W., Liu, Q., Liu, Q., Zhu, L., Wang, L. (2008). A combinatorial study of the corrosion and mechanical properties of Zn-Al material library fabricated by ion beam sputtering. *Journal of Alloys and Compounds.* 459. p. 261-266.

[52] Pagh Almtoft, K., Kristensen, M., Chevallier, J., Bøttiger, J. (2007). Characterization of nanostructured Cr_2N_x/Cu multilayers deposited by reactive DC magnetron sputtering. *Surface & Coatings Technology*, 201, p. 4767-4776.

[53] Thornton, J. A., Hoffman, D. W. (1989). Stress-related Effects in Thin Films. *Thin Solid Films,* 171, p. 5-31.

[54] Tamylevicius, S. (1998). Stress and strain in the vacuum deposited thin films. *Vacuum,* 51, 2, p. 127-139.

[55] Xilian, S., Jianda, S. (2006). Influence of Cr interlayer on the structure and optical properties of Ag films on grass substrate by magnetron sputtering. *Applied Surface Science.* 253 p. 2093-2095.

[56] Scofield, J. H., Duda, A., Albin, D., Ballard, B.L., Predecki, B. L. (1995). Sputtered molybdenum bilayer back contact for copper indium diselenide-based polycrystalline thin-film solar cells. *Thin Solid Films*, 260, p. 26-31.

[57] Ko, J. H., Kim, I. H., Kim, D., Lee, K.S., Lee, T.S., Cheong, B., Kim, W.M. (2007). Transparent and conducting Zn-Sn-O thin films prepared by combinatorial approach. *Applied Surface Science,* 253, p. 7398-7403.

[58] Deng, Y. P., Guan, Y. F., Fowles, J. D., Wen, S. Q., Liu, F. X., Pharr, G. M., Liaw, P.K., Liu, C. T., Rack, P. D. (2007). A combinatorial thin film sputtering approach for synthesizing and characterizing ternary ZrCuAl metallic glasses. *Intermetallics*, 15, p. 1208-1216.

[59] Chunsheng, E., Smith, D., Svedberg, E., Khizroev, Litvinov, D. (2006). Combinatorial synthesis of Co/Pd magnetic multilayers. *Journal of applied physics,* 99, p. 1-6.

[60] Meredith, J. C., Smith, A. P., Karim, A., Amis, E. J. (2000). Combinatorial materials science for polymer thin-film dewetting. *Macromlecules*, 33, p. 9747-9756.

[61] Medvedev, G. I., Makrushin, N. A. (2001). Electrodeposition of tin-antomony-copper alloy from sulphate electrolytes with organic additives. *Russian Journal of Applied Chemistry,* 74, 8, p. 1400-1402.

[62] Tittes, K., Plieth, W. (2007). Electrochemical deposition of ternary and binary systems from an alkaline electrolyte-a demanding way for manufacturing p-doped bismuth and antimony tellurides for the use in thermoelectric elements. *Journal of Solid State Electrochemistry*, 11, p. 155-164.

[63]Golia, S., Arora, M., Sharma, R. K., Rastogi, A. C. (2003). Electrochemically deposited bismuth telluride thin films. *Applied Physics*, 3, p. 195-197.

[64] Scragg, J. J., Dale, P. J., Peter, L. M. (2008). Towards sustainable materials for solar energy conversion: preparation and photoelectrochemical characterization of Cu_2ZnSnS_4. *Electrochemistry Communications,* 10, p. 639-642.

[65] Baeck, S. H., McFarland, E. W. (2002). Combinatorial electrochemical synthesis and characterization of tungsten-molybdenum mixed metal oxides. *Korean Journal of Chemical Engineering*, 19(4), p. 593-596.

[66] Jaramillo, T. F., Baeck, S. H., Kleiman-Shwarsctein, A., McFaland, E. W. (2004). Combinatorial electrochemical synthesis and screening of mesoporous ZnO for photocatalysis. *Macromolecular Rapid Communications,* 25, p. 297-301.

[67] Masuku E.S. Mileham A.R. Hardisty H. Bramley A.N Johal C. Detassis P. (2001) A Finite element simulation of the Electroplating process. *Electroplating*.

[68] Landolt, D. (1994) Electrochemical and materials science aspects of alloy deposition. *Electrochimica Acta,* 39, p. 1075-1090.

[69] Beattie, S. D., Dahn, J. R. (2005). Masked Electrodeposition of a composition-spread library of Sn-Zn alloys onto a 64-channel combinatorial cell plate. *Journal of the Electrochemical Society,* 152 (8) p.549-551.

[70] Beattie, S. D., Dahn, J. R. (2003). Comparison of electrodeposited copper-zinc alloys prepared individually and combinatorially. *Journal of the Eletrochemical Society,* 150, 11, p. 802-806.

[71] Beattie, S. D., Dahn, J. R. (2003). Single-bath electrodeposition of a combinatorial library of binary $Cu_{1-x}Sn_x$ alloys. *Journal of the Electrochemical Society,* 150(7), p. 457-460.

[72] Jayaraman, S., Hillier, A. C. (2005). Electrochemical synthesis and reactivity screening of a ternary composition gradient for combinatorial discovery of fuel cell catalysts. *Measurement Science and Technology,* 16, p.5-13.

[73] Jaworek, A., Sobczyk, A. T. (2008). Electrospraying route to nanotechnology: An overview. *Journal of Electrostatcs*, 66, p. 197-219.

[74] Hou, X., Choy, K-L. (2005). Synthesis and characteristics of $CuInS_2$ films for photovoltaic applications. *Thin Solid Films*, 480-481, p. 13-18.

[75] Ghimbeu, C. M., van Landschoot, R. C., Schoonman, J., Lumbreras, M. (2007). Tungsten trioxide thin films prepared by electrostatic spray deposition technique. *Thin Solid Films*, 515, P. 5498-5504.

[76] Mohamedi, M., Lee, S-J., Takahashi, D., Nishizawa, M., Itoh, T., Uchida, I. (2001). Amorphous tin oxide films: preparation and characterisation as an anode active material for lithium ion batteries. *Electrochimica Acta,* 46, p. 1161-1168.

[77] Dascalescu, L., Samuila, A., Rafiroiu, D., Iuga, A., Morar, R. (1999). Multiple-needle corona electrodes for electrostatic processes application. *IEEE Transactions on Industry Applications,* 35, 3, p. 543-548.

[78] Jaworek, A. (2007). Electrospray droplet sources for thin film deposition. *Journal of Material Science.* 42, p. 266-297.

[79] Colbert S.A. Cairncross R.A. (2005) A computer simulation for predicting electrostatic spray coating patterns. *Power technology*, 151, p. 77-86.

[80] Jayasinghe, S. N., Edirisinghe, M. J. Effect of viscosity on the size of relics produced by electrostatic atomization. *Aersol Science,* 33, p. 1379-1388.

[81] Ksapabutr, B., Panapoy, M, Choncharoen, K., Wongkasemjit, S., Traversa, E. (2008). Investigation of nozzle shape effect on $Sm_{0.1}Ce_{0.9}O_{1.95}$ thin film prepared by electrostatic spray deposition. *Thin Solid Films*, 516, p. 5618-5624.

[82] Cloupeau, M., Prunet-Foch, B. (1994). Electrohydrodynamic spraying functioning modes: a criticl review. *Journal of Aersol Science,* 25, 6, p. 1021-1036.

[83] Oh, H., Kim, K., Kim, S. (2008). Characterization of deposition patterns produced by twin-nozzle electrospray. *Aerosol Science,* 39, p. 801-813.

[84] Ghimbeu, C. M., Schoonman, J., Lumbreras, M., Siadat, M. (2007). Electrostatic spray deposited zinc oxide films for gas sensor applications. *Applied Surface Science*, 253, p. 7483-7489.

[85] Ghimbeu, C. M., Lumbreras, M., Siadat, M., van Landschoot, R. C., Schoonman, J. (2008). Electrostatic sprayed SnO_2 and Cu-doped SnO_2 films foe H_2S detection. *Sensors and Actuators B,* 133, p. 694-698.

[86] Li, J., Fan, H., Jia, X., Chen, J., Cao, Z., Chen, X. (2009). Electrostatic spray deposited polycrystalline zinc oxide films for ultraviolet luminescence device applications. *Journal of Alloys and Compounds,* 481, p. 735-739.

[87] Fujimoto, K., Onoda, K., Sato, M., Matsuo, H., Yamaguchi, T., Ito, S. (2008). High-throughput synthesis and evalution of thermochromic materials by a combinatorial approach. *Materials Science and Engineering.* 475, p. 52-56.

[88] Regele, J. D., Papac, M. J., Rickard, M. J. A., Dunn-Rankin, D. (2002). Effects of capillary spacing on EHD spraying from an array of cone jets. *Aerosol Science,* 33, p. 1471-1479.

[89] Tu K. N. (1973). Interdiffusion and reaction in bimetallic Cu-Sn thin films. Acta Metallurgica, 21, p. 347-353.

[90] Darken L.S. Oriani (1954). Thermal diffusion in solid alloys. Acta metallugica, 2, p. 841- 847.

[91] Tamura N. Ohshita R. Fujimoto M. Fujitani S. Kamino M. Yonezu I. (2002). Study on the anode behaviour of Sn and Sn-Cu alloy thin-film electrodes. Journal of power sources, 107, p. 48-55.

[92] Panjan P. Cekada M. Dolinsek J. Vrtic B. Zalar A. (2008) Diffusion processes during heat treatment of Al-Cr-Fe thin films. *Vacuum*, 82, p. 286-289.

[93] Hadouda H. Pouzet J Berede J.C. Barreau A (1995). MoS_2 thin film synthesis by soft sulfurisation of a molybdenum layer. *Materials Chemistry and Physics*, 42, p. 291-297.

[94] Estrella V. Nair M.T.s. Nair P.K (2003) semiconducting Cu_3BiS_3 thin films formed by the solid-state reaction of CuS and bismuth thin films. *Semiconductor science technology*, 18, p. 190-194.

[95] Guillen C. Martinez M.A. Herrero J. (2000). $CuInSe_2$ thin films obtained by a novel electrodeposition and sputtering combined method. *Vacuum*, 58, p.594-601.

[96] Pisarkiewicz T. Jankowski H. (2003) Vacuum selenisation of metallic multilayers for CIS solar cells. *Vacuum*, 70, p.435-438.

[97] Watanabe H. (2001) Interface engineering of a ZrO_2 / SiO_2 / Si layered structure by in situ re-oxidation and its oxygen-pressure-dependent thermal stabilisation. *Applied physics letters*. 78, 24, p. 3803-3806.

[98] Verma H.R. (2007) Atomic and nuclear methods. *Springer-Verlag Berlin Heidelberg.* ISBN 10-3-540-30277-8.

[99] Cullity, B. D., Elements of X-ray diffraction. Second Edition. (1978). ISBN 0-201-01174-3. Addison-Wesley publishing company, inc.

[100] Kulkarni A.K. Schulz K.H. Lim T.S. Khan M. (1999) Dependence of the sheet resistance of indium-tin-oxide thin films on grain size and grain orientation determination from X-ray diffraction techniques. *Thin solid films*, 345, p. 273-277.

[101] Van Heerden J.L. Swanepoel R. (1997) XRD analysis of ZnO thin films prepared by spray pyrolysis. *Thin solid films*, 299 p. 72-77.

[102] Purica M. Budianu E. Rusu E. Danila M. Gavrila R. (2002) Optical and structural investigation of ZnO thin films prepared by chemical vapour deposition (CVD). *Thin solid films*, 403, 404, p. 485-488.

[103] Contreras M. A. Romero M. J. Noufi R. (2006) Characterisation of Cu(In,Ga)Se_2 materials used in record performance solar cells. *Thin solid Films*, 511, 512 p. 51-54.

[104] Vigil O. Zelaya-angel O. Rodriguez Y. (2000) Changes in the structure and optical properties of cubic CdS films on annealing in H2 and air atmospheres. *Semiconductor science technology*, 15, p.259-262.

[105] Shao L.X. Chang K.H. Hwang H. L. (2003) Zinc sulphide thin films deposited by RF reactive sputtering for photovoltaic applications. *Applied Surface Science*, 212 p. 305-310.

[106] Jenkins, R., Snyder, R. L. Introduction to X-ray powder diffractometry. (1996). ISBN 0-471-51339-3. John Wiley and Sons Inc.

[107] Phatak S.B. Bedair S.M. (1980) Electrical properties of manganese doper $Ga_{1-x}In_xAs$ grown by liquid phase epitaxy. *Solid-state electronics*, 23 p. 839-844.

[108] Damonte L.C. Donderis V. Hernandez-fenollosa M.A. (2009) Trivalent dopents on ZnO semiconductor obtained by mechanical milling. *Journal of alloys and compounds*, 483 p. 442-444.

[109] Takeuchi, I., Long, C. J., Famodu, O. O., Murakami, M., Hattrick-Simpers, J., Rubloff, G. W. (2005). Data management and visualization of X-ray diffraction spectra from thin film ternary composition spreads. *Review of Scientific Instruments.* 76, 062223, p. 1-8.

[110] Hatchard T.D. Dahn J.R. Trussler S. Fleischauer Bonakarpour A. Mueller-Neuhaus J.R. Hewitt K.C. (2003) The amorphous range in sputtered Si-Al-Sn films. *Thin solid films*, 443 p. 144-150.

[111] Ohtani, M., Fukumura, T., Kawasaki, M., Omote, K., Kikuchi, T., Harada, J., Ohtomo, A., Lippmaa, M., Ohnishi, T., Komiyama, D.., Takahashi, R., Matsumoto, Y. Concurrent x-ray diffractometer for high throughput structural diagnosis of epitaxial thin films. *Applied Physics Letters,* 79, 22, p. 3594-3596.

[112] Jenkins, R., Gould, R W., Gedcke, D. (1995). Quantitative X-ray spectrometry. Marcel Dekker inc ISBN 0-8247-9554-7.

[113] Dinnebier R.E. Bilinge S.J.L. (2008) Powder diffraction theory and practice. *RSC publishing* p. 24-43 ISBN 978-0-854404-231-9.

[114] Rogers, K. D., Painter, J.D., Lane, D. W., Healy, M. (1999). The Structural Changes in CdS-CdTe Thin Films Due to Annealing. *Journal of Electronic Materials*, 28, 2, p. 112-117.

[115] Cui, J., Chu, Y. S., Famodu, O. O., Furuya, Y., Hattrick-Simpers, J., James, R. D., Ludwig, A., Thienhaus, S., Wuttig, M., Zhang, Z., Takeuchi, I. (2006). Combinatorial search of thermoelastic shape-memory alloys with extremely small hysteresis width. *Nature Materials,* 5, p. 286-291.

[116] Chu, Y. S., Tkachuk, A., Vogt, S., Ilinski, P., Walko, D. A., Mancini, D. C., Dufresne, E. M., He, L., Tsi, F. (2004). Structural investigation of CoMnGe combinatorial epitaxial thin films using microfocused syncotron X-ray. *Applied Surface Science,* 223, p. 175-182.

[117] Brundle R.C. Evens C.A. Wilson S. (1992) Encyclopaedia of materials characterisation – surface interfaces thin films *Elsvier*.

[118] Roy, P., Srivastava, S. K. Chemical bath deposition of MoS_2 thin film using ammonium tetrathiomolybdate as a single source for molybdenum and sulphur. (2006). *Thin Solid Films.* 496, p. 293-298.

[119] Goldstein J. Newbury D. Joy D. Lyman C. Echlin P. Lifshin E. Sawyer L. Michael J. (2007) Scanning electron microscopy and X-ray microanalysis. *Springer science*, ISBN 987-0-306-47272-3, p. 427-436.

[120] Goodhew PJ, Humphreys.J, Beanland R, electron microscopy and analysis, Taylor and Francis,(2001), ISBN 0-7484-0968-8

[121] Sahal, M., Mari, B., Mollar, M. (2009). $CuInS_2$ thin films obtained by spray pyrolysis for photovoltaic applications. *Thin Solid films,* 517, p. 2202-2204.

[122] Bozzini, B., Baker, M. A., Cavallotti, P. L., Cerri, E., Lenardi, C. (2000). Electrodeposition of ZnTe for photovoltaic cells. *Thin Solid Films,* 361-362, p. 388-395.

[123] Walls, J. (1988). Methods of surface analysis. Cambridge university press, ISBN 0-521-30564-0 p299-337.

[124] Feldman, L.C., Mayer, J.W. (1986). Fundamentals of surface and thin film analysis. North-Holland ISBN 0-444-00989-2, p 13-20.

[125] Peter L.M. Tribursch H. Nanostructured and photoelectrochemical systems for solar photonconversion. Imperial college press ISBN 978-1-86094-255-6.

[126] Gregoire, J. M., Dover, R. B., Jin, J., Disalvo, J., Abruna, D. (2007). Getter sputtering system for high-throughput fabrication of composition spreads. *Review of Scientific Instruments,* 78, p. 1-6.

[127] Scragg, J. J., Dale, P. J., Peter, L. M. (2009). Synthesis and characterization of Cu_2ZnSnS_4 absorber layers by an electrodeposition-annealing route. *Thin Solid Films ,*517, p. 2481-2484.

[128] Barbosa, L. L., de Almeida, M. R. H., Carlos, R. M., Yonashiro, M., Oliveira, G. M., Carlos, I. A. (2005). Study and development of an alkaline bath for copper deposition containing sorbitol as complexing agent and morphological characterization of the copper film. *Surface and Coating Technology,* 192, p. 145-153.

[129] Subramanian, B., Sanjeeviraja, C. (2001). Cathodic electrodepositon and analysis of SnS films for photoelectrochemical cells. *Materials Chemistry and Physics,* 71, p. 40-46.

[130] Katagiri H. Cu_2ZnSnS_4 thin film solar cells. *Thin solid films*, 480, p. 426-432

[131] Katagiri H. Sasaguchi N. Hando S. Hoshino S. Ohshi J. Yokota T. (1997) Preparation and evaluation of Cu2ZnSnS4 thin films by sulurization of E-B evaporated precursors. Solar energy materials and solar cells. 49, p.407-414.

[132] Jiang, S., Huang, Y-H., Luo, F., Du, N., Yan, C-H. (2003). Synthesis of bismuth with various morphologies by electrodeposition. *Inorganic Chemistry Communications,* 6, p. 781-785.

[133] Sandnes, E., Williams, M. E., Bertocci, U., Vaudin, M. D., Stafford, G. R. (2007). Electrodeposition of bismuth from nitric acid electrolyte. *Electrochimica Acta,* 52, p. 6221-6228.

[134] Roncallo, S., Painter, J. D., Cousins, M. A., Lane, D. W., Rogers, K. D. (2008). A method to quantify the degree of uniformity of thickness of thin films. *Thin Solid Films*, 516, p. 8493-8497.

[135] Rees D.G. (2001) Essential statistics, *Chapman and Hall* p.343-344.

[136] Hu C. Wang C.K. Lee G.L. (2006) Composition control of tin-zinc deposits using experimental strategies. *Electrochimica acta*, 51, p. 3692-3698.

[137] Jiang B. Xian A. (2007) observations of ribbon-like whiskers on tin finish surface*. Journal of material science*, 18, p. 513-518.

[138] Massalski T.B. Murray J.L. Bennett L.H. Baher H. (1996) Binary alloy phase diagrams. American society of metals.

[139] Gremaud R. Broedersz C. Bosra D. Borgschult A. Mauron P. Schreuders H. Rector J. Dan B. Griessen R. (2007) Hydrogenography; An optical combinatorial method to find new light weight hydrogen storage materials*. Advanced materials*, 19, p. 2813-2817.

[140] Acosta M. Ares O. Sosa V. Acosta C. Pena J.L. (1999) Influence of the sputtering variables in the ion bombardment during off-axis deposition of $YBa_2Cu_3O_x$. *Journal of vacuum science and technology A*, 17, 5, p. 2879-2884.

[141] Spencer P.J. (1986) A thermal evaluation of the Cu-Zn system. Calphad, 10, 2 p. 175-185.

[142] Chen S. Chen C. Gierlotka W. Zi A. Chen P. Wu H. (2008) Phase equilibria of the Sn-Sb binary system. *Journal of electronic materials*, 37, 7, p. 992-1002.

[143] Fujiwara Y. (2003) Sn deposition onto Cu and alloy layer growth by a contact immersion process. Thin solid films, 425, p. 121-126.

[144] Abel F. Cohen C. Davies J.A. Moulin J. Schmaus D. (1990) Thin-film growth of Sn on Cu. *Applied surface science,* 44, p.17-27.

[145] Tu, K. N. (1996). Cu/Sn interfacial reactions: thin-film case versus bulk case. *Materials Chemistry and Physics*, 46, p. 217-223.

[146] Ashiru O.A. Shirokoff J. (1996) Electrodeposition and characterisation of tin-zinc alloy coatings. *Applied surface science,* 103, p. 159-169.

[147] Hartmann O. Harris I.R. Fort D. King P.J.C. Cox S.F.J. (2009) μSR studies of grey and white, tin α and β tin. *Physica B*, 404, p. 884-887.

[148] Gerein N.J. Harber J. (2005) Production of Cu_3BiS_3 photo absorbers. Photovoltaic specialists conference. Record of the thirty-first IEEE, 159.

[149] Mitsui K. Takahashi M. (1998) Effect of ternary addition on the formation of Cu_3Pt and CuPt order phases in the Cu-Pt system. *Philosophical magazine letters*, 77, p. 49-57.

[150] Krunks M. Mellikov E. (1995) Zinc oxide thin films by the spray pyrolysis method. Thin solid films, 270, p.33-36.

[151] Cottrell A. (1975) An introduction to metallurgy. *Edward Arnold,* ISBN 0-7131-2510-1.

[152] Krill C.E. Birringer R. (1998) Estimating grain-size distributions in nanocrystalline materials from X-ray diffraction profile analysis. *Philosophical magazine A*, 77, 3, p. 621-640.

[153] Gerin, N. J. Harber J. A. (2006). Synthesis of Cu_3BiS_3 thin films by heating metal and metal sulphide precursor films under hydrogen sulphide. *Chemistry of materials*, 18, p. 6289-6296.

[154] Bromba M and Zlegler H. (1981) Application hints for savitzky-golay digital smoothing filters. *Analytical Chemistry*, 53, p. 1583-1586.

[155] Major S. Banerjee A. Chopra K.L. (1986) Thickness dependent properties of Indium doped ZnO Films. *Thin solid films*, 143, p. 19-30.

[156] Chang J.F. Kuo H.H. Leu I.C. Hon M.H. (2002) The effect of thickness and operation temperature on ZnO Al thin film Co gas sensor. *Sensors and actuators B*, 84, p.258-264.

[157] Qiao Z. Latz R. Margel D. (2004) Thickness dependence of the In_2O_3:Sn film growth. *Thin solid films*, 466, p. 250-258.

[158] Padmaprabu C. Kuppusami P. Terrance A.L.E. Mohandas E. Raghunathan V.S. Banerjee S. Sanyal M.K. (2000) Microstructural characterisation of TiAl thin films grown by DC magnetron co-sputtering technique. *Material letters*, 43, p.106-113.

[159] Weast R.C. (1975) Handbook of chemistry and physics. *Chemical rubber publishing*, E-144 – E-182.

[160] Cheverrier V. Dahn J.R. (2006) The production and visualisation of quaternary combinatorial thin films. *Measurements in science and technology*, 17, p. 1399-1404.

[161] Wang N. (1994) the Cu-Bi-S system: results from low-temperature experiments. *Mineralogical magazine*, 58, p. 201-204.

[162] Wijesundera R.P. Siripala W. (2004) Preparation of $CuInS_2$ thin films by electrodeposition and sulphurisation for applications in solar cells. *Solar energy materials & solar cells*, 81, p. 147-154.

[163] Chi D.H. Binh L.T.T. Binh N.T. Khanh L.D. Long N.N. (2006) Band-edge photoluminescence in nanocrystalline ZnO:In films prepared by electrostatic spray deposition. *Applied surface science*, 252, p. 2770-2775.

[164] Choy K.L. Su B. (2001) Growth behaviour and microstructure of CdS thin films deposited by an electrostatic spray assisted vapour deposition (ESAVD) process. *Thin solid films*, 388, p. 9-14.

[165] Morales J. Sanchez L. Martin F. Ramos-barrado J.R. Sanchez M. (2005) Use of low temperature nanostructured CuO thin films deposited by spray-pyrolysis in lithium cells. *Thin solid films*, 474, p. 133-140.

[166] Kim J.H. Babushok V.I. Germer T.A. Mulholland G.W. Ehrman S.H. (2003) Cosolvent-assisted pyrolisis for the generation of metal particles. *Materials research society*, 18, 7, p. 1614-1622.

[167] Barletta M. Gisario A. Tagliaferri V. (2006) Electrostatic spary deposition (ESD) of polymeric powders on thermoplastic (PA66) substrate. *Surface coatings technology*, 201, p. 296-308.

[168] Aberle A.G. (2009) Thin-film solar cells. *Thin solid films*, 517, p. 4706-4710.

[169] Roncallo S. Painter J.D. Ritchie S.A. Cousins M.A. Finnis M.V. Rogers K.D. (2010) Evaluation of the different deposition conditions on thin films deposited by electrostactatic spray deposition using a uniformity test. *Thin solid films.* Available online.

[170] Baeck S.H. Jaramillo T.F. Brandli C. McFarland E.W. (2002) Combinatorial electrochemical synthesis and characterisation of tungsten-based mixed-metal oxides. *Journal of combinatorial chemistry*, 4, 6, p. 563-568.

[171] Ohring M. (1991) The Materials science of thin films. *Academic press INC*. p. 355 – 398. ISBN 0-12-524990-X.

[172] Kurihara M. Berg D. Fischer J. Siebentritt S. Dale P. (2009) Kesterite absorber layer uniformity from electrodeposited pre-cursors. *Physica statue solidi*, 6, 5, p. 1241-1244.

[173] Chou C. Chen S. (2006) Phase equilibria of Sn-Zn-Cu ternary system. *Acta materialia* 54, 9, p. 2393-2400.

[174] Taylor D.J. Fleig P.F. Hietala S.L. (1998) Technique for characterization of thin film porosity. *Thin solid films p.257-261.*

[175] Monolache S. Duta A. Isac L. Nanu M. Goossens A. Schoonman J. (2007) The influence of the precursor concentration on $CuSbS_2$ thin films deposited from aqueous solutions. *Thin solid films*, 515, p. 5957-5960.

[176] Gierlotka W. Jendrzejczyk-Handzlik D. (2009) Thermoodynamic description of the Cu-Sb binary system. *Journal of alloys and compounds*, 484, p. 172-176.

[177] Saha R. Barnard J.A. (1997) effect of structure on the mechanical properties of Ta and Ta(N) thin films prepared by reactive DC magnetron sputtering. *Journal of crystal growth*, 174, p. 495-500.

[178] Dicken A. Rogers K. Evens P. Rogers J. Chan J.W. (2010) the separation of X-ray diffraction patterns for threat detection. *Applied radiation and isotope*, 68, p. 439-443.

[179] Denton A. R. Ashcroft N. W. (1990) Vegard's law. *Physical review A*, 43, 6, p. 3161-3164.

[180] Ding Y.F Chen J.S. Liu E. (2005) Epitaxial $L1_0$ FePt films on $SrTiO_3$ (100) by sputtering. *Journal of crystal growth*, 276, p.111-115.

[181] Albinati A. Willis B.T.M. (2006) The Rietveld method. *International tables for crystallography* 8, 6, pp 710-712.

[182] Young R.A. (1993) The Rietveld method. *Oxford university press*. ISBN 0-19-855912-7.

[183] Volobujeva O. Raudoja J. Mellikov R.E. Grossberg M. Bereznev S. Traksmaa R. (2009) $Cu_2ZnSnSe_4$ films by selenization of Sn-ZnCu sequential films. *Journal of physics and chemistry of solids*, 70, p. 567-570.

9 Appendix

9.1 Instrument details

Sputter coater 1 - Bulzers ultra high vacuum UTT400 linked to a turbo pumped vacuum system the power supply is an Advanced Energy MDX1K. The targets are a US inc. low profile targets US gun 2 sputter source.

Sputter coater 2 - Angstrom sciences Onyx-2 magnetron sputtering system with a four gun arrangement.

XRD – Bruker D8 with a general analysis diffraction detector system GADDS detector.

SEM – Jeol 84A using genesis EDAX collection and processing software.

Alpha step - Ten Core surface profiler.

Interferometer – Micro XAM Interferomic surface profiles.

9.2 List of publications

Research paper – Roncallo S. Karimi O. Rogers K.D. Lane D.W. Ansari S.A. (2009). An approach to high-throughput X-ray diffraction analysis of combinatorial polycrystalline thin film libraries. *Journal of applied crystallography* 42, 2, p. 174-178.

Research paper – Roncallo S. Karimi O. Rogers K.D. Gregoire J.M. Lane D.W. Scragg J.J. Ansari S.A. (2010) High throughput X-ray diffraction analysis of combinatorial polycrystalline thin films. *Analytical chemistry* 82, 11, p. 4564-4569.

Poster presentation Analytical Research Forum 21st to 23rd July 2008 University of Hull

Poster presentation Analytical Research Forum 13th to 15th July 2009 University of Kent

Poster presentation 17th Interdisciplinary Surface Science Conference 30th March to 2nd April 2009 University of Reading